

INERTIAL ELECTROSTATIC  
CONFINEMENT: THEORETICAL AND  
EXPERIMENTAL STUDIES OF SPHERICAL  
DEVICES

---

A Dissertation  
presented to  
the Faculty of the Graduate School  
at the University of Missouri-Columbia

---

In Partial Fulfillment  
of the Requirements for the Degree

Doctor of Philosophy

---

by  
RYAN MEYER

Dr. Mark Prelas, Dissertation Supervisor  
Dr. Sudarshan Loyalka, Dissertation Supervisor

DECEMBER 2007

The undersigned, appointed by the dean of the Graduate School, have examined the dissertation entitled

INERTIAL ELECTROSTATIC CONFINEMENT: THEORETICAL AND  
EXPERIMENTAL STUDIES OF SPHERICAL DEVICES

presented by Ryan Meyer,

a candidate for the degree of doctor of philosophy,

and hereby certify that, in their opinion, it is worthy of acceptance.

Professor Sudarshan Loyalka

---

Professor Mark Prelas

---

Professor Edbertho Leal-Quiros

---

Professor Scott Kovaleski

---

Professor Paul Miceli

This is dedicated to my parents, Gerald and Rose, and to my siblings: Vickie, Kevin, Terry, Sheila, Tim, Jill, Darren, and Elizabeth. The support and structure they provided me was instrumental. I wish I could say my motives were pure, but I admit that sibling competitiveness is somewhat responsible for this undertaking. Finally, this dissertation is dedicated to my fiancé Pimphan (Aye) Kiatsimkul. She has been loving, supportive, and motivation for completing this dissertation in a timely fashion.

## ACKNOWLEDGEMENTS

Dr. Mark Prelas and Dr. Sudarshan Loyalka deserve my deepest appreciation for giving me the opportunity to focus my energy on such a fun project. In addition, the rest of the faculty and staff of the Nuclear Science and Engineering Institute deserve similar gratitude for providing the support necessary for me to focus my energy on my technical pursuit. I thank Tushar Ghosh, Robert Tompson, William Miller, and Dabir Viswanath. Their comradery and spirit of cooperation provide an environment conducive to productivity. I also give Robert Tompson credit for my efficiency with word processing and production of graphics (thanks to nuclear reactor laboratory!).

The other members of my committee deserve recognition for their input: Edbertho Leal-Quiros, Scott Kovaleski, and Paul Miceli.

Zeb Smith is responsible for the Monte Carlo simulations of the probe shadowing phenomena. I thank him for his hard work, endurance, and patience.

I want to recognize Scott Kovaleski for suggesting the AD210 isolation amplifiers. Without this suggestion, I would inevitably be delayed.

Edbertho Leal-Quiros deserves my thanks for the opportunity to work with him at the Polytechnic University of Puerto Rico mirror and cusp plasma laboratory. I learned so much practical knowledge related fabrication of Langmuir probes and sweeping techniques while at San Juan. In addition, I thank the following for their guidance, assistance, and their warm welcome: Angel Gonzáles, David Leal, Franklyn Colmenares, Ramón Rivera, Miguel Rivera, Giovanni Leonart, Jorge Gaudier, Lotte Aalling, Fátima Hiraldo, and Verónica Olivo.

Early on, I traveled to the IEC laboratory at the University of Illinois-Urbana-Champaign where I learned how to make the cathode grids and pestered George Miley and Robert Stubbers with all kinds of questions. This trip was very important at the time, as I had no experimental device running then, and I thank them for their patience.

I have somehow managed to utilize every machine shop on campus and I want to thank the machinists who have been so instrumental in my project. I thank Richard McWhorter and the rest of the Science and Instrument Shop crew for their excellent machining abilities. Likewise, I extend thanks to Sam Potts and Rod Schlotzhauer at the Physics Shop, also for their fantastic work. I am also grateful to have had access to Brian Samuels, Rex Gish, and Rick Wells of the engineering machine shops. Without their help, I could not have produced this dissertation.

The assistance/advice I received from engineering technical services (ETS) is appreciated. For this, I thank Richard Oberto, Michael Absheer, and Michael Klote.

Former electrical engineering comrades, Peter Norgard and Mark Kemp, deserve recognition for their patience and helpful attitude. I have sought advice from them on several occasions.

Finally, the following programs relieved me of financial constraints allowing me to focus sharply on research: Missouri Space Grant Consortium (MSGC), University of Missouri Huggin's Fellowship, Department of Education's Graduate Assistance in the Area of National Need (GAANN), Innovations in Nuclear Education and Infrastructure (INIE).

# TABLE OF CONTENTS

ACKNOWLEDGEMENTS.....	ii
LIST OF FIGURES .....	viii
LIST OF TABLES.....	xxx
ABSTRACT.....	xxx
I. Introduction.....	1
A. Motivation.....	1
B. Physical Description .....	2
C. Glow Discharge Modes.....	6
1. <i>Discharges between planar electrodes</i> .....	6
2. <i>IXL SIEC Glow Discharge Characteristics</i> .....	7
D. Definitions.....	11
1. <i>Observables (Dependent Variables)</i> .....	11
2. <i>Controls (Independent Variables)</i> .....	13
E. Previous Work .....	16
1. <i>Before 1980</i> .....	16
2. <i>After 1980</i> .....	21
F. Scope of Work .....	27
II. 1D Orbital Modeling.....	28
A. The model .....	29

B.	Uni-polar Injection in Spherical Geometry.....	30
C.	Bi-Polar Discharge Modeling and Double Potential Well Regimes.....	40
III.	Experimental Set-up.....	52
A.	Vacuum System .....	52
B.	Pressure Monitoring.....	53
C.	Electrodes and Power Supply .....	53
D.	Electrostatic Probes.....	55
1.	<i>Probe Construction</i> .....	55
2.	<i>Probe Manipulation</i> .....	56
3.	<i>Probe Sweeping</i> .....	57
4.	<i>RF noise</i> .....	58
IV.	Probe Ion Shadowing .....	71
A.	The Ion Core Region.....	71
B.	Ion Shadowing .....	75
C.	Infinitesimal Probe.....	76
D.	Finite probe of diameter $d$ .....	76
E.	Monte Carlo Simulations .....	79
V.	Experimental Results .....	93
A.	Double Probe ( $d_2$ ).....	93
1.	<i>Electric Field Components</i> .....	94
2.	<i>Electron Temperature and Plasma Density Profiles</i> .....	95

B.	Single Probe .....	95
C.	Probe Shadowing .....	96
D.	Virtual Electrodes .....	97
VI.	Discussions .....	133
A.	Quasi-neutrality in Micro-Channels .....	133
B.	Heterogeneous Structure .....	134
C.	“Star-Mode” to “Jet-Mode” Transition.....	134
D.	Electron Populations .....	135
E.	Ion Flow Characterization.....	136
F.	Virtual Electrodes .....	137
VII.	Conclusions, Contributions, Future Work .....	148
A.	Conclusions and Contributions .....	148
1.	<i>Theoretical Mapping of Observables</i> .....	148
2.	<i>Verification of Ion Micro-Channeling, Characterization of Glow Discharge Modes</i>	149
3.	<i>Ion Flow Characterization</i> .....	150
4.	<i>Contributions</i> .....	150
B.	Narrow Suggestions .....	151
C.	Broader Suggestions .....	153
	BIBLIOGRAPY .....	155
	APPENDIX A: Bi-polar 1-D Orbital Results .....	162

APPENDIX B: Langmuir Probe Analysis .....	196
A. Sheath Structure .....	196
B. Current Collected by a Negatively Biased Probe .....	197
C. Single Langmuir Probe Analysis .....	198
D. Double Probe Analysis .....	199
APPENDIX C: List of Materials and Components .....	201
VITA .....	202

## LIST OF FIGURES

Figure	Page
1. Paschen curve diagram to illustrate GD and AGD modes of IXL IEC operation. The operational curve for AGD mode is shifted to lower values of $pd$ due to the aid of electron emitting filaments, ion guns, etc.....	5
2. Structure of a glow discharge between parallel planar electrodes for $\lambda \ll d$ , where $\lambda$ is the mean free path of ions or electrons and $d$ is the distance between electrodes. This figure is an approximation to one that appears in multiple texts <sup>77,78,79</sup> discussing glow discharges.....	9
3. Photo of GD IXL SIEC in “Star Mode” operation at University of Missouri-Columbia. Luminous spokes are visible indicating the heterogeneous discharge structure. ....	10
4. Photo of GD IXL SIEC in “Jet Mode” operation at University of Missouri-Columbia. The electron jet is clearly visible. ....	10
5. A representation of a single potential well structure. In this case, the minimum normalized potential, $Y_{min}$ , coincides with the core potential, $Y_{core} = Y(r = 0)$ . The fractional well depth, $FWD$ is defined as $FWD = 1 - Y_{min}$ . ....	14
6. A representation of a double potential well structure. In this case, fractional well depth, $FWD$ , is defined as $FWD = 1 - Y_{min}$ , and the double well depth ( $DWD$ ) as $Y_{peak} - Y_{min}$ . Here, $Y_{peak}$ coincides with $Y_{core}$ .....	14
7. Representation of a typical injected or trapped particle radial density profile, $n_j(r)$ , within the inner grid of an SIEC. The density at $r = 0$ is defined as $n_j(0)$ , where $j = 0$ represents injected particles, and $j = 1$ represents trapped particles. The width of the density profile is indicated by the “half width at half max”, $HWHM$ . ....	15

8. Representation of an injected particle radial density profile, $n_0(r)$ , for the case in which mutual repulsion of the injected particles results in significant space charge spreading of the core. In this case, the peak density, $np_0$ occurs at a radius $r \neq 0$ , and $n_0(0) \neq np_0$ .....	15
9. Summary of results from early e-beam probe measurements of FWD in USEXLS. ....	20
10. Core density vs. $P_0$ for uni-polar injection in spherical geometry with singly charged ions with 1amu mass, with $\sigma_{i\phi} = 0.05$ .....	32
11. Peak density vs. $P_0$ for uni-polar injection in spherical geometry with singly charged ions with 1amu mass, with $\sigma_{i\phi} = 0.05$ .....	32
12. Convergence Factor ( $CF$ ) vs. $P_0$ for uni-polar injection in spherical geometry with singly charged ions with 1amu mass, with $\sigma_{i\phi} = 0.05$ .....	33
13. $HWHM$ vs. $P_0$ for uni-polar injection in spherical geometry with singly charged ions with 1amu mass, with $\sigma_{i\phi} = 0.05$ .....	33
14. Ratio of peak density to core density vs. $P_0$ for uni-polar injection in spherical geometry with singly charged ions with 1amu mass, with $\sigma_{i\phi} = 0.05$ .....	34
15. Ratio of peak density to grid density vs. $P_0$ for uni-polar injection in spherical geometry with singly charged ions with 1amu mass, with $\sigma_{i\phi} = 0.05$ .....	34
16. Plot of $n_i(0)$ vs. $\sigma_{i\phi}$ for uni-polar injection in spherical geometry with singly charged ions of mass 1 amu with $P_i = 3 \text{ mA } kV^{3/2}$ .....	35
17. Plot of $CF$ vs. $\sigma_{i\phi}$ for uni-polar injection in spherical geometry with singly charged ions of mass 1 amu with $P_i = 3 \text{ mA } kV^{3/2}$ .....	35
18. Plot of $HWHM$ vs. $\sigma_{i\phi}$ for uni-polar injection in spherical geometry with singly charged ions of mass 1 amu with $P_i = 3 \text{ mA } kV^{3/2}$ .....	36
19. Contour plot of $FWD$ vs. ion perveance $P_i$ and the spread in normalized ion angular energy, $\sigma_{i\phi}$ .....	36
20. Contour plot of $\text{Log}_{10}(n_i(0))$ vs. ion perveance, $P_i$ , and the spread in normalized ion angular energy, $\sigma_{i\phi}$ . ....	37
21. Contour plot of $\text{Log}_{10}(n_{pi})$ vs. ion perveance, $P_i$ , and the spread in normalized ion angular energy, $\sigma_{i\phi}$ . ....	37

22. Contour plot of $\text{Log}_{10}(n_{i\text{peak}}/n_i(R_g))$ vs. ion perveance, $P_i$ , and the spread in normalized ion angular energy, $\sigma_{i\phi}$ .	38
23. Contour plot of $\text{Log}_{10}(CF)$ vs. ion perveance, $P_i$ , and the spread in normalized ion angular energy, $\sigma_{i\phi}$ .	38
24. Contour plot of $\text{Log}_{10}(HWHM)$ vs. ion perveance, $P_i$ , and the spread in normalized ion angular energy, $\sigma_{i\phi}$ .	39
25. Comparison of $FWD$ vs. $P_e$ for USEXLs from experiments and 1D orbital modeling.	39
26. Injected and trapped radial density profiles, $n_o(r)$ and $n_l(r)$ , for an IXL SIEC. In this case, control variables have the values $P_0 = 40 \text{ mA kV}^{-3/2}$ , $\sigma_{1\phi} = 0.001$ , $\sigma_{0\phi} = 0.05$ , and $\beta = 1.2$ .	42
27. Radial potential profiles for an IXL SIEC. In this case, control variables have the values $P_0 = 40 \text{ mA kV}^{-3/2}$ , $\sigma_{1\phi} = 0.001$ , $\sigma_{0\phi} = 0.05$ , and $\beta = 1.2$ .	42
28. Injected and trapped radial density profiles, $n_o(r)$ and $n_l(r)$ , for an IXL SIEC. In this case, control variables have the values $P_0 = 40 \text{ mA kV}^{-3/2}$ , $\sigma_{1\phi} = 0.001$ , $\sigma_{0\phi} = 0.05$ , and $\beta = 0.45$ .	43
29. Radial potential profiles for an IXL SIEC. In this case, control variables have the values $P_0 = 40 \text{ mA kV}^{-3/2}$ , $\sigma_{1\phi} = 0.001$ , $\sigma_{0\phi} = 0.05$ , and $\beta = 0.45$ .	43
30. Injected and trapped radial density profiles, $n_o(r)$ and $n_l(r)$ , for an IXL SIEC. In this case, control variables have the values $P_0 = 40 \text{ mA kV}^{-3/2}$ , $\sigma_{1\phi} = 0.001$ , $\sigma_{0\phi} = 0.05$ , and $\beta = 0.2$ .	44
31. Radial potential profiles for an IXL SIEC. In this case, control variables have the values $P_0 = 40 \text{ mA kV}^{-3/2}$ , $\sigma_{1\phi} = 0.001$ , $\sigma_{0\phi} = 0.05$ , and $\beta = 0.2$ .	44
32. Comparison of $FWD$ vs. $P_e$ for USEXLs from experiments and 1D orbital modeling. In this case, the assumption that the devices are purely unipolar is dropped, and a trapped ion current is added to the model. It should be noted that the theoretically derived curves are not necessarily unique, in that other combinations of control variables may result in a similar curve.	45
33. Contour plot of $DWD$ with respect to $P_i$ and $\beta$ . This plot is computed with $\sigma_{e\phi} = 0.005$ and $\sigma_{i\phi} = 0.05$ .	46

34. Contour plot of <i>DWD</i> with respect to $P_i$ and $\beta$ . This plot is computed with $\sigma_{e\phi} = 0.005$ and $\sigma_{i\phi} = 0.10$ .....	46
35. Contour plot of <i>DWD</i> with respect to $^M P_i = m_i^{1/2} * P_i$ and $^M \beta = m_i^{1/2} * \beta$ , where $m_i$ is the ion mass in amu. This plot is computed with $\sigma_{e\phi} = 0.005$ and $\sigma_{i\phi} = 0.15$ . .....	47
36. Contour plot of <i>DWD</i> with respect to $\sigma_{e\phi}$ and $\sigma_{i\phi}$ . This plot is computed with $P_i = 100 \text{ mA kV}^{-3/2}$ and $\beta = 0.25$ .....	47
37. Contour plot of <i>DWD</i> with respect to $\sigma_{e\phi}$ and $\sigma_{i\phi}$ . This plot is computed with $P_i = 138 \text{ mA kV}^{-3/2}$ and $\beta = 0.25$ .....	48
38. Contour plot of <i>DWD</i> with respect to $\sigma_{e\phi}$ and $\sigma_{i\phi}$ . This plot is computed with $P_i = 100 \text{ mA kV}^{-3/2}$ and $\beta = 0.33$ .....	48
39. Contour plot of <i>DWD</i> with respect to $\sigma_{e\phi}$ and $\sigma_{i\phi}$ . This plot is computed with $P_i = 138 \text{ mA kV}^{-3/2}$ and $\beta = 0.33$ .....	49
40. Contour plot of <i>DWD</i> with respect to $\sigma_{e\phi}$ and $\sigma_{i\phi}$ . This plot is computed with $P_i = 100 \text{ mA kV}^{-3/2}$ and $\beta = 0.50$ .....	49
41. Contour plot of <i>DWD</i> with respect to $\sigma_{e\phi}$ and $\sigma_{i\phi}$ . This plot is computed with $P_i = 138 \text{ mA kV}^{-3/2}$ and $\beta = 0.50$ .....	50
42. Contour plot of <i>DWD</i> with respect to $\sigma_{e\phi}$ and $\sigma_{i\phi}$ . This plot is computed with $P_i = 100 \text{ mA kV}^{-3/2}$ and $\beta = 0.67$ .....	50
43. Contour plot of <i>DWD</i> with respect to $\sigma_{e\phi}$ and $\sigma_{i\phi}$ . This plot is computed with $P_i = 138 \text{ mA kV}^{-3/2}$ and $\beta = 0.67$ .....	51
44. GD IXL SIEC at the University of Missouri-Columbia. Spherical cathode and anode are housed within the cylindrical bell jar.....	60
45. Anode constructed out of 6.35mm OD ss tubing. An aluminum structure supports the anode and brackets for future mounting of electron guns or electron emitters.....	60
46. Top view of the GD IXL SIEC at the University of Missouri-Columbia. Four 2-3/4” conflate flanges are indicated for electrostatic probe access. These access ports are labeled as “Probe Location 1-4” in the diagram. Also indicated are the HV feedthrough, the viewport, the Langmuir probes, the cathode, and an ion micro-channel. The ion micro-channel is depicted to	

emphasize the observed phenomena of micro-channel formation in the direction of Probe Location 1 and the absence of an accessible micro-channel to a probe inserted at Probe Location 2. ....	61
47. “Geodesic” cathode grid formed of 1mm thick stainless wire. The grid is composed of seven 3.75” diameter rings. ....	62
48. Schematic of front view of the alumina silicate cup mounted at the end of the probe shaft for the double probe, d1. ....	62
49. Schematic of side view of alumina silicate cup for the double probe, d1. ....	63
50. Photos of the double and single probes, d1 and s1, respectively. ....	63
51. This is a photo of double probe, d2. ....	64
52. Photo of the probe manipulator with stepper motor and uni-polar driver. ....	64
53. Photo of automated Langmuir probe with manipulator, stepper motor and uni-polar driver. ....	65
54. Schematic illustrating the use of a resistor dump for single probe operation to bias the programmable power supply. ....	65
55. Schematic for double probe sweeping circuit. ....	66
56. Schematic of the sweeping circuit for the single probe. ....	67
57. Aluminum cabinet designed to shield the DAQ bus from RF interference. ....	68
58. Aluminum mesh is riveted into an aluminum structure to shield the optical encoder from RF noise. ....	68
59. Aluminum mesh covering viewport to attenuate RF emissions. ....	69
60. Aluminum cap encases the HV feedthrough insulator to block this path of RF leakage. ....	69
61. Signal collection circuit is placed inside of an aluminum box to block the re-emitted interference signals conducted by the electrostatic probes. ....	70
62. Photo of aluminum box housing the signal collection circuit. ....	70

63. Depiction of “fan beam” model of ion orbits through the center of the cathode grid region, with the insertion of an infinitesimal probe (shown in green, extending from left side of illustration). The model assumes an infinite number of such fan beams, with a divergence $\phi = \text{Sin}^{-1}(R_c/R_g)$ intersecting in the core region. ....	80
64. A close up of the core region, indicating the projection, $k$ , of the probe onto the diameter of the ion beam. Also depicted, are the beam diameter, $bd$ , along $k$ , the core radius, $R_c$ , in addition to the probe, indicated in green.....	80
65. Depiction of “fan beam” model of ion orbits through the center of the cathode grid region, with the insertion of a probe of diameter $d$ (shown in green, extending from left side of illustration). The model assumes an infinite number of such fan beams, with a divergence $\phi = \text{Sin}^{-1}(R_c/R_g)$ intersecting in the core region. ....	81
66. All beams below the critical angle $\theta_1$ are obstructed by the probe as depicted in this illustration. ....	81
67. For $\theta_1 < \theta < \theta_2$ , the projection of the probe onto the beam diameter is $k1$ , while the beam diameter along $k1$ is $bd1$ .....	82
68. For $\theta_2 < \theta < \pi$ , the projection of the probe onto the beam diameter is $k2$ , while the beam diameter along $k2$ is $bd2$ .....	82
69. The projection of the probe onto the beam diameter and the beam diameter must be defined separately for regions separated by the critical angle, $\theta_2$ .....	83
70. The fraction of shadowed ions in 3 dimensions is indicated, where $c$ represents the ion beam radius and $b$ is the projection of the probe onto the ion beam.....	83
71. This is a plot of $F(l)$ for two core radii, for a cylindrical probe diameter of $d = 1.3\text{cm}$ and a cathode grid radius of $R_g = 4.7\text{cm}$ . ....	84
72. This is a plot of $F(l)$ for three different probe diameters and a core radius, $R_c = 0.5\text{cm}$ and a cathode grid radius of $R_g = 4.7\text{cm}$ . ....	84
73. $F(l)$ for double probe, $d1$ , depicted in Fig. 48 and Fig. 49 for the case $R_g/R_c = 3$ .....	85
74. $F(l)$ for double probe, $d1$ , depicted in Fig. 48 and Fig. 49 for the case $R_g/R_c = 5$ .....	85

75. $F(l)$ for double probe, d1, depicted in Fig. 48 and Fig. 49 for the case $R_g/R_c = 8$ .....	86
76. $F(l)$ for double probe, d1, depicted in Fig. 48 and Fig. 49 for the case $R_g/R_c = 10$ .....	86
77. $F(l)$ for double probe, d1, depicted in Fig. 48 and Fig. 49 for the case $R_g/R_c = 12$ .....	87
78. $F(l)$ for double probe, d1, depicted in Fig. 48 and Fig. 49 for the case $R_g/R_c = 15$ .....	87
79. Animation simultaneously depicting $F(l)$ and the probe location for a core radius of $R_g/R_c = 10$ . In this case, the probe is located at $l \sim 17$ mm. ....	88
80. Animation simultaneously depicting $F(l)$ and the probe location for a core radius of $R_g/R_c = 10$ . In this case, the probe is located at $l \sim 3$ mm. ....	89
81. Animation simultaneously depicting $F(l)$ and the probe location for a core radius of $R_g/R_c = 10$ . In this case, the probe is located at $l \sim -11$ mm.....	90
82. Animation simultaneously depicting $F(l)$ and the probe location for a core radius of $R_g/R_c = 10$ . In this case, the probe is located at $l \sim -26$ mm.....	91
83. Animation simultaneously depicting $F(l)$ and the probe location for a core radius of $R_g/R_c = 10$ . In this case, the probe is located at $l \sim -39$ mm.....	92
84. Typical I-V trace at radius $r = 0$ with respect to the center of the device. The cathode is located at a radius $R_g = 4.7$ cm and the anode is at a radius $R_a \sim 22$ cm from the center of the device.....	99
85. Typical I-V trace at radius $r = 1$ cm with respect to the center of the device. The cathode is located at a radius $R_g = 4.7$ cm and the anode is at a radius $R_a \sim 22$ cm from the center of the device.....	99
86. Typical I-V trace at radius $r = 2$ cm with respect to the center of the device. The cathode is located at a radius $R_g = 4.7$ cm and the anode is at a radius $R_a \sim 22$ cm from the center of the device.....	100
87. Typical I-V trace at radius $r = 3$ cm with respect to the center of the device. The cathode is located at a radius $R_g = 4.7$ cm and the anode is at a radius $R_a \sim 22$ cm from the center of the device.....	100

88. Typical I-V trace at radius $r = 4\text{cm}$ with respect to the center of the device. The cathode is located at a radius $R_g = 4.7\text{cm}$ and the anode is at a radius $R_a \sim 22\text{cm}$ from the center of the device.....	101
89. Typical I-V trace at radius $r = 5\text{cm}$ with respect to the center of the device. The cathode is located at a radius $R_g = 4.7\text{cm}$ and the anode is at a radius $R_a \sim 22\text{cm}$ from the center of the device.....	101
90. Typical I-V trace at radius $r = 6\text{cm}$ with respect to the center of the device. The cathode is located at a radius $R_g = 4.7\text{cm}$ and the anode is at a radius $R_a \sim 22\text{cm}$ from the center of the device.....	102
91. Typical I-V trace at radius $r = 7\text{cm}$ with respect to the center of the device. The cathode is located at a radius $R_g = 4.7\text{cm}$ and the anode is at a radius $R_a \sim 22\text{cm}$ from the center of the device.....	102
92. Typical I-V trace at radius $r = 8\text{cm}$ with respect to the center of the device. The cathode is located at a radius $R_g = 4.7\text{cm}$ and the anode is at a radius $R_a \sim 22\text{cm}$ from the center of the device.....	103
93. The I-V trace data in Fig. 92 is fit with a one-hundredth order polynomial using the least squares method. All double probe I-V curves are fitted this way for analysis purposes. ....	103
94. Difference in floating potentials of the two disks of double probe d2 for “Star Mode” cases, providing an experimental indication of the tangential components of the electric field due to the discrete cathode grid structure.....	104
95. Difference in floating potentials of the two disks of double probe d2 for “Jet Mode” cases and a few of the “Star Mode” cases, providing an experimental indication of the tangential components of the electric field due to the discrete cathode grid structure. ....	104
96. Radial floating potential profiles, $V_f(r)$ , for “Star Mode” cases in Table VII. These profiles are indicators of the radial component of the electric field.....	105
97. Radial floating potential profiles, $V_f(r)$ , for “Jet Mode” cases and some “Star Mode” cases in Table VII. These profiles are indicators of the radial component of the electric field. ....	105
98. Radial electron temperature profiles, $T_e(r)$ , for “Star Mode” cases in Table VII. ....	106

99. Radial electron temperature profiles, $T_e(r)$ , for “Jet Mode” cases and some “Star Mode” cases in Table VII. ....	106
100. Linear plot of the radial ion density profiles, $n_i(r)$ , for all cases in Table VII. This linear representation of the $n_i(r)$ is provided to emphasize the core region. ....	107
101. Logarithmic plot of the radial ion density profiles, $n_i(r)$ , for “Star Mode” cases in Table VII. ....	107
102. Logarithmic plot of the radial ion density profiles, $n_i(r)$ , for “Jet Mode” cases and some “Star Mode” cases in Table VII. ....	108
103. Single probe I-V curve obtained with single probe s2 inserted into Probe Location 2, as shown in Fig. 46. The trace is obtained at a position $r = 7$ cm with a cathode radius of 4.7cm. The discharge characteristics for this case are $V_s = -5.01$ kV, $I_s = 27.91$ mA and $P = 2.49$ mA kV <sup>-3/2</sup> .....	108
104. Single probe I-V curve obtained with single probe s2 inserted into Probe Location 2, as shown in Fig. 46. The trace is obtained at a position $r = 7$ cm with a cathode radius of 4.7cm. The discharge characteristics for this case are $V_s = -3.76$ kV, $I_s = 39.97$ mA and $P = 5.48$ mA kV <sup>-3/2</sup> .....	109
105. Single probe I-V curve obtained with single probe s2 inserted into Probe Location 2, as shown in Fig. 46. The trace is obtained at a position $r = 7$ cm with a cathode radius of 4.7cm. The discharge characteristics for this case are $V_s = -2.56$ kV, $I_s = 39.97$ mA and $P = 9.75$ mA kV <sup>-3/2</sup> .....	109
106. Single probe I-V curve obtained with disk 1 (nearest the cathode grid wire) of double probe d2 inserted into Probe Location 1, as shown in Fig. 46. The trace is obtained at a position $r = 8$ cm with a cathode radius of 4.7cm. The discharge characteristics for this case are $V_s = -5.04$ kV, $I_s = 13.1$ mA and $P = 1.16$ mA kV <sup>-3/2</sup> .....	110
107. Single probe I-V curve obtained with disk 2 (farthest from the cathode grid wire) of double probe d2 inserted into Probe Location 1, as shown in Fig. 46. The trace is obtained at a position $r = 8$ cm with a cathode radius of 4.7cm. The discharge characteristics for this case are $V_s = -5.04$ kV, $I_s = 11.52$ mA and $P = 1.02$ mA kV <sup>-3/2</sup> .....	110
108. Single probe I-V curve obtained with disk 1 (nearest the cathode grid wire) of double probe d2 inserted into Probe Location 1, as shown in Fig. 46. The trace is obtained at a position $r = 8$ cm with a cathode radius of 4.7cm.	

The discharge characteristics for this case are $V_s = -5.05\text{kV}$ , $I_s = 28.91\text{mA}$ and $P = 2.55 \text{ mA kV}^{-3/2}$ .....	111
109. Single probe I-V curve obtained with disk 2 (farthest from the cathode grid wire) of double probe d2 inserted into Probe Location 1, as shown in Fig. 46. The trace is obtained at a position $r = 8 \text{ cm}$ with a cathode radius of 4.7cm. The discharge characteristics for this case are $V_s = -5.04\text{kV}$ , $I_s = 28.33\text{mA}$ and $P = 2.5 \text{ mA kV}^{-3/2}$ .....	111
110. Single probe I-V curve obtained with disk 1 (nearest the cathode grid wire) of double probe d2 inserted into Probe Location 1, as shown in Fig. 46. The trace is obtained at a position $r = 8 \text{ cm}$ with a cathode radius of 4.7cm. The discharge characteristics for this case are $V_s = -4.67\text{kV}$ , $I_s = 39.97\text{mA}$ and $P = 3.96 \text{ mA kV}^{-3/2}$ .....	112
111. Single probe I-V curve obtained with disk 2 (farthest from the cathode grid wire) of double probe d2 inserted into Probe Location 1, as shown in Fig. 46. The trace is obtained at a position $r = 8 \text{ cm}$ with a cathode radius of 4.7cm. The discharge characteristics for this case are $V_s = -4.7\text{kV}$ , $I_s = 39.97\text{mA}$ and $P = 3.93 \text{ mA kV}^{-3/2}$ .....	112
112. Single probe I-V curve obtained with disk 1 (nearest the cathode grid wire) of double probe d2 inserted into Probe Location 1, as shown in Fig. 46. The trace is obtained at a position $r = 8 \text{ cm}$ with a cathode radius of 4.7cm. The discharge characteristics for this case are $V_s = -3.89\text{kV}$ , $I_s = 39.97\text{mA}$ and $P = 5.21 \text{ mA kV}^{-3/2}$ .....	113
113. Single probe I-V curve obtained with disk 2 (farthest from the cathode grid wire) of double probe d2 inserted into Probe Location 1, as shown in Fig. 46. The trace is obtained at a position $r = 8 \text{ cm}$ with a cathode radius of 4.7cm. The discharge characteristics for this case are $V_s = -3.89\text{kV}$ , $I_s = 39.97\text{mA}$ and $P = 5.2 \text{ mA kV}^{-3/2}$ .....	113
114. Single probe I-V curve obtained with disk 1 (nearest the cathode grid wire) of double probe d2 inserted into Probe Location 1, as shown in Fig. 46. The trace is obtained at a position $r = 8 \text{ cm}$ with a cathode radius of 4.7cm. The discharge characteristics for this case are $V_s = -2.53\text{kV}$ , $I_s = 39.97\text{mA}$ and $P = 9.96 \text{ mA kV}^{-3/2}$ .....	114
115. Single probe I-V curve obtained with disk 2 (farthest from the cathode grid wire) of double probe d2 inserted into Probe Location 1, as shown in Fig. 46. The trace is obtained at a position $r = 8 \text{ cm}$ with a cathode radius of 4.7cm. The discharge characteristics for this case are $V_s = -2.55\text{kV}$ , $I_s = 39.97\text{mA}$ and $P = 9.84 \text{ mA kV}^{-3/2}$ .....	114

116. Single probe I-V characteristic obtained with disk 1 (nearest to cathode grid wire) of probe d2 at Probe Location 1 as indicated in Fig. 46. This curve is obtained at a radial position of  $r = 0$  cm from the center of the device. Discharge charge conditions are  $V_s = -5.04$  kV,  $I_s = 10.5$  mA and  $P = 0.93$  mA kV<sup>-3/2</sup>. The cathode grid radius is  $R_g = 4.7$  cm. .... 115
117. Single probe I-V characteristic obtained with disk 2 (farthest from the cathode grid wire) of probe d2 at Probe Location 1 as indicated in Fig. 46. This curve is obtained at a radial position of  $r = 0$  cm from the center of the device. Discharge charge conditions are  $V_s = -5.04$  kV,  $I_s = 11.52$  mA and  $P = 1.02$  mA kV<sup>-3/2</sup>. The cathode grid radius is  $R_g = 4.7$  cm. .... 115
118. Single probe I-V characteristic obtained with disk 1 (nearest to cathode grid wire) of probe d2 at Probe Location 1 as indicated in Fig. 46. This curve is obtained at a radial position of  $r = 0.8$  cm from the center of the device. Discharge charge conditions are  $V_s = -5.04$  kV,  $I_s = 10.5$  mA and  $P = 0.93$  mA kV<sup>-3/2</sup>. The cathode grid radius is  $R_g = 4.7$  cm. .... 116
119. Single probe I-V characteristic obtained with disk 2 (farthest from the cathode grid wire) of probe d2 at Probe Location 1 as indicated in Fig. 46. This curve is obtained at a radial position of  $r = 0.7$  cm from the center of the device. Discharge charge conditions are  $V_s = -5.04$  kV,  $I_s = 11.52$  mA and  $P = 1.02$  mA kV<sup>-3/2</sup>. The cathode grid radius is  $R_g = 4.7$  cm. .... 116
120. Single probe I-V characteristic obtained with disk 1 (nearest to cathode grid wire) of probe d2 at Probe Location 1 as indicated in Fig. 46. This curve is obtained at a radial position of  $r = 1.0$  cm from the center of the device. Discharge charge conditions are  $V_s = -5.04$  kV,  $I_s = 10.5$  mA and  $P = 0.93$  mA kV<sup>-3/2</sup>. The cathode grid radius is  $R_g = 4.7$  cm. .... 117
121. Single probe I-V characteristic obtained with disk 2 (farthest from the cathode grid wire) of probe d2 at Probe Location 1 as indicated in Fig. 46. This curve is obtained at a radial position of  $r = 1.0$  cm from the center of the device. Discharge charge conditions are  $V_s = -5.04$  kV,  $I_s = 11.52$  mA and  $P = 1.02$  mA kV<sup>-3/2</sup>. The cathode grid radius is  $R_g = 4.7$  cm. .... 117
122. Single probe I-V characteristic obtained with disk 1 (nearest to cathode grid wire) of probe d2 at Probe Location 1 as indicated in Fig. 46. This curve is obtained at a radial position of  $r = 2.0$  cm from the center of the device. Discharge charge conditions are  $V_s = -5.04$  kV,  $I_s = 10.5$  mA and  $P = 0.93$  mA kV<sup>-3/2</sup>. The cathode grid radius is  $R_g = 4.7$  cm. .... 118
123. Single probe I-V characteristic obtained with disk 2 (farthest from the cathode grid) of probe d2 at Probe Location 1 as indicated in Fig. 46.

This curve is obtained at a radial position of  $r = 2.0$  cm from the center of the device. Discharge charge conditions are  $V_s = -5.04$  kV,  $I_s = 11.52$  mA and  $P = 1.02$  mA kV<sup>-3/2</sup>. The cathode grid radius is  $R_g = 4.7$  cm. .... 118

124. Single probe I-V characteristic obtained with disk 1 (nearest to cathode grid wire) of probe d2 at Probe Location 1 as indicated in Fig. 46. This curve is obtained at a radial position of  $r = 3.0$  cm from the center of the device. Discharge charge conditions are  $V_s = -5.04$  kV,  $I_s = 10.5$  mA and  $P = 0.93$  mA kV<sup>-3/2</sup>. The cathode grid radius is  $R_g = 4.7$  cm. .... 119

125. Single probe I-V characteristic obtained with disk 2 (farthest from the cathode grid wire) of probe d2 at Probe Location 1 as indicated in Fig. 46. This curve is obtained at a radial position of  $r = 3.0$  cm from the center of the device. Discharge charge conditions are  $V_s = -5.04$  kV,  $I_s = 11.52$  mA and  $P = 1.02$  mA kV<sup>-3/2</sup>. The cathode grid radius is  $R_g = 4.7$  cm. .... 119

126. Single probe I-V characteristic obtained with disk 1 (nearest to cathode grid wire) of probe d2 at Probe Location 1 as indicated in Fig. 46. This curve is obtained at a radial position of  $r = 4.0$  cm from the center of the device. Discharge charge conditions are  $V_s = -5.04$  kV,  $I_s = 10.5$  mA and  $P = 0.93$  mA kV<sup>-3/2</sup>. The cathode grid radius is  $R_g = 4.7$  cm. .... 120

127. Single probe I-V characteristic obtained with disk 2 (farthest from the cathode grid wire) of probe d2 at Probe Location 1 as indicated in Fig. 46. This curve is obtained at a radial position of  $r = 4.0$  cm from the center of the device. Discharge charge conditions are  $V_s = -5.04$  kV,  $I_s = 11.52$  mA and  $P = 1.02$  mA kV<sup>-3/2</sup>. The cathode grid radius is  $R_g = 4.7$  cm. .... 120

128. Single probe I-V characteristic obtained with disk 1 (nearest to cathode grid wire) of probe d2 at Probe Location 1 as indicated in Fig. 46. This curve is obtained at a radial position of  $r = 5.0$  cm from the center of the device. Discharge charge conditions are  $V_s = -5.04$  kV,  $I_s = 10.5$  mA and  $P = 0.93$  mA kV<sup>-3/2</sup>. The cathode grid radius is  $R_g = 4.7$  cm. .... 121

129. Single probe I-V characteristic obtained with disk 2 (farthest from the cathode grid wire) of probe d2 at Probe Location 1 as indicated in Fig. 46. This curve is obtained at a radial position of  $r = 5.0$  cm from the center of the device. Discharge charge conditions are  $V_s = -5.04$  kV,  $I_s = 11.52$  mA and  $P = 1.02$  mA kV<sup>-3/2</sup>. The cathode grid radius is  $R_g = 4.7$  cm. .... 121

130. Single probe I-V characteristic obtained with disk 1 (nearest to cathode grid wire) of probe d2 at Probe Location 1 as indicated in Fig. 46. This curve is obtained at a radial position of  $r = 6.0$  cm from the center of the device.

Discharge charge conditions are $V_s = -5.04$ kV, $I_s = 10.5$ mA and $P = 0.93$ mA kV <sup>-3/2</sup> . The cathode grid radius is $R_g = 4.7$ cm.....	122
131. Single probe I-V characteristic obtained with disk 2 (farthest from the cathode grid wire) of probe d2 at Probe Location 1 as indicated in Fig. 46. This curve is obtained at a radial position of $r = 6.0$ cm from the center of the device. Discharge charge conditions are $V_s = -5.04$ kV, $I_s = 11.52$ mA and $P = 1.02$ mA kV <sup>-3/2</sup> . The cathode grid radius is $R_g = 4.7$ cm. ....	122
132. Single probe I-V characteristic obtained with disk 1 (nearest to cathode grid wire) of probe d2 at Probe Location 1 as indicated in Fig. 46. This curve is obtained at a radial position of $r = 7.0$ cm from the center of the device. Discharge charge conditions are $V_s = -5.04$ kV, $I_s = 10.5$ mA and $P = 0.93$ mA kV <sup>-3/2</sup> . The cathode grid radius is $R_g = 4.7$ cm.....	123
133. Single probe I-V characteristic obtained with disk 2 (farthest from the grid wire) of probe d2 at Probe Location 1 as indicated in Fig. 46. This curve is obtained at a radial position of $r = 7.0$ cm from the center of the device. Discharge charge conditions are $V_s = -5.04$ kV, $I_s = 11.52$ mA and $P = 1.02$ mA kV <sup>-3/2</sup> . The cathode grid radius is $R_g = 4.7$ cm.....	123
134. Single probe I-V characteristic obtained with disk 1 (nearest to cathode grid wire) of probe d2 at Probe Location 1 as indicated in Fig. 46. This curve is obtained at a radial position of $r = 8.0$ cm from the center of the device. Discharge charge conditions are $V_s = -5.04$ kV, $I_s = 10.5$ mA and $P = 0.93$ mA kV <sup>-3/2</sup> . The cathode grid radius is $R_g = 4.7$ cm.....	124
135. Single probe I-V characteristic obtained with disk 2 (farthest from the cathode grid wire) of probe d2 at Probe Location 1 as indicated in Fig. 46. This curve is obtained at a radial position of $r = 8.0$ cm from the center of the device. Discharge charge conditions are $V_s = -5.04$ kV, $I_s = 11.52$ mA and $P = 1.02$ mA kV <sup>-3/2</sup> . The cathode grid radius is $R_g = 4.7$ cm. ....	124
136. Portions of electron density profiles, $n_e(r)$ , for several discharge conditions listed in Table VIII.....	126
137. Portions of electron temperature profiles, $T_e(r)$ , for several discharge conditions listed in Table VIII. ....	126
138. Measurements of the power supply current, $I_s$ , are plotted as a function of radius to indicate the shadowing effect of a probe as it is inserted into the center of a GD IXL SIEC device. These plots are for cases $P = 2.03, 2.62, 2.69, 3.02, 3.54,$ and $3.82$ mA kV <sup>-3/2</sup> . The legend for this plot is provided in Table IX. ....	128

139. Measurements of the power supply current, $I_s$ , are plotted as a function of radius to indicate the shadowing effect of a probe as it is inserted into the center of a GD IXL SIEC device. These plots are for cases $P = 1.28$ and $1.49 \text{ mA kV}^{-3/2}$ . The legend for this plot is provided in Table IX. ....	128
140. Measurements of the power supply current, $I_s$ , are plotted as a function of radius to indicate the shadowing effect of a probe as it is inserted into the center of a GD IXL SIEC device. These plots are for cases $P = 0.87$ and $1.01 \text{ mA kV}^{-3/2}$ . The legend for this plot is provided in Table IX. ....	129
141. Measurements of the power supply current, $I_s$ , are plotted as a function of radius to indicate the shadowing effect of a probe as it is inserted into the center of a GD IXL SIEC device. These plots are for cases $P = 0.46$ and $0.48 \text{ mA kV}^{-3/2}$ . The legend for this plot is provided in Table IX. ....	129
142. Measurements of the power supply current, $I_s$ , are plotted as a function of radius to indicate the shadowing effect of a probe as it is inserted into the center of a GD IXL SIEC device. This plot is for the case $P = 0.13 \text{ mA kV}^{-3/2}$ . The legend for this plot is provided in Table IX. ....	130
143. Radial floating potential profile, $V_f(r)$ , for a supply voltage of $V_s = -3.2 \text{ kV}$ , a supply current of $I_s = 39.92 \text{ mA}$ , and $P = 6.97 \text{ mA kV}^{-3/2}$ . These measurements are obtained with single probe s2 inserted into Probe Location 2. ....	130
144. Radial floating potential profile, $V_f(r)$ , for a supply voltage of $V_s = -2.76 \text{ kV}$ , a supply current of $I_s = 39.92 \text{ mA}$ , and $P = 8.69 \text{ mA kV}^{-3/2}$ . These measurements are obtained with single probe s2 inserted into Probe Location 2. ....	131
145. Radial floating potential profile, $V_f(r)$ , for a supply voltage of $V_s = -2.17 \text{ kV}$ , a supply current of $I_s = 39.93 \text{ mA}$ , and $P = 12.45 \text{ mA kV}^{-3/2}$ . These measurements are obtained with single probe s2 inserted into Probe Location 2. ....	131
146. Radial floating potential profile, $V_f(r)$ , for a supply voltage of $V_s = -1.45 \text{ kV}$ , a supply current of $I_s = 39.92 \text{ mA}$ , and $P = 22.93 \text{ mA kV}^{-3/2}$ . These measurements are obtained with single probe s2 inserted into Probe Location 2. ....	132
147. Plasma potential, $V_\infty$ , and floating potential, $V_f$ , profiles for the discharge conditions $I_s = 4.19 \text{ mA}$ , $V_s = -5.03 \text{ kV}$ , and $P = 0.37 \text{ mA kV}^{-3/2}$ from Table VIII.....	138

148. Plasma potential, $V_\infty$ , and floating potential, $V_f$ , profiles for the discharge conditions $I_s = 11.52$ mA, $V_s = -5.04$ kV, and $P = 1.02$ mA kV <sup>-3/2</sup> from Table VIII.....	138
149. Plasma potential, $V_\infty$ , and floating potential, $V_f$ , profiles for the discharge conditions $I_s = 39.97$ mA, $V_s = -4.67$ kV, and $P = 3.96$ mA kV <sup>-3/2</sup> from Table VIII.....	139
150. Plasma potential, $V_\infty$ , and floating potential, $V_f$ , profiles for the discharge conditions $I_s = 39.97$ mA, $V_s = -2.53$ kV, and $P = 9.96$ mA kV <sup>-3/2</sup> from Table VIII.....	139
151. Electron density measurements averaged over the inter-electrode space, $\langle n_e \rangle$ , and plasma or ion density measurements over the inter-electrode space, $\langle n_j \rangle$ , for a number of discharge conditions. In this case, $\langle n_j \rangle$ is obtained from double probe, d2, and the conditions in Table VII, and $\langle n_e \rangle$ are obtained from single probe sweeps for conditions in Table VIII. ....	140
152. Radial electron density profile, $n_e(r)$ , obtained with single probe sweeps for the discharge conditions $I_s = 10.50$ mA, $V_s = -5.04$ kV, and $P = 0.93$ mA kV <sup>-3/2</sup> from Table VIII. Radial plasma, or ion density profile, $n_j(r)$ , obtained with double probe, d2, for the discharge conditions $I_s = 10.06$ mA, $V_s = -4.97$ kV, and $P = 0.91$ mA kV <sup>-3/2</sup> from Table VII. ....	140
153. Radial electron density profile, $n_e(r)$ , obtained with single probe sweeps for the discharge conditions $I_s = 39.97$ mA, $V_s = -4.70$ kV, and $P = 3.93$ mA kV <sup>-3/2</sup> from Table VIII. Radial plasma, or ion density profile, $n_j(r)$ , obtained with double probe, d2, for the discharge conditions $I_s = 38.73$ mA, $V_s = -4.38$ kV, and $P = 4.22$ mA kV <sup>-3/2</sup> from Table VII. ....	141
154. I-V characteristic obtained with double probe, d2, for the discharge conditions $I_s = 38.73$ mA, $V_s = -4.38$ kV, and $P = 4.22$ mA kV <sup>-3/2</sup> from Table VII at a location of 55 mm along the probes path, and where the grid is located at 42 mm and the device center is at 89 mm for reference.....	141
155. I-V characteristic obtained with double probe, d2, for the discharge conditions $I_s = 38.73$ mA, $V_s = -4.38$ kV, and $P = 4.22$ mA kV <sup>-3/2</sup> from Table VII at a location of 54 mm along the probes path, and where the grid is located at 42 mm and the device center is at 89 mm for reference.....	142
156. I-V characteristic obtained with double probe, d2, for the discharge conditions $I_s = 38.73$ mA, $V_s = -4.38$ kV, and $P = 4.22$ mA kV <sup>-3/2</sup> from Table VII at a location of 53 mm along the probes path, and where the grid is located at 42 mm and the device center is at 89 mm for reference.....	142

157. I-V characteristic obtained with double probe, d2, for the discharge conditions  $I_s = 38.73$  mA,  $V_s = -4.38$  kV, and  $P = 4.22$  mA kV<sup>-3/2</sup> from Table VII at a location of 52 mm along the probes path, and where the grid is located at 42 mm and the device center is at 89 mm for reference..... 143
158. I-V characteristic obtained with double probe, d2, for the discharge conditions  $I_s = 38.73$  mA,  $V_s = -4.38$  kV, and  $P = 4.22$  mA kV<sup>-3/2</sup> from Table VII at a location of 51 mm along the probes path, and where the grid is located at 42 mm and the device center is at 89 mm for reference..... 143
159. I-V characteristic obtained with double probe, d2, for the discharge conditions  $I_s = 38.73$  mA,  $V_s = -4.38$  kV, and  $P = 4.22$  mA kV<sup>-3/2</sup> from Table VII at a location of 50 mm along the probes path, and where the grid is located at 42 mm and the device center is at 89 mm for reference..... 144
160. I-V characteristic obtained with double probe, d2, for the discharge conditions  $I_s = 38.73$  mA,  $V_s = -4.38$  kV, and  $P = 4.22$  mA kV<sup>-3/2</sup> from Table VII at a location of 49 mm along the probes path, and where the grid is located at 42 mm and the device center is at 89 mm for reference..... 144
161. I-V characteristic obtained with double probe, d2, for the discharge conditions  $I_s = 38.73$  mA,  $V_s = -4.38$  kV, and  $P = 4.22$  mA kV<sup>-3/2</sup> from Table VII at a location of 48 mm along the probes path, and where the grid is located at 42 mm and the device center is at 89 mm for reference..... 145
162. Supply current,  $I_s$ , as a function of probe position for discharge conditions  $I_s = 9.92$  mA,  $V_s = -5.09$  kV, and  $P = 0.87$  mA kV<sup>-3/2</sup>. Experimental data is compared with theoretical results obtained with the analytical expression in Eq. (27) with  $R_g/R_c = 9.4$  and from Monte Carlo simulations with  $R_g/R_c = 10$ . ..... 146
163. Supply current,  $I_s$ , as a function of probe position for discharge conditions  $I_s = 31.96$  mA,  $V_s = -5.21$  kV, and  $P = 2.69$  mA kV<sup>-3/2</sup>. Experimental data is compared with theoretical results obtained with the analytical expression in Eq. (27) with  $R_g/R_c = 9.4$  and from Monte Carlo simulations with  $R_g/R_c = 8$ . ..... 146
164. Supply current,  $I_s$ , as a function of probe position for discharge conditions  $I_s = 34.62$  mA,  $V_s = -5.08$  kV, and  $P = 3.02$  mA kV<sup>-3/2</sup>. Experimental data is compared with theoretical results obtained with the analytical expression in Eq. (27) with  $R_g/R_c = 9.4$  and from Monte Carlo simulations with  $R_g/R_c = 6$ . ..... 147

165. “Width” with respect to $P_i$ and $\beta$ . This plot is computed with $\sigma_{e\phi} = 0.005$ and $\sigma_{i\phi} = 0.05$ .	163
166. “Width” with respect to $P_i$ and $\beta$ . This plot is computed with $\sigma_{e\phi} = 0.005$ and $\sigma_{i\phi} = 0.10$ .	163
167. “Width” with respect to $\sigma_{e\phi}$ and $\sigma_{i\phi}$ . This plot is computed with $P_i = 100$ mA $kV^{-3/2}$ and $\beta = 0.25$ .	164
168. “Width” with respect to $\sigma_{e\phi}$ and $\sigma_{i\phi}$ . This plot is computed with $P_i = 138$ mA $kV^{-3/2}$ and $\beta = 0.25$ .	164
169. “Width” with respect to $\sigma_{e\phi}$ and $\sigma_{i\phi}$ . This plot is computed with $P_i = 100$ mA $kV^{-3/2}$ and $\beta = 0.33$ .	165
170. “Width” with respect to $\sigma_{e\phi}$ and $\sigma_{i\phi}$ . This plot is computed with $P_i = 138$ mA $kV^{-3/2}$ and $\beta = 0.33$ .	165
171. “Width” with respect to $\sigma_{e\phi}$ and $\sigma_{i\phi}$ . This plot is computed with $P_i = 100$ mA $kV^{-3/2}$ and $\beta = 0.50$ .	166
172. “Width” with respect to $\sigma_{e\phi}$ and $\sigma_{i\phi}$ . This plot is computed with $P_i = 138$ mA $kV^{-3/2}$ and $\beta = 0.50$ .	166
173. “Width” with respect to $\sigma_{e\phi}$ and $\sigma_{i\phi}$ . This plot is computed with $P_i = 100$ mA $kV^{-3/2}$ and $\beta = 0.67$ .	167
174. “Width” with respect to $\sigma_{e\phi}$ and $\sigma_{i\phi}$ . This plot is computed with $P_i = 138$ mA $kV^{-3/2}$ and $\beta = 0.67$ .	167
175. $\log_{10}(Y_{\min})$ with respect to $P_i$ and $\beta$ . This plot is computed with $\sigma_{e\phi} = 0.005$ and $\sigma_{i\phi} = 0.05$ .	168
176. $Y_{\min}$ with respect to $P_i$ and $\beta$ . This plot is computed with $\sigma_{e\phi} = 0.005$ and $\sigma_{i\phi} = 0.10$ .	168
177. $Y_{\min}^{3/2}$ with respect to $\sigma_{e\phi}$ and $\sigma_{i\phi}$ . This plot is computed with $P_i = 100$ mA $kV^{-3/2}$ and $\beta = 0.25$ .	169
178. $Y_{\min}^{3/2}$ with respect to $\sigma_{e\phi}$ and $\sigma_{i\phi}$ . This plot is computed with $P_i = 138$ mA $kV^{-3/2}$ and $\beta = 0.25$ .	169

179. $Y_{\min}^{3/2}$ with respect to $\sigma_{e\phi}$ and $\sigma_{i\phi}$ . This plot is computed with $P_i = 100$ mA kV <sup>-1</sup> and $\beta = 0.33$ .	170
180. $Y_{\min}^{3/2}$ with respect to $\sigma_{e\phi}$ and $\sigma_{i\phi}$ . This plot is computed with $P_i = 138$ mA kV <sup>-1</sup> and $\beta = 0.33$ .	170
181. $Y_{\min}^{3/2}$ with respect to $\sigma_{e\phi}$ and $\sigma_{i\phi}$ . This plot is computed with $P_i = 100$ mA kV <sup>-1</sup> and $\beta = 0.50$ .	171
182. $Y_{\min}^{3/2}$ with respect to $\sigma_{e\phi}$ and $\sigma_{i\phi}$ . This plot is computed with $P_i = 138$ mA kV <sup>-1</sup> and $\beta = 0.50$ .	171
183. $Y_{\min}^{3/2}$ with respect to $\sigma_{e\phi}$ and $\sigma_{i\phi}$ . This plot is computed with $P_i = 100$ mA kV <sup>-1</sup> and $\beta = 0.67$ .	172
184. $Y_{\min}^{3/2}$ with respect to $\sigma_{e\phi}$ and $\sigma_{i\phi}$ . This plot is computed with $P_i = 138$ mA kV <sup>-1</sup> and $\beta = 0.67$ .	172
185. $\text{Log}_{10}(Y_{\text{core}})$ with respect to $P_i$ and $\beta$ . This plot is computed with $\sigma_{e\phi} = 0.005$ and $\sigma_{i\phi} = 0.05$ .	173
186. $\text{Log}_{10}(Y_{\text{core}})$ with respect to $P_i$ and $\beta$ . This plot is computed with $\sigma_{e\phi} = 0.005$ and $\sigma_{i\phi} = 0.10$ .	173
187. $\text{Log}_{10}(Y_{\text{core}})$ with respect to $P_i$ and $\beta$ . This plot is computed with $\sigma_{e\phi} = 0.005$ and $\sigma_{i\phi} = 0.25$ .	174
188. $Y_{\text{core}}$ with respect to $\sigma_{e\phi}$ and $\sigma_{i\phi}$ . This plot is computed with $P_i = 100$ mA kV <sup>-3/2</sup> and $\beta = 0.25$ .	174
189. $Y_{\text{core}}$ with respect to $\sigma_{e\phi}$ and $\sigma_{i\phi}$ . This plot is computed with $P_i = 138$ mA kV <sup>-3/2</sup> and $\beta = 0.25$ .	175
190. $Y_{\text{core}}$ with respect to $\sigma_{e\phi}$ and $\sigma_{i\phi}$ . This plot is computed with $P_i = 200$ mA kV <sup>-3/2</sup> and $\beta = 0.25$ .	175
191. $Y_{\text{core}}$ with respect to $\sigma_{e\phi}$ and $\sigma_{i\phi}$ . This plot is computed with $P_i = 100$ mA kV <sup>-3/2</sup> and $\beta = 0.33$ .	176
192. $Y_{\text{core}}$ with respect to $\sigma_{e\phi}$ and $\sigma_{i\phi}$ . This plot is computed with $P_i = 138$ mA kV <sup>-3/2</sup> and $\beta = 0.33$ .	176

193. $Y_{\text{core}}$ with respect to $\sigma_{e\phi}$ and $\sigma_{i\phi}$ . This plot is computed with $P_i = 276$ mA kV <sup>-3/2</sup> and $\beta = 0.33$ . .....	177
194. $Y_{\text{core}}$ with respect to $\sigma_{e\phi}$ and $\sigma_{i\phi}$ . This plot is computed with $P_i = 100$ mA kV <sup>-3/2</sup> and $\beta = 0.50$ . .....	177
195. $Y_{\text{core}}$ with respect to $\sigma_{e\phi}$ and $\sigma_{i\phi}$ . This plot is computed with $P_i = 138$ mA kV <sup>-3/2</sup> and $\beta = 0.50$ . .....	178
196. $Y_{\text{core}}$ with respect to $\sigma_{e\phi}$ and $\sigma_{i\phi}$ . This plot is computed with $P_i = 276$ mA kV <sup>-3/2</sup> and $\beta = 0.50$ . .....	178
197. $Y_{\text{core}}$ with respect to $\sigma_{e\phi}$ and $\sigma_{i\phi}$ . This plot is computed with $P_i = 100$ mA kV <sup>-3/2</sup> and $\beta = 0.67$ . .....	179
198. $Y_{\text{core}}$ with respect to $\sigma_{e\phi}$ and $\sigma_{i\phi}$ . This plot is computed with $P_i = 138$ mA kV <sup>-3/2</sup> and $\beta = 0.67$ . .....	179
199. $Y_{\text{core}}$ with respect to $\sigma_{e\phi}$ and $\sigma_{i\phi}$ . This plot is computed with $P_i = 276$ mA kV <sup>-3/2</sup> and $\beta = 0.67$ . .....	180
200. $\text{Log}_{10}(n_e(0))$ with respect to $P_i$ and $\beta$ . This plot is computed with $\sigma_{e\phi} = 0.005$ and $\sigma_{i\phi} = 0.05$ . The units are $V^{-1} \text{cm}^{-1}$ as density scales with $ V_g /R_g^2$ where $V_g$ is the grid potential and $R_g$ is the grid radius. ....	180
201. $\text{Log}_{10}(n_e(0))$ with respect to $P_i$ and $\beta$ . This plot is computed with $\sigma_{e\phi} = 0.005$ and $\sigma_{i\phi} = 0.10$ . The units are $V^{-1} \text{cm}^{-1}$ as density scales with $ V_g /R_g^2$ where $V_g$ is the grid potential and $R_g$ is the grid radius. ....	181
202. $\text{Log}_{10}(n_e(0))$ with respect to $P_i$ and $\beta$ . This plot is computed with $\sigma_{e\phi} = 0.005$ and $\sigma_{i\phi} = 0.10$ . The units are $V^{-1} \text{cm}^{-1}$ as density scales with $ V_g /R_g^2$ where $V_g$ is the grid potential and $R_g$ is the grid radius. ....	181
203. $\text{Log}_{10}(n_e(0))$ with respect to $\sigma_{e\phi}$ and $\sigma_{i\phi}$ . This plot is computed with $P_i = 100$ mA kV <sup>-3/2</sup> and $\beta = 0.25$ . The units are $V^{-1} \text{cm}^{-1}$ as density scales with $ V_g /R_g^2$ where $V_g$ is the grid potential and $R_g$ is the grid radius. ....	182
204. $\text{Log}_{10}(n_e(0))$ with respect to $\sigma_{e\phi}$ and $\sigma_{i\phi}$ . This plot is computed with $P_i = 138$ mA kV <sup>-3/2</sup> and $\beta = 0.25$ . The units are $V^{-1} \text{cm}^{-1}$ as density scales with $ V_g /R_g^2$ where $V_g$ is the grid potential and $R_g$ is the grid radius. ....	182

205.  $\text{Log}_{10}(n_e(0))$  with respect to  $\sigma_{e\phi}$  and  $\sigma_{i\phi}$ . This plot is computed with  $P_i = 200$  mA  $\text{kV}^{-3/2}$  and  $\beta = 0.25$ . The units are  $V^{-1} \text{cm}^{-1}$  as density scales with  $|V_g|/R_g^2$  where  $V_g$  is the grid potential and  $R_g$  is the grid radius. .... 183
206.  $\text{Log}_{10}(n_e(0))$  with respect to  $\sigma_{e\phi}$  and  $\sigma_{i\phi}$ . This plot is computed with  $P_i = 100$  mA  $\text{kV}^{-3/2}$  and  $\beta = 0.33$ . The units are  $V^{-1} \text{cm}^{-1}$  as density scales with  $|V_g|/R_g^2$  where  $V_g$  is the grid potential and  $R_g$  is the grid radius. .... 183
207.  $\text{Log}_{10}(n_e(0))$  with respect to  $\sigma_{e\phi}$  and  $\sigma_{i\phi}$ . This plot is computed with  $P_i = 138$  mA  $\text{kV}^{-3/2}$  and  $\beta = 0.33$ . The units are  $V^{-1} \text{cm}^{-1}$  as density scales with  $|V_g|/R_g^2$  where  $V_g$  is the grid potential and  $R_g$  is the grid radius. .... 184
208.  $\text{Log}_{10}(n_e(0))$  with respect to  $\sigma_{e\phi}$  and  $\sigma_{i\phi}$ . This plot is computed with  $P_i = 276$  mA  $\text{kV}^{-3/2}$  and  $\beta = 0.33$ . The units are  $V^{-1} \text{cm}^{-1}$  as density scales with  $|V_g|/R_g^2$  where  $V_g$  is the grid potential and  $R_g$  is the grid radius. .... 184
209.  $\text{Log}_{10}(n_e(0))$  with respect to  $\sigma_{e\phi}$  and  $\sigma_{i\phi}$ . This plot is computed with  $P_i = 100$  mA  $\text{kV}^{-3/2}$  and  $\beta = 0.50$ . The units are  $V^{-1} \text{cm}^{-1}$  as density scales with  $|V_g|/R_g^2$  where  $V_g$  is the grid potential and  $R_g$  is the grid radius. .... 185
210.  $\text{Log}_{10}(n_e(0))$  with respect to  $\sigma_{e\phi}$  and  $\sigma_{i\phi}$ . This plot is computed with  $P_i = 138$  mA  $\text{kV}^{-3/2}$  and  $\beta = 0.50$ . The units are  $V^{-1} \text{cm}^{-1}$  as density scales with  $|V_g|/R_g^2$  where  $V_g$  is the grid potential and  $R_g$  is the grid radius. .... 185
211.  $\text{Log}_{10}(n_e(0))$  with respect to  $\sigma_{e\phi}$  and  $\sigma_{i\phi}$ . This plot is computed with  $P_i = 276$  mA  $\text{kV}^{-3/2}$  and  $\beta = 0.50$ . The units are  $V^{-1} \text{cm}^{-1}$  as density scales with  $|V_g|/R_g^2$  where  $V_g$  is the grid potential and  $R_g$  is the grid radius. .... 186
212.  $\text{Log}_{10}(n_e(0))$  with respect to  $\sigma_{e\phi}$  and  $\sigma_{i\phi}$ . This plot is computed with  $P_i = 100$  mA  $\text{kV}^{-3/2}$  and  $\beta = 0.67$ . The units are  $V^{-1} \text{cm}^{-1}$  as density scales with  $|V_g|/R_g^2$  where  $V_g$  is the grid potential and  $R_g$  is the grid radius. .... 186
213.  $\text{Log}_{10}(n_e(0))$  with respect to  $\sigma_{e\phi}$  and  $\sigma_{i\phi}$ . This plot is computed with  $P_i = 138$  mA  $\text{kV}^{-3/2}$  and  $\beta = 0.67$ . The units are  $V^{-1} \text{cm}^{-1}$  as density scales with  $|V_g|/R_g^2$  where  $V_g$  is the grid potential and  $R_g$  is the grid radius. .... 187
214.  $\text{Log}_{10}(n_e(0))$  with respect to  $\sigma_{e\phi}$  and  $\sigma_{i\phi}$ . This plot is computed with  $P_i = 276$  mA  $\text{kV}^{-3/2}$  and  $\beta = 0.67$ . The units are  $V^{-1} \text{cm}^{-1}$  as density scales with  $|V_g|/R_g^2$  where  $V_g$  is the grid potential and  $R_g$  is the grid radius. .... 187
215.  $\text{Log}_{10}(n_i(0))$  with respect to  $P_i$  and  $\beta$ . This plot is computed with  $\sigma_{e\phi} = 0.005$  and  $\sigma_{i\phi} = 0.05$ . The units are  $V^{-1} \text{cm}^{-1}$  as density scales with  $|V_g|/R_g^2$  where  $V_g$  is the grid potential and  $R_g$  is the grid radius. .... 188

216.  $\text{Log}_{10}(n_i(0))$  with respect to  $P_i$  and  $\beta$ . This plot is computed with  $\sigma_{e\phi} = 0.005$  and  $\sigma_{i\phi} = 0.10$ . The units are  $V^{-1} \text{ cm}^{-1}$  as density scales with  $|V_g|/R_g^2$  where  $V_g$  is the grid potential and  $R_g$  is the grid radius. .... 188
217.  $\text{Log}_{10}(n_i(0))$  with respect to  $P_i$  and  $\beta$ . This plot is computed with  $\sigma_{e\phi} = 0.005$  and  $\sigma_{i\phi} = 0.25$ . The units are  $V^{-1} \text{ cm}^{-1}$  as density scales with  $|V_g|/R_g^2$  where  $V_g$  is the grid potential and  $R_g$  is the grid radius. .... 189
218.  $\text{Log}_{10}(n_i(0))$  with respect to  $\sigma_{e\phi}$  and  $\sigma_{i\phi}$ . This plot is computed with  $P_i = 100$  mA  $\text{kV}^{-3/2}$  and  $\beta = 0.25$ . The units are  $V^{-1} \text{ cm}^{-1}$  as density scales with  $|V_g|/R_g^2$  where  $V_g$  is the grid potential and  $R_g$  is the grid radius. .... 189
219.  $\text{Log}_{10}(n_i(0))$  with respect to  $\sigma_{e\phi}$  and  $\sigma_{i\phi}$ . This plot is computed with  $P_i = 138$  mA  $\text{kV}^{-3/2}$  and  $\beta = 0.25$ . The units are  $V^{-1} \text{ cm}^{-1}$  as density scales with  $|V_g|/R_g^2$  where  $V_g$  is the grid potential and  $R_g$  is the grid radius. .... 190
220.  $\text{Log}_{10}(n_i(0))$  with respect to  $\sigma_{e\phi}$  and  $\sigma_{i\phi}$ . This plot is computed with  $P_i = 200$  mA  $\text{kV}^{-3/2}$  and  $\beta = 0.25$ . The units are  $V^{-1} \text{ cm}^{-1}$  as density scales with  $|V_g|/R_g^2$  where  $V_g$  is the grid potential and  $R_g$  is the grid radius. .... 190
221.  $\text{Log}_{10}(n_i(0))$  with respect to  $\sigma_{e\phi}$  and  $\sigma_{i\phi}$ . This plot is computed with  $P_i = 100$  mA  $\text{kV}^{-3/2}$  and  $\beta = 0.33$ . The units are  $V^{-1} \text{ cm}^{-1}$  as density scales with  $|V_g|/R_g^2$  where  $V_g$  is the grid potential and  $R_g$  is the grid radius. .... 191
222.  $\text{Log}_{10}(n_i(0))$  with respect to  $\sigma_{e\phi}$  and  $\sigma_{i\phi}$ . This plot is computed with  $P_i = 138$  mA  $\text{kV}^{-3/2}$  and  $\beta = 0.33$ . The units are  $V^{-1} \text{ cm}^{-1}$  as density scales with  $|V_g|/R_g^2$  where  $V_g$  is the grid potential and  $R_g$  is the grid radius. .... 191
223.  $\text{Log}_{10}(n_i(0))$  with respect to  $\sigma_{e\phi}$  and  $\sigma_{i\phi}$ . This plot is computed with  $P_i = 276$  mA  $\text{kV}^{-3/2}$  and  $\beta = 0.33$ . The units are  $V^{-1} \text{ cm}^{-1}$  as density scales with  $|V_g|/R_g^2$  where  $V_g$  is the grid potential and  $R_g$  is the grid radius. .... 192
224.  $\text{Log}_{10}(n_i(0))$  with respect to  $\sigma_{e\phi}$  and  $\sigma_{i\phi}$ . This plot is computed with  $P_i = 100$  mA  $\text{kV}^{-3/2}$  and  $\beta = 0.50$ . The units are  $V^{-1} \text{ cm}^{-1}$  as density scales with  $|V_g|/R_g^2$  where  $V_g$  is the grid potential and  $R_g$  is the grid radius. .... 192
225.  $\text{Log}_{10}(n_i(0))$  with respect to  $\sigma_{e\phi}$  and  $\sigma_{i\phi}$ . This plot is computed with  $P_i = 138$  mA  $\text{kV}^{-3/2}$  and  $\beta = 0.50$ . The units are  $V^{-1} \text{ cm}^{-1}$  as density scales with  $|V_g|/R_g^2$  where  $V_g$  is the grid potential and  $R_g$  is the grid radius. .... 193
226.  $\text{Log}_{10}(n_i(0))$  with respect to  $\sigma_{e\phi}$  and  $\sigma_{i\phi}$ . This plot is computed with  $P_i = 276$  mA  $\text{kV}^{-3/2}$  and  $\beta = 0.50$ . The units are  $V^{-1} \text{ cm}^{-1}$  as density scales with  $|V_g|/R_g^2$  where  $V_g$  is the grid potential and  $R_g$  is the grid radius. .... 193

227.  $\text{Log}_{10}(n_i(0))$  with respect to  $\sigma_{e\phi}$  and  $\sigma_{i\phi}$ . This plot is computed with  $P_i = 100$  mA  $\text{kV}^{-3/2}$  and  $\beta = 0.67$ . The units are  $V^{-1} \text{cm}^{-1}$  as density scales with  $|V_g|/R_g^2$  where  $V_g$  is the grid potential and  $R_g$  is the grid radius. .... 194
228.  $\text{Log}_{10}(n_i(0))$  with respect to  $\sigma_{e\phi}$  and  $\sigma_{i\phi}$ . This plot is computed with  $P_i = 138$  mA  $\text{kV}^{-3/2}$  and  $\beta = 0.67$ . The units are  $V^{-1} \text{cm}^{-1}$  as density scales with  $|V_g|/R_g^2$  where  $V_g$  is the grid potential and  $R_g$  is the grid radius. .... 194
229.  $\text{Log}_{10}(n_i(0))$  with respect to  $\sigma_{e\phi}$  and  $\sigma_{i\phi}$ . This plot is computed with  $P_i = 276$  mA  $\text{kV}^{-3/2}$  and  $\beta = 0.67$ . The units are  $V^{-1} \text{cm}^{-1}$  as density scales with  $|V_g|/R_g^2$  where  $V_g$  is the grid potential and  $R_g$  is the grid radius. .... 195
230. Depiction of sheath and pre-sheath regions adjacent to a planar probe surface. ...200
231. Straight lines a-a' and b-b' are fit to portions of the curve on either side of the kink that occurs near the plasma potential. The slope of line a-a' determines  $kT_e$  while the intersection of lines a-a' and b-b' can determine the plasma potential,  $V_\infty$  and electron saturation current,  $I_{es}$ .....200

## LIST OF TABLES

Table	Page
I. Summary of standard two electrode IEC varieties and associated nomenclature. The variants considered include electrode geometry, electrode positioning, and ion source mechanism. ....	4
II. Summary of trends observed from modeling on the relationships between the control variables and the observables, <i>FWD</i> and <i>DWD</i> for IXL SIECs. ....	18
III. Summary of IEC experiments before 1980. These experiments generally classify as electron beam probe measurements of the potential well structure or measurements of the particle densities. ....	19
IV. Summary of single potential well measurements in SIEC devices. ....	25
V. Summary of experimental double potential well measurements in SIEC devices. ....	26
VI. Summary of different discharge modes and their particle source mechanisms. ....	74
VII. Ten different cases for which data is collected with double probe d2 in Probe Location 1, aligned with an ion micro-channel. Results for these ten cases are provided in Fig. 94 through Fig. 102. ....	98
VIII. Legend for electron density, $n_e$ , and electron temperature, $T_e$ , measurements obtained from single probe investigations. ....	125
IX. Legend for probe shadowing data collected with double probe d1 inserted into Probe Location 1 as indicated in Fig. 46. ....	127
X. Ion density profile characteristics for three of the discharge conditions represented in Fig. 100 through Fig. 102. ....	145

XI. Maps of observables in control variable space are given in Fig. 165 through Fig. 229 as indicated. ....162

XII. List of materials and components for double and single Langmuir probe measurements.....201

## ABSTRACT

Inertial Electrostatic Confinement (IEC) is a means to confine ions for fusion purposes with electrostatic fields in a converging geometry. Its engineering simplicity makes it appealing when compared to magnetic confinement devices. It is hoped that such a device may one day be a net energy producer, but it has near term applications as a neutron generator. We study spherical IECs (SIECs), both theoretically and experimentally. Theoretically, we compute solutions in the free molecular limit and map out regions in control parameter space conducive to the formation of double potential wells. In addition, several other observables are mapped in the control parameter space. Such studies predict the threshold for the phenomena of “core splitting” to occur when the fractional well depth (FWD) is  $\sim 70\%$ - $80\%$ . With respect to double potential wells, it is shown that an optimal population of electrons exists for double well formation. In addition, double well depth is relatively insensitive to space charge spreading of ion beams.

Glow discharge devices are studied experimentally with double and single Langmuir probes. The postulated micro-channeling phenomenon is verified with density measurements along a micro-channel and along the radius where micro-channels are absent. In addition, the measurements allow an evaluation of the neutrality of micro-channels and the heterogeneous structure of “Star Mode”. It is shown that, despite visual evidence, micro-channeling persists well into jet mode. In addition, the threshold for the “Star” mode to “Jet” mode transition is obtained experimentally. The studies have revealed new techniques for estimating tangential electric field components and studying the focusing of ion flow.

## I. Introduction

### A. *Motivation*

Inertial Electrostatic Confinement (IEC) is a fusion concept in which fuel ions are trapped with purely electrostatic fields in a convergent geometry, as opposed to magnetic confinement. Credit for its invention is independently given to U.S. scientist Philo Farnsworth (also inventor of the television) and Russian scientist Oleg Lavrent'yev, as both formulated means of electrostatic confinement almost simultaneously throughout the 1950's and into the 1960's.<sup>1,2,3,4</sup> Features of a device based on this concept that make it appealing are (a) its relatively small size and engineering simplicity, (b) its ability to maintain the fuel source in a non-maxwellian state (allows usage of advanced fuels producing only charged fusion products), and (c) its natural integration with a direct energy conversion system (via capture of charged fusion products from advanced reactions).<sup>5</sup> However, IEC reactors to date have operated at very low Q values ( $10^{-9} - 10^{-5}$ ), where Q is the ratio of fusion power produced  $P_f$  to power consumed  $P_{in}$ , and it remains to be seen if its above cited advantages will scale to high Q values ( $Q \sim 1$ ).<sup>6,7</sup>

Applications of high Q IEC reactors are obvious as they could be used for terrestrial energy generation and also as the main energy sources for space vehicles.<sup>8-13</sup> Another application of the high Q IEC reactor is the breeding of advanced fuels such as  $^3\text{He}$  and T.<sup>14,15</sup> Low Q IEC devices also have a substantial number of applications as they can produce a copious amount of neutrons for neutron detector calibration<sup>16,17</sup>, several NAA applications<sup>18-21</sup>, transmutation applications<sup>22,23</sup>, and material studies.<sup>24</sup> Of course, high Q devices can also perform all of these functions.

## ***B. Physical Description***

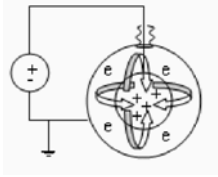
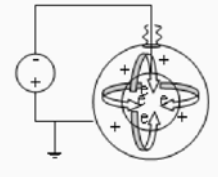
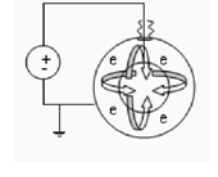
To better understand the physical nature of an IEC device, we will consider a glow discharge (GD) operated IEC. A typical IEC device would consist of two electrodes with different sizes and similar convergent geometries, with the smaller electrode located concentrically within the larger electrode, and with both electrodes placed in a vacuum environment. In addition, the smaller, or “inner” electrode would normally be constructed out of thin wire to form a grid-like structure that is mostly transparent to the flow of particles. If we further consider the inner electrode to be the cathode, then we can create ions by backfilling the vacuum with the desired gas and applying a high magnitude negative potential to the cathode. In the case of GD operation, ions are created through ionization reactions between projectile particles (ions, electrons, fast neutral particles) and target particles (the background gas). The resulting ions are accelerated by the field in the inter-electrode space to the center of the highly transparent cathode. A number of ion orbits will be expected to intersect in a region at the center of the cathode defined as the core. These intersecting ions will have a non-zero probability of fusing given by the fusion cross-section for the particles. However, in a GD device, it should be mentioned that fusion reactions between projectile ions and fast neutrals with the target background gas dominate the fusion reactivity.

To aide the reader in navigating through the rest of this manuscript, it is appropriate to develop nomenclature that distinguishes a number of the IEC variants. The variations occur in the geometry (i.e. cylindrical or spherical), the order of the electrodes, and the ion source mechanism, as noted by Nadler.<sup>16</sup> Other variations can be considered, but are less common, so we will refer to these other devices individually. A

few words need to be mentioned regarding the ion source mechanism nomenclature. Namely, GD is used to refer to glow discharge and, in particular, those devices that operate on the  $\frac{dV_s}{d(pd)} \leq 0$  portion of the striking voltage vs. pressure times electrode spacing,  $V_s$  vs.  $pd$ , characteristic, or paschen curve, for the particular IEC device. The acronym AGD refers to assisted glow discharge, and is used to refer to a device that relies on the background neutral gas molecules for a source of ions, but operates on a curve shifted in the direction of decreasing  $pd$  from the paschen curve of an unassisted device, as illustrated in Fig. 1. This shift is caused by the insertion of electron emitters, electron guns, or the use of ion guns. The variations and their nomenclature are summarized in Table I. It should also be noted in Table I that “Injected Particle” refers to the particle born at the outer-electrode or somewhere within the inter-electrode space and arrives at the inner electrode with maximum kinetic energy. “Trapped Particle” refers to the particle born within the inner electrode, and is ideally confined within the inner electrode volume.

Other variations include the Polywell™ concept<sup>5,25,26</sup>, the Penning trap<sup>27,28</sup>, the Periodically Oscillating Plasma Sphere (POPS)<sup>29</sup>, the Multi-pole Ion Beam Experiment (MIX) concept<sup>30</sup>, and multi-electrode (#electrodes >2) devices.<sup>11,12,13</sup> All of these devices include some feature that make them more complex than the simple two electrode devices, but with the intention of circumventing some of the loss mechanisms known to plague (or predicted to plague) IEC devices.

Table I: Summary of standard two electrode IEC varieties and associated nomenclature. The variants considered include electrode geometry, electrode positioning, and ion source mechanism.

<i>Schematic</i>	<i>Injected Particle</i>	<i>Trapped Particle</i>	<i>Geometry</i>	<i>Ion Source Mechanism</i>	<i>Nomenclature</i>
	electron	ion	Cylindrical	Glow Discharge (GD) Assisted Glow Discharge (AGD)	GD EXL CIEC AGD EXL CIEC
			Spherical	GD AGD	GD EXL SIEC AGD EXL SIEC
	ion	electron	Cylindrical	GD AGD	GD IXL CIEC AGD IXL CIEC
			Spherical	GD AGD	GD IXL SIEC AGD IXL SIEC
	electron	-----	Cylindrical	GD AGD	GD UCEXL AGD UCEXL
			Spherical	GD AGD	GD USEXL AGD USEXL

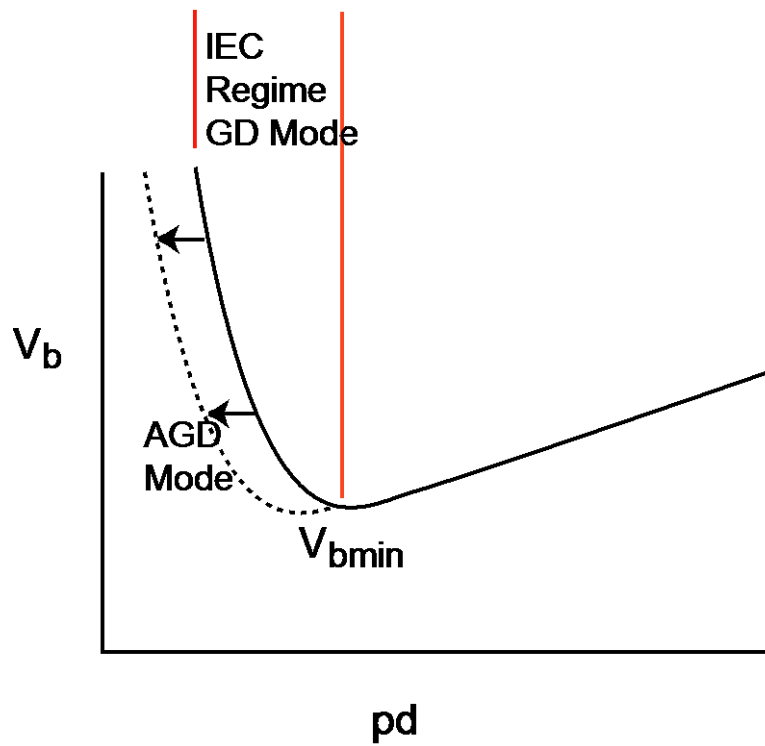


Fig. 1: Paschen curve diagram to illustrate GD and AGD modes of IXL IEC operation. The operational curve for AGD mode is shifted to lower values of  $pd$  due to the aid of electron emitting filaments, ion guns, etc.

### ***C. Glow Discharge Modes***

A large portion of this dissertation will be concerned with IXL SIECs operating in the glow discharge mode. In this section, we will discuss these modes by first reviewing a few characteristics of glow discharges between planar electrodes in glass tubes. We will also highlight the relationship of these discharges to the glow discharges in IXL SIECs, relying much on the analysis by Jurczyk.<sup>59</sup> Then a description of two GD modes, “Star Mode” and “Jet Mode”, will be provided.

#### **1. Discharges between planar electrodes**

The structure of a glow discharge between parallel planar electrodes for  $\lambda \ll d$ , is well known, where  $\lambda$  is the mean free path of ions or electrons and  $d$  is the dimension between the two electrodes. Such a discharge consists of a layered structure of dark and luminous regions, as shown in Fig. 2.<sup>77-79</sup> Discharge accounting requires that electron source and sink processes must balance. Source mechanisms include secondary emissions from the electrodes and ionizations in the negative glow and positive column. Loss mechanisms mostly include transport to the chamber walls.

Starting from the cathode, one enters the adjacent sheath region, which is populated with ions. The thickness of the voltage sheath,  $x_s$ , is normally such that it is less than  $\lambda$  for electrons so that secondary emission by impinging ions on the cathode produces a nearly mono-energetic source of electrons with an energy equivalent to the cathode sheath voltage drop. The energy of these primary electrons is mostly deposited in the negative glow, but the electrons remain highly anisotropic with three populations of electrons emerging.<sup>78</sup> These populations are:

- Primary electrons: monoenergetic electrons produced by secondary emission from the cathode and accelerated across the cathode sheath
- Secondary electrons: maxwellian distributed electrons with a temperature proportional to the beam energy of the primary electron group
- Ultimate electrons: maxwellian distributed electrons with a temperature of a few eV and a density of  $10^3$  greater than those of the primaries and secondaries

Traversing further into the positive column, the electron energies are further attenuated until a single maxwellian distribution emerges. It has been noted that as the length of the discharge tube is decreased, the structure of the glow discharge remains the same except that the length of the positive column decreases. The positive column is not really necessary for discharge sustenance and the length of the tube can be decreased until the positive column disappears. As the tube continues to shrink into the negative glow region, one enters a mode known as the obstructed glow discharge. In this mode, many of the primary electrons stream through the whole tube and deposit their entire energy in the anode. In this case, the discharge is much less efficient with respect to electron impact ionization and must rely more on ion impact ionization. This requires that the discharge operates at higher voltages.<sup>59</sup>

## **2. IXL SIEC Glow Discharge Characteristics**

The glow discharge of an IXL SIEC is different than the parallel planar electrode discharges for several reasons.<sup>59</sup> The IXL SIEC is essentially a severely obstructed glow discharge with a hollow cathode. The obstructed nature results in a high voltage operation which is necessary for fusion neutron production, and the hollow cathode

results in a lower operating pressure due to recirculating ions. It has been noted the glow discharge should be mostly “sheath-like”<sup>59</sup>, however, in this case the sheath dimension is several times  $\lambda$  for both electrons and ions. Given this condition, a significant amount of the electron kinetic energy is deposited at the anode.

“Star Mode” is a GD mode that occurs due to the complex structure of the sheath in a GD IXL SIEC. In the planar discharges, we only have to consider the sheath in 1 dimension, but the discrete nature of the cathode grid of a GD IXL SIEC results in a complicated 3D potential structure. This results in the cathode acting as an effective charged particle lens due to the curvature of the field between the individual cathode grid wires. This means that we do not have a homogenous flow of particles between electrodes, but rather a heterogeneous flow structure of plasma “spokes” transporting particles between the electrodes. These spokes, which are often referred to as “ion micro-channels”, are also luminous as indicated in Fig. 3. “Star Mode” occurs at pressures of  $\sim$  1 to 25mTorr.

As the pressure is increased above “Star Mode” operating regimes, the discharge is visibly more uniform with the exception of radial variance and is accompanied by an electron jet through a particular grid hole of the cathode grid. For this reason, this mode is referred to as “Jet Mode”. It will be seen in the results of this dissertation that despite the visual uniformity, a heterogeneous electron flow structure still exists between the anode and cathode in “Jet Mode”.

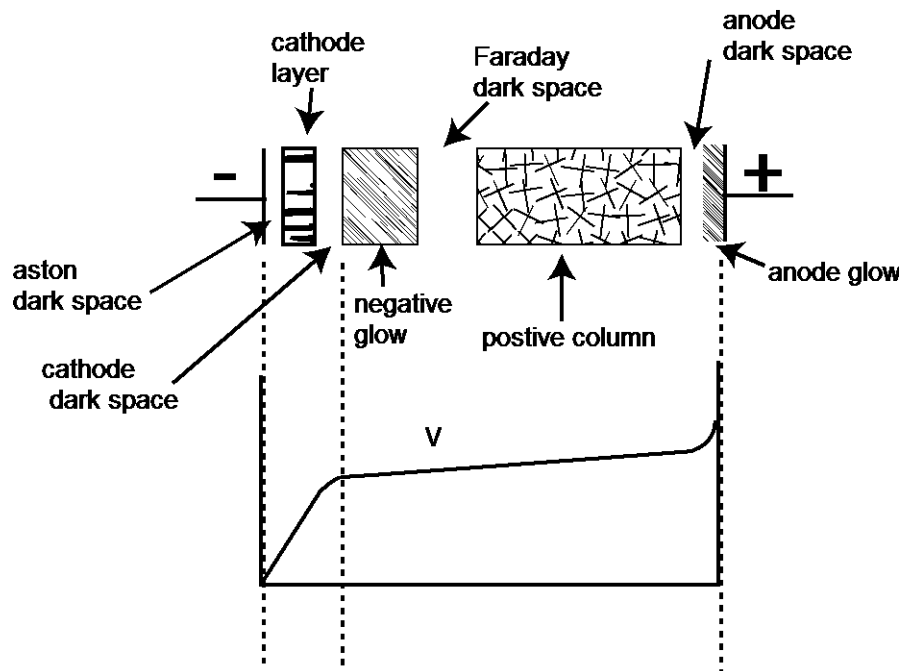


Fig. 2: Structure of a glow discharge between parallel planar electrodes for  $\lambda \ll d$ , where  $\lambda$  is the mean free path of ions or electrons and  $d$  is the distance between electrodes. This figure is an approximation to one that appears in multiple texts<sup>77,78,79</sup> discussing glow discharges.

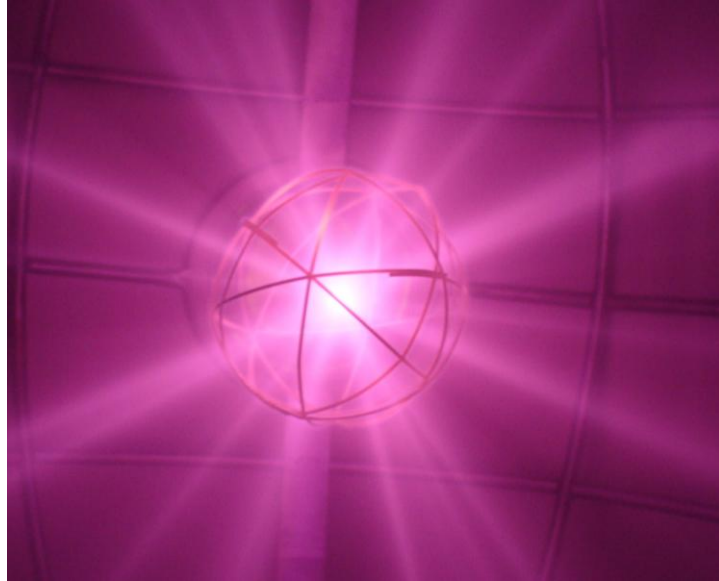


Fig. 3: Photo of GD IXL SIEC in “Star Mode” operation at University of Missouri-Columbia. Luminous spokes are visible indicating the heterogeneous discharge structure.

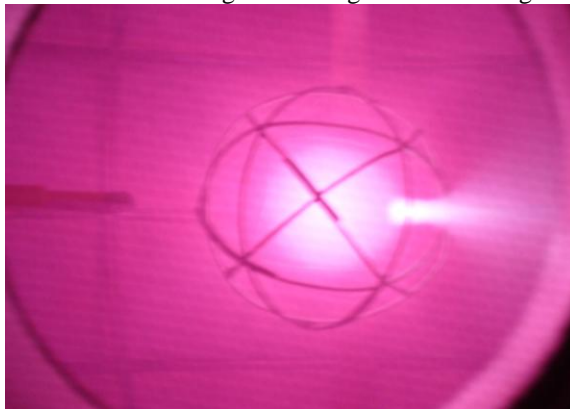


Fig. 4: Photo of GD IXL SIEC in “Jet Mode” operation at University of Missouri-Columbia. The electron jet is clearly visible.

## **D. Definitions**

### **1. Observables (Dependent Variables)**

#### **a) Potential Well Structures**

The formation of deep confining electrodes, with 100% transparency due to the distribution of space charge within the inner electrode of the IEC device, is a phenomena central to many investigations. It is a central issue because the existence of a complex well structure could significantly reduce ion loss to the cathode structure. In addition, it has been speculated that the existence of such a structure should result in a neutron production rate (npr) that exhibits highly non-linear scaling with device current (i.e.  $npr \propto I^n$  where  $n \geq 2$ ).<sup>31,32</sup>

Structures of primary interest are the single potential well, in Fig. 5, and the double potential well, depicted in Fig. 6. These figures represent the shape of the normalized radial potential profile,  $Y = \varphi/\varphi_g$ , within the innermost electrode of the devices tabulated in Table I. In this case,  $\varphi$  is the potential at normalized radius,  $X = r/R_g$ , and  $\varphi_g$  is the potential applied to the inner electrode ( $X = 1$ ) and  $Y$  is the normalized potential at  $X$ .  $R_g$  is the radius of the inner electrode.

For the single well case of Fig. 5, we are mostly interested in the value of the potential at  $X = 0$ . The normalized potential at this location is denoted as the core normalized potential,  $Y_{core}$ . We also note that  $dY/dX = 0$  and  $d^2Y/dX^2 > 0$  at  $X = 0$ , and this is denoted as the minimum normalized potential,  $Y_{min}$ . For the single well,  $Y_{min} = Y_{core}$ . The double well case in Fig. 6 is more complex and requires the definition of more quantities to describe it. In this case, the normalized potential at  $X = 0$  is still denoted as

$Y_{core}$ , however,  $d^2Y/dX^2 < 0$  at  $X = 0$ , so the normalized potential at  $X = 0$  is also denoted as  $Y_{peak}$ . At some intermediate radius,  $X = width$ ,  $dY/dX = 0$  and  $d^2Y/dX^2 > 0$ , so the normalized potential at  $X = width$  is denoted as  $Y_{min}$ . Double well depth ( $DWD$ ) is an important metric for quantifying double potential well structures, and will be defined here as  $DWD = Y_{peak} - Y_{min}$ . A quantity known as fractional well depth ( $FWD$ ) can be applied to both single and double well descriptions and is defined as  $FWD = 1 - Y_{min}$ . In the double well studies by Tzonev<sup>32</sup>, the usage of a relative  $DWD$ , or  $relDWD$ , is noted and defined as  $relDWD = DWD/FWD$ .

## b) Particle Density Profiles

Fig. 7 represents a typical particle distribution along the radius of an IXL or EXL SIEC. The distribution is representative of the injected or trapped particles. This spatial distribution consists of a single central peak. Four metrics are introduced here to characterize the distributions in Fig. 7 and Fig. 8: the half width at half max ( $HWHM$ ) provides a measure of the width of the density peak,  $n_j(0)$  is the value of the injected ( $j = 0 = i$  for IXL devices,  $= e$  for EXL devices) or trapped ( $j = 1 = e$  for IXL devices,  $= i$  for EXL devices) particles at  $r = 0$ , the peak density,  $np_j$ , is the maximum value of  $n_j(r)$  within the inner electrode volume, and the compression factor ( $CF$ ) which is defined as  $n_0(0)/n_0(R_g)$ , where  $R_g$  is the radius of the inner electrode. For this case, the peak density,  $np_j$ , is equal to  $n_j(0)$ . Fig. 8 is a representation of  $n_0(r)$  for the situation in which the core region becomes space charge saturated. The splitting of the central peak into two peaks (“wings”) occurs due to the mutual repulsion of injected particles. Here, we can clearly see that  $np_0 \neq n_0(0)$ , and we should also note that  $CF < np_0/n_0(R_g)$ . In addition, we can see that  $HWHM$  must be larger to accommodate the peak splitting. One more metric that

is useful for characterizing  $n_0(r)$  is the core radius ( $CR$ ). It can be arbitrarily defined in many ways. One definition is  $CR = HWHM$ . Another way  $CR$  is defined is in terms of the ballistic trajectories of the particles. In this case,  $CR$  is referred to as the ballistic core radius ( $BCR$ ).

## 2. Controls (Independent Variables)

While operating, one generally is only able to directly manipulate the injected particle perveance,  $P_0 = I_0 / \varphi_g^{3/2}$ , of the IEC device, where  $I_0$  is the injected particle current. However, the user does have some control over other parameters such as the ratio of injected to trapped particle perveance,  $\beta$ , spreads in the normalized angular energies of injected and trapped particles,  $\sigma_{j,\phi}$ , and spreads in the normalized total energies of injected and trapped particles,  $\sigma_{j,E}$ . Control over these other variables comes through careful design of the device, and the mode of operation (i.e. GD, or AGD).  $P_0$  is convenient to work with because it provides an indication of space charge effects. 1D orbital models show that behavior is not affected by  $I_0$  or  $\varphi_g$  independently, but by the combined quantity,  $P_0$ . Practically, this is not the case, as nearly all molecular interactions have some energy dependence, so  $\varphi_g$  independently impacts device behavior.

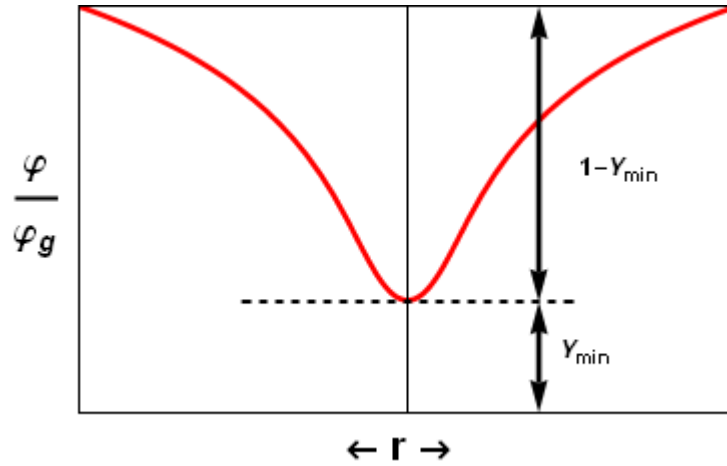


Fig. 5: A representation of a single potential well structure. In this case, the minimum normalized potential,  $Y_{min}$ , coincides with the core potential,  $Y_{core} = Y(r = 0)$ . The fractional well depth,  $FWD$  is defined as  $FWD = 1 - Y_{min}$ .

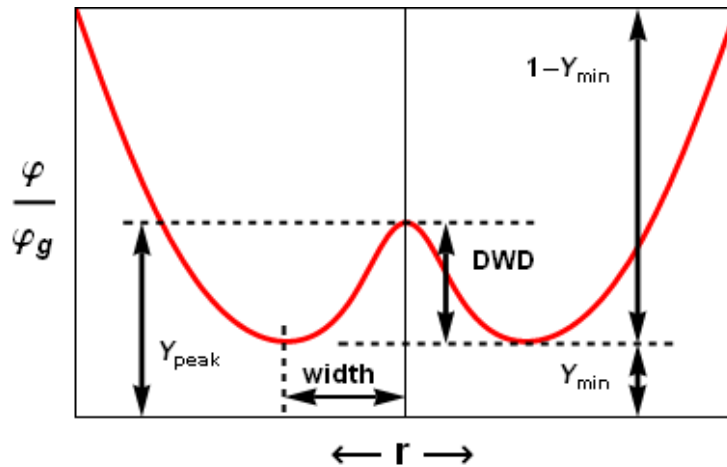


Fig. 6: A representation of a double potential well structure. In this case, fractional well depth,  $FWD$ , is defined as  $FWD = 1 - Y_{min}$ , and the double well depth ( $DWD$ ) as  $Y_{peak} - Y_{min}$ . Here,  $Y_{peak}$  coincides with  $Y_{core}$ .

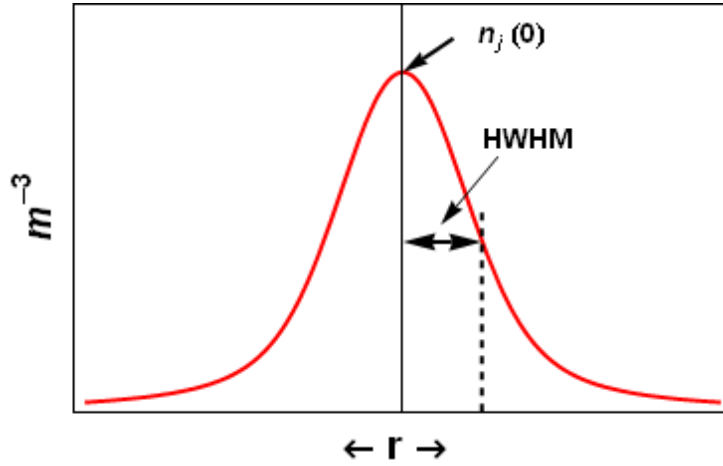


Fig. 7: Representation of a typical injected or trapped particle radial density profile,  $n_j(r)$ , within the inner grid of an SIEC. The density at  $r = 0$  is defined as  $n_j(0)$ , where  $j = 0$  represents injected particles, and  $j = 1$  represents trapped particles. The width of the density profile is indicated by the “half width at half max”,  $HWHM$ .

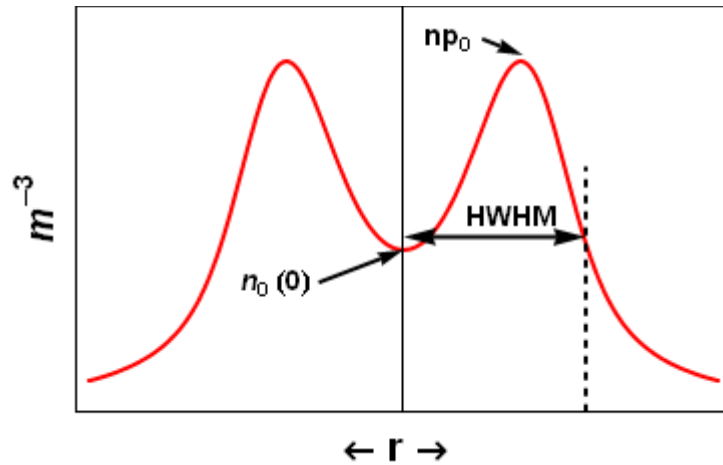


Fig. 8: Representation of an injected particle radial density profile,  $n_0(r)$ , for the case in which mutual repulsion of the injected particles results in significant space charge spreading of the core. In this case, the peak density,  $np_0$  occurs at a radius  $r \neq 0$ , and  $n_0(0) \neq np_0$ .

## ***E. Previous Work***

### **1. Before 1980**

#### **a) Theoretical Work**

One dimensional (1D) orbital modeling was used almost exclusively in the earliest works.<sup>33-42</sup> The 1D orbital model was primarily used to explore the relationship between the inner-electrode radial potential profile, and the shapes of the distribution functions for the injected and trapped particles. Farnsworth hypothesized the formation of an infinite number of virtual electrodes<sup>2</sup> based on a bi-polar version of analytical work by Langmuir and Blodgett.<sup>43</sup> This potential well structure was later confirmed with a numerical solution by Hirsch.<sup>34</sup> Hu and Klevans<sup>39</sup> showed that the placement of these virtual electrodes can be altered when spreads of a finite width in the radial energies of the injected and trapped particles are considered. However, all of these investigations assumed pure radial focusing of the injected and trapped particles.<sup>2,34,39</sup> The potential structure consisting of an infinite number of alternating virtual electrodes disappears when angular energy spreads with finite widths are considered.

An extensive investigation of finite angular energy spreads is the result of the combined works of Dolan<sup>35,36</sup>, Swanson<sup>38,37</sup>, Black and Klevans<sup>40</sup>, and Imel<sup>41</sup>. In particular, Dolan searched for solutions with large spreads in particle angular energy<sup>36</sup>, while Imel investigated small angular energy spreads<sup>41</sup>. Mostly, the distribution functions were approximated with rectangular shapes, with the exception of Swanson<sup>38,37</sup>, who modeled the angular energy spreads with maxwellian shapes. Table II includes a summary of the relationships between the control variables and *FWD*, for IXL SIECs, for

the structure in Fig. 5 from this early modeling. Exceptions to the above 1D orbital modeling include 2D dynamic modeling of uni-polar and bi-polar discharges by Hockney<sup>44</sup> and Barnes<sup>45</sup>, respectively. Hockney<sup>44</sup> produced a result similar to the structure in Fig. 8, and found that it was stable. Barnes<sup>45</sup> results indicated that the double well structure in Fig. 6 is only a transient phenomenon. The work of Barnes represents the only theoretical prediction of a double potential well during this early era.

## **b) Experimental Work**

Most notable in this time period is the seminal work by Hirsch.<sup>34</sup> Hirsch detected a steady state neutron output of  $\sim 10^8$  n/s from D-D reactions and  $\sim 10^{10}$  n/s from D-T reactions. Spatially fluctuation neutron and x-ray collimation data seemed to support the early hypothesis of an oscillating, or layered, virtual electrode structure.<sup>34</sup> The rest of the experimental work in this period generally falls into one of two categories: (1) e-beam probe measurements of *FWD* in USEXLS<sup>46-49</sup>, and (2) injected or trapped particle density measurements.<sup>35,36,50-52</sup> Electron beam probe measurements were performed by Hirsch<sup>46</sup>, Black and Robinson<sup>48</sup>, and Swanson.<sup>47</sup> The results of the e-beam experiments are shown in Fig. 9. A summary of all experiments, listing diagnostic method, device type, range of  $P_0$  considered, investigators, and notable result, is provided in Table III. It should be noted that Gardner<sup>52</sup> attempted to duplicate the work of Hirsch, but was not able to achieve equivalent yields.

Table II: Summary of trends observed from modeling on the relationships between the control variables and the observables, *FWD* and *DWD* for IXL SIECs.

Control	<i>FWD</i>	<i>DWD</i>
$P_0$	$P \uparrow \rightarrow FWD \uparrow$	$P \uparrow \rightarrow DWD \uparrow$
$\beta$	$\beta \uparrow \rightarrow FWD \uparrow$	<i>Optimum <math>0 &lt; \beta \ll 1</math> for <i>DWD</i></i>
$\sigma_{0,\phi}$	$\sigma_{0,\phi} \downarrow \rightarrow FWD \uparrow$	$\sigma_{0,\phi} \uparrow \rightarrow DWD \uparrow$ <i>plateaus for <math>\sigma_{0,\phi} \sim 1</math></i>
$\sigma_{1,\phi}$	$\sigma_{1,\phi} \downarrow \rightarrow FWD \uparrow$	$\sigma_{1,\phi} \downarrow \rightarrow DWD \uparrow$

Table III: Summary of IEC experiments before 1980. These experiments generally classify as electron beam probe measurements of the potential well structure or measurements of the particle densities.

<i>Investigator</i>	<i>Type</i>	<i>P(mA kV-3/2)</i>	<i>Technique</i>	<i>Notable Result</i>
Hirsch <sup>34</sup> (1967)	AGD IXL SIEC	0.06	neutron, x-ray counts	$n_0(0) \sim 10^{12} - 10^{14} \text{ cm}^{-3}$ $10^8 (10^{10}) \text{ n/s DD(DT)}$
Hirsch <sup>46</sup> (1968)	AGD USEXL	75	electron beam probe	FWD $\sim 90\%$
Black and Robinson <sup>48</sup> (1974)	AGD USEXL	$\leq 12$	electron beam probe	no detectable potential wells
Black and Robinson <sup>48</sup> (1974)	AGD IXL SIEC	$\leq 5.3$	electron beam probe	no detectable potential wells
Black <sup>49</sup> (1971)	AGD USEXL	11	electron beam probe	FWD $\sim 30\%$
Swanson <sup>47</sup> (1973)	AGD USEXL	21 - 170	electron beam probe	Measurable potential wells over entire range with FWD up to 60%
Dolan <sup>35</sup> (1972)	AGD IXL CIEC pulsed	$\leq 1660$	laser heterodyne	$n_0(0) \leq 10^{11} \text{ cm}^{-3}$
Dolan <sup>35</sup> (1972)	AGD EXL CIEC pulsed	$\leq 23000$	laser heterodyne	$n_1(0) \leq 10^{11} \text{ cm}^{-3}$
Meeker <sup>50</sup> (1973)	AGD IXL CIEC pulsed	$\leq 18000$	microwave resonance	$n_1(0) \leq 8 \cdot 10^{11} \text{ cm}^{-3}$
Meeker <sup>50</sup> (1973)	AGD EXL CIEC pulsed	$\leq 44500$	microwave resonance	$n_0(0) \leq 8 \cdot 10^{11} \text{ cm}^{-3}$
Grush <sup>51</sup> (1973)	AGD IXL SIEC	$\leq 37$	microwave resonance	$n_1(0) \leq 10^{10} \text{ cm}^{-3}$
Grush <sup>51</sup> (1973)	AGD EXL SIEC	$\leq 6375$	microwave resonance	$n_0(0) \leq 10^{10} \text{ cm}^{-3}$
Gardner <sup>52</sup> (1975)	AGD IXL SIEC	$\leq 0.27$	microwave resonance	$\langle n_1 \rangle \sim 10^9 \text{ cm}^{-3}$

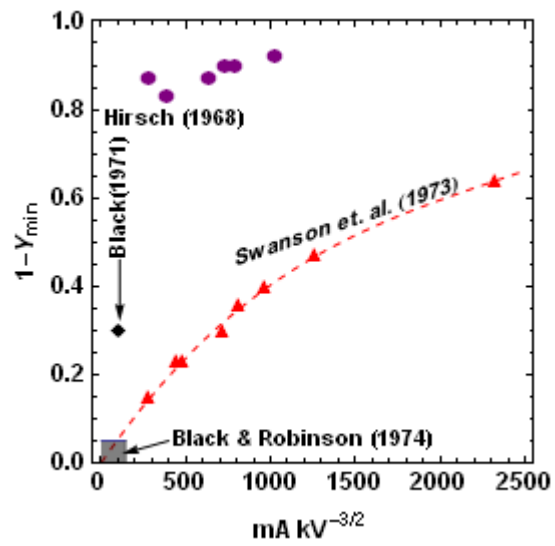


Fig. 9: Summary of results from early e-beam probe measurements of FWD in USEXLS.

## **2. After 1980**

### **a) “Rebirth” (High Q and Low Q)**

After a dormant period of nearly a decade, a “rebirth” in IEC research was stimulated by Bussard’s Polywell™ concept<sup>25,26</sup> and a simple gridded cathode GD IXL SIEC introduced by Miley and colleagues at the University of Illinois-Urbana-Champaign (UIUC).<sup>16</sup> These two concepts illustrate well the two distinct targets of IEC research efforts: (1) high Q devices for the generation of positive net energy, and (2) low Q devices with low capital cost that will be immediately competitive in neutron source markets. High Q is the prime motivation for the Polywell™ concept as the physical cathode structure is replaced with a virtual cathode due to the space charge of electrons within a magnetic trap at the center of a spherical chamber. The device also includes external particle sources so that it may operate at lower pressure than GD devices. With these modifications, two important loss mechanisms are minimized: (1) ion bombardment of the physical cathode structure, and (2) losses due electron transport to the anode. These loss mechanisms are simply unacceptable for a high Q device, but for low Q applications, the losses are viewed as the tradeoff for a device that can be immediately marketable as a neutron generator.

### **b) Glow Discharge Devices**

The simple gridded cathode GD IXL SIEC introduced at UIUC is recognized for its simplicity and the discovery of a favorable discharge mode known as “Star Mode”<sup>16,53,54</sup> which enhances ion focusing, resulting in fewer grid losses. This device differs from the early experimental efforts in that no machinery is added to aid in ion

generation. The discharge process is the sole source of ions. In addition, early devices often employed accelerating grids with small grid holes to minimize perturbations in the field structure. This was due to 1D orbital calculations that indicated that deviations from symmetry of the accelerating electrode would have a huge impact on the formation of favorable virtual wells for ion trapping.<sup>40</sup> The larger grid holes in the new devices are crucial to the formation of “Star Mode”. “Star Mode” has been a driver for several modeling efforts. The state of the art modeling efforts have advanced beyond the 1D orbital simulations to models that can self consistently account for dominant molecular processes, and/or model multiple dimensions.<sup>55-60</sup>

Recent work at the Massachusetts Institute of Technology (MIT) has concluded that the single cathode devices are confinement limited.<sup>11,12</sup> The “confinement limited” mode is significant, because neutron scaling with pressure measurements on single gridded cathode GD devices, have indicated a peak in neutron production efficiency with pressure. If the confinement limitation is removed, the “sweet spot” in neutron production efficiency with pressure is predicted to disappear, and improved efficiencies can be achieved by continually decreasing the pressure.

**c) Virtual Electrodes**

Although superior models have been developed for the GD devices, the 1D orbital model is still relevant to devices in which decoupling of the ion and electron sources from the background gas fill occurs. In principle, since high Q devices will rely on externally generated ions, the 1D orbital model should be relevant to these devices. Several double potential well structures, such as the one in Fig. 6, have been computed

with the 1D orbital model.<sup>32,61-65</sup> The relationship between several control variables and *DWD* is provided in Table II for IXL SIECs.

Experimentally, several virtual anode measurements have been made in AGD devices by Nadler<sup>16</sup>, Thorson<sup>66,67</sup>, and Kachan.<sup>68</sup> The quantitative *FWD* estimates by Nadler are questionable due to the reliance on 1D orbital model predictions, and the relatively small  $P_0$ . In addition, the detection of a virtual anode, by Kachan<sup>68</sup>, in an essentially “Star-Mode” operation seems to be in direct contradiction with Thorson<sup>67</sup>, who noted a flat potential profile in “Star-Mode”, and Yoshikawa et. al.<sup>70</sup>, who noted negligible electric fields within the core region of a “Star-Mode” device. However, Kachan’s<sup>68</sup> cathode is distinct from others, in that it simply consisted of two parallel conducting rings separated by only 2cm. Experimental detection of virtual anodes is summarized in Table IV.

In parallel to virtual anode measurements, double potential well sightings have been somewhat inconsistent and often provoke skepticism. Several indications of double potential well structures have been reported, but many of the measurements involve indirect measurements, contain significant error, require assumptions that are not strictly true, and/or are only qualitative in nature.<sup>34,47,50,69,30,54</sup> Recently, double potential wells of substantial depth (~20%-30%) had been reported in star mode based on an oscillation in the radial fusion profile,<sup>54</sup> but an alternative mechanism for this oscillation in the spatial profile of the fusion output has been proposed.<sup>62</sup> In spite of this, these results can not be totally disregarded, as several of these measurements consistently indicate the formation of double wells as  $P_0$  increases.<sup>54,63,69,70</sup> In some cases, the double wells are detected

after one has transitioned completely out of “Star-Mode” in the direction of increasing pressure.<sup>63,70</sup> These double potential well measurements are shown in Table V.

**d) Application**

Several proof-of-principle experiments have been conducted at the University of Wisconsin-Madison (UW), which are responsible for producing the most neutrons since the experiments by Hirsch ( $2 \cdot 10^8$  n/s).<sup>72</sup> These experiments include the first production of a medical isotope in an IXL SIEC<sup>22,23</sup>, the detection of highly enriched uranium (HEU)<sup>19</sup>, and the first ever observation of the  $\text{He}^3$ - $\text{He}^3$  fusion reaction.<sup>74</sup> Kyoto University has made significant progress in efforts to commercialize an SIEC for the detection of landmines.<sup>20</sup> In addition, efforts were pursued to commercialized the GD devices at UIUC, for neutron source applications, in collaboration with Daimler Chrysler.<sup>17</sup>

Table IV: Summary of single potential well measurements in SIEC devices.

<i>Investigator</i>	Nadler <sup>16</sup> (1992)	Thorson <sup>66,67</sup> (1996)	Kachan <sup>68</sup> (2003)
<i>Device</i>	AGD IXL SIEC	AGD IXL SIEC	GD IXL SIEC
<i>Diagnostic</i>	Proton Collimation	Emissive Probe	Single Probe
<i><math>mA kV^{-3/2}</math></i>	0.012-0.073	1.79-3.5	~0.35
<i><math>\eta</math></i>	80%-0.97%	0.85%-0.94%	-----
<i>mTorr</i>	1-5	0.1-0.2	5
<i>Inner Grid <math>\emptyset</math></i>	15.2cm	10cm	2cm
<i>Outer <math>\emptyset</math></i>	61cm	40cm	16cm
<i>Notable Result</i>	0.1-0.47 FWD	0.38-0.78 FWD	0.30 FWD
<i>Comments</i>	<ul style="list-style-type: none"> <li>• 2 ion gun source</li> <li>• Quantitative FWD estimates based on 1D orbital model</li> </ul>	A third grid employed w/ electron emitters	<ul style="list-style-type: none"> <li>• RF ion generation</li> <li>• 2 ring cathode</li> </ul>

Table V: Summary of experimental double potential well measurements in SIEC devices.

<i>Investigators</i>	Hirsch <sup>34</sup> (1967)	Swanson et. al. <sup>47</sup> (1973)	Meeker et. al. <sup>50</sup> (1973)	Meeker et. al. <sup>50</sup> (1973)	Satsangi <sup>69</sup> (1996)	Gu et. al. <sup>30</sup> (1996)	Yoshikawa et. al. <sup>70</sup> (1999)	Gu and Miley <sup>54</sup> (2000)	Dobson and Hrbub <sup>63</sup> (2004)
<i>Device</i>	ES IXL SIEC	AGD EXL SIEC pulsed	AGD EXL CIEC pulsed	AGD IXL CIEC pulsed	GD IXL SIEC	GD IXL SIEC pulsed	GD IXL SIEC	GD IXL SIEC	GD IXL SIEC
<i>Diagnostic</i>	Neutron,X-ray collimation	e-beam deflection	$\mu$ -wave res.; laser heterodyne	$\mu$ -wave res.; laser heterodyne	Light coll.; neutron counts	Global neutron counts	Stark shift via LIF	proton coll.	$\mu$ -wave interfer.
<i>mA kV<sup>-3/2</sup></i>	0.0054-0.061	5.06	5657-42426	1414-18385	0.061-0.632	> 2.2	1.95	1.38	28-49
<i><math>\eta</math></i>	-----	93%	82%	82%	95%	-----	95%-96%	82%	97%-98%
<i>mTorr</i>	0.1 – 7.8	2-10	0.5-15	0.5-15	4-60	-----	31	5-20	15-30
<i>Inner Grid <math>\emptyset</math></i>	11.4cm	6.35cm	8cm	8cm	3.5cm	-----	5.5cm	3.7cm	15.2/22.9cm
<i>Outer <math>\emptyset</math></i>	17.8cm	20cm	15cm	15cm	31cm	31cm	34cm	60cm	60cm
<i>Notable Result</i>	Fluctuating neutron,x-ray profiles	0.3% DWD	Dip in $n_0$ at center	Peak in $n_1$ at center	Ion energy $\uparrow$ as mA $\uparrow$	non-linear npr scaling with I	2.67% DWD	22-27% DWD	Dip in transverse $n_1$ near $0.5 R_g$

## ***F. Scope of Work***

The rest of this dissertation consists of two parts. The first part will be covered in the next chapter and will focus on solutions to the 1D orbital model. The 1D orbital model will be used to predict CR and CF scalings with various control variables for comparison with experimental results, as discussed in Chapter VI. In addition, the 1D orbital model is used to extensively map out regimes within the space of control variables which are conducive to the formation of double potential well structures.

The second part of the manuscript covers the experimental part of this dissertation, in which ion flow and structural characteristics of the “Star Mode” and “Jet Mode” discharge regimes are evaluated and/or verified. The experimental setup, including the GD IXL SIEC at the University of Missouri-Columbia, and the diagnostic tools, which include Langmuir probes, will be described in Chapter III. Chapter IV will include a discussion about probe shadowing effects and how the phenomenon may be useful in evaluating ion flow characteristics. The results of double and single Langmuir probe measurements, probe shadowing measurements, and measurements of the electrostatic field perturbation due to the discrete cathode structure will be presented in Chapter V. Chapter VI will include a discussion of the results presented in Chapter V and recommendations for future work will be made in Chapter VII.

## II. 1D Orbital Modeling

The 1D orbital model is the lynchpin of many theoretical investigations of IEC devices, as noted in Chapter I. The model is most appropriate for devices in which the ion and electron source mechanisms are decoupled. Efforts have been undertaken to extend the model to more collision dominant devices by “fudging” the distribution functions of the particles.<sup>36,40,51,63,65</sup> These instances require one to specify values to a number of unknown parameters in a rather arbitrary way. As a consequence, it has been possible to achieve reasonable quantitative predictions of overall indicators associated with particle densities ( $n_j(0)$ ), however, more detailed benchmarking efforts (predictions of  $Y(r)$  or  $n_j(r)$ ) are generally inadequate. In devices that are not collision dominant, ions and electrons have much longer lifetimes. Thus, significant energetic coupling between the two species can occur in these situations.<sup>81</sup> To the author’s knowledge, there has been no effort to directly account for this via 1D orbital modeling, present analysis included.

The rest of this chapter is devoted to presenting the results of extensive 1D orbital modeling performed by the author, keeping in mind the above mentioned limitations. Details of our model have already been published<sup>64,65</sup> so only the most brief description of the model is provided in this dissertation. Following an introduction of the model, results are presented for USIXL configurations, presenting some scaling relationships useful for comparison with experimental data, and taking note of the conditions resulting in the phenomena of “peak splitting”. Bi-polar results follow, with emphasis placed on

control variable regimes conducive to the formation of double potential well structures. Results for other observables are included in Appendix A.

### A. The model

The model described here is simply the one presented by Cherrington et. al.<sup>37</sup> and Swanson<sup>38</sup>, with some modifications. It is a one-dimensional steady state model in which the path traveled by a particle in an IEC device is determined only by its initial trajectory and the radial potential profile  $\varphi(r)$ . The initial trajectory of a particle is specified by the selected distribution function of the particular species. Here, it is assumed that the ions and electrons have Maxwellian shaped distribution functions. The governing equations, then, are the Poisson's equation,

$$Y''(X) + \frac{n}{X} Y'(X) = \left[ \left( 1 - (2X) \frac{R_g}{l} \right) n - \left( 1 - (4X) \frac{R_g}{l} \right) \right] * \sum_{j=0}^1 (-1)^j F(X, Y)_j \quad (1)$$

with,

$$F(X, Y)_j = \frac{k_j}{X} \left( \frac{2 \sigma_{jE} \sigma_{j\phi}^{3/2}}{\sigma_{j\phi} - \sigma_{jE} X^2} \right) \times \left\{ D \left[ X \sqrt{\frac{j+(1-2j)Y}{\sigma_{j\phi}}} \right] - X \sqrt{\frac{\sigma_{jE}}{\sigma_{j\phi}}} D \left[ \sqrt{\frac{j+(1-2j)Y}{\sigma_{jE}}} \right] \right\}, \quad (2)$$

$$k_j = \left( \frac{1}{4\pi\epsilon_0} \right) \left( \frac{m_j}{2e} \right)^{1/2} P_j \left( \frac{1}{\sigma_{j\phi} \sigma_{jE}} \right) \times \left\{ 1 - \text{Exp} \left[ \frac{(j * Y_{\min} - 1)}{\sigma_{jE}} \right] - \left( \frac{\sigma_{j\phi}}{\sigma_{j\phi} - \sigma_{jE}} \right) * \left( \text{Exp} \left[ \frac{(j * Y_{\min} - 1)}{\sigma_{j\phi}} \right] - \text{Exp} \left[ \frac{(j * Y_{\min} - 1)}{\sigma_{jE}} \right] \right) \right\}^{-1}, \quad (3)$$

$$D[z] = \frac{\sqrt{\pi}}{2} * \text{Exp}[-z^2] * \text{Erfi}[z], \quad (4)$$

$$\text{Erfi}[z] = -i * \text{Erf}[i * z], \quad (5)$$

$$\text{Erf}[x] = \int_0^x \text{Exp}[-t^2] dt, \quad (6)$$

and, the boundary specifications,

$$Y(X = 1) = 1, Y'(X = 0) = 0. \quad (7)$$

Many of the variables in Eqs. (1)-(7) have already been defined in Chapter I, Section D. It is necessary to indicate that  $n = 1$  for a cylindrical IEC device and  $n = 2$  for a spherical IEC device, and  $l$  denotes the length of a cylindrical device. In addition,  $m_j$  denotes the mass of species  $j$ ,  $e$  denotes the unit of electronic charge, and  $\epsilon_0$  is the permittivity of free space.

An initial guess for  $Y_{min}$  is specified in Eq. (3), and the shooting method is employed to find a solution compatible with both boundary conditions in Eq. (7). The value of  $Y_{min}$  thus computed is inserted back into Eq. (3), and the procedure is repeated until the solution converges. In all of the results to follow, solutions are computed assuming an ion mass of 1 amu. However, these results are general for ions of any mass. All that is required is to divide  $P_i$  and  $\beta$  axes by  $m_i^{1/2}$  where  $m_i$  represents the ion mass in amu. In Fig. 35, this is indicated with axis label  $^M\beta$  where  $^M\beta = m_i^{1/2} \beta$ .

### ***B. Uni-polar Injection in Spherical Geometry***

The injection of a single species of charged particles in a spherical device will result in a peak in density at the center, as shown in Fig. 7. This collection of charges results in the formation of a virtual electrode due to the collecting space charge, as shown in Fig. 5. The injection of more particles results in a larger  $n_0(0)$  and  $FWD$ , until the central region becomes space charge saturated and the peak begins to split, as indicated in Fig. 8. The separate peaks have been referred to as “wings”<sup>61</sup> due to the appearance of

the density profile in 1D. In reality, the “wings” represent a spherical shell, where the charges collect, similar to the way charges on a conducting sphere are confined to a shell-like region at the surface. The splitting is apparent in plots indicating the scaling of  $n_i(0)$ ,  $n_{i\text{peak}}$ ,  $HWHM$ , and  $CF$  in addition to plots of  $n_{i\text{peak}}/n_i(0)$  and  $n_{i\text{peak}}/n_i(R_g)$  in Fig. 10-Fig. 15. It is also of interest to note the scaling of the above observables with the spread in angular energy,  $\sigma_{i\theta}$ , and this is indicated in Fig. 16-Fig. 18. The dependence of these observables on  $P_i$  and  $\sigma_{i\theta}$  can be viewed simultaneously with the contour plots in Fig. 19 - Fig. 24. Finally, the model can be benchmarked by comparing the results of e-beam probing experiments in Fig. 9 with  $FWD$  predicted by the model, as in Fig. 25.

In observing Fig. 19 through Fig. 24, it is apparent that the onset of splitting occurs for  $FWD \sim 0.7-0.8$ . This is interesting in light of results by Thorson<sup>66,67</sup> in which virtual anodes with an  $FWD$  of approximately 0.8 were observed. This would indicate that the core of the device was space charge saturated and this space charge would likely have a significant influence on the core radius, particularly if splitting occurs. Thorson’s results do indicate that space charge and physical characteristics of the grid have a dominant influence on the core size. However, the light intensity measurements do not seem to indicate any splitting of the core.

Micro-wave resonant cavity measurements of  $n_o(0)$  on a USEXL device by Grush<sup>51</sup> indicate this splitting phenomena. The splitting is indicated in scaling relationships between  $n_o(0)$  and  $P_o$ , which look similar to Fig. 10. The values of  $P_o$ , for which splitting occurs, match up reasonably well with values from the theory. In addition, much of Grush’s data show that the peaks shift to high values of  $P_o$  and decrease in magnitude as the accelerating voltage is reduced. In light of Fig. 20, a logical

conclusion is that the significance of the energy imparted to electrons upon emission increases as the accelerating potential is reduced.

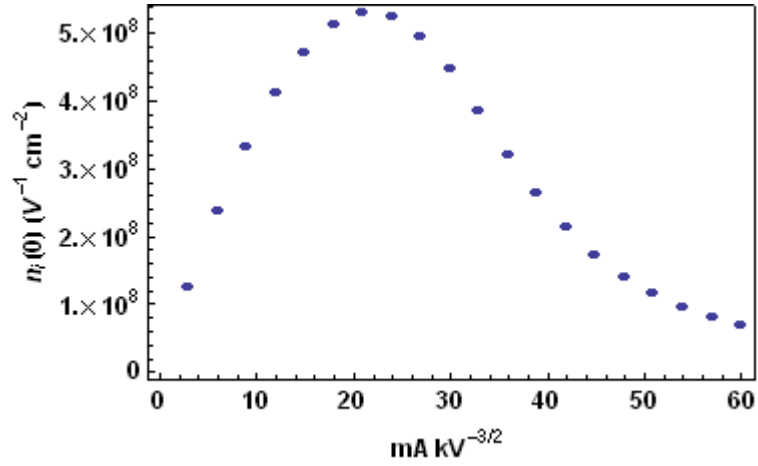


Fig. 10: Core density vs.  $P_0$  for uni-polar injection in spherical geometry with singly charged ions with 1amu mass, with  $\sigma_{i0} = 0.05$ .

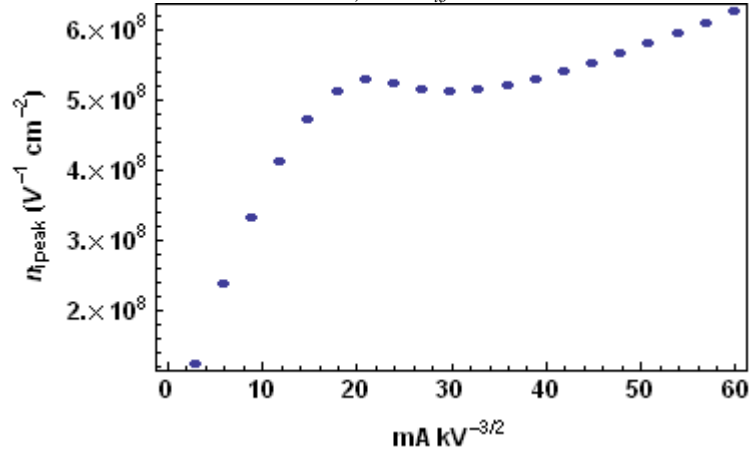


Fig. 11: Peak density vs.  $P_0$  for uni-polar injection in spherical geometry with singly charged ions with 1amu mass, with  $\sigma_{i0} = 0.05$ .

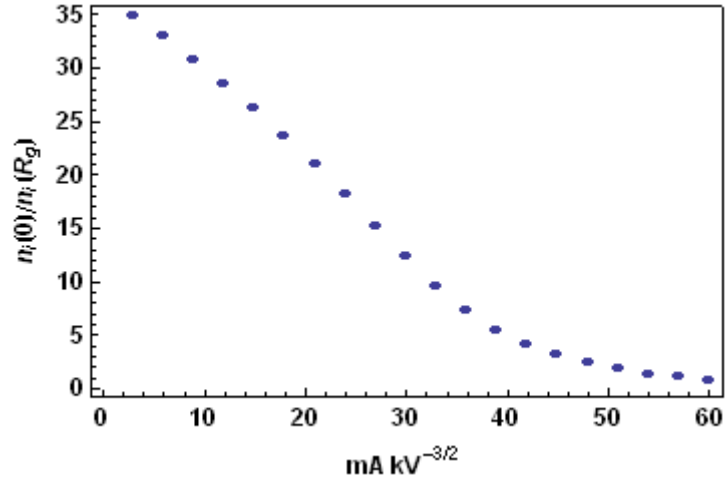


Fig. 12: Convergence Factor ( $CF$ ) vs.  $P_0$  for uni-polar injection in spherical geometry with singly charged ions with 1amu mass, with  $\sigma_{i\phi} = 0.05$ .

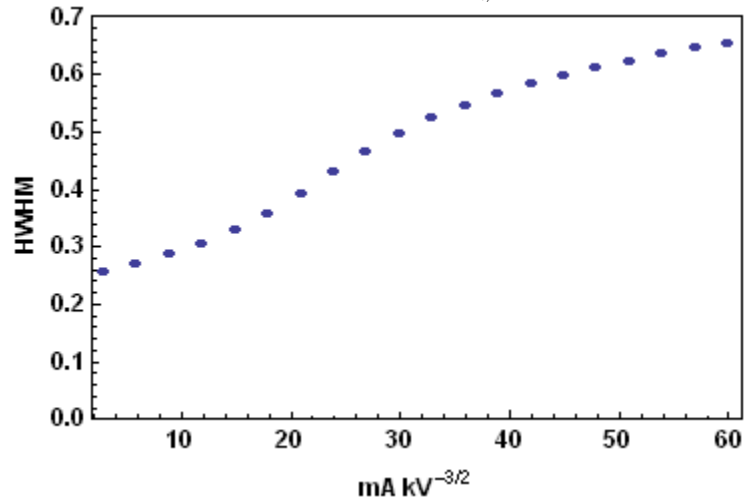


Fig. 13:  $HWHM$  vs.  $P_0$  for uni-polar injection in spherical geometry with singly charged ions with 1amu mass, with  $\sigma_{i\phi} = 0.05$ .

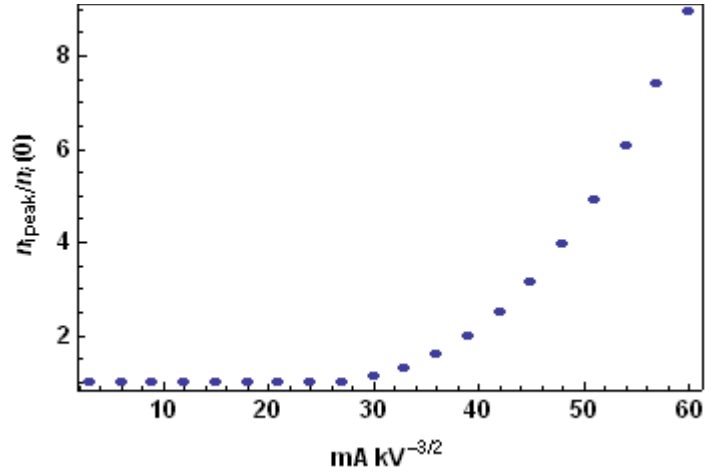


Fig. 14: Ratio of peak density to core density vs.  $P_0$  for uni-polar injection in spherical geometry with singly charged ions with 1amu mass, with  $\sigma_{i0} = 0.05$ .

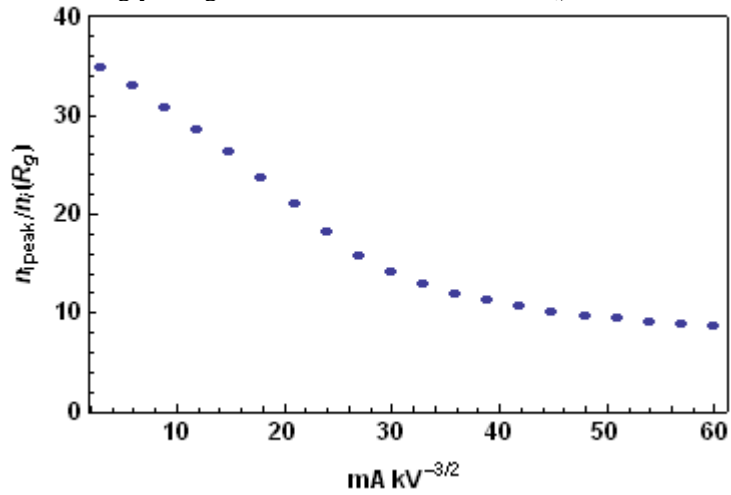


Fig. 15: Ratio of peak density to grid density vs.  $P_0$  for uni-polar injection in spherical geometry with singly charged ions with 1amu mass, with  $\sigma_{i0} = 0.05$ .

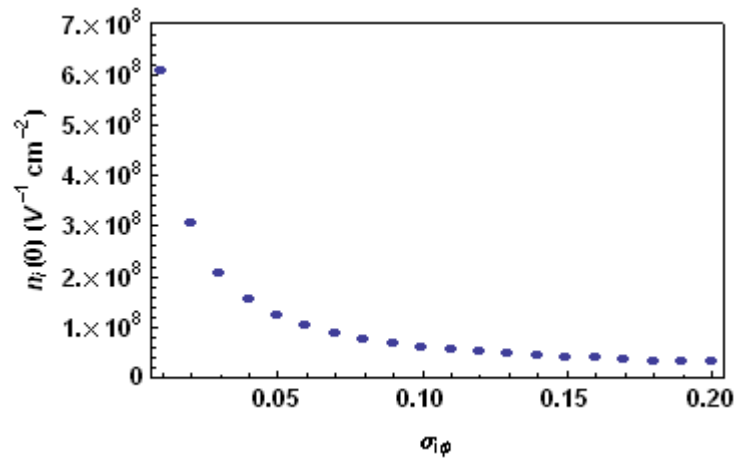


Fig. 16: Plot of  $n_i(0)$  vs.  $\sigma_{i\phi}$  for uni-polar injection in spherical geometry with singly charged ions of mass 1 amu with  $P_i = 3 \text{ mA kV}^{3/2}$

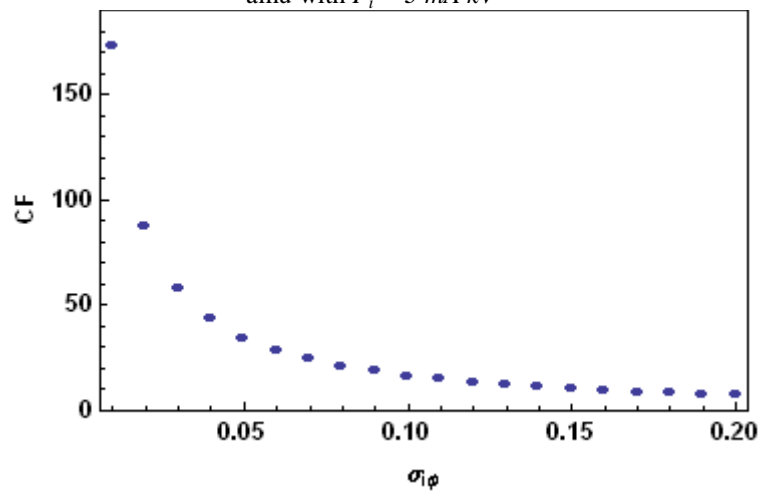


Fig. 17: Plot of  $CF$  vs.  $\sigma_{i\phi}$  for uni-polar injection in spherical geometry with singly charged ions of mass 1 amu with  $P_i = 3 \text{ mA kV}^{3/2}$

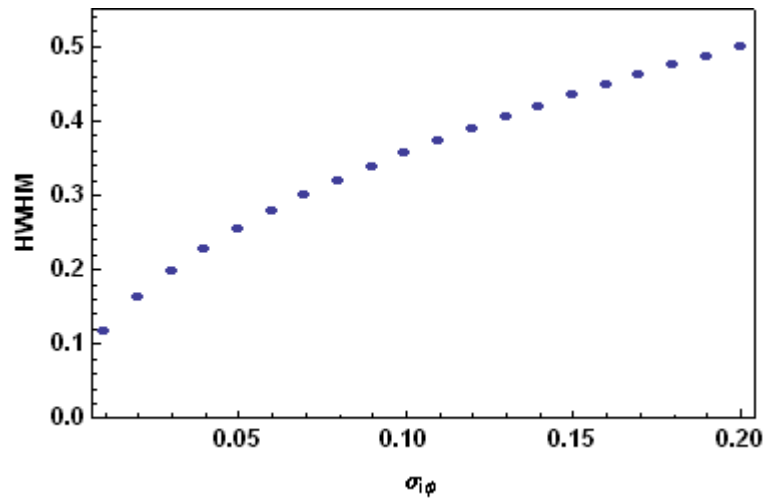


Fig. 18: Plot of  $HWHM$  vs.  $\sigma_{i\phi}$  for uni-polar injection in spherical geometry with singly charged ions of mass 1 amu with  $P_i = 3 \text{ mA kV}^{-3/2}$

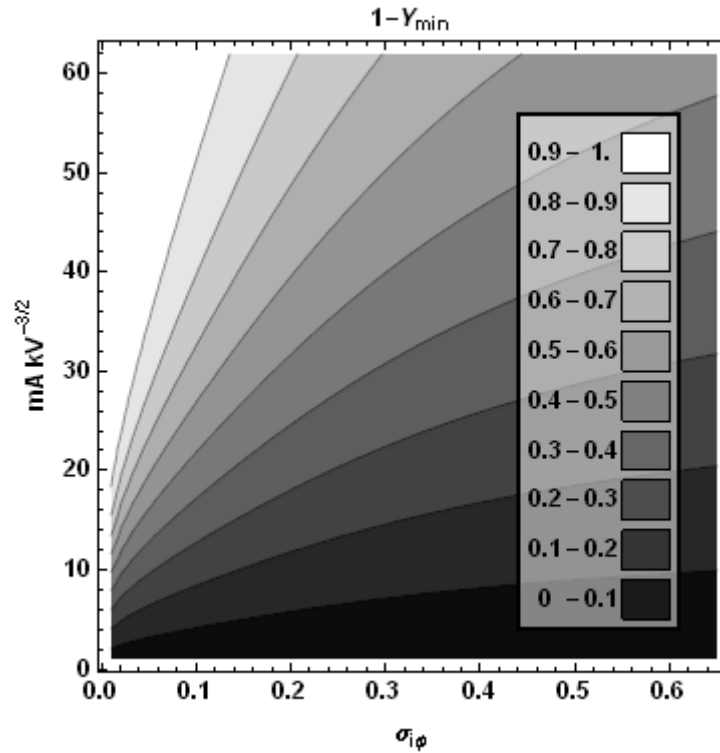


Fig. 19: Contour plot of  $FWD$  vs. ion perveance  $P_i$  and the spread in normalized ion angular energy,  $\sigma_{i\phi}$ .

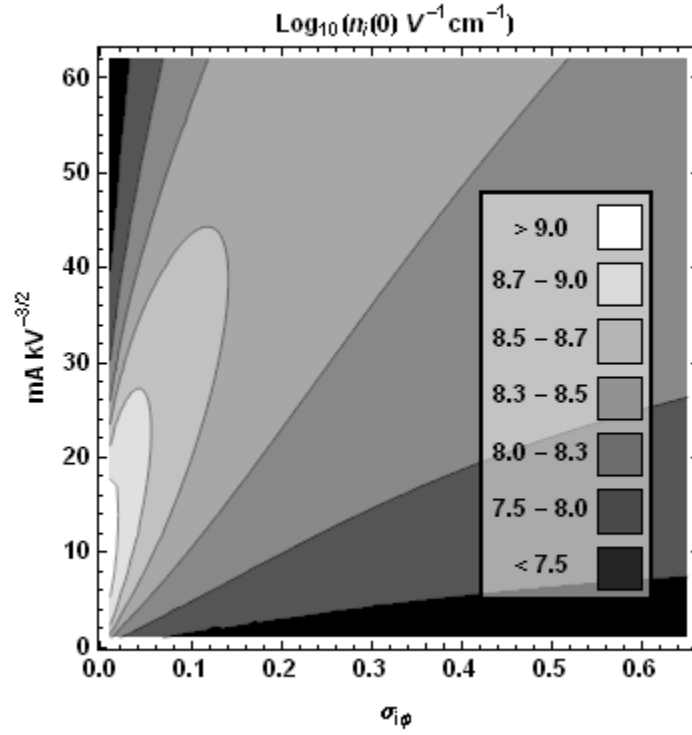


Fig. 20: Contour plot of  $\text{Log}_{10}(n_i(0))$  vs. ion perveance,  $P_i$ , and the spread in normalized ion angular energy,  $\sigma_{i\phi}$ .

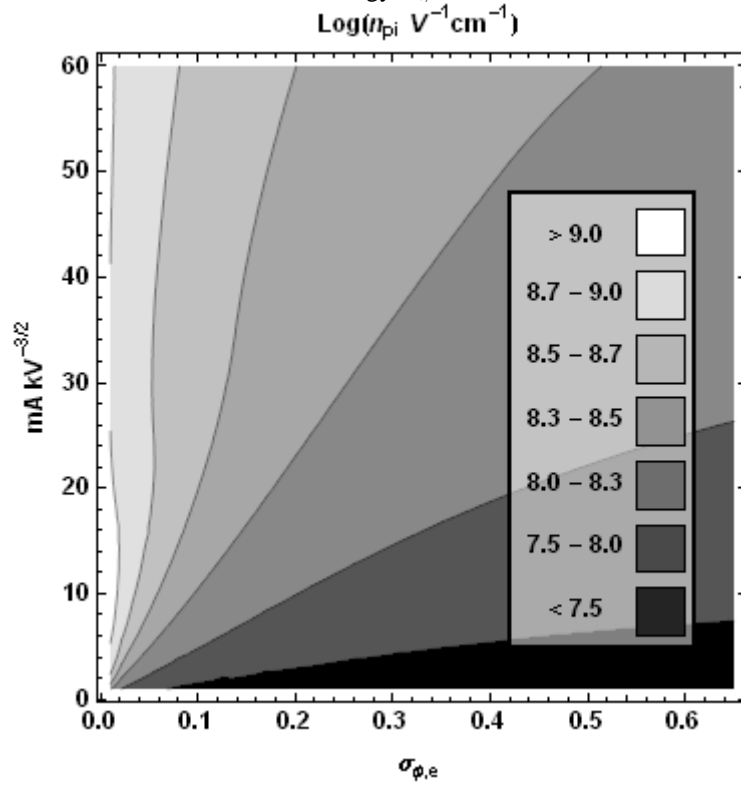


Fig. 21: Contour plot of  $\text{Log}_{10}(n_{pi})$  vs. ion perveance,  $P_i$ , and the spread in normalized ion angular energy,  $\sigma_{i\phi}$ .

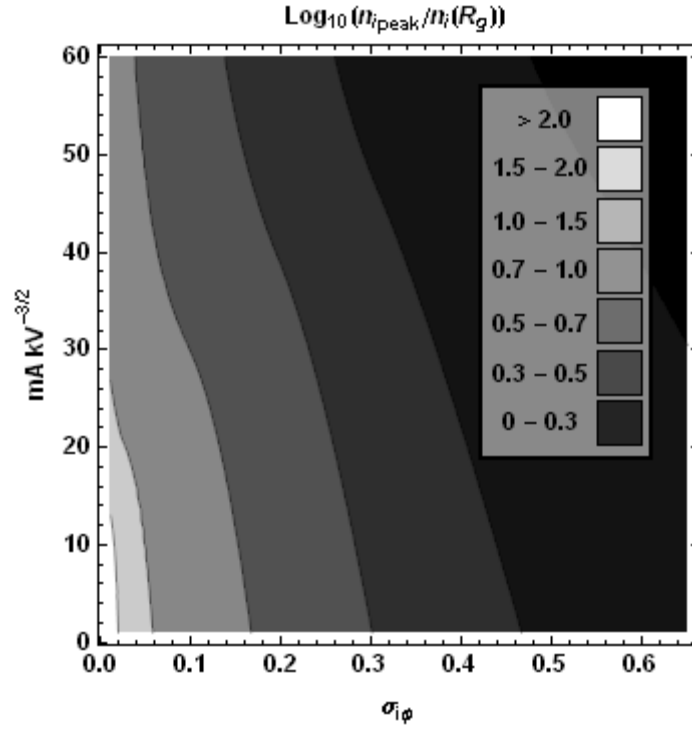


Fig. 22: Contour plot of  $\text{Log}_{10}(n_{i\text{peak}}/n_i(R_g))$  vs. ion perveance,  $P_i$ , and the spread in normalized ion angular energy,  $\sigma_{i\phi}$ .

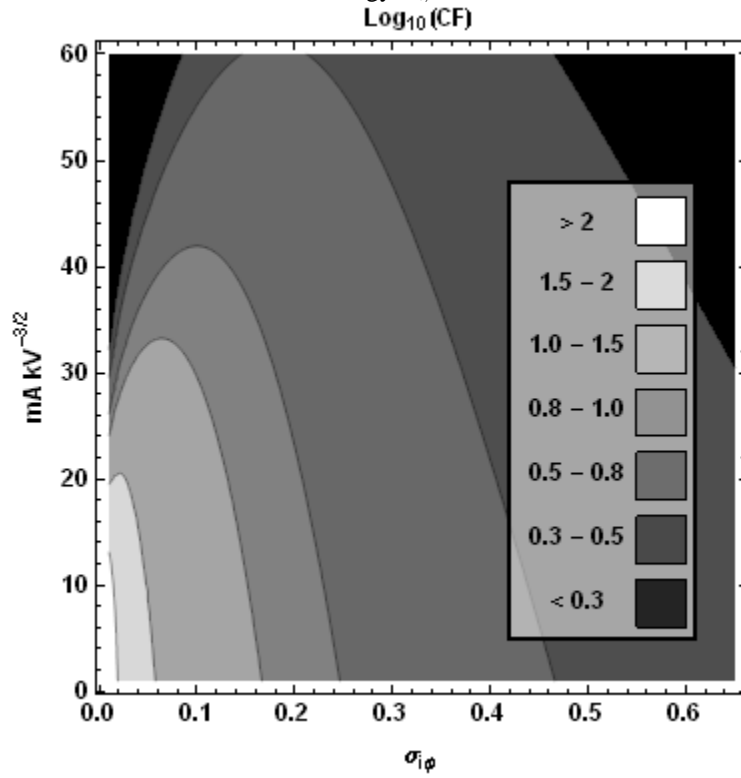


Fig. 23: Contour plot of  $\text{Log}_{10}(CF)$  vs. ion perveance,  $P_i$ , and the spread in normalized ion angular energy,  $\sigma_{i\phi}$ .

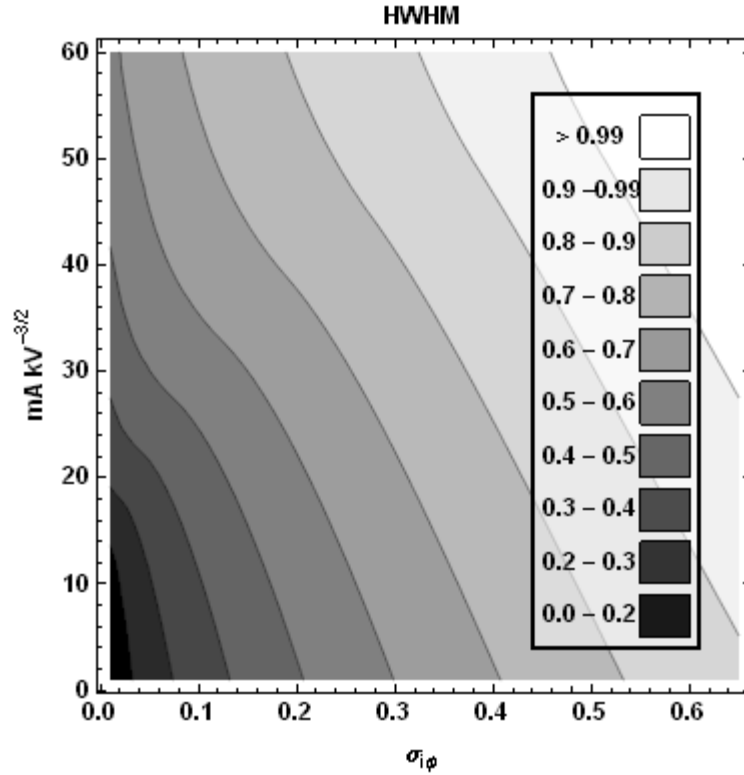


Fig. 24: Contour plot of  $\text{Log}_{10}(\text{HWHM})$  vs. ion perveance,  $P_i$ , and the spread in normalized ion angular energy,  $\sigma_{i\phi}$ .

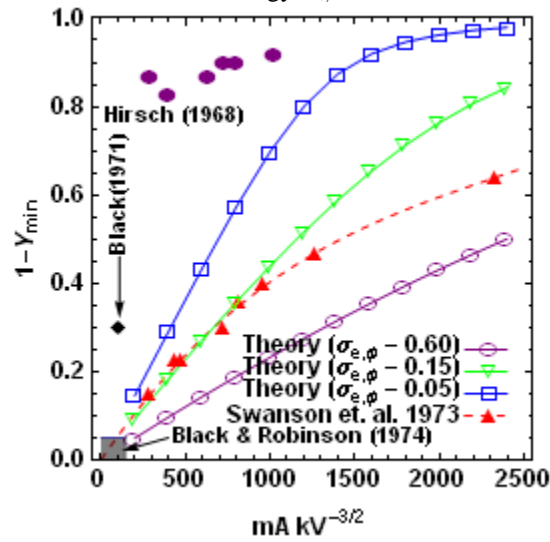


Fig. 25: Comparison of  $FWD$  vs.  $P_e$  for USEXLs from experiments and 1D orbital modeling.

### C. *Bi-Polar Discharge Modeling and Double Potential Well Regimes*

In the case of the bi-polar discharge, the addition of an extra species greatly expands the number of observables of interest, particularly, because we are interested in the behavior of both trapped and injected particles. A pretty good match between the 1D orbital model and e-beam probing by Swanson<sup>47</sup> is found after a trapped ion population is added to the model, as shown in Fig. 32. Of course, it should be noted that the theoretical curve may not be unique, since it may be possible to generate a similar curve with a different combination of control variables.

The evolution of a double potential wells in IXL SIECs can be observed as a population of electrons are considered in addition to the injected species. In this case, we can consider a radial ion density profile as shown in Fig. 8. The added electrons neutralize the ions and allow the hollowed out spherical shell of ions to “fill in”. Radial injected and trapped density profiles, for decreasing values of  $\beta$ , along with the corresponding potential profiles are shown in Fig. 26 through Fig. 31.

In the rest of this chapter, we present computations for the observable  $DWD$ , and also explore the dependence of  $DWD$  with respect to all control variables ( $P_i, \beta, \sigma_{i\phi}, \phi_{e\phi}$ ) with the use of two contour plots for  $P_i\text{-}\beta$  and  $\sigma_{i\phi} - \phi_{e\phi}$  spaces, respectively. Results for other observables are presented in Appendix A as contour plots of  $FWD$ ,  $Y(0)$ ,  $width$ ,  $n_i(0)$ , and  $n_e(0)$  for  $P_i\text{-}\beta$  and  $\sigma_{i\phi} - \phi_{e\phi}$  spaces, respectively. Plots of  $DWD$  in  $P_i\text{-}\beta$  space are shown in Fig. 33 through Fig. 35, while plots of observables in  $\sigma_{i\phi} - \phi_{e\phi}$  space are shown in Fig. 36 through Fig. 43. In Fig. 33 through Fig. 35, it is noticeable that  $DWD$  is sensitive with respect to  $\beta$ . It has already been noted that many of the experimental observations of  $DWD$  in Table V indicate the appearance of a double well as  $P_i$  increases.

Yoshikawa et. al.<sup>70,71</sup> have given this increase in ionic space charge credit for explaining their detection of a double potential well in “Central-Spot” mode, and the absence of a double potential well in “Star-Mode”. However, Fig. 33 through Fig. 35 reveal that the increase in electron production due to an increase in ionizations at higher pressure should also be credited for any double potential well formations in these higher pressure discharge regimes. Finally, Fig. 36 through Fig. 43 show that the accumulation of ion angular energy does not inhibit DWD. This is significant in one respect because it indicates that space charge spreading at high currents is not a problem. McGuire<sup>12</sup> has indicated that pulsing strategies are doomed due to space charge spreading, but here we see that it is not necessarily such a bad thing.

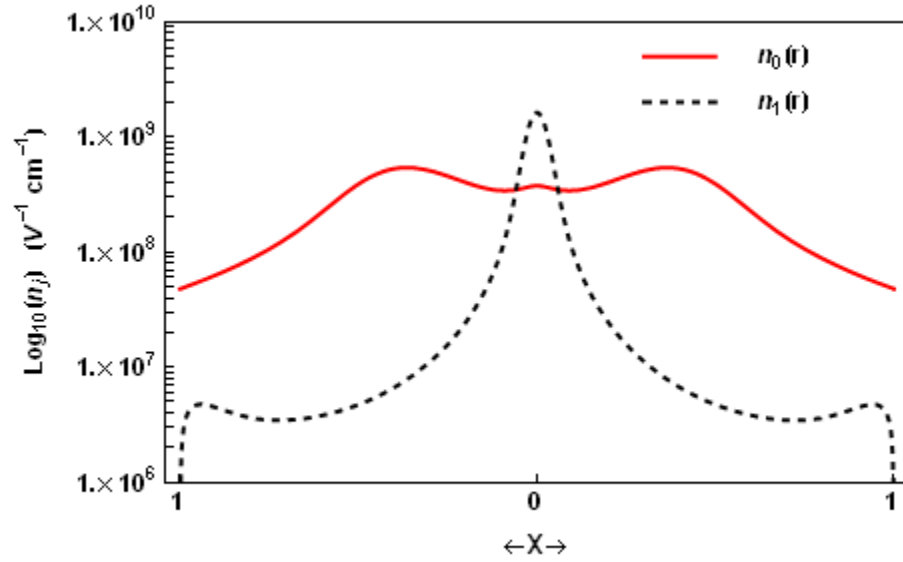


Fig. 26: Injected and trapped radial density profiles,  $n_0(r)$  and  $n_1(r)$ , for an IXL SIEC. In this case, control variables have the values  $P_0 = 40 \text{ mA kV}^{-3/2}$ ,  $\sigma_{1\phi} = 0.001$ ,  $\sigma_{0\phi} = 0.05$ , and  $\beta = 1.2$ .

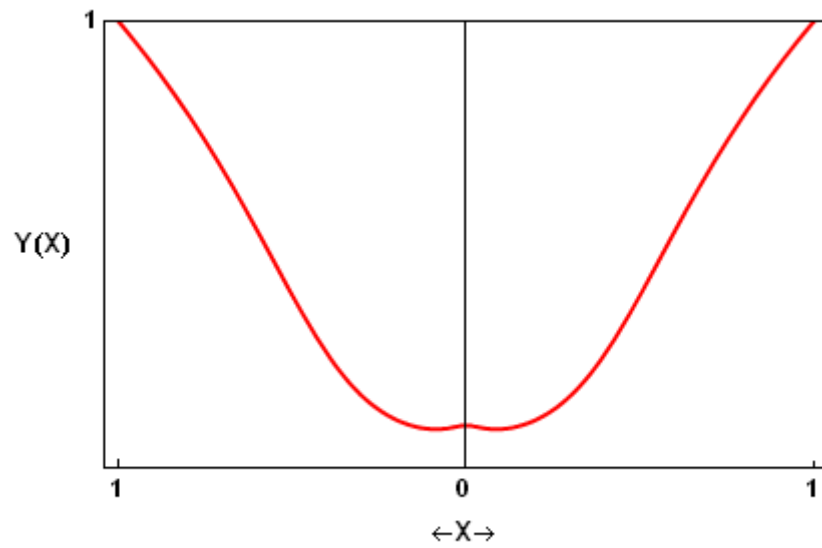


Fig. 27: Radial potential profiles for an IXL SIEC. In this case, control variables have the values  $P_0 = 40 \text{ mA kV}^{-3/2}$ ,  $\sigma_{1\phi} = 0.001$ ,  $\sigma_{0\phi} = 0.05$ , and  $\beta = 1.2$ .

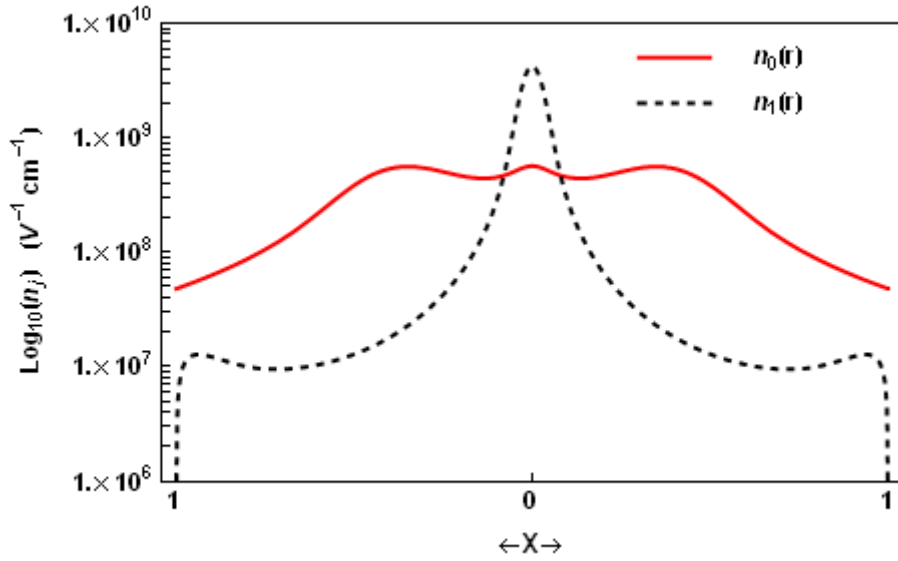


Fig. 28: Injected and trapped radial density profiles,  $n_0(r)$  and  $n_1(r)$ , for an IXL SIEC. In this case, control variables have the values  $P_0 = 40 \text{ mA kV}^{-3/2}$ ,  $\sigma_{1\phi} = 0.001$ ,  $\sigma_{0\phi} = 0.05$ , and  $\beta = 0.45$ .

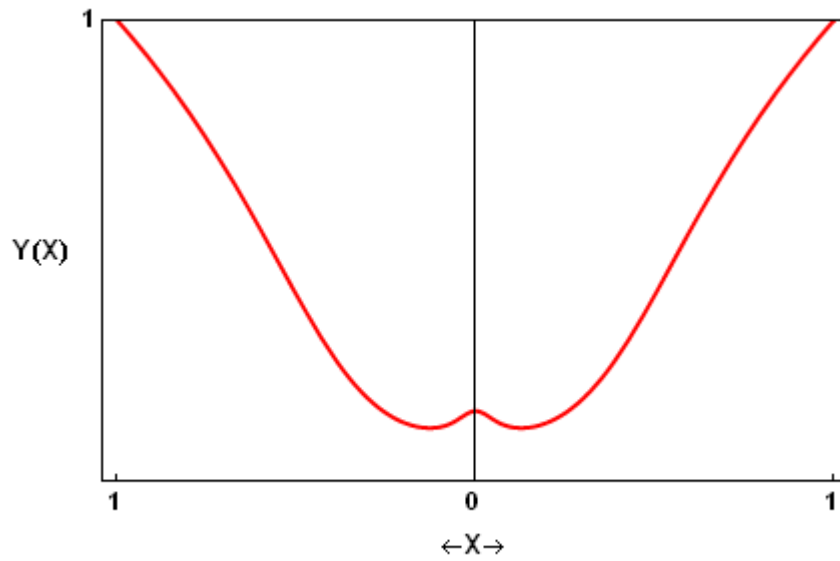


Fig. 29: Radial potential profiles for an IXL SIEC. In this case, control variables have the values  $P_0 = 40 \text{ mA kV}^{-3/2}$ ,  $\sigma_{1\phi} = 0.001$ ,  $\sigma_{0\phi} = 0.05$ , and  $\beta = 0.45$ .

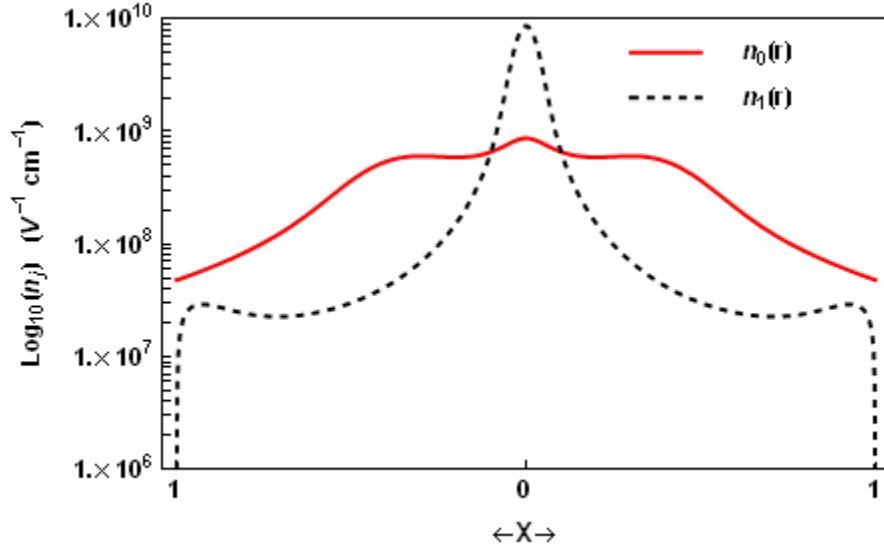


Fig. 30: Injected and trapped radial density profiles,  $n_0(r)$  and  $n_1(r)$ , for an IXL SIEC. In this case, control variables have the values  $P_0 = 40 \text{ mA kV}^{-3/2}$ ,  $\sigma_{1\theta} = 0.001$ ,  $\sigma_{0\theta} = 0.05$ , and  $\beta = 0.2$ .

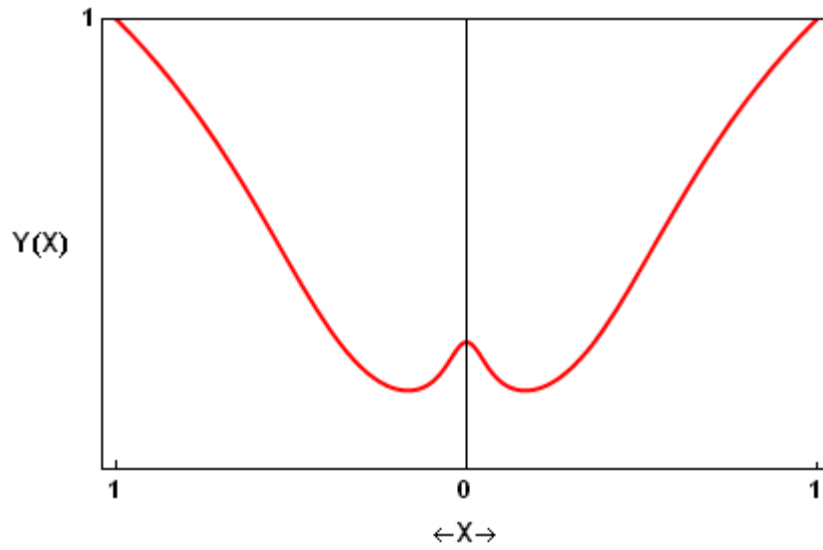


Fig. 31: Radial potential profiles for an IXL SIEC. In this case, control variables have the values  $P_0 = 40 \text{ mA kV}^{-3/2}$ ,  $\sigma_{1\theta} = 0.001$ ,  $\sigma_{0\theta} = 0.05$ , and  $\beta = 0.2$ .

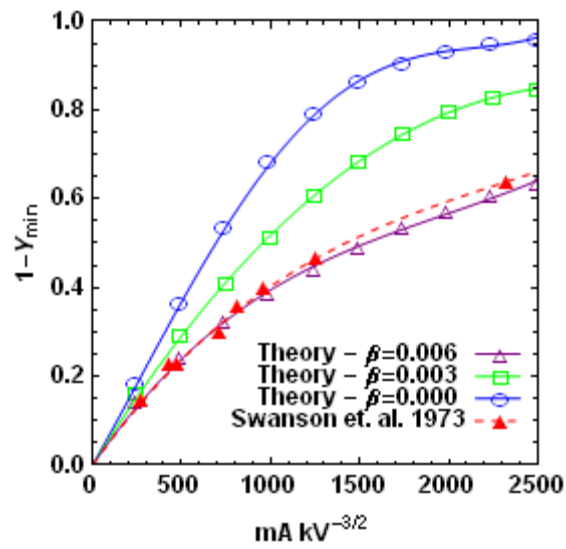


Fig. 32: Comparison of  $FWD$  vs.  $P_e$  for USEXLs from experiments and 1D orbital modeling. In this case, the assumption that the devices are purely uni-polar is dropped, and a trapped ion current is added to the model. It should be noted that the theoretically derived curves are not necessarily unique, in that other combinations of control variables may result in a similar curve.

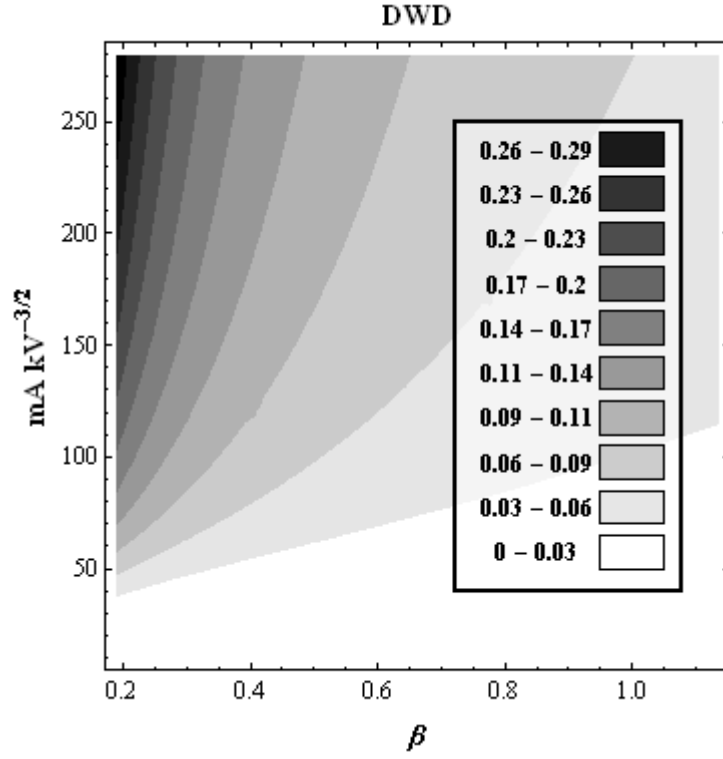


Fig. 33: Contour plot of  $DWD$  with respect to  $P_i$  and  $\beta$ . This plot is computed with  $\sigma_{e\theta} = 0.005$  and  $\sigma_{i\theta} = 0.05$ .

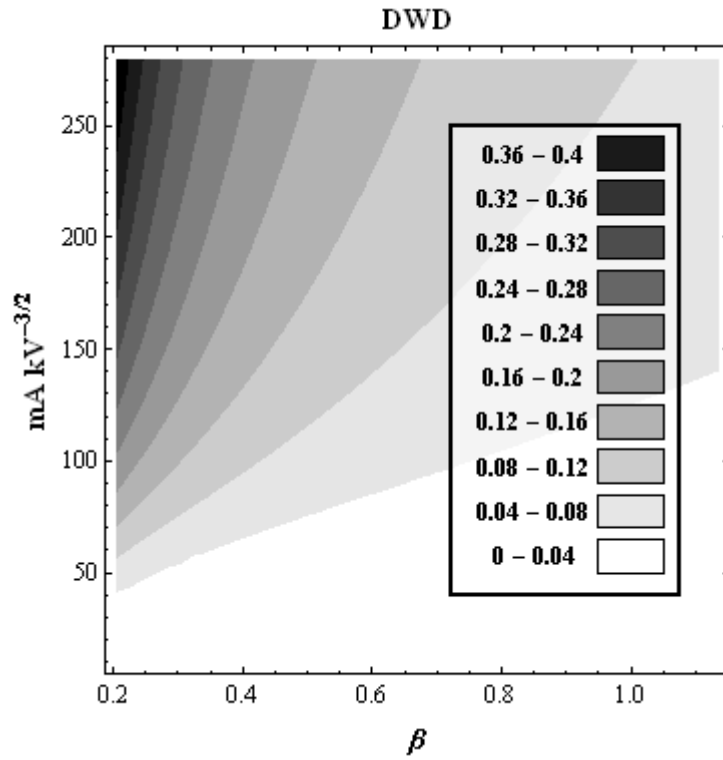


Fig. 34: Contour plot of  $DWD$  with respect to  $P_i$  and  $\beta$ . This plot is computed with  $\sigma_{e\theta} = 0.005$  and  $\sigma_{i\theta} = 0.10$ .

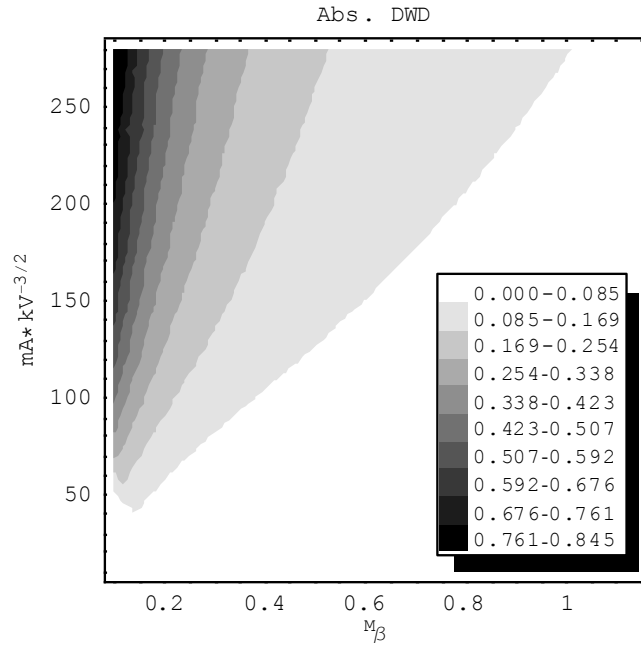


Fig. 35 Contour plot of  $DWD$  with respect to  ${}^M P_i = m_i^{1/2} * P_i$  and  ${}^M \beta = m_i^{1/2} * \beta$ , where  $m_i$  is the ion mass in amu. This plot is computed with  $\sigma_{e\phi} = 0.005$  and  $\sigma_{i\phi} = 0.15$ .

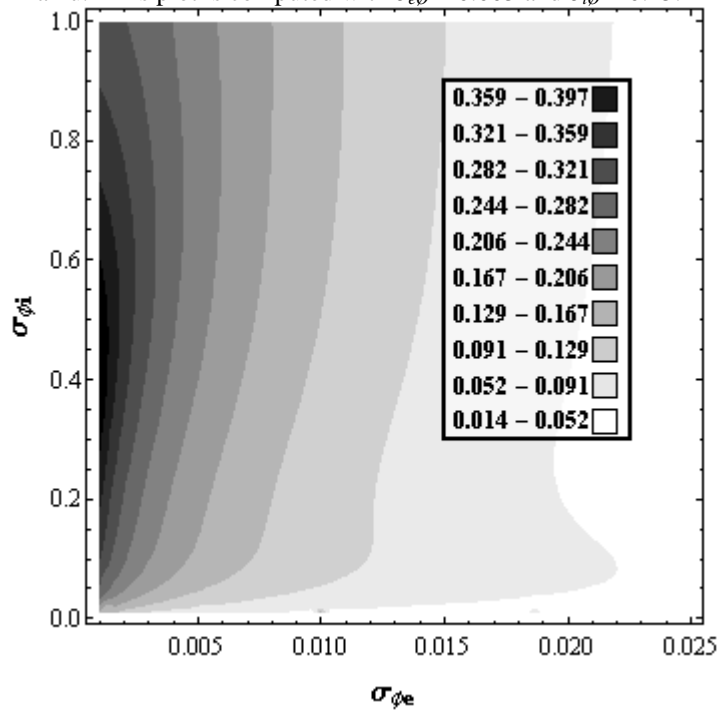


Fig. 36: Contour plot of  $DWD$  with respect to  $\sigma_{e\phi}$  and  $\sigma_{i\phi}$ . This plot is computed with  $P_i = 100 \text{ mA kV}^{-3/2}$  and  $\beta = 0.25$ .

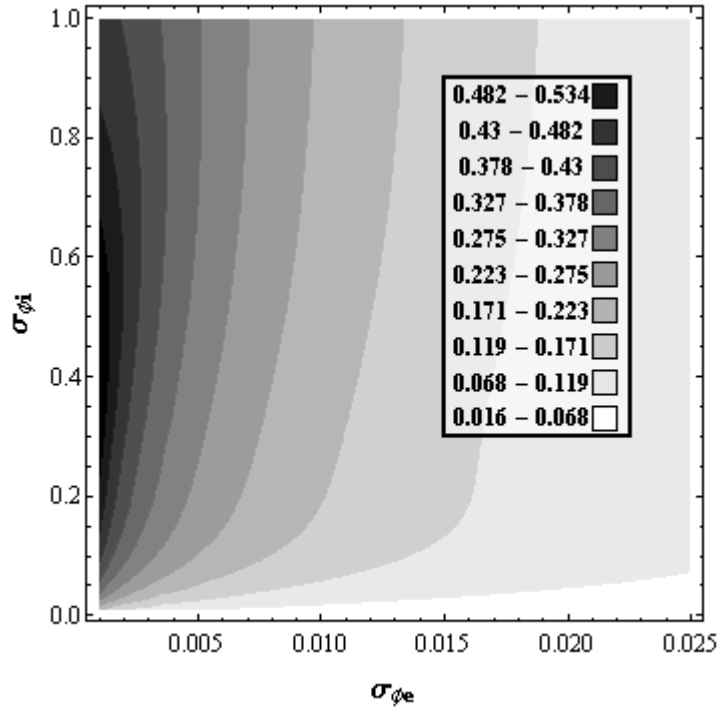


Fig. 37: Contour plot of  $DWD$  with respect to  $\sigma_{e0}$  and  $\sigma_{i0}$ . This plot is computed with  $P_i = 138 \text{ mA kV}^{-3/2}$  and  $\beta = 0.25$ .

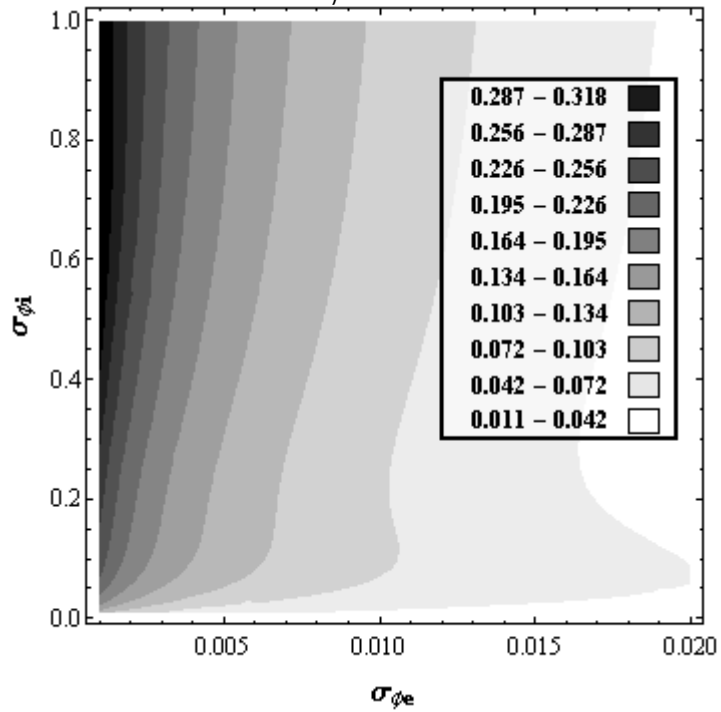


Fig. 38: Contour plot of  $DWD$  with respect to  $\sigma_{e0}$  and  $\sigma_{i0}$ . This plot is computed with  $P_i = 100 \text{ mA kV}^{-3/2}$  and  $\beta = 0.33$ .

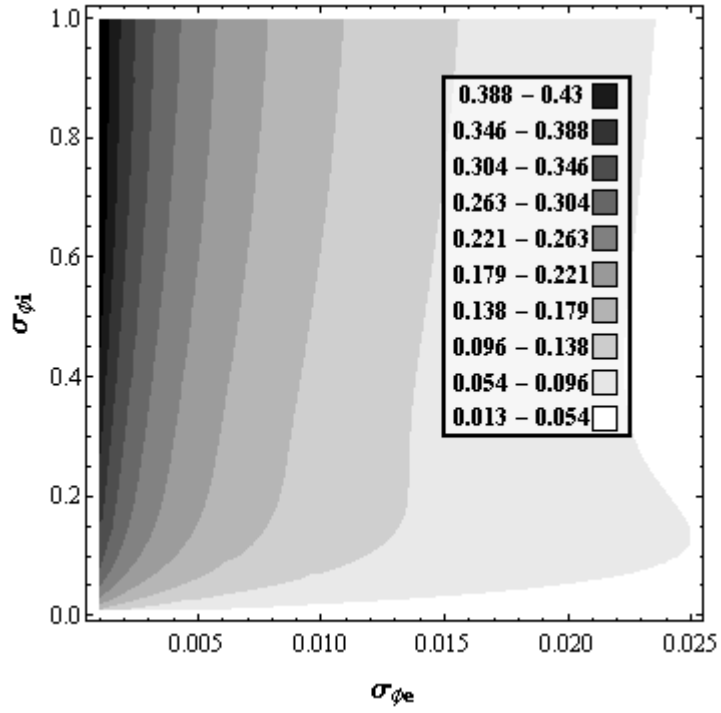


Fig. 39: Contour plot of DWD with respect to  $\sigma_{e0}$  and  $\sigma_{i0}$ . This plot is computed with  $P_i = 138 \text{ mA kV}^{-3/2}$  and  $\beta = 0.33$ .

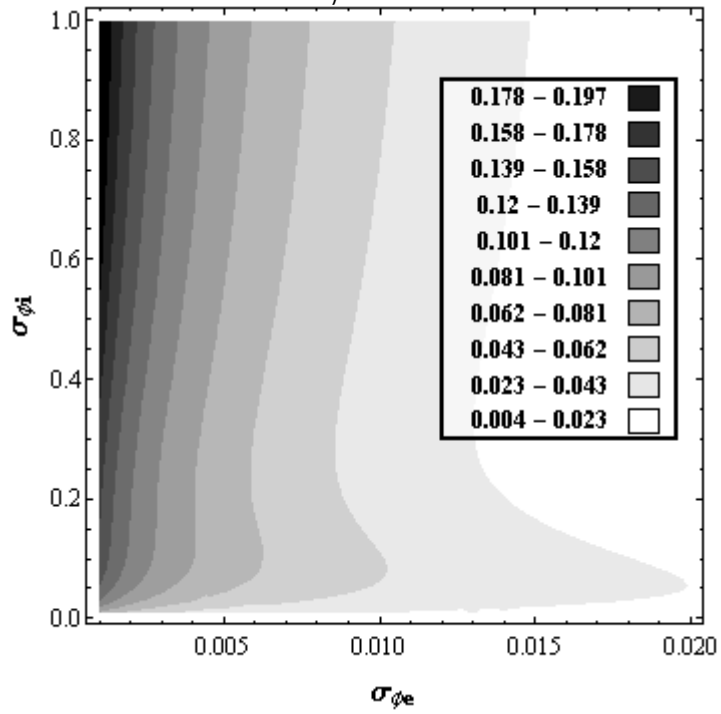


Fig. 40: Contour plot of DWD with respect to  $\sigma_{e0}$  and  $\sigma_{i0}$ . This plot is computed with  $P_i = 100 \text{ mA kV}^{-3/2}$  and  $\beta = 0.50$ .

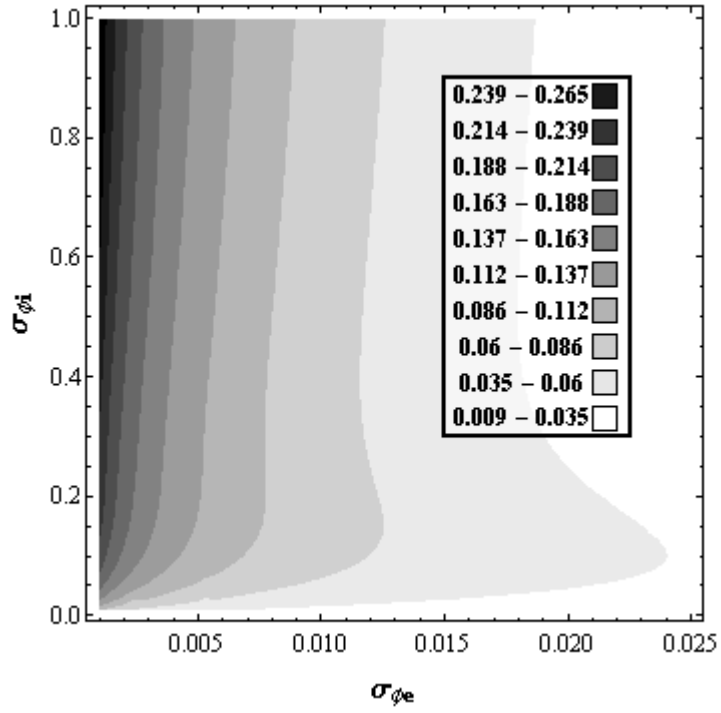


Fig. 41: Contour plot of  $DWD$  with respect to  $\sigma_{e0}$  and  $\sigma_{i0}$ . This plot is computed with  $P_i = 138 \text{ mA kV}^{-3/2}$  and  $\beta = 0.50$ .

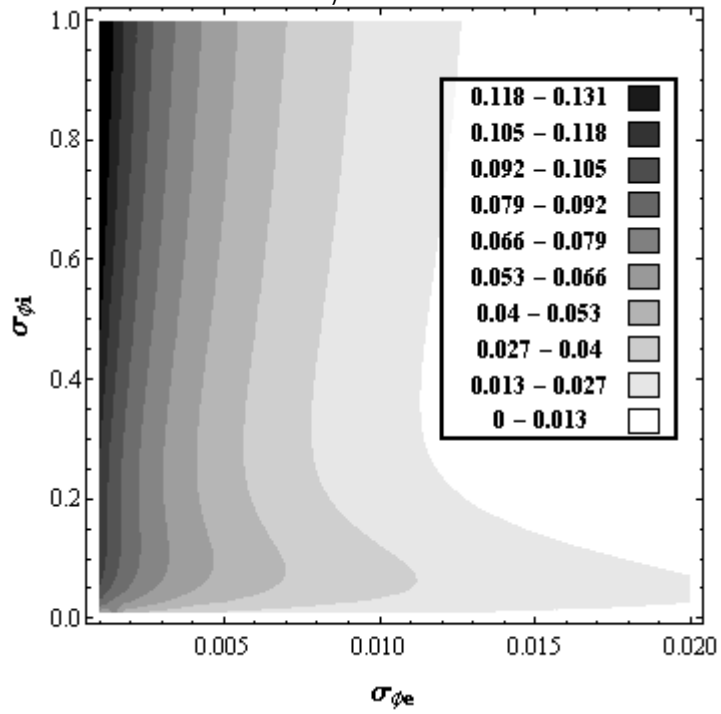


Fig. 42: Contour plot of  $DWD$  with respect to  $\sigma_{e0}$  and  $\sigma_{i0}$ . This plot is computed with  $P_i = 100 \text{ mA kV}^{-3/2}$  and  $\beta = 0.67$ .

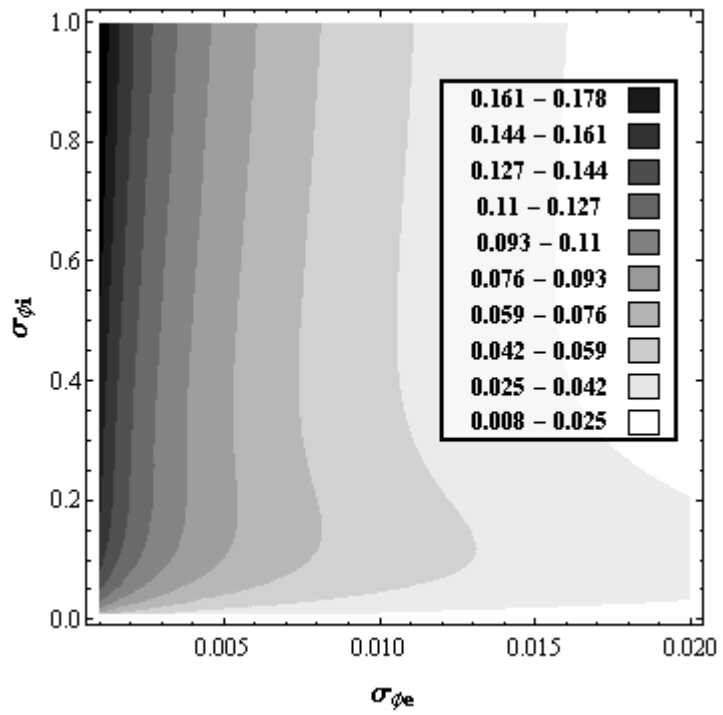


Fig. 43: Contour plot of  $DWD$  with respect to  $\sigma_{e\phi}$  and  $\sigma_{i\phi}$ . This plot is computed with  $P_i = 138 \text{ mA kV}^{-3/2}$  and  $\beta = 0.67$ .

### III. Experimental Set-up

This chapter provides a description of the physical GD IXL SIEC experiment in the Nuclear Science and Engineering Institute (NSEI) at the University of Missouri-Columbia. Descriptions of the Langmuir probe diagnostics are included, also, as equipment is described in the following sequence:

- Vacuum System
- Pressure Monitoring
- Electrodes and Power Supply
- Langmuir Probes

#### A. *Vacuum System*

A GD IXL SIEC has been constructed at the University of Missouri-Columbia and is shown in Fig. 44. The spherical electrodes are enclosed within a cylindrical stainless steel bell jar that has an 18” inner diameter and is 30” tall. The bell jar consists of four 2-3/4” conflat flanges at 12” from the bottom of the jar for electrostatic probe access, and two opposing 6” viewports, also at 12” from the bottom of the bell jar, as depicted in Fig. 46. One of the viewports is used as an access port for the cathode. The access ports for electrostatic probes are labeled as “Probe Location 1-4” in Fig. 46. An ion micro-channel is also depicted showing that an ion micro-channel is consistently accessible to probes inserted into Probe Location 1 and no ion micro-channel is accessible to probes inserted into Probe Location 2. The bell jar is clamped to a feed through collar with four C-clamps, and a vacuum seal is achieved between the bell jar and feed through collar with a Viton O-ring. The feed through collar consists of eight 2-

3/4" conflat flange ports allowing internal access to the chamber for gas inlet, venting, and pressure gauges. The feed through collar sits on top of a base well, which connects to a *Varian* turbo-molecular pump capable of pumping at 200L/s. The turbo pump is connected to a *Welch* mechanical pump which serves as a roughing pump and a backing pump. The turbo-pump is able to bring system pressure down to about to  $1 \cdot 10^{-6}$  Torr before the chamber is then back-filled with hydrogen gas to pressures in the range of 1 to 10 mTorr.

### ***B. Pressure Monitoring***

The pressure within the vacuum chamber is monitored by two capacitance manometers and a cold cathode ionization gauge. One capacitance manometer covers the pressure range from atmospheric to approximately 10 Torr. The other capacitance manometer allows the chamber pressure to be monitored within the 10 Torr – 10mTorr range, while the cold cathode ionization gauge monitors pressures in the range  $10^{-2}$ - $10^{-9}$  Torr range. The output of the pressure gauges are fed to digital readouts mounted in a rack bin.

### ***C. Electrodes and Power Supply***

The anode grid, or “globe”, is formed via 18” diameter rings of 0.25” diameter stainless steel tubing. It consists of three rings forming six lines of longitude, each separated by 60°. Five stainless steel rings of latitude complete the structure, with access for electrostatic probes and the cathode feed through at the “equator”. The anode is filled in further by welding stainless steel flat ribbon between the lines of longitude formed by the tubing. It is supported by an aluminum structure made from aluminum channel.

Brackets for future electron guns or electron emitters are attached to the aluminum channel and have several degrees of adjustment. A photo of the anode and its support structure is provided in Fig. 45.

The cathode grid is much smaller, having a diameter of 3.75". It is typically constructed from stainless wire with a thickness of 1mm. The cathode grid is formed by creating seven 3.75" diameter rings, which are spot welded together to form a "geodesic" pattern<sup>57</sup>, as shown in Fig. 47. The geometric transparency of the cathode is thus,  $\eta \sim 0.94$ . The cathode feedthru is constructed out of a commercially available HV feedthrough. In this case, a flange compatible with the viewport flange has been welded to the weld lip of the HV feedthrough. The cathode feedthrough is insulated from the anode wall on the vacuum side by adhesively attaching an alumina tube around the feedthrough conductor. The coaxial gap created by the alumina tube and feedthrough is filled in with an alumina potting compound. Cathodes of multiple sizes from 3.25" diameter to 4.75" diameter may be accommodate in increments of 0.5" via aluminum "spacer rings" sandwiched between the HV feedthrough flange and the flange on the vacuum chamber.

The cathode is attached to a *Glassman* high voltage (HV) dc power supply. Voltages of up to -50 kV and currents up to 40 mA may be generated with this power supply. For the electrostatic probe studies, discussed in this dissertation, accelerating voltages of -1kV to -5kV will be used.

## **D. *Electrostatic Probes***

### **1. Probe Construction**

#### **a) Double Langmuir Probe**

The shaft of the double Langmuir probe is constructed from insulating alumina tubing with a 6.35mm OD. An alumina silicate cup with a base diameter of 13mm and a length of 15mm is glued to the end of the probe shaft using an alumina adhesive. Circular depressions are drilled in one end of the cup for the placement of 3mm diameter Molybdenum disks. The disks are spot welded to stripped micro-coaxial cable and they are glued to the end of the cup. The alumina probe shaft is connected to a shaft adaptor with a 6.35mm ID stainless steel shaft collar. The shaft adaptor connects to the probe manipulator and the micro-coaxial cable is fed through the adaptor to a HV coaxial vacuum feedthrough. Two different double Langmuir probes are utilized, the first with the alumina silicate cup shown in Fig. 48-Fig. 50. In an attempt to decrease the size of the probe, much of the alumina silicate cup was ground off using a dremel tool, resulting in the probe shown Fig. 51. For future reference, the double probe with the cup depicted in Fig. 48-Fig. 50, will be denoted as d1, while the double probe in Fig. 51 is denoted as d2.

#### **b) Single Langmuir Probe**

The shaft of the single Langmuir probe is constructed from insulating alumina tubing with a 6.35mm OD. A 6.35mm diameter Molybdenum disk is spotwelded to stripped micro-coaxial cable and glued to the end of the probe shaft. The alumina probe shaft is connected to a shaft adaptor with a 6.35mm ID stainless steel shaft collar. The

shaft adaptor connects to the probe manipulator and the micro-coaxial cable is fed through the adaptor to a HV coaxial vacuum feedthrough. A second single Langmuir probe was constructed by gluing a 3mm Molybdenum disk to a 3mm OD alumina shaft. The 3mm shaft is glued to the inner surface of a 6.35mm OD tube and attached to the shaft adaptor as described previously. For future reference, the single probes will be referred to as s1 and s2, respectively. A photo of s1 is in Fig. 50.

## **2. Probe Manipulation**

For the experiments, it is desired to move the probes linearly along the radii of the spherical electrodes. A linear manipulator with a 101mm stroke and welded bellows is used for this purpose. The anode has a radius of 225 mm, so it is obvious that we can not sample the entire radius of the device. Therefore, we obtain traces for the entire cathode grid radius and for approximately two inches of the A-K gap adjacent to the cathode. However, not all of the probes are the same length and generally, the probes collect data beyond the center point of the device.

A NEMA 21 size stepper motor with a  $0.9^\circ$  step resolution is used to push the manipulator through its 101mm stroke. The stepper motor is controlled with a unipolar stepper motor driver, which receives the appropriate signals through LabVIEW. An optical encoder with a 1000 counts per revolution resolution and indexing enable precise measurements of the probe location. In fact, since approximately 30 revolutions are equivalent to 1" of linear travel, the optical encoder is capable of measurements to within  $1\mu\text{m}$ . For our experiments, the probes are moved in 1mm steps. As mentioned, a shaft adaptor is used to connect the probe shaft to the manipulator. Finally, strain reliefs are added to the HV coaxial feedthroughs to transfer any stress away from the spot weld

connection between the micro-coaxial cable and the HV feedthrough termination. Photos of the Langmuir probes with manipulators are shown in Fig. 52-Fig. 53.

### **3. Probe Sweeping**

Typical voltage sweeps of +/- 1000 volts are applied to the probes. The sweeping signal is obtained with a function generator through a bi-polar operational amplifier (BOP). The frequency of the function generator is placed on its lowest setting (0.5 Hz) to minimize the impact of the leakage capacitance of the circuit. The function generator and the BOP are isolated from the line voltages using two 175W isolation transformers hi-pot tested up to 4000V and connected in parallel. The BOP and function generator are placed inside of an aluminum box, which is grounded for safety.

The sweeping is continuous, but data is only collected at discrete positions in increments of 1mm as the probe moves toward the device center. The DAQ system collects 1000 points per trace, and the sampling rate is adjusted to ensure a full cycle of the sweeping waveform has been collected (~500 samples/s). The sweep utilizes a triangular waveform, as opposed to sinusoidal, because the sampled points are more evenly distributed over one sweep cycle.

The voltage signal is obtained with a voltage divider and the current signal is extracted with a current sensing resistor. These signals cannot be collected directly by the DAQ bus, so they are isolated from the plasma potential via isolation amplifiers. The isolation amplifiers are transformer coupled and can withstand up to 3500Vrms between the input and output modules. Therefore, two of them are connected in series for the voltage and current signals.

The above description is actually modified slightly for single probe sweeping. In this case, the single probe first runs through the 100mm stroke without any sweeping signal to collect floating voltage signals. The floating voltage data is used to bias the output of a programmable high voltage power supply. The sweeping signal is then superimposed on the output signal of the programmable supply. In addition the programmable power supply can not sink any current, so a resistor dump is used to bias the output of the supply as illustrated in Fig. 54. The double and single probe signal collection circuits are shown in Fig. 55 and Fig. 56, respectively.

#### **4. RF noise**

Occasional arcing has been documented on other GD devices<sup>57</sup> and observed on this GD device. The arcing produces RF signals that damage the isolation amplifier ICs and interfere with the signals of the optical encoder. The isolation amplifier to which the current signal is input, experienced damage due to the common mode signal induced in the double probe by the arcing. This issue was fixed by clamping the inputs of the ICs with zener diodes as indicated in Fig. 55.

Generally, electromagnetic compatibility issues involve a source and a target, in which a signal generated at the source interferes with the operation of the target. In this case, the GD IXL SIEC is the source, and the optical encoder, DAQ Bus, and associated cables act as the target. Initially, an attempt was made to shield the target from the source, but this was complicated by the pick up of noise by the power and USB cables of the DAQ Bus. This attempt resulted in the construction of an aluminum cabinet for the DAQ Bus, and an aluminum box to shield the optical encoders as shown in Fig. 57 and Fig. 58, respectively. This procedure was later abandoned in favor of shielding the

source, which involved placing aluminum mesh over the view port, encasing the sweeping circuits in metal boxes, and placing an aluminum cap over the HV feedthrough insulator, as indicated in Fig. 59-Fig. 62. It should be mentioned that there is merit in shielding the target instead of the source, as it would allow the sweep circuitry to remain unshielded, and it would then be possible to reduce the capacitive reactance of the circuit, perhaps by another order of magnitude.



Fig. 44: GD IXL SIEC at the University of Missouri-Columbia. Spherical cathode and anode are housed within the cylindrical bell jar.



Fig. 45: Anode constructed out of 6.35mm OD ss tubing. An aluminum structure supports the anode and brackets for future mounting of electron guns or electron emitters.

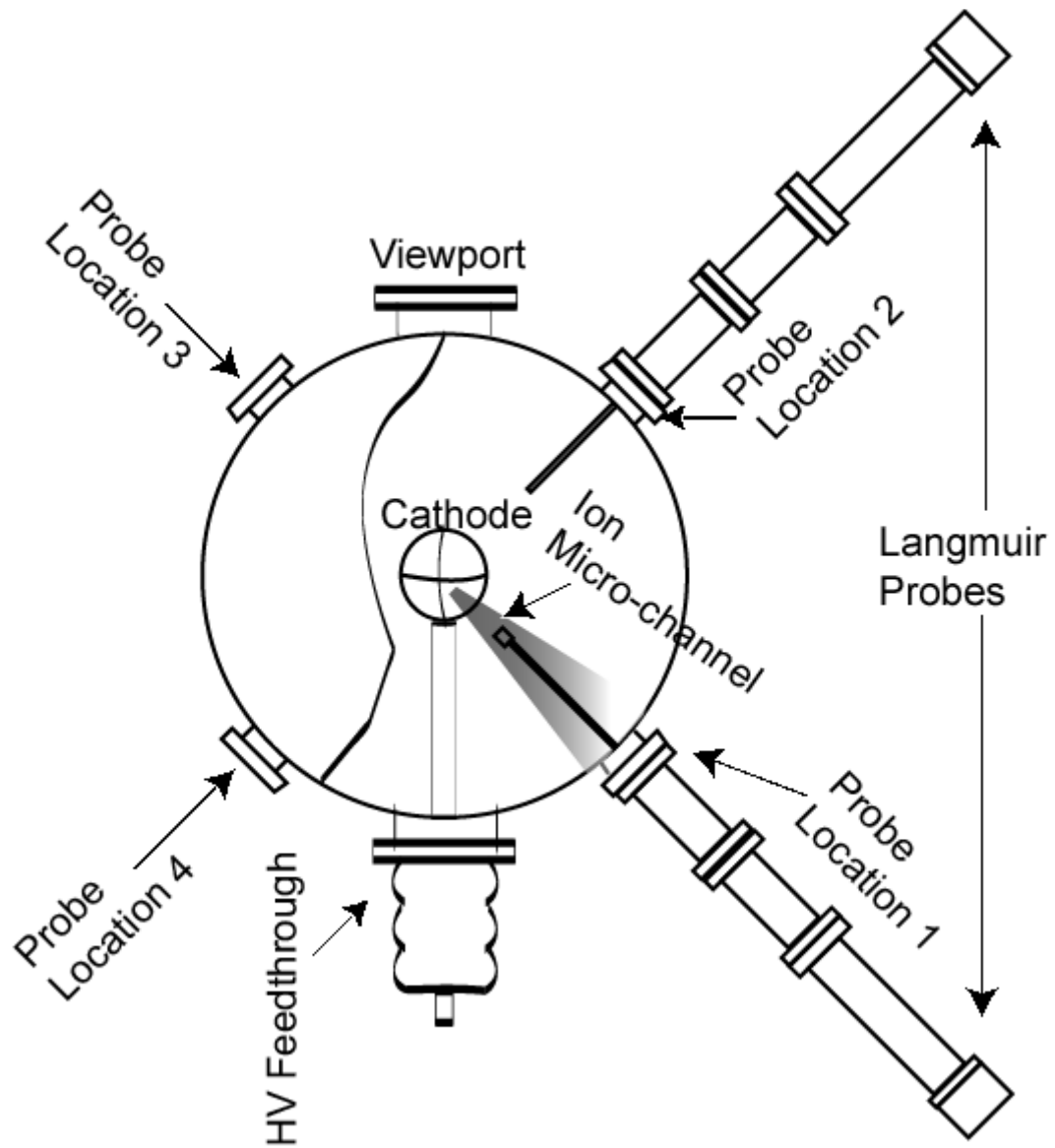


Fig. 46: Top view of the GD IXL SIEC at the University of Missouri-Columbia. Four 2-3/4" conflate flanges are indicated for electrostatic probe access. These access ports are labeled as "Probe Location 1-4" in the diagram. Also indicated are the HV feedthrough, the viewport, the Langmuir probes, the cathode, and an ion micro-channel. The ion micro-channel is depicted to emphasize the observed phenomena of micro-channel formation in the direction of Probe Location 1 and the absence of an accessible micro-channel to a probe inserted at Probe Location 2.



Fig. 47: “Geodesic” cathode grid formed of 1mm thick stainless wire. The grid is composed of seven 3.75” diameter rings.

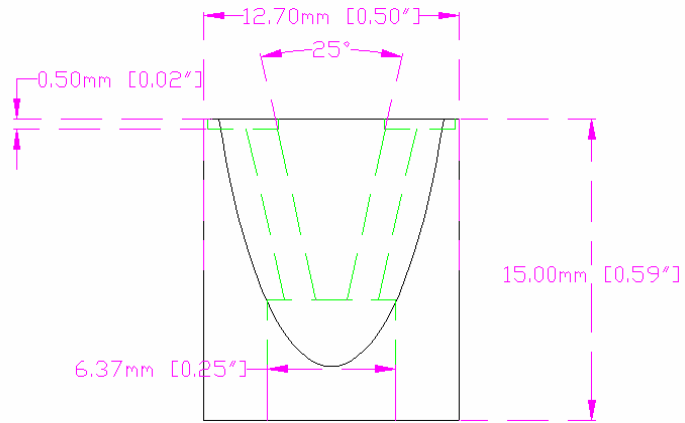


Fig. 48: Schematic of front view of the alumina silicate cup mounted at the end of the probe shaft for the double probe, d1.

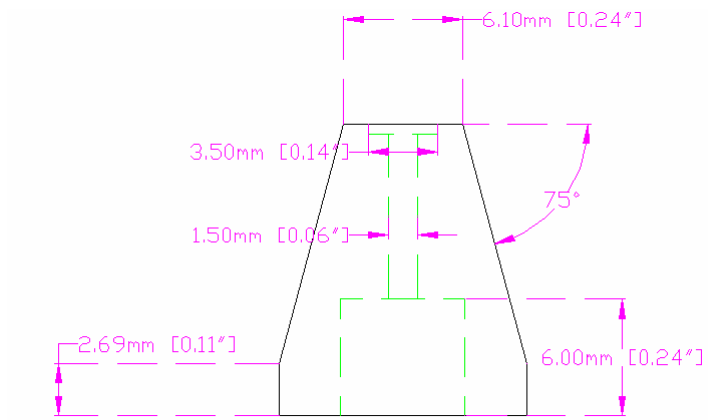


Fig. 49: Schematic of side view of alumina silicate cup for the double probe, d1.

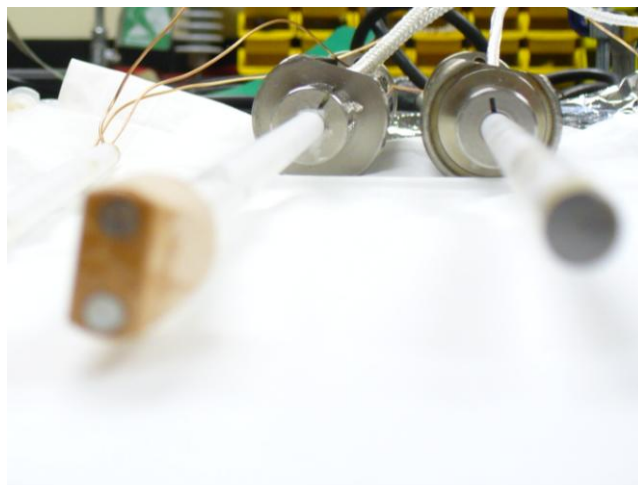


Fig. 50: Photos of the double and single probes, d1 and s1, respectively.



Fig. 51: This is a photo of double probe, d2.

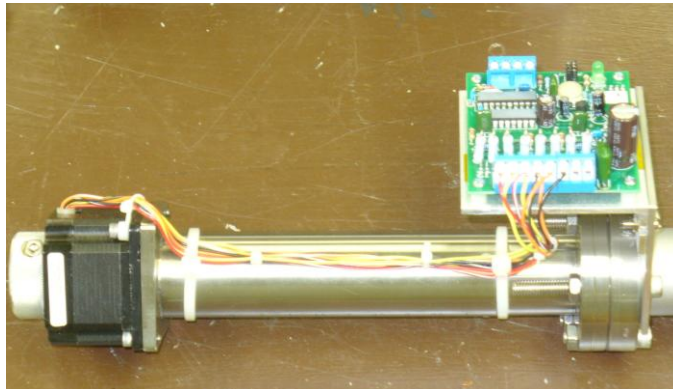


Fig. 52: Photo of the probe manipulator with stepper motor and uni-polar driver.



Fig. 53: Photo of automated Langmuir probe with manipulator, stepper motor and uni-polar driver.

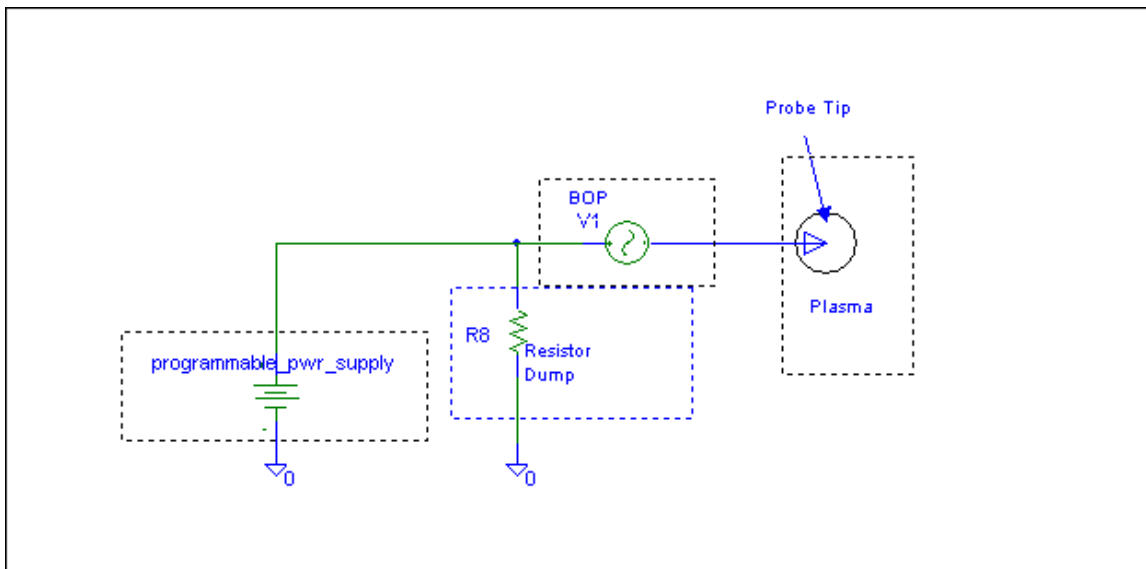


Fig. 54: Schematic illustrating the use of a resistor dump for single probe operation to bias the programmable power supply.

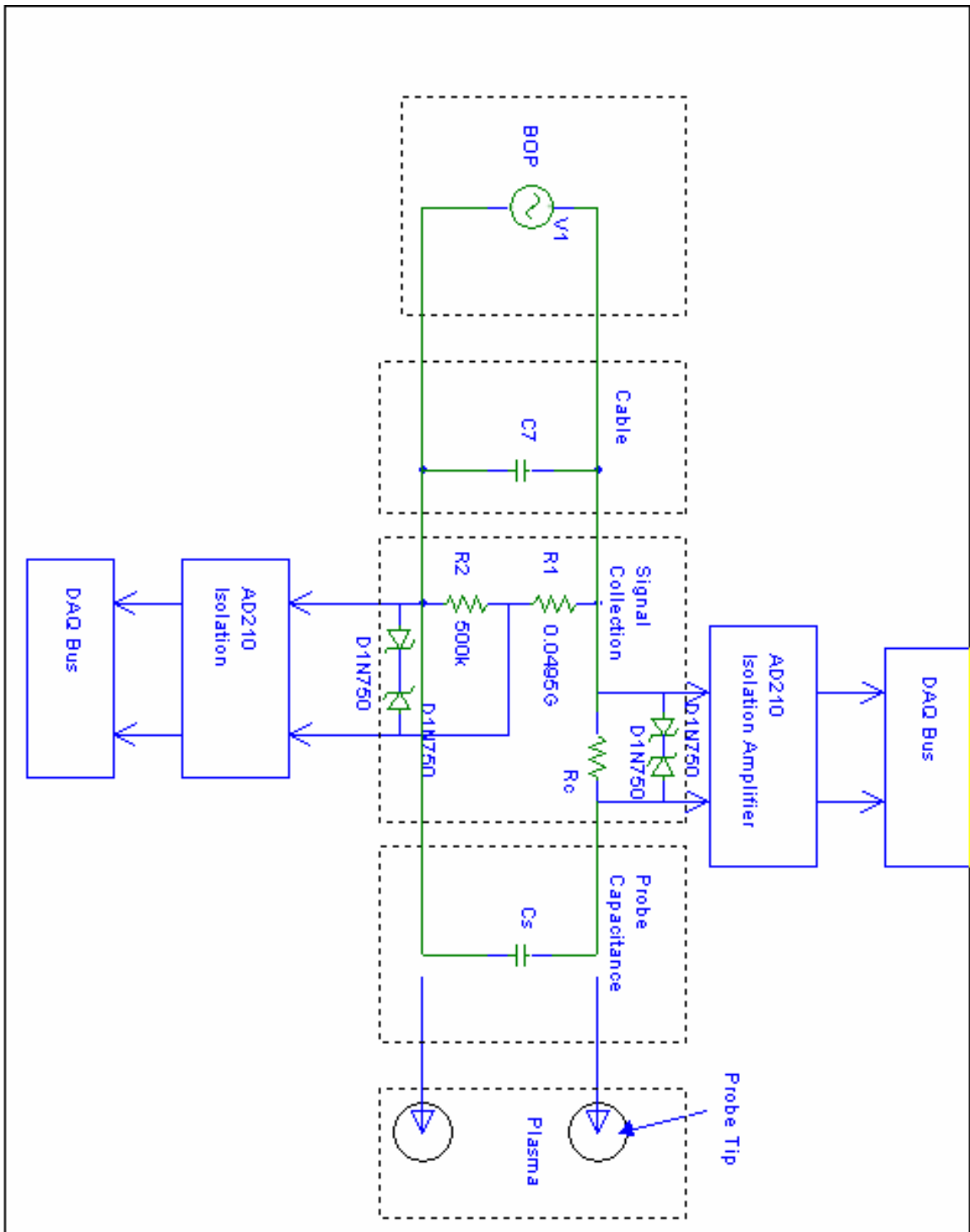


Fig. 55: Schematic for double probe sweeping circuit.

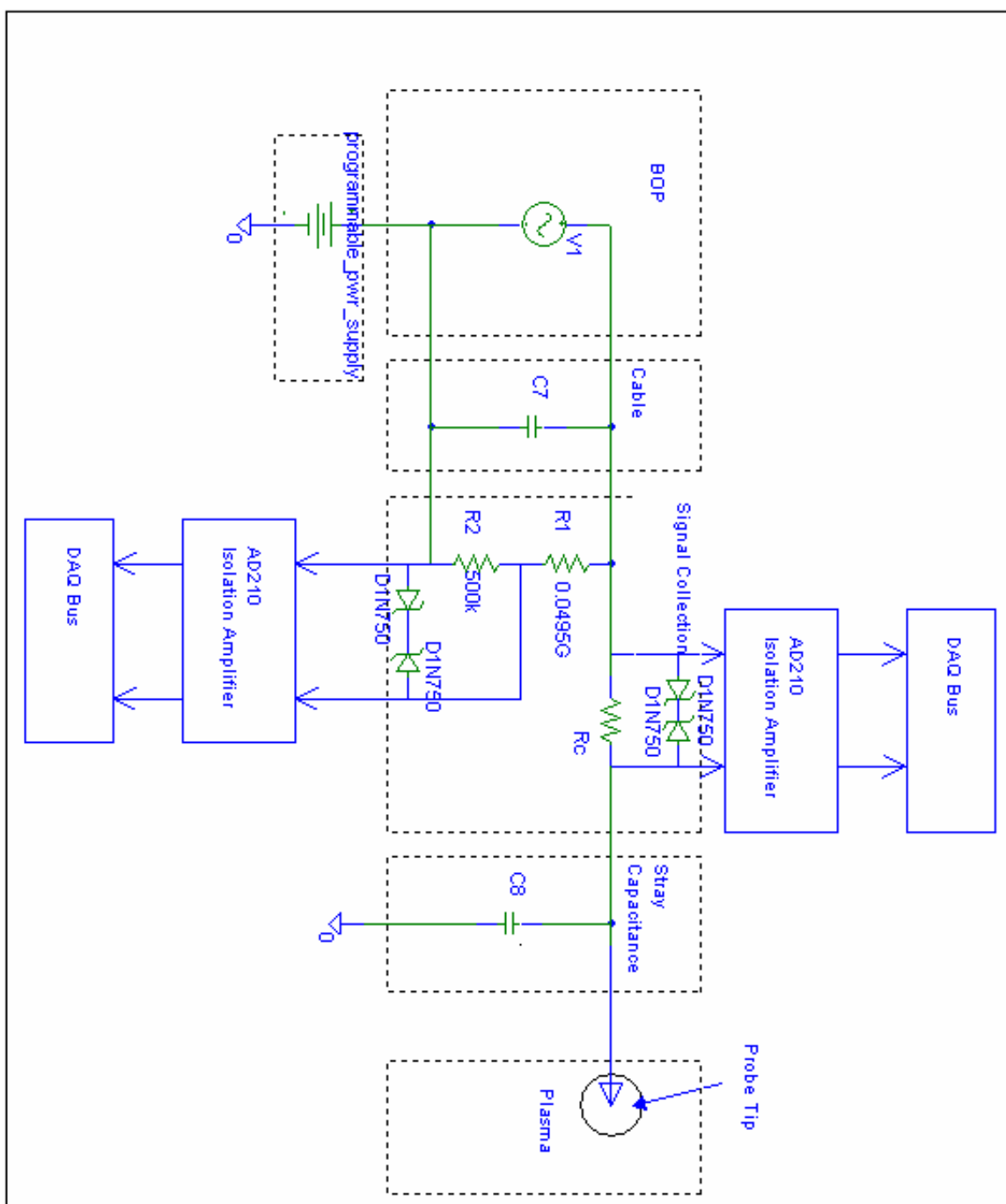


Fig. 56: Schematic of the sweeping circuit for the single probe.



Fig. 57: Aluminum cabinet designed to shield the DAQ bus from RF interference.



Fig. 58: Aluminum mesh is riveted into an aluminum structure to shield the optical encoder from RF noise.

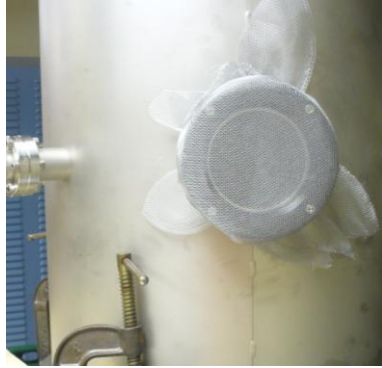


Fig. 59: Aluminum mesh covering viewport to attenuate RF emissions.



Fig. 60: Aluminum cap encases the HV feedthrough insulator to block this path of RF leakage.



Fig. 61: Signal collection circuit is placed inside of an aluminum box to block the re-emitted interference signals conducted by the electrostatic probes.

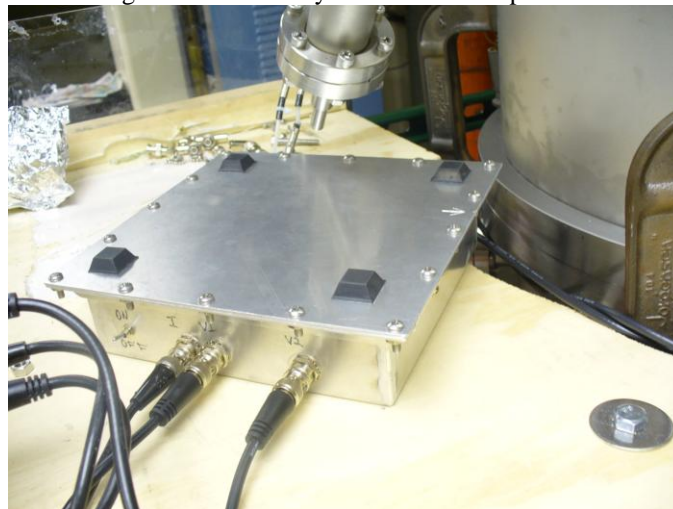


Fig. 62: Photo of aluminum box housing the signal collection circuit.

## IV. Probe Ion Shadowing

### A. *The Ion Core Region*

A technique for estimating the ion core radius of an IXL SIEC is described. The technique exploits the shadowing effect that a probe has on ions flowing through the core region as the probe moves in the radial direction through the center of the device. A theory is developed for ( $\lambda > R_g > d \gg 2R_c$ ), where  $\lambda$  is the mean free path of the ions,  $R_g$  is the radius of the cathode grid,  $d$  is the diameter of a cylindrical probe inserted in an IXL SIEC, and  $R_c$  is the ion core radius.

It has been postulated<sup>5</sup> that the  $n_i(r \leq R_c) \propto R_c^{-2}$ , which implies the beam-beam fusion rate in the core,  $Fr_{bm-bm}(r \leq R_c)$ , should have the following scaling law,  $Fr_{bm-bm}(r \leq R_c) \propto R_c^{-4}$ . This indicates that a small  $R_c$ , or tightly focused ion beams, are essential for beam-beam dominated devices. It also indicates that the fusion reactions are essentially confined to the core region of beam-beam dominated devices. However, in star-mode operation, beam-background reactions dominate the fusion output. In this case, a model has been proposed<sup>58</sup> assuming intersecting “cylinders”, with radius  $R_c$ , of ions to represent the “spokes” of light observed in star mode. The ion density is assumed constant within the cylinders, and in this case, the fusion output is expected to scale with the volume of the cylinders. Therefore, the beam-background fusion rate,  $Fr_{bm-bk}$ , is expected to scale as  $Fr_{bm-bk} \propto R_c^2$ . Of course, this assumes  $n_i$  is constant with respect to  $R_c$ .

As noted in Chapter I, IXL IEC devices may essentially operate in one of two modes. These modes are classified according to their particle source mechanisms and the

relationship among  $\lambda$ ,  $R_g$ , and  $R_a$ , where  $R_a$  is the anode radius, and are summarized in Table VI. Two sub-modes of GD mode are indicated in Table VI. These modes are Star mode and Jet mode and can be distinguished by the relationship between  $\lambda$  and  $R_g$  for the device described in Chapter III. If one imagines the ion flow through the core region as a collection of a large number of ion beams, then  $R_c$  may be viewed as an indicator of the ion beam emittance.<sup>76</sup> Electric field perturbations due to the discrete cathode grid, molecular interactions, and space charge repulsion of ions in the core region can be thought of as emittance growth mechanisms (i.e. result in larger  $R_c$ )

Experimentally,  $R_c$  has been investigated by Thorson et. al.<sup>66,67</sup> on an AGD IXL SIEC and by Satsangi<sup>69</sup> on a GD IXL SIEC device. Thorson noted that  $R_c$  decreased with increasing pressure and increasing voltage. The increase in  $R_c$  at lower pressures is attributed to the defocusing effect of the grid. In effect, an ion receives increments in angular momentum each time it passes through the grid; as the pressure increases, the number of transits through the grid decreases, thus, the amount of angular momentum accumulated by an ion is less. In addition, it was found that as the grid wire spacing decreased, the core radius decreased.<sup>66,67</sup> This is consistent with the defocusing theory as ions would make fewer transits through a grid with a lower geometric transparency. Typical core radii ranged from 2cm to 0.6cm in Thorson's experiments. Satsangi measured an average core radius of 0.36cm in a GD IXL SIEC and observed no significant change in the core size for cathode currents from 10mA to 20mA and voltages from -10kV to -30kV.<sup>69</sup>

An analytical method of relating the shadowing effect of the probe to the current collected by the grid is described in the rest of this Chapter. Although we only consider

the following case ( $\lambda > R_g > d > 2R_c$ ), the method can be adapted for other conditions and more complex probe geometry features. However the computational effort grows exponentially, figuratively speaking, as complicated geometry features are considered. Experimentally, shadowing data has been obtained with double probe d1, which is described in Chapter III. The geometry of d1 is very irregular, and we have resorted to Monte Carlo simulations to model it. The material that follows is still relevant, because it illustrates the concept of estimating core dimensions based on shadowing effects. The method is useful in illustrating the relationships between  $d$ ,  $R_c$ , and  $F(l)$ . In addition, the Monte Carlo simulations are based on the ion beam model presented in the following sections.

Table VI: Summary of different discharge modes and their particle source mechanisms.

<i>Mode</i>	<i>Electron source mechanism</i>	<i>Ion source mechanism</i>
<i>Glow Discharge (GD)</i>		
<i>Star Mode</i> ( $R_a > \lambda \geq R_g$ )	<i>Collisional Ionization</i>	<i>Collisional Ionization</i>
<i>Jet Mode</i> ( $\lambda \ll R_g < R_a$ )	<i>Secondary Cathode Emission</i>	
<i>Assisted Glow Discharge (AGD)</i> ( $R_a \sim \lambda \gg R_g$ )	<i>Collisional Ionization</i> <i>Secondary Cathode Emission</i> <i>Thermionic Emitter Emission</i> <i>E-guns</i>	<i>Collisional Ionization</i> <i>Ion guns</i>

## B. Ion Shadowing

Consider a single ion with charge  $Q$  circulating through an IXL SIEC with no probe. The ion will be collected by the cathode grid after making  $\delta$  passes between the cathode grid wires so that the cathode ion current will be  $I_c = Q/T$ , where  $T$  is the average time it takes for the ion to be collected by the grid. Now, consider a single ion intercepted after its first pass through the cathode grid wires by a probe inserted into the central region of an IXL SIEC. In this case, we assume the grid collects a fictitious current,  $I_c = Q/(\delta*T)$ . If we consider one ion intercepted by the probe and one ion collected by the grid, the collected ion current is  $I_c = (Q/T)*(1 + (1/\delta))$ . This can be extended to the case of  $N$  total ions passing through the cathode grid with  $A$  ions intercepted by the probe and  $N-A$  ions collected by the grid. The ion current collected by the grid can be written as:

$$I_c = \frac{NQ}{T} \left[ 1 + F(l) \left( \frac{1}{\delta} - 1 \right) \right], \quad (8)$$

Where  $F(l) = A/N$ , is the fraction of ions blocked by a probe positioned a distance  $l$  from the center of the cathode. If the secondary electron emission coefficient of the cathode grid is  $\Delta$ , then the measured grid current will be

$$I_g = I_c(1 + \Delta). \quad (9)$$

For  $\lambda \gg R_a$ , then,

$$\delta = \frac{2\eta}{1 - \eta^2}, \quad (10)$$

where  $\eta$  is the geometric transparency of the cathode grid. Typically  $\eta \sim 90\%$ , and  $\delta \sim 10$ .

### C. *Infinitesimal Probe*

Fig. 63 depicts several fan beams of ions originating at the cathode grid radius and intersecting in the core region. In Fig. 64, an infinitesimally small probe is inserted into the core region to a distance  $r = \ell$  from the center. The axis of an ion beam with divergence  $\phi$  is oriented at an angle  $\theta$  with respect to the probe. The 1D projection of the probe onto the cross-section of the beam, as seen in Fig. 64, is given by:

$$k(\ell, \theta) = (R_g - \ell \cos \theta) \tan \phi - \ell \sin \theta. \quad (11)$$

The beam diameter along the projection is:

$$bd(\ell, \theta) = 2(R_g - \ell \cos \theta) \tan \phi. \quad (12)$$

For 2D geometry, the differential angular fraction of ion flow obstructed by the probe is simply the projection divided by the beam diameter along the projection:

$$f(\ell, \theta) = \frac{1}{2} \left[ 1 - \frac{\ell \sin \theta}{(R_g - \ell \cos \theta) \tan \phi} \right]. \quad (13)$$

The total number of ions shadowed by the probe can then be found by averaging over  $\theta$  from  $0 \leq \theta \leq \pi$ . Thus, keeping in mind that  $0 \leq f(\ell, \theta) \leq 1$ , then,

$$F(\ell) = \frac{1}{\pi} \int_0^\pi d\theta \left[ \begin{array}{c} f(\ell, \theta) U[f(\ell, \theta)] U[1 - f(\ell, \theta)] \\ + U[f(\ell, \theta) - 1] \end{array} \right], \quad (14)$$

where  $U[x]$  is the unit step function.

### D. *Finite probe of diameter $d$*

Fig. 65 is an illustration of a probe with diameter  $d > 2R_c$  inserted into the core region. The finite probe width requires that we consider different regions with respect to  $\theta$ . Fig. 66 shows that all of the ions are shadowed by the probe below a certain critical beam angle,  $\theta_l$ .  $\theta_l$  is found by solving the following expression for  $\theta_l$ ,

$$\frac{R_c \text{Cos}\left[\text{Tan}^{-1}\left(\frac{2\ell}{d}\right)\right]}{\text{Sin}\left[\frac{\pi}{2} - \text{Tan}^{-1}\left(\frac{2\ell}{d}\right) - (\theta_1 - \phi)\right]} = \frac{d}{2}. \quad (15)$$

Thus,  $f(\ell, \theta) = 1$  for  $\theta \leq \theta_1$ . Next we consider the region  $\theta_1 \leq \theta \leq \theta_2$  and illustrated in Fig. 67, where  $\theta_2$  is a second critical angle. In this region, the projection,  $k1(\ell, \theta, d)$  is defined as,

$$k1(\ell, \theta, d) = br1(\ell, \theta, d) + \left(\frac{d}{2} \text{Cos}\theta - \ell \text{Sin}\theta\right), \quad (16)$$

where  $br1(\ell, \theta, d)$  is the beam's radius along  $k1(\ell, \theta, d)$ , and is given by,

$$br1(\ell, \theta, d) = \left[ R_g - \left(\frac{d}{2} \text{Sin}\theta + \ell \text{Cos}\theta\right) \right] \text{Tan}\phi. \quad (17)$$

The beam diameter along  $k1(\ell, \theta, d)$  is thus,

$$bd1(\ell, \theta, d) = 2br1(\ell, \theta, d). \quad (18)$$

Next, we can investigate the region  $\theta_2 \leq \theta \leq \pi$ , shown in Fig. 68. In this region, the projection,  $k2(\ell, \theta, d)$  is,

$$k2(\ell, \theta, d) = br2(\ell, \theta, d) - \left(\ell \text{Sin}\theta + \frac{d}{2} \text{Cos}\theta\right), \quad (19)$$

where  $br2(\ell, \theta, d)$  is the beam's radius along  $k2(\ell, \theta, d)$ , and is given by,

$$br2(\ell, \theta, d) = \left[ R_g + \left(\frac{d}{2 \text{Sin}\theta}\right) - \left(\ell + \frac{d}{2} \text{Cot}\theta\right) \text{Cos}\theta \right] \text{Tan}\phi. \quad (20)$$

The beam diameter along  $k2(\ell, \theta, d)$  is thus,

$$bd2(\ell, \theta, d) = 2br2(\ell, \theta, d). \quad (21)$$

The critical angle, shown in Fig. 69, is determined by solving the following equation for  $\theta_2$ ,

$$\frac{k1(\ell, \theta 2, d)}{bd1(\ell, \theta 2, d)} = \frac{k2(\ell, \theta 2, d)}{bd2(\ell, \theta 2, d)}, \quad (22)$$

from which we get,

$$\theta 2(\ell) = \text{Cos}^{-1}\left(\frac{\ell}{R_g}\right). \quad (23)$$

Thus, we can write the combined projection as,

$$k(\ell, \theta, d) = \left[ \begin{array}{l} k1(\ell, \theta, d)U(bd1(\ell, \theta, d) - k1(\ell, \theta, d)) + \\ bd1(\ell, \theta, d)U(k1(\ell, \theta, d) - bd1(\ell, \theta, d)) \end{array} \right] U(\theta 2(\ell) - \theta) + \left[ \begin{array}{l} k2(\ell, \theta, d)U(bd2(\ell, \theta, d) - k2(\ell, \theta, d)) + \\ bd2(\ell, \theta, d)U(k2(\ell, \theta, d) - bd2(\ell, \theta, d)) \end{array} \right] U(\theta - \theta 2(\ell)) \quad (24)$$

and the beam radii can be combined similarly:

$$br(\ell, \theta, d) = br1(\ell, \theta, d)U(\theta 2(\ell) - \theta) + br2(\ell, \theta, d)U(\theta - \theta 2(\ell)). \quad (25)$$

The angular fraction of ion flow blocked by the protruding probe is equal to the ratio of the shaded area of the disk, in Fig. 70, to the total area of the disk. This value is given by  $f(k(\ell, \theta, d), br(\ell, \theta, d))$ , where,

$$f(b, c) = \frac{\left[ (b-c)(2cb-b^2)^{1/2} + c^2 \left( \pi - \text{Cos}^{-1}\left(\frac{b}{c}-1\right) \right) \right]}{\pi c^2} U(c-b) + \frac{\left[ -i(b-c)(2cb-b^2)^{1/2} + c^2 \left( \frac{\pi}{2} + \text{Cos}^{-1}\left(\frac{b}{c}-1\right) \right) \right]}{\pi c^2} U(b-c) \quad (26)$$

Thus, the fraction of the ion flow blocked by the probe as a function of  $\ell$  is,

$$F(\ell) = \frac{1}{\pi} \int_0^\pi d\theta [U(\theta 1 - \theta) + f(k(\ell, \theta, d), br(\ell, \theta, d))U(\theta - \theta 1)]. \quad (27)$$

Some sample calculations to show the relationships between  $R_c$ ,  $d$ , and  $F(\ell)$ , are in Fig. 71 and Fig. 72.

### ***E. Monte Carlo Simulations***

Monte Carlo techniques are employed to accurately predict  $F(l)$  for double probe d1. This probe consists of a 6.35 cylindrical alumina shaft with the cup depicted in Fig. 48 and Fig. 49 glued to the end. The probe is approximated by a cylinder and a half spheroid for modeling purposes. Results are shown in Fig. 73 through Fig. 78 for the following core sizes;  $R_g/R_c = 3,5,8,10,12,15$ . A distinct “hump” in  $F(l)$  near  $l = -10\text{mm}$  is noticeable in most of these plots. This is an affect of the complex geometry of probe d1, as the “hump” fades for the largest core sizes,  $R_g/R_c = 3$ , and disappears for the smallest core sizes,  $R_g/R_c = 15$ , as the core dimensions become less than the smallest features of the probe. The location of the probe is correlated with  $F(l)$  for the core radius,  $R_g/R_c = 10$ , with several depictions in Fig. 79 through Fig. 83.

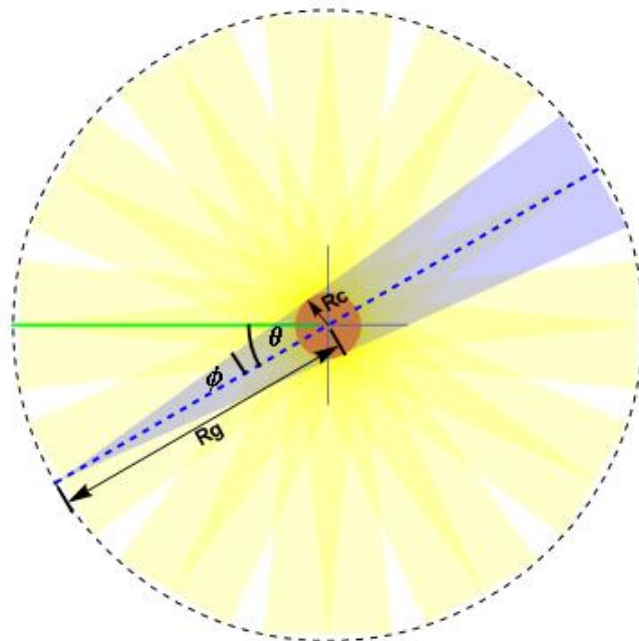


Fig. 63: Depiction of “fan beam” model of ion orbits through the center of the cathode grid region, with the insertion of an infinitesimal probe (shown in green, extending from left side of illustration). The model assumes an infinite number of such fan beams, with a divergence  $\phi = \text{Sin}^{-1}(R_c/R_g)$  intersecting in the core region.

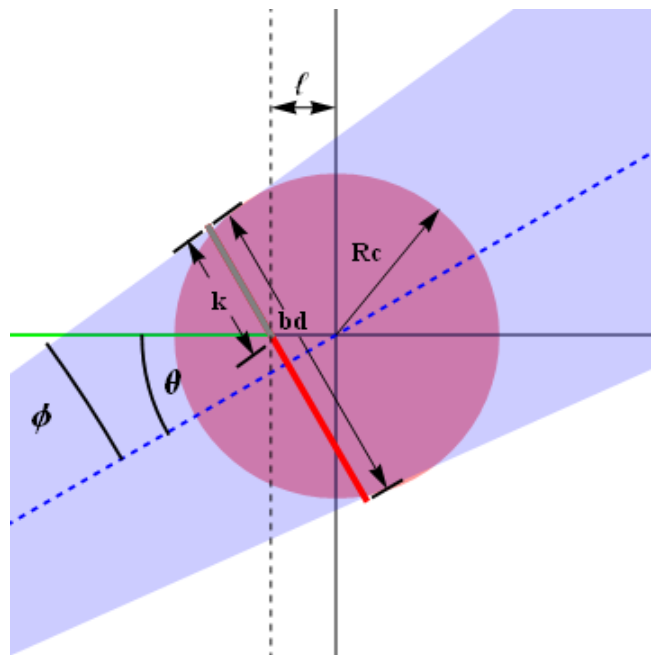


Fig. 64: A close up of the core region, indicating the projection,  $k$ , of the probe onto the diameter of the ion beam. Also depicted, are the beam diameter,  $bd$ , along  $k$ , the core radius,  $R_c$ , in addition to the probe, indicated in green.

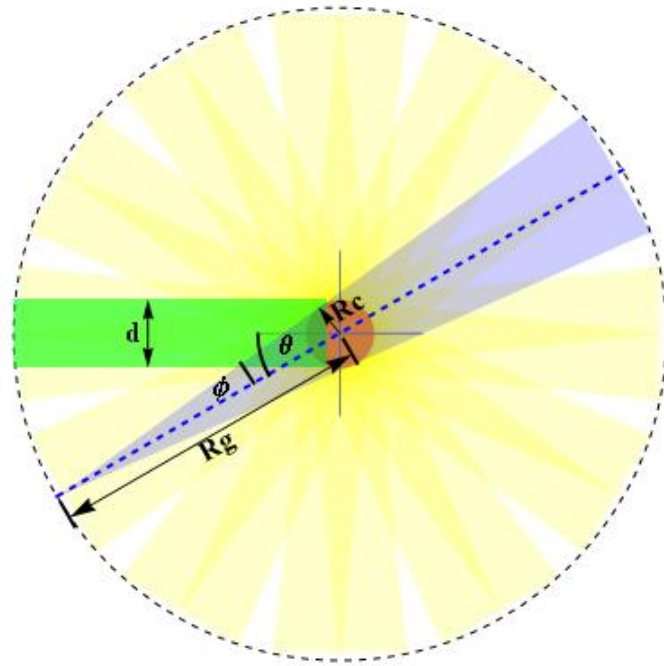


Fig. 65: Depiction of “fan beam” model of ion orbits through the center of the cathode grid region, with the insertion of a probe of diameter  $d$  (shown in green, extending from left side of illustration). The model assumes an infinite number of such fan beams, with a divergence  $\phi = \text{Sin}^{-1}(R_c/R_g)$  intersecting in the core region.

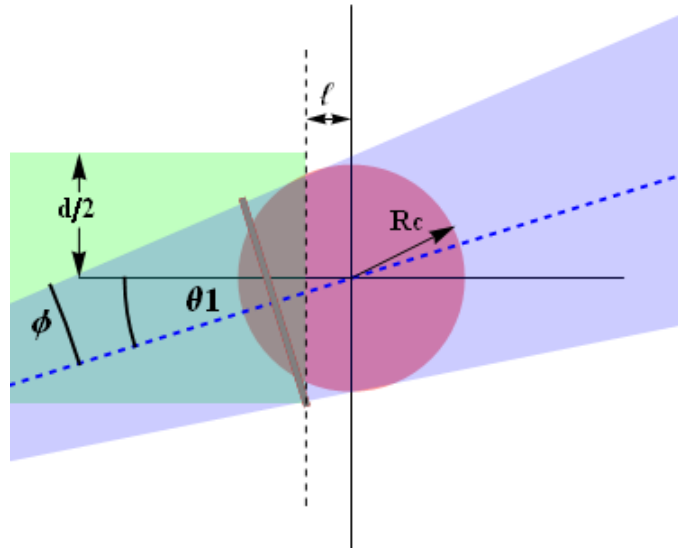


Fig. 66: All beams below the critical angle  $\theta_1$  are obstructed by the probe as depicted in this illustration.

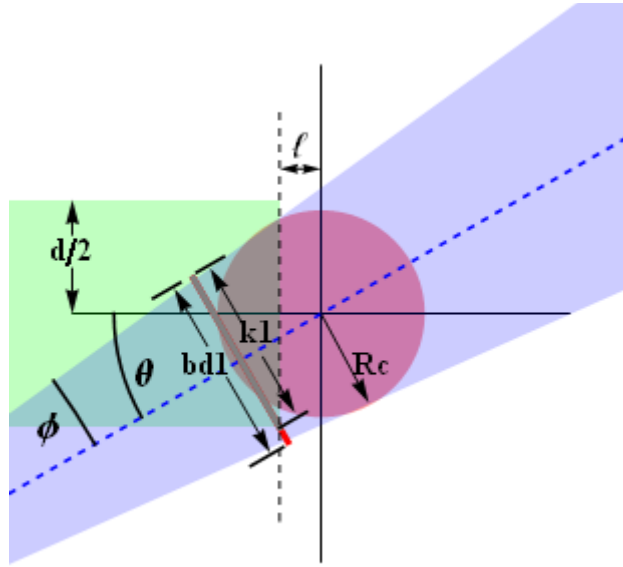


Fig. 67: For  $\theta_1 < \theta < \theta_2$ , the projection of the probe onto the beam diameter is  $k_1$ , while the beam diameter along  $k_1$  is  $bd_1$ .

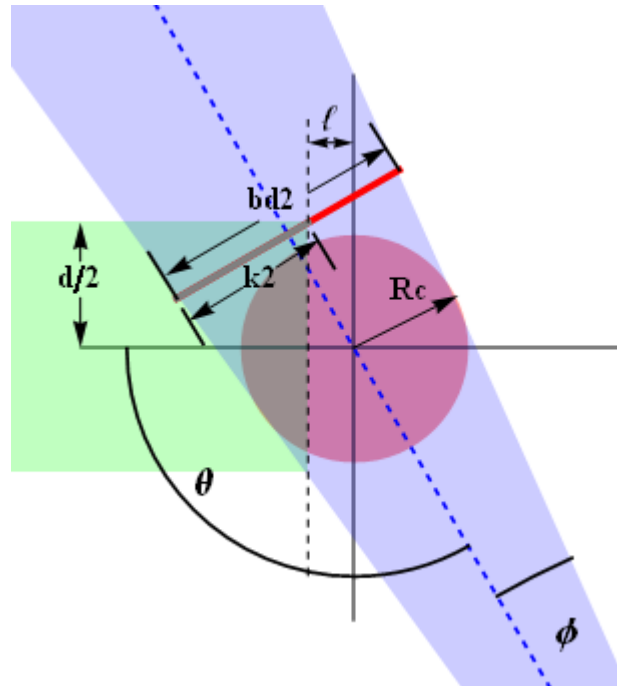


Fig. 68: For  $\theta_2 < \theta < \pi$ , the projection of the probe onto the beam diameter is  $k_2$ , while the beam diameter along  $k_2$  is  $bd_2$ .

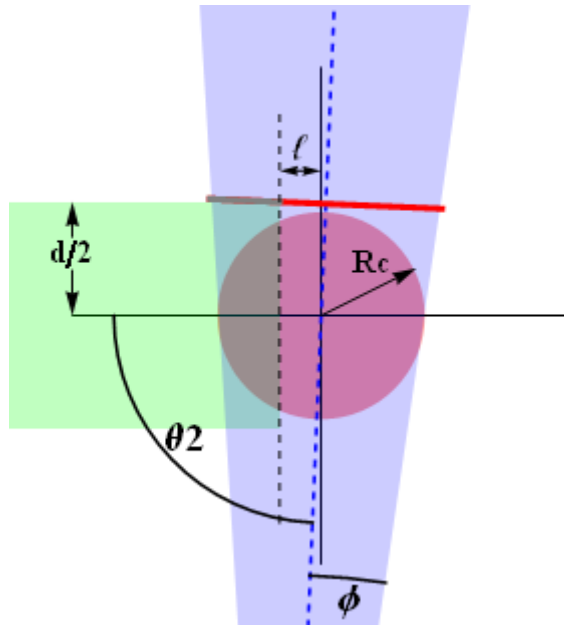


Fig. 69: The projection of the probe onto the beam diameter and the beam diameter must be defined separately for regions separated by the critical angle,  $\theta_2$ .

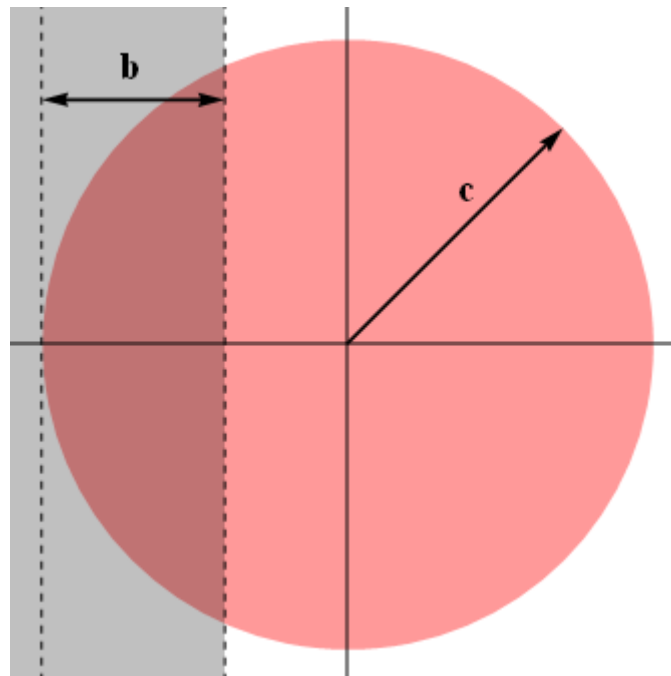


Fig. 70: The fraction of shadowed ions in 3 dimensions is indicated, where  $c$  represents the ion beam radius and  $b$  is the projection of the probe onto the ion beam.

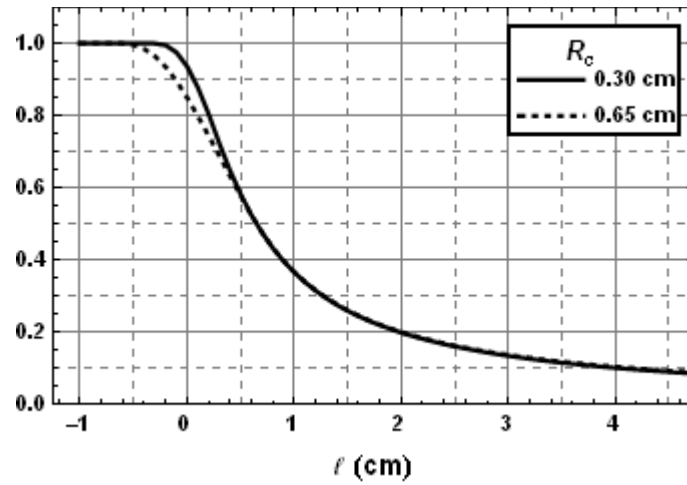


Fig. 71: This is a plot of  $F(l)$  for two core radii, for a cylindrical probe diameter of  $d = 1.3\text{cm}$  and a cathode grid radius of  $R_g = 4.7\text{cm}$ .

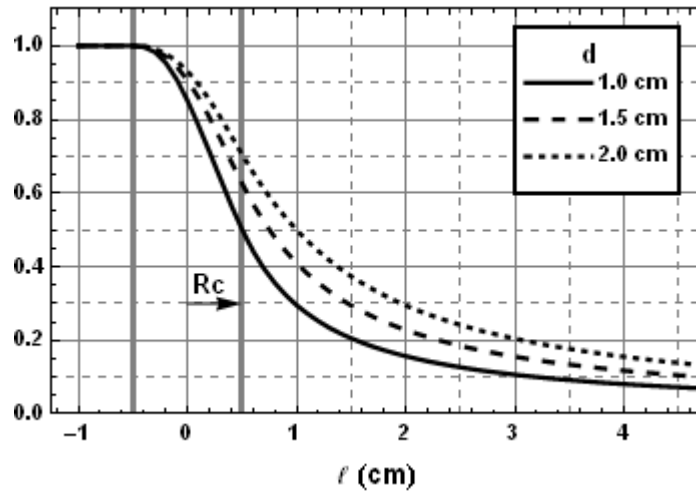


Fig. 72: This is a plot of  $F(l)$  for three different probe diameters and a core radius,  $R_c = 0.5\text{cm}$  and a cathode grid radius of  $R_g = 4.7\text{cm}$ .

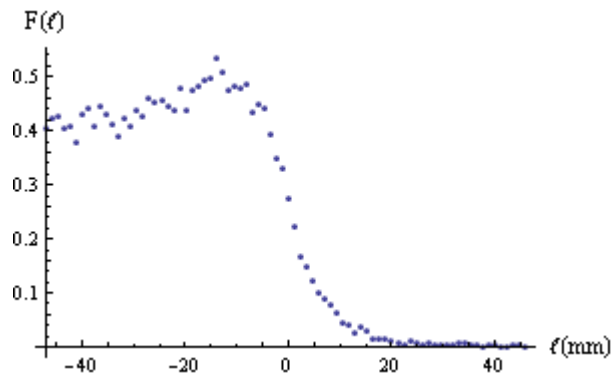


Fig. 73:  $F(l)$  for double probe, d1, depicted in Fig. 48 and Fig. 49 for the case  $R_g/R_c = 3$ .

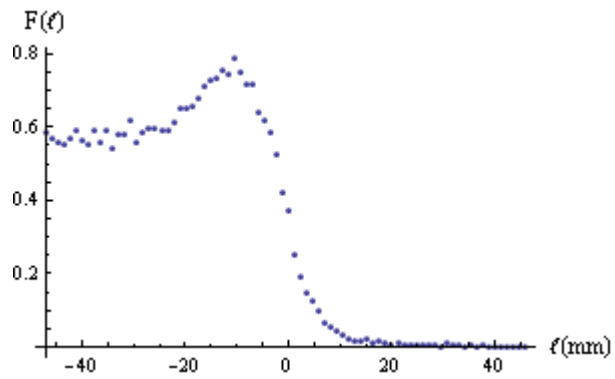


Fig. 74:  $F(l)$  for double probe, d1, depicted in Fig. 48 and Fig. 49 for the case  $R_g/R_c = 5$ .

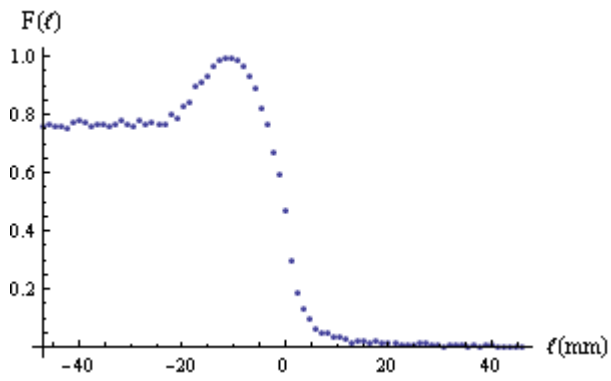


Fig. 75:  $F(l)$  for double probe, d1, depicted in Fig. 48 and Fig. 49 for the case  $R_g/R_c = 8$ .

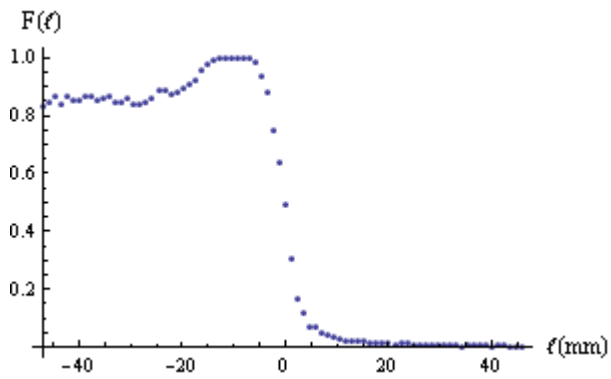


Fig. 76:  $F(l)$  for double probe, d1, depicted in Fig. 48 and Fig. 49 for the case  $R_g/R_c = 10$ .

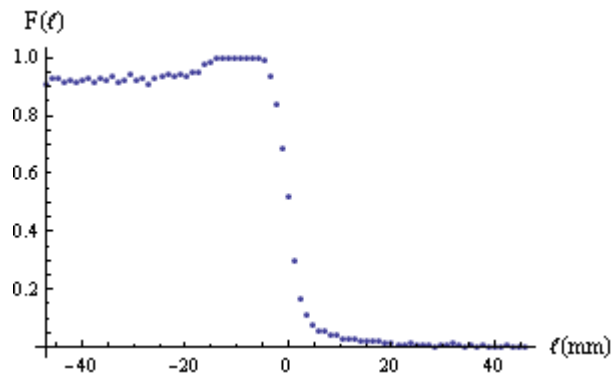


Fig. 77:  $F(l)$  for double probe, d1, depicted in Fig. 48 and Fig. 49 for the case  $R_g/R_c = 12$ .

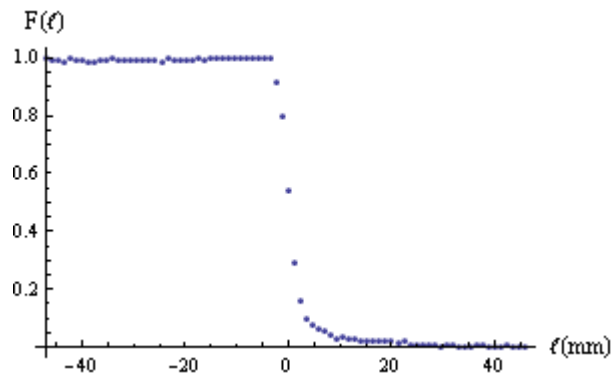


Fig. 78:  $F(l)$  for double probe, d1, depicted in Fig. 48 and Fig. 49 for the case  $R_g/R_c = 15$ .

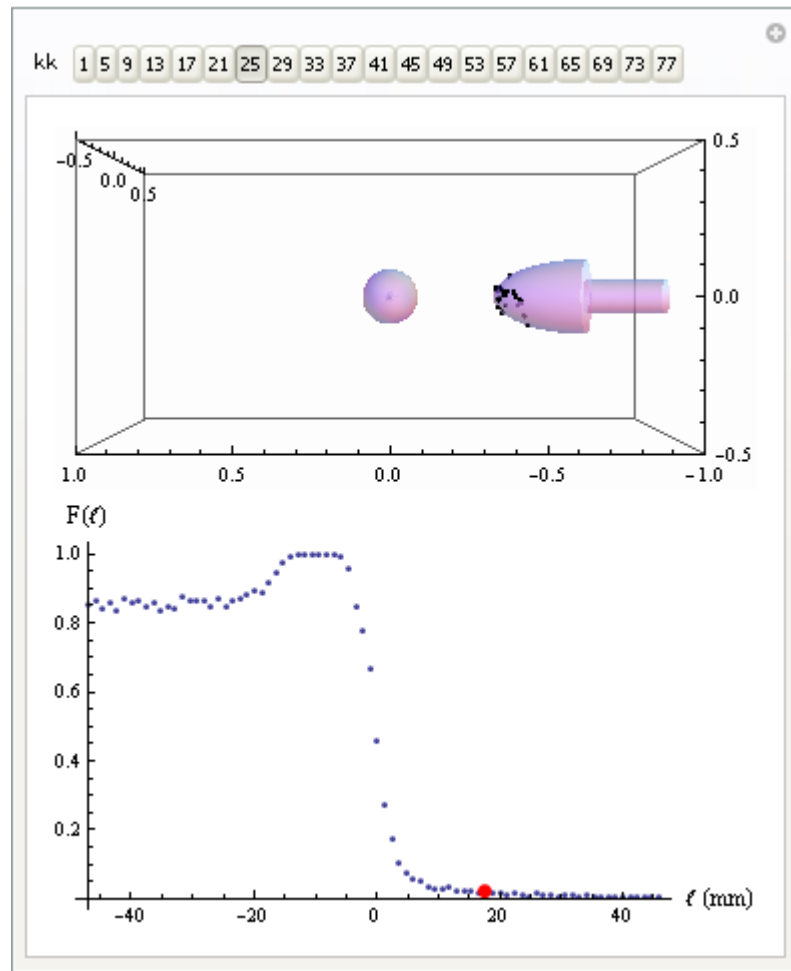


Fig. 79: Animation simultaneously depicting  $F(l)$  and the probe location for a core radius of  $R_g/R_c = 10$ . In this case, the probe is located at  $l \sim 17$ mm.

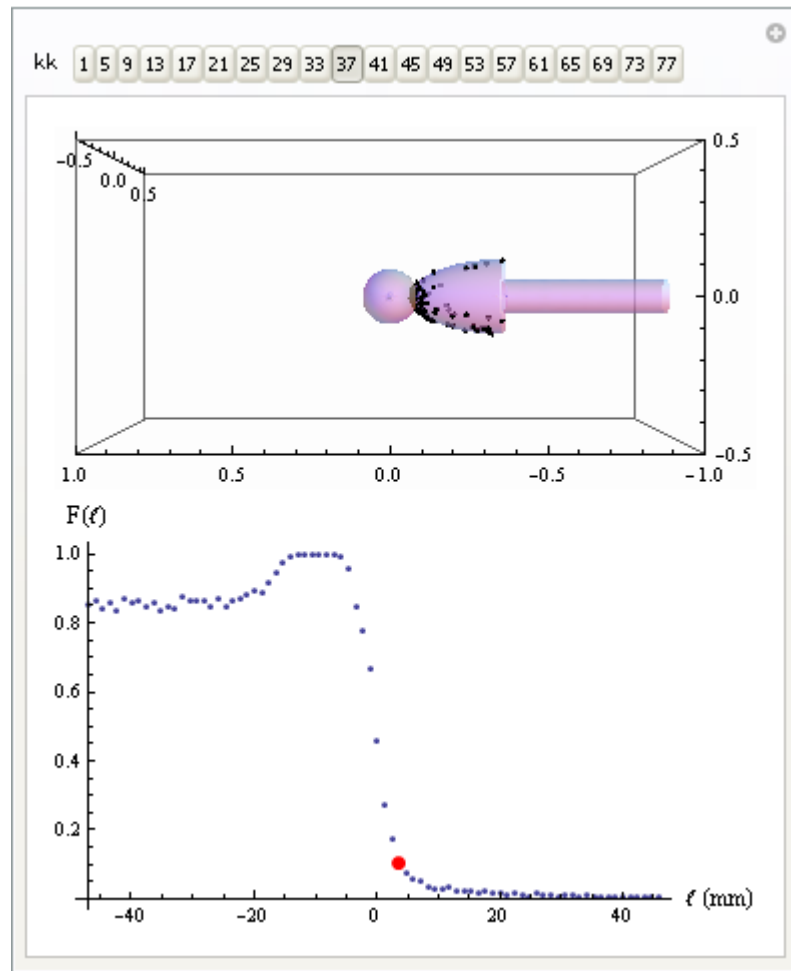


Fig. 80: Animation simultaneously depicting  $F(l)$  and the probe location for a core radius of  $R_g/R_c = 10$ . In this case, the probe is located at  $l \sim 3$ mm.

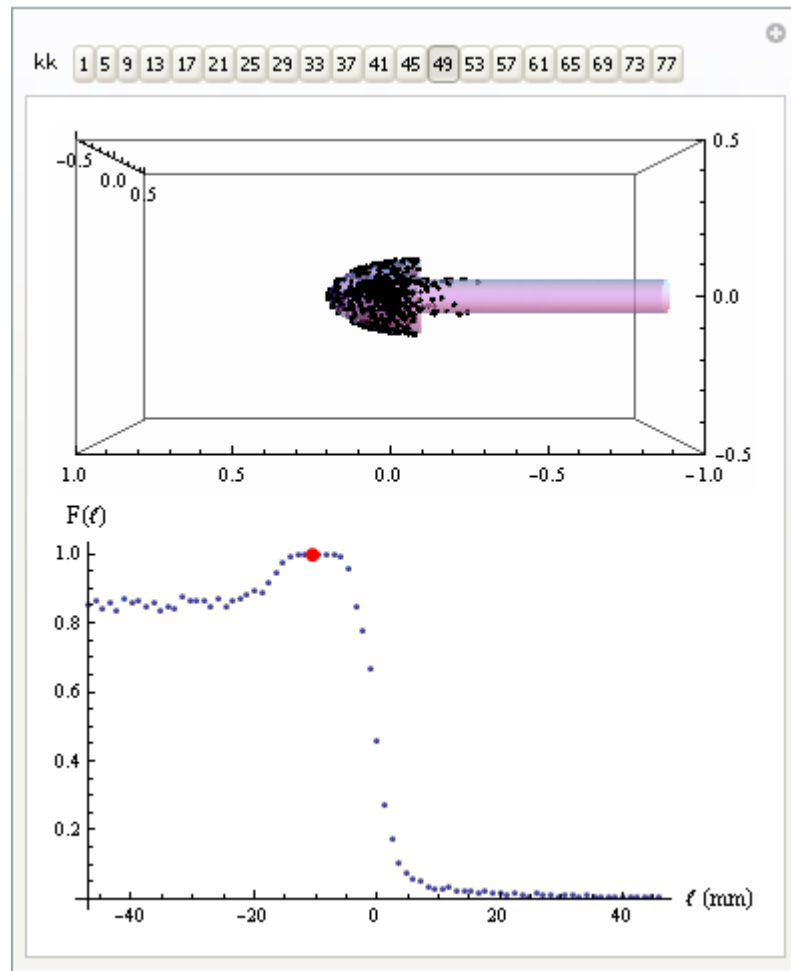


Fig. 81: Animation simultaneously depicting  $F(l)$  and the probe location for a core radius of  $R_g/R_c = 10$ . In this case, the probe is located at  $l \sim -1$  mm.

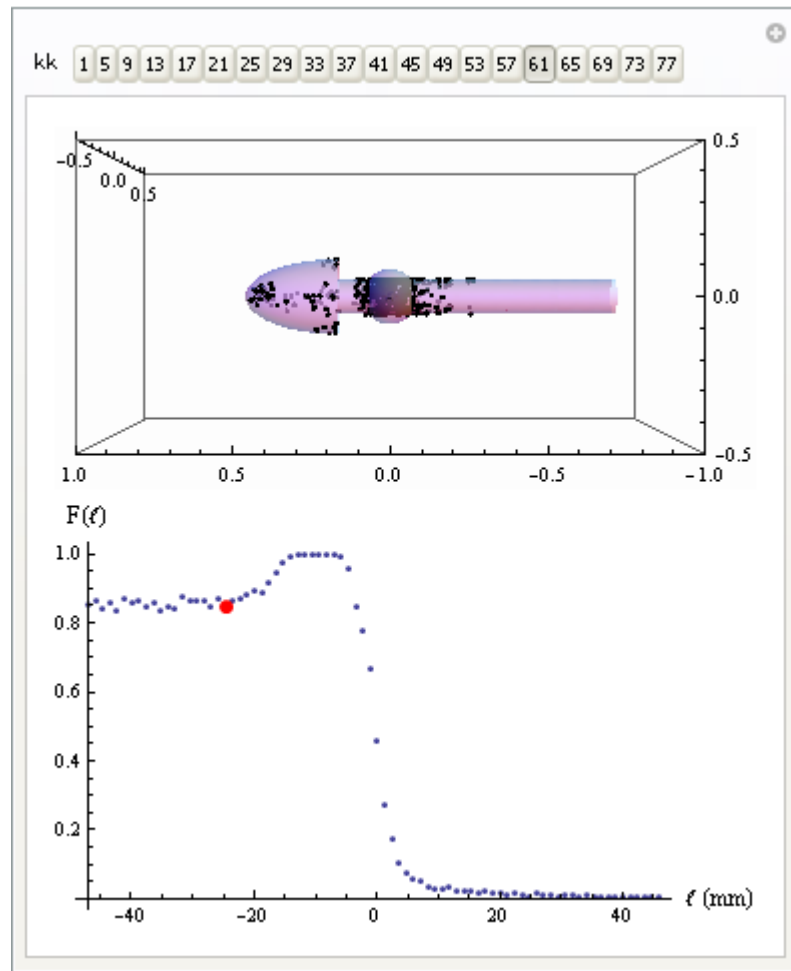


Fig. 82: Animation simultaneously depicting  $F(l)$  and the probe location for a core radius of  $R_g/R_c = 10$ . In this case, the probe is located at  $l \sim -26$ mm.

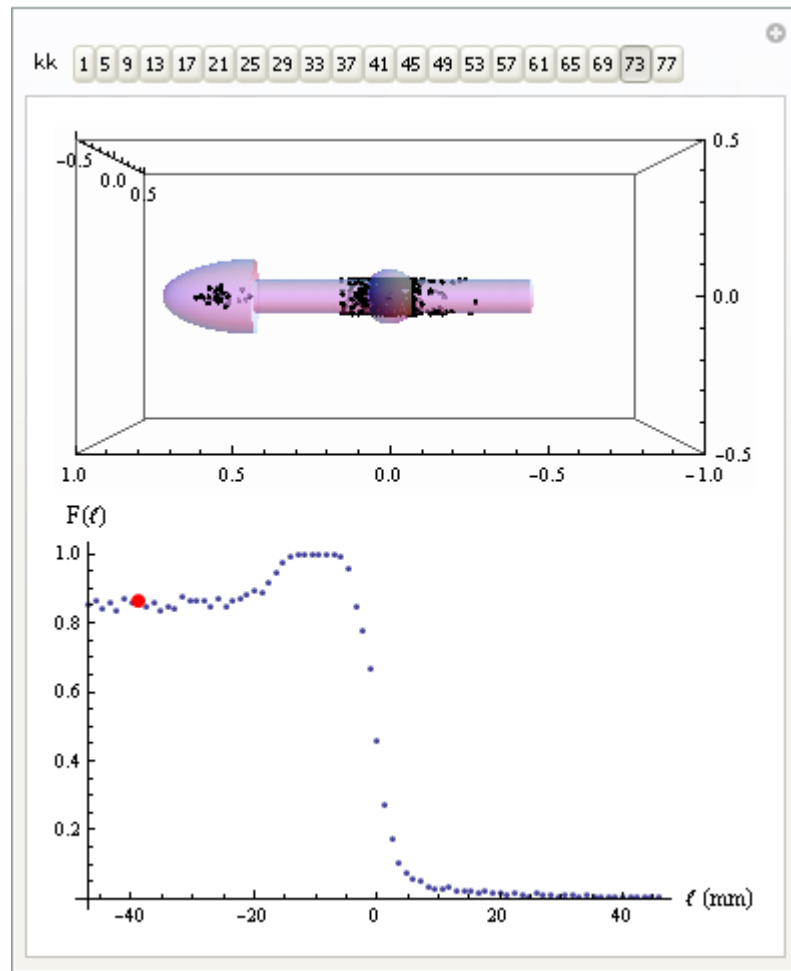


Fig. 83: Animation simultaneously depicting  $F(l)$  and the probe location for a core radius of  $R_g/R_c = 10$ . In this case, the probe is located at  $l \sim -39$ mm.

## V. Experimental Results

Results of double probe and single probe measurements on the GD IXL SIEC will be presented here. In cases where the data is analyzed to obtain information about the plasma density and temperature, the analysis has been based on the assumption of a thin collision-less sheath. Further, double probe analysis is carried out with additional assumptions, including quasi-neutrality, and  $kT_i \ll kT_e$ . More details regarding the analysis methods used for single and double probe traces are included in Appendix B. As indicated by Thorson<sup>66,67</sup>, a region deficient in electrons can be identified, as the floating potential in that region is positive with respect to the plasma potential. We will see that the double probe traces are very different than those of Thorson, indicating a greater degree of neutralization in this GD device versus the AGD device studied by Thorson.

### A. *Double Probe (d2)*

Typical double probe traces, with double probe d2, at various radial locations within the device, are provided in Fig. 84 through Fig. 92. For these measurements, the double probe is inserted at Probe Location 1, as indicated in Fig. 46, and aligned with an ion micro-channel. To compute the plasma densities and electron temperatures as outlined in Appendix B, one-hundredth order polynomials are fit to the data points for each curve using the least-squares method, an example of which is shown in Fig. 93. The ion saturation current,  $I_0$  is manually read from each I-V trace.

## 1. Electric Field Components

Data is collected for ten different cases as specified in Table VII. In this table, the observed discharge mode is indicated as “Star Mode” or “Jet Mode”. The asymmetry of the I-V curves in Fig. 84 through Fig. 92 is obvious, as curves generally do not cross the voltage axis at zero volts, as is expected of double probe traces. The cause of this asymmetry is attributed to the strong electric fields and misalignment of the probe with the center of the grid hole. Fortunately, then, the double probe traces provide a measure of the tangential electric fields produced by the discrete grid structure. As noted in Chapter IV, and by Thorson<sup>66,67</sup>, these tangential field components are one factor that influence ion focusing and thus, CR. Thus, a plot of the point of intersection of the I-V curve with the voltage axis is provided in Fig. 94 for the “Star Mode” cases listed in Table VII. The “Jet Mode” cases are included with a few of the “Star Mode” cases in Fig. 95. The purpose of this second plot is to emphasize the “Jet Mode” results and emphasize the distinguishing features of the tangential electric field components between “Jet Mode” and “Star Mode”.

Floating potential measurements are obtained with probe d2 for all of the situations listed in Table VII. Although the floating potential is not a true representation of the plasma potential, we expect that the shape of the radial floating potential profile is similar in shape to the plasma potential profile. The floating potential profile, then, serves as an indicator of the radial electric field component. Radial floating potential profiles for the “Star Mode” cases in Table VII are provided in Fig. 96. To emphasize the “Jet Mode” cases, they are included in a second plot with just a few of the “Star Mode” cases, as shown in Fig. 97.

## **2. Electron Temperature and Plasma Density Profiles**

Once again, these measurements are made for the cases listed in Table VII, and electron temperature profiles for the “Star-Mode” cases are provided in Fig. 98, while electron temperature profiles for the “Jet-Mode” cases are included with a few of the “Star-Mode” cases in Fig. 99. Plasma density profiles are depicted in both linear and log plots. The linear plot of plasma density profiles is provided to reinforce the core region idea and illustrate the sharp increase in ion density as one approaches the center of the device where multiple ion beams overlap. A linear plot for all cases in Table VII is provided in Fig. 100. Finally, log plots of the plasma density profiles for “Star-Mode” cases are provided in Fig. 101, while “Jet-Mode” and some “Star-Mode” cases are depicted in Fig. 102.

### ***B. Single Probe***

Several single probe I-V curves are obtained at multiple radial positions, for multiple probes, and for several different discharge conditions. Rather than display all single probe curves, only some of the curves will be displayed to illustrate the heterogeneous nature of the plasma in a GD IXL SIEC device.

To show how this heterogeneous structure is affected by discharge conditions, single probe curves for multiple probes at particular radial positions are compared. Single probe I-V traces are obtained with single probe s2 inserted at Probe Location 2 of Fig. 46, and from the individual disks of double probe d2 inserted in Probe Location 1 of Fig. 46. I-V characteristics collected with probe s2, for multiple discharge conditions, are shown in Fig. 103 through Fig. 105. I-V curves for each disk of the double probe in Probe Location 1 are shown in Fig. 106 through Fig. 115. In this case, the disk that

passes most closely to a wire of the cathode grid is labeled as disk 1 while the disk located farthest from the grid wire is labeled as disk 2.

The evolution of the single probe I-V characteristics along the radius of the device are displayed for disks 1 and 2 of probe d2 inserted at Probe Location 1 as indicated in Fig. 46. The discharge condition for each disk is slightly different. For disk 1, the discharge condition is  $V_s = -5.04$  kV,  $I_s = 10.5$  mA and  $P = 0.93$  mA kV<sup>-3/2</sup>, while for disk 2, the discharge condition is  $V_s = -5.04$  kV,  $I_s = 11.52$  mA and  $P = 1.02$  mA kV<sup>-3/2</sup>. These characteristics are displayed in Fig. 116 through Fig. 135.

Single Langmuir probe curves have been analyzed to obtain estimates of the electron temperatures  $T_e$  and the electron densities,  $n_e$ . Several measurements along the radius of the device are included in Fig. 136 and Fig. 137. A discussion regarding the observation of multiple electron species will be provided in Chapter VI.

### ***C. Probe Shadowing***

In Chapter IV, it was shown that information regarding the core size could be obtained from a curve of the fraction of ions obstructed by a probe as a function of probe position. Experimentally, such a curve is generated by obtaining measurements of the cathode grid current as a function of probe position. The probe used in these measurements is double probe d1 inserted into probe location 1, aligned with an ion micro-channel. Shadowing data is collected for 13 cases as listed in Table IX and shown in Fig. 138 through Fig. 142.

#### ***D. Virtual Electrodes***

From the floating potential measurements in Fig. 97, we see what appears to be a virtual anode for the 6.0 mA  $kV^{-3/2}$  case. Thus, more floating probe measurements are obtained with single probe s2 inserted into Probe Location 2 for several “Jet Mode” situations. The measurements are obtained with this probe because it is deemed to be the least invasive. The results are presented in Fig. 143 through Fig. 146. The supply voltage is monitored and plotted with the floating potential signal so that perturbations to the system due to the probe could be viewed simultaneously with the floating potential measurements. The purpose of this is to evaluate the genuineness of any potential perturbations detected from the floating potential measurements. In all of these cases, the supply current remains saturated at the supply maximum of 40mA.

Table VII: Ten different cases for which data is collected with double probe d2 in Probe Location 1, aligned with an ion micro-channel. Results for these ten cases are provided in Fig. 94 through Fig. 102.

#		$V_s$ (kV)	$I_s$ (mA)	$P$ (mA kV <sup>-3/2</sup> )	Mode
1	$x$	-4.96	3.50	0.32	Star Mode
2	◇	-4.96	6.54	0.59	Star Mode
3	◇	-4.97	10.06	0.91	Star Mode
4	□	-4.97	13.22	1.19	Star Mode
5	▽	-5.04	16.22	1.44	Star Mode
6	○	-4.97	24.70	2.23	Star Mode
7	■	-4.98	33.07	2.97	Star Mode
8	◆	-4.83	36.37	3.42	Star Mode
9	▲	-4.38	38.73	4.22	Jet Mode
10	●	-3.54	39.97	6.00	Jet Mode

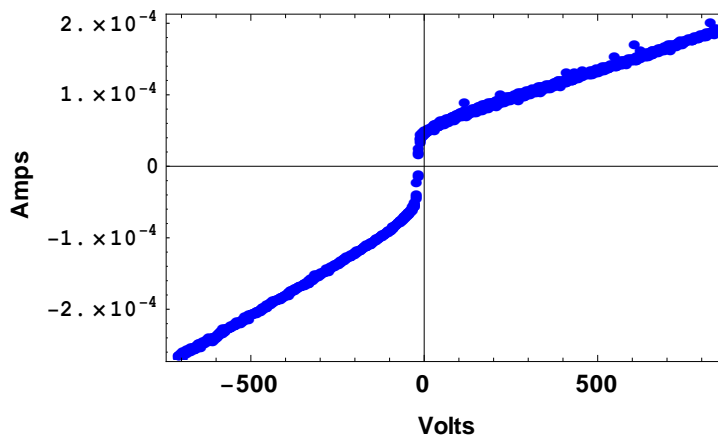


Fig. 84: Typical I-V trace at radius  $r = 0$  with respect to the center of the device. The cathode is located at a radius  $R_g = 4.7\text{cm}$  and the anode is at a radius  $R_a \sim 22\text{cm}$  from the center of the device.

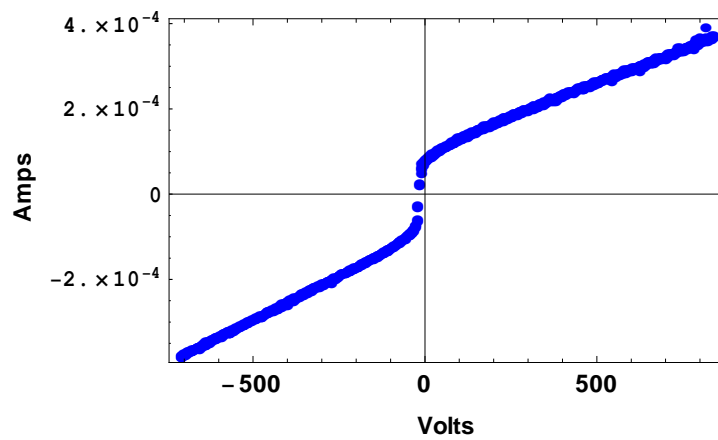


Fig. 85: Typical I-V trace at radius  $r = 1\text{cm}$  with respect to the center of the device. The cathode is located at a radius  $R_g = 4.7\text{cm}$  and the anode is at a radius  $R_a \sim 22\text{cm}$  from the center of the device.

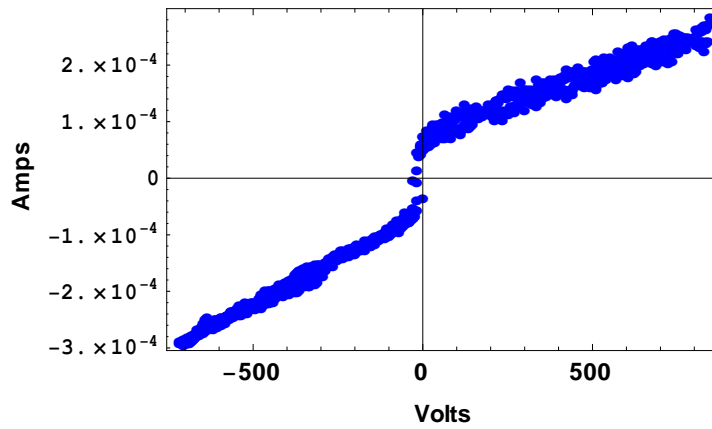


Fig. 86: Typical I-V trace at radius  $r = 2\text{cm}$  with respect to the center of the device. The cathode is located at a radius  $R_g = 4.7\text{cm}$  and the anode is at a radius  $R_a \sim 22\text{cm}$  from the center of the device.

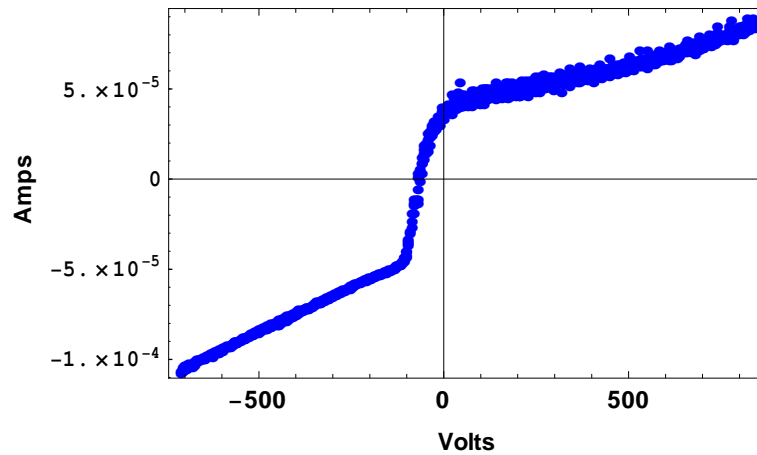


Fig. 87: Typical I-V trace at radius  $r = 3\text{cm}$  with respect to the center of the device. The cathode is located at a radius  $R_g = 4.7\text{cm}$  and the anode is at a radius  $R_a \sim 22\text{cm}$  from the center of the device.

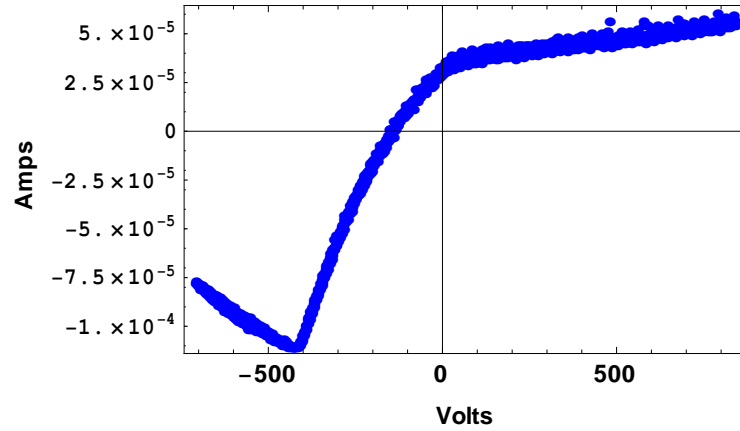


Fig. 88: Typical I-V trace at radius  $r = 4\text{cm}$  with respect to the center of the device. The cathode is located at a radius  $R_g = 4.7\text{cm}$  and the anode is at a radius  $R_a \sim 22\text{cm}$  from the center of the device.

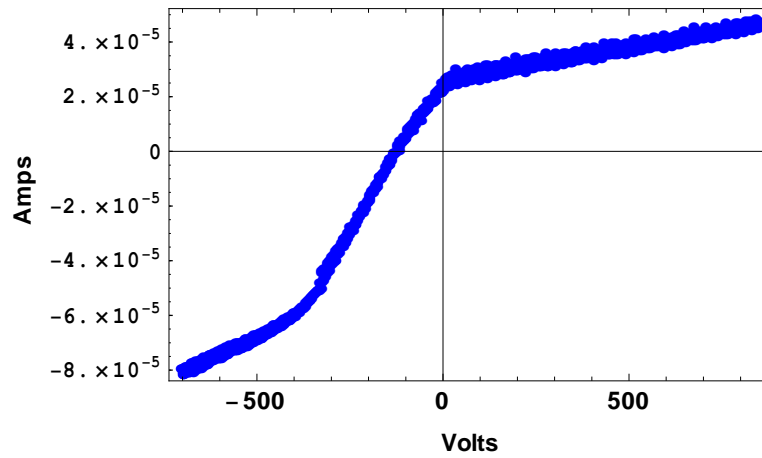


Fig. 89: Typical I-V trace at radius  $r = 5\text{cm}$  with respect to the center of the device. The cathode is located at a radius  $R_g = 4.7\text{cm}$  and the anode is at a radius  $R_a \sim 22\text{cm}$  from the center of the device.

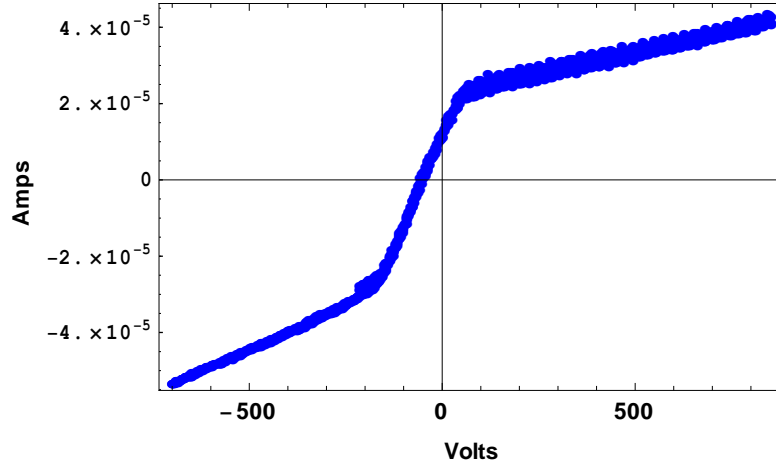


Fig. 90: Typical I-V trace at radius  $r = 6\text{cm}$  with respect to the center of the device. The cathode is located at a radius  $R_g = 4.7\text{cm}$  and the anode is at a radius  $R_a \sim 22\text{cm}$  from the center of the device.

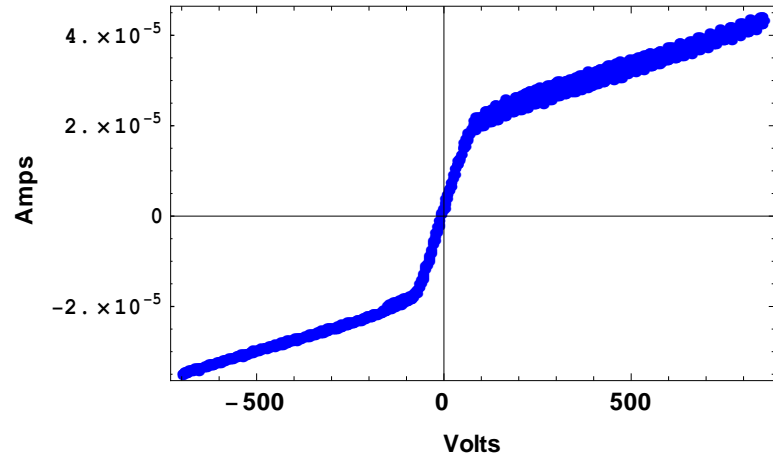


Fig. 91: Typical I-V trace at radius  $r = 7\text{cm}$  with respect to the center of the device. The cathode is located at a radius  $R_g = 4.7\text{cm}$  and the anode is at a radius  $R_a \sim 22\text{cm}$  from the center of the device.

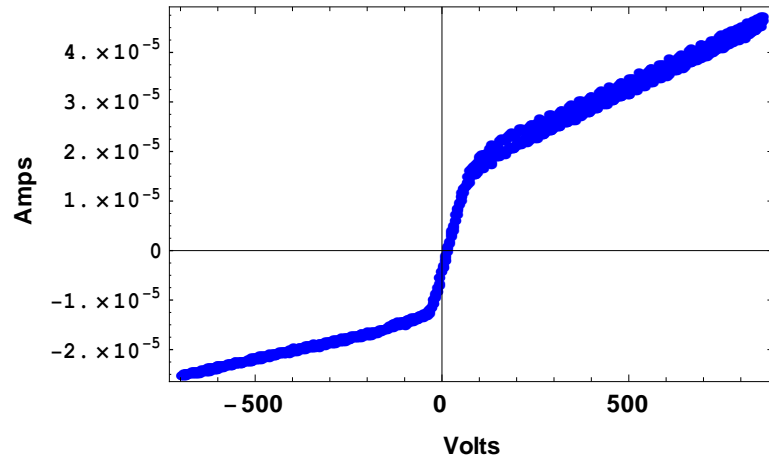


Fig. 92: Typical I-V trace at radius  $r = 8\text{cm}$  with respect to the center of the device. The cathode is located at a radius  $R_g = 4.7\text{cm}$  and the anode is at a radius  $R_a \sim 22\text{cm}$  from the center of the device.

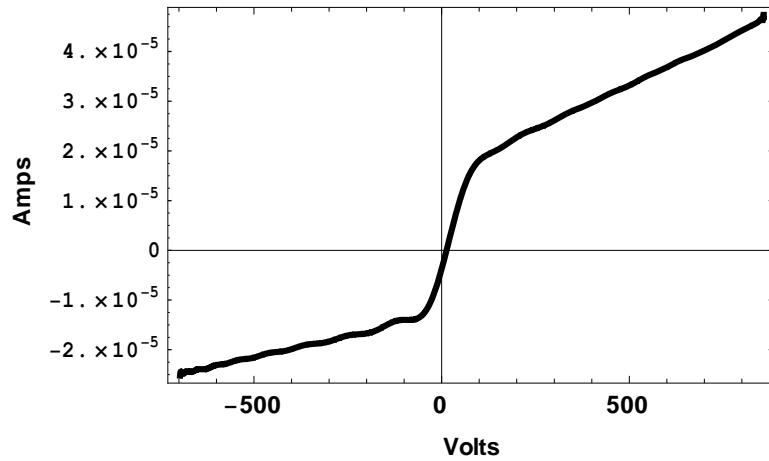


Fig. 93: The I-V trace data in Fig. 92 is fit with a one-hundredth order polynomial using the least squares method. All double probe I-V curves are fitted this way for analysis purposes.

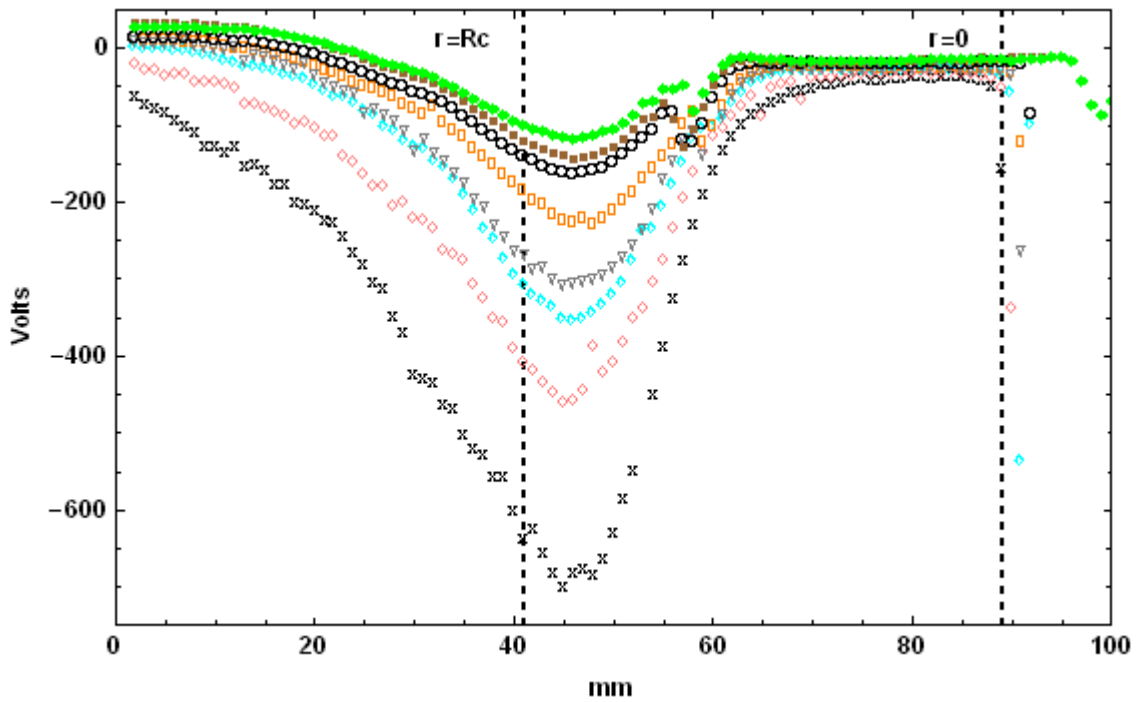


Fig. 94: Difference in floating potentials of the two disks of double probe d2 for “Star Mode” cases, providing an experimental indication of the tangential components of the electric field due to the discrete cathode grid structure.

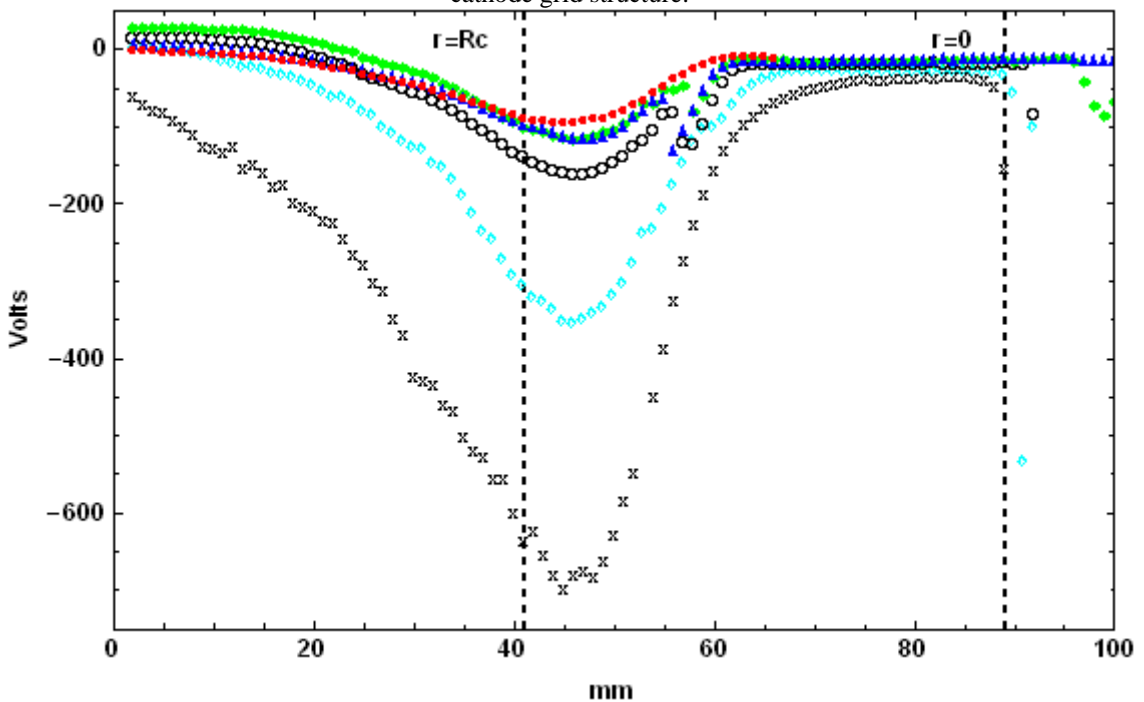


Fig. 95 Difference in floating potentials of the two disks of double probe d2 for “Jet Mode” cases and a few of the “Star Mode” cases, providing an experimental indication of the tangential components of the electric field due to the discrete cathode grid structure.

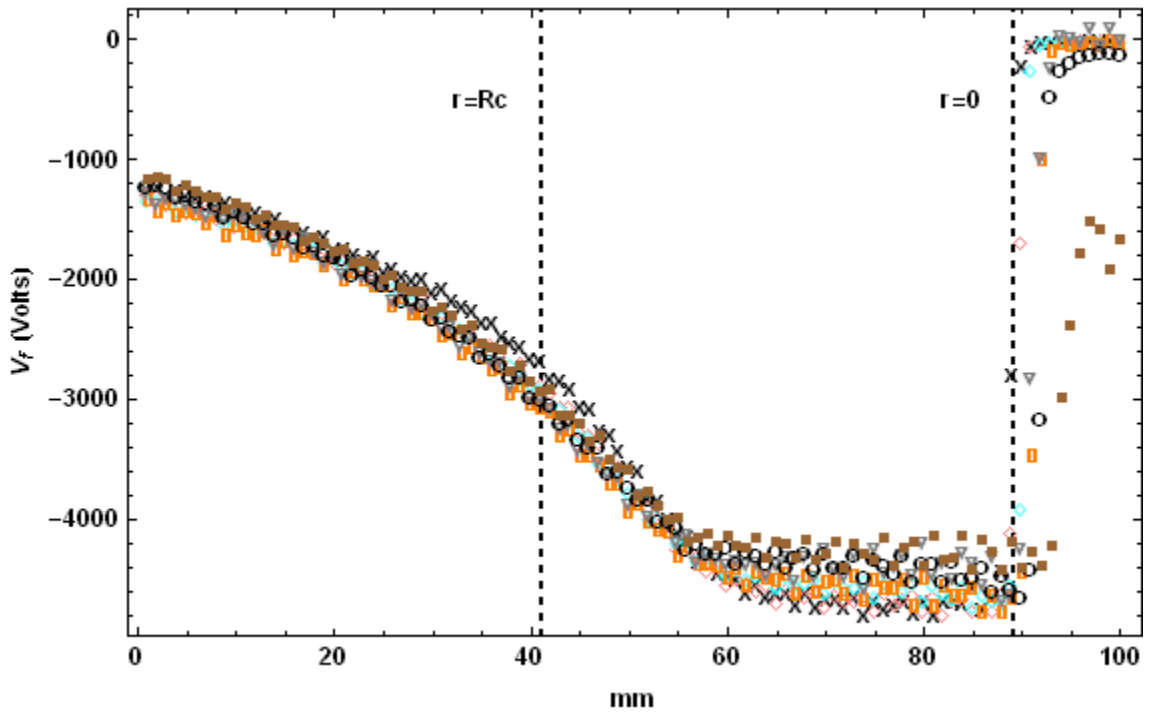


Fig. 96: Radial floating potential profiles,  $V_f(r)$ , for “Star Mode” cases in Table VII. These profiles are indicators of the radial component of the electric field.

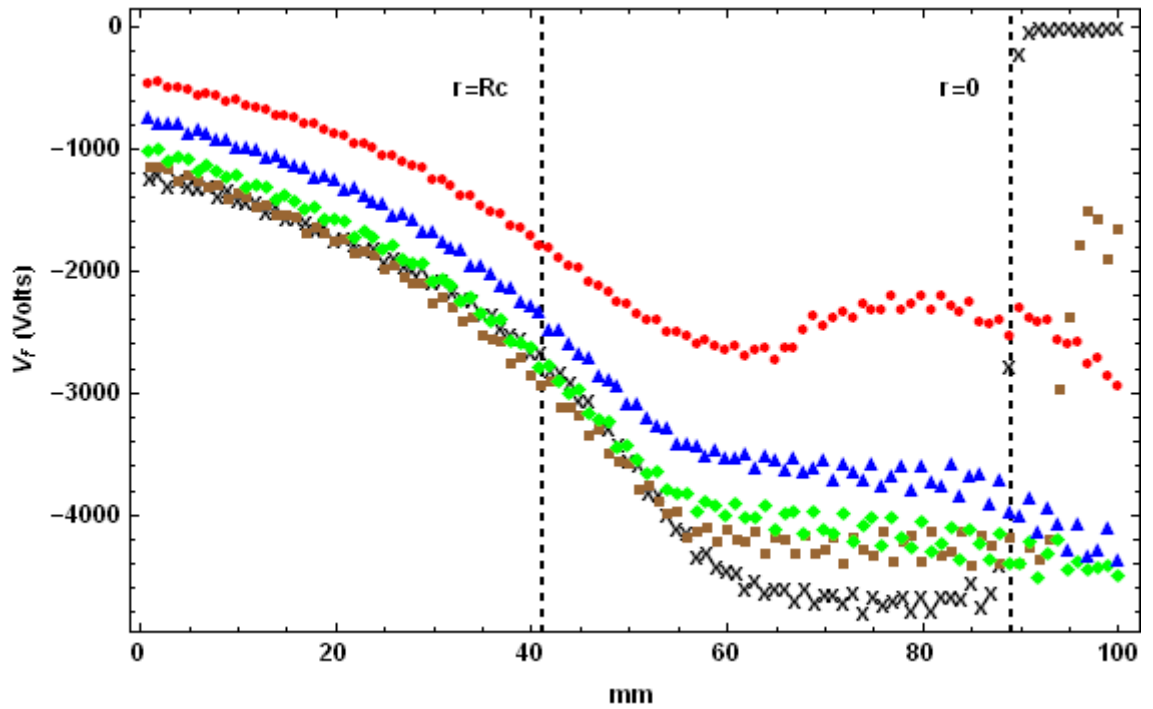


Fig. 97: Radial floating potential profiles,  $V_f(r)$ , for “Jet Mode” cases and some “Star Mode” cases in Table VII. These profiles are indicators of the radial component of the electric field.

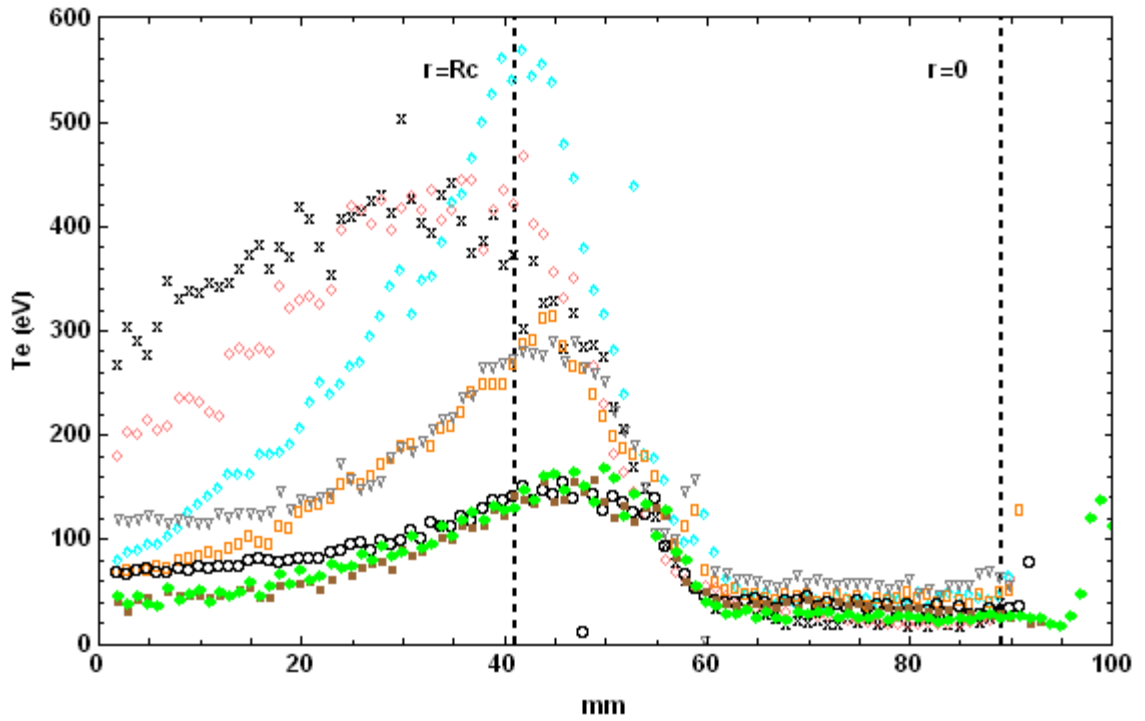


Fig. 98: Radial electron temperature profiles,  $T_e(r)$ , for “Star Mode” cases in Table VII.

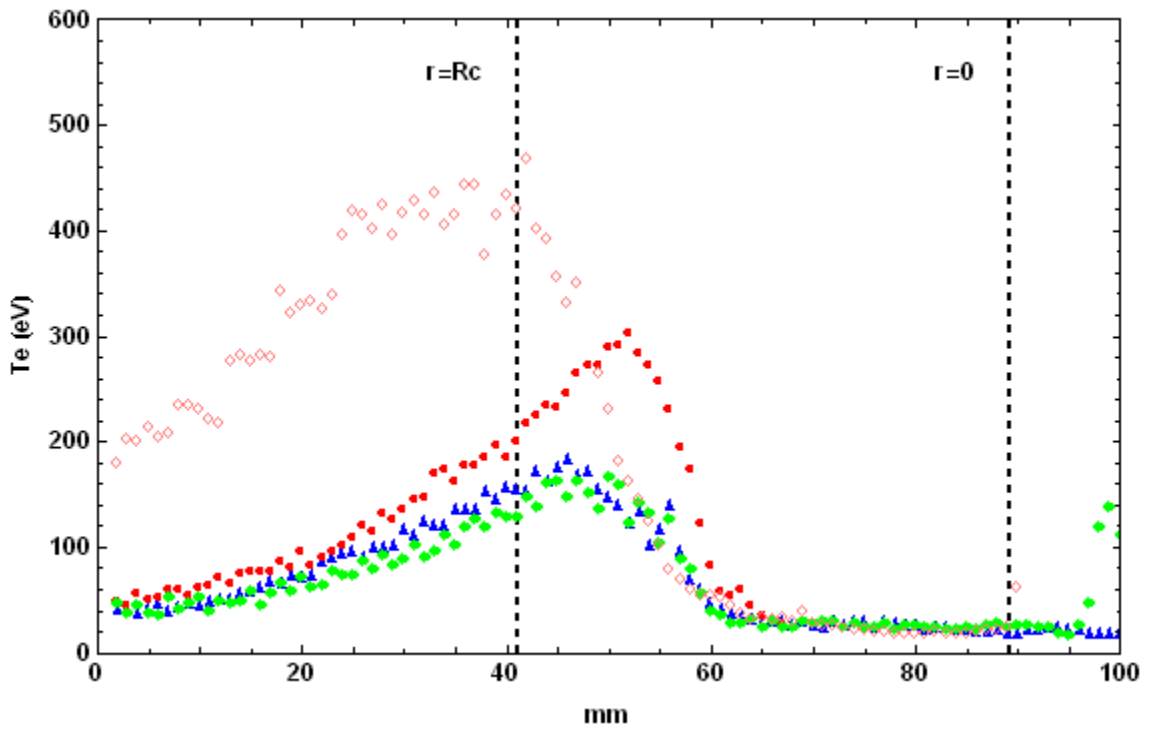


Fig. 99: Radial electron temperature profiles,  $T_e(r)$ , for “Jet Mode” cases and some “Star Mode” cases in Table VII.

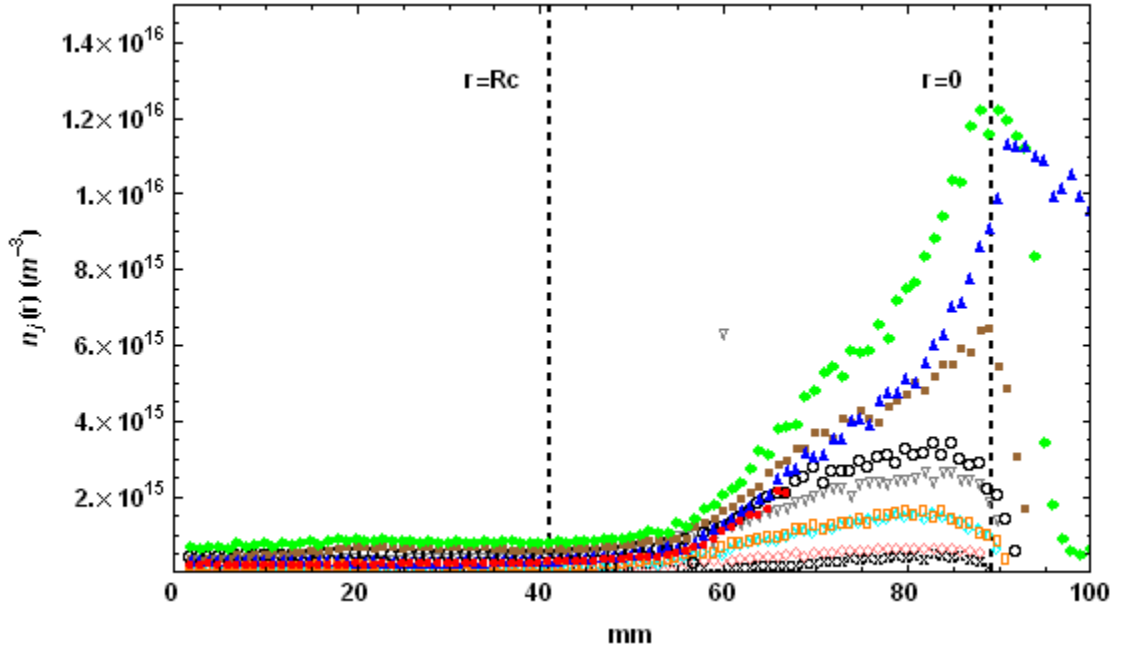


Fig. 100: Linear plot of the radial ion density profiles,  $n_i(r)$ , for all cases in Table VII. This linear representation of the  $n_i(r)$  is provided to emphasize the core region.

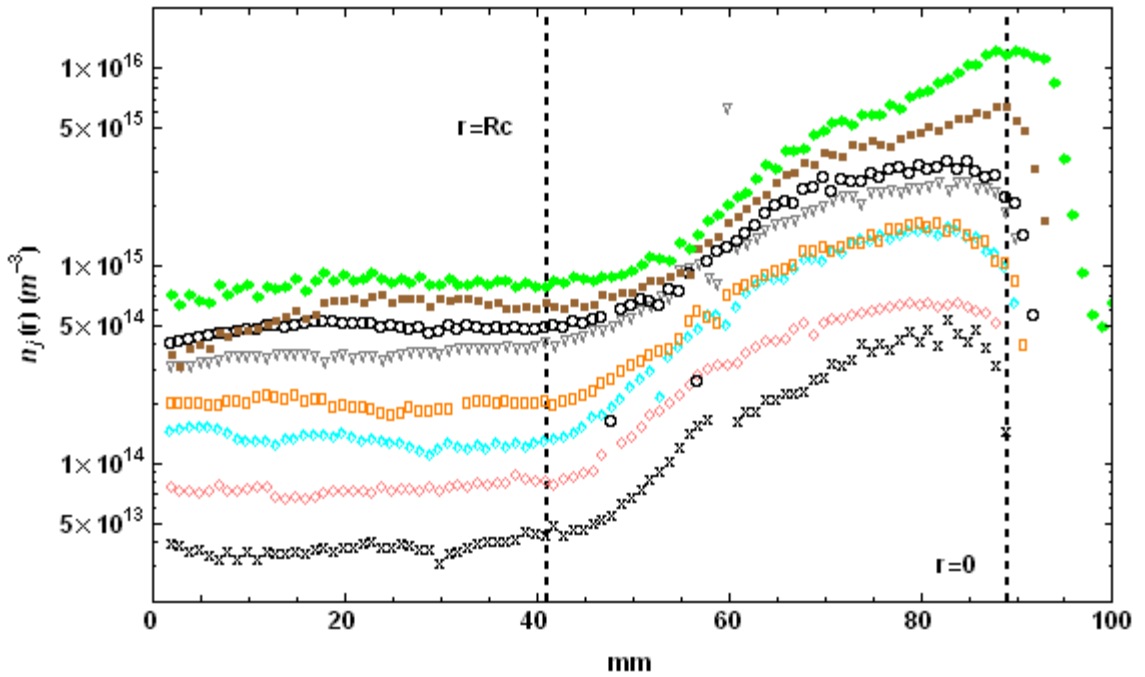


Fig. 101: Logarithmic plot of the radial ion density profiles,  $n_i(r)$ , for “Star Mode” cases in Table VII.

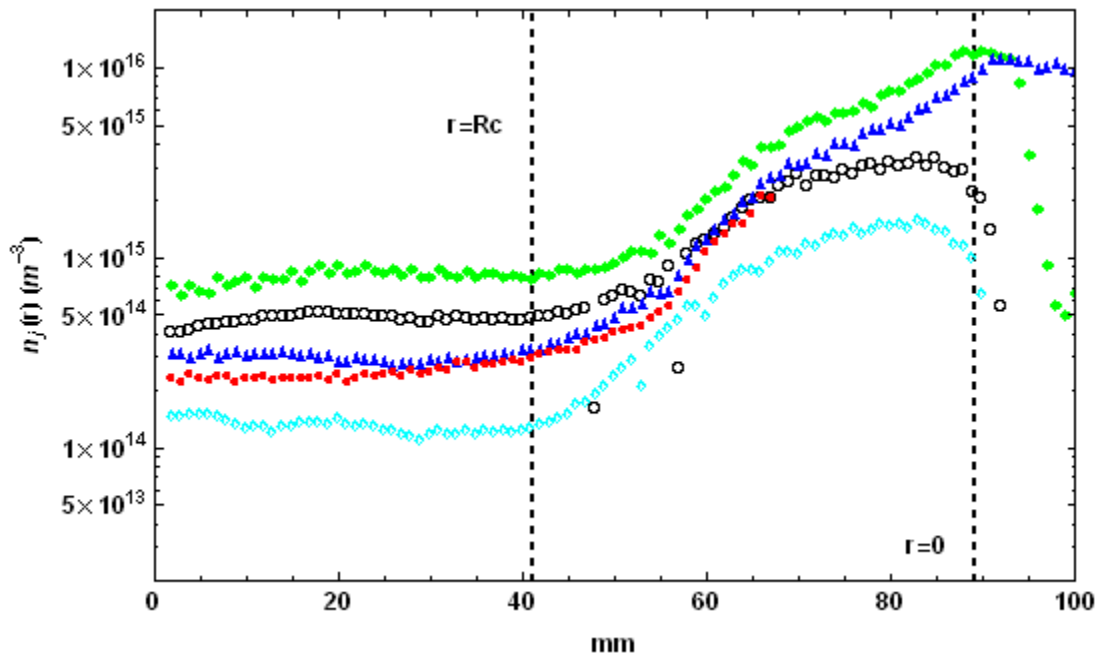


Fig. 102: Logarithmic plot of the radial ion density profiles,  $n_i(r)$ , for “Jet Mode” cases and some “Star Mode” cases in Table VII.

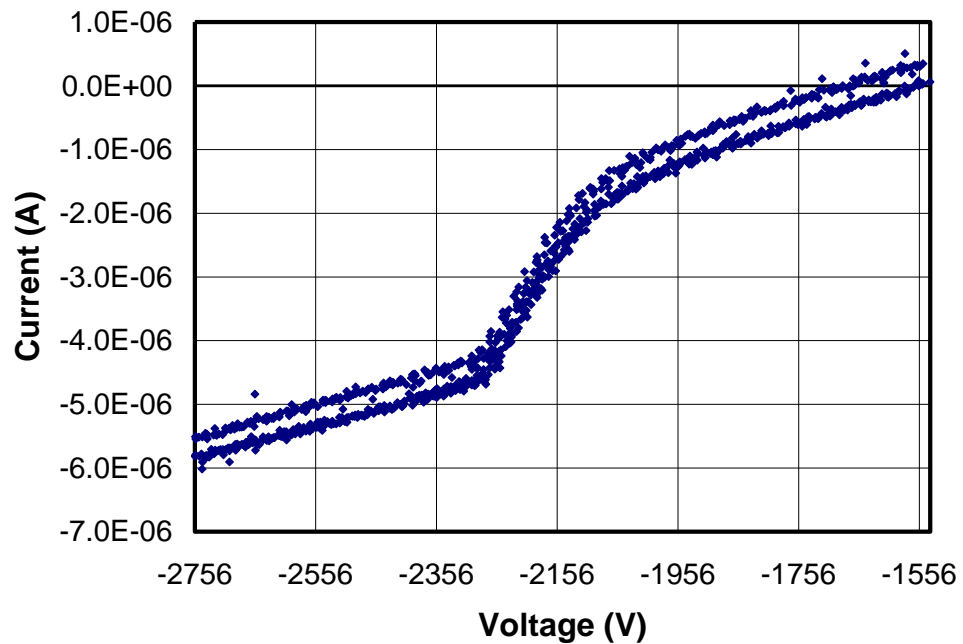


Fig. 103: Single probe I-V curve obtained with single probe s2 inserted into Probe Location 2, as shown in Fig. 46. The trace is obtained at a position  $r = 7$  cm with a cathode radius of 4.7cm. The discharge characteristics for this case are  $V_s = -5.01$  kV,  $I_s = 27.91$  mA and  $P = 2.49$  mA kV<sup>-3/2</sup>.

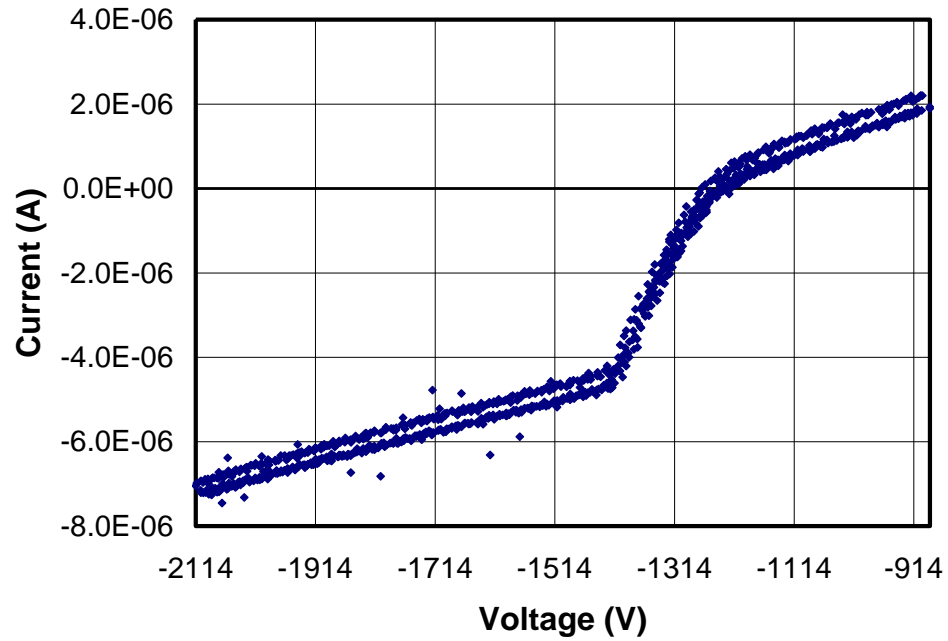


Fig. 104: Single probe I-V curve obtained with single probe s2 inserted into Probe Location 2, as shown in Fig. 46. The trace is obtained at a position  $r = 7$  cm with a cathode radius of 4.7cm. The discharge characteristics for this case are  $V_s = -3.76$  kV,  $I_s = 39.97$  mA and  $P = 5.48$  mA kV<sup>-3/2</sup>.

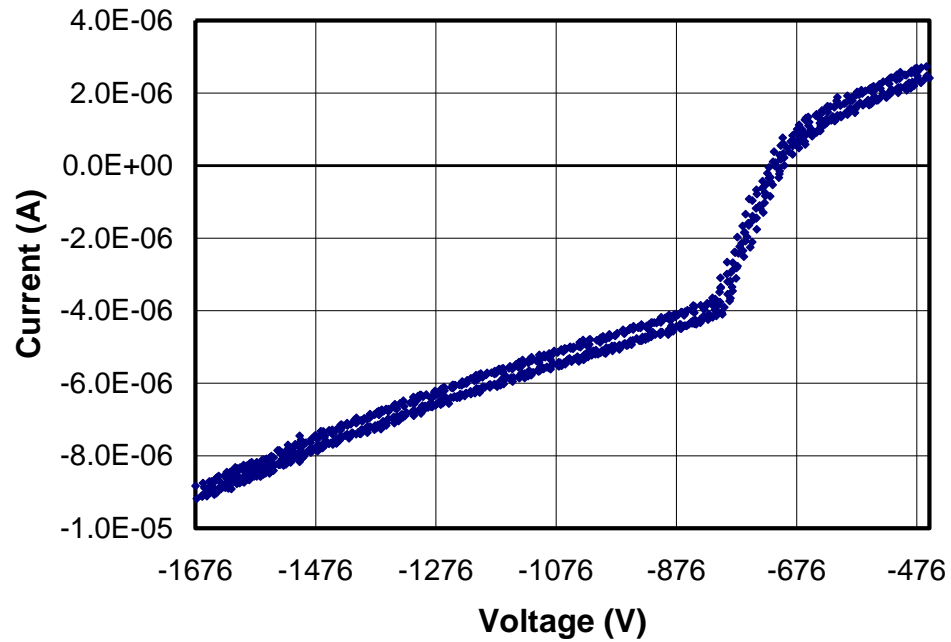


Fig. 105: Single probe I-V curve obtained with single probe s2 inserted into Probe Location 2, as shown in Fig. 46. The trace is obtained at a position  $r = 7$  cm with a cathode radius of 4.7cm. The discharge characteristics for this case are  $V_s = -2.56$  kV,  $I_s = 39.97$  mA and  $P = 9.75$  mA kV<sup>-3/2</sup>.

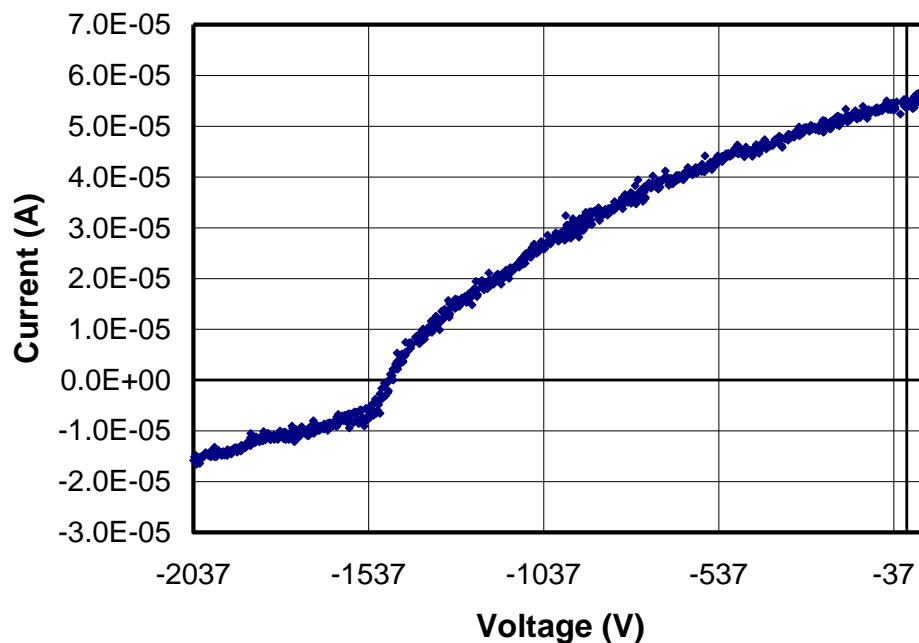


Fig. 106: Single probe I-V curve obtained with disk 1 (nearest the cathode grid wire) of double probe d2 inserted into Probe Location 1, as shown in Fig. 46. The trace is obtained at a position  $r = 8$  cm with a cathode radius of 4.7cm. The discharge characteristics for this case are  $V_s = -5.04$ kV,  $I_s = 13.1$ mA and  $P = 1.16$  mA kV<sup>-3/2</sup>.

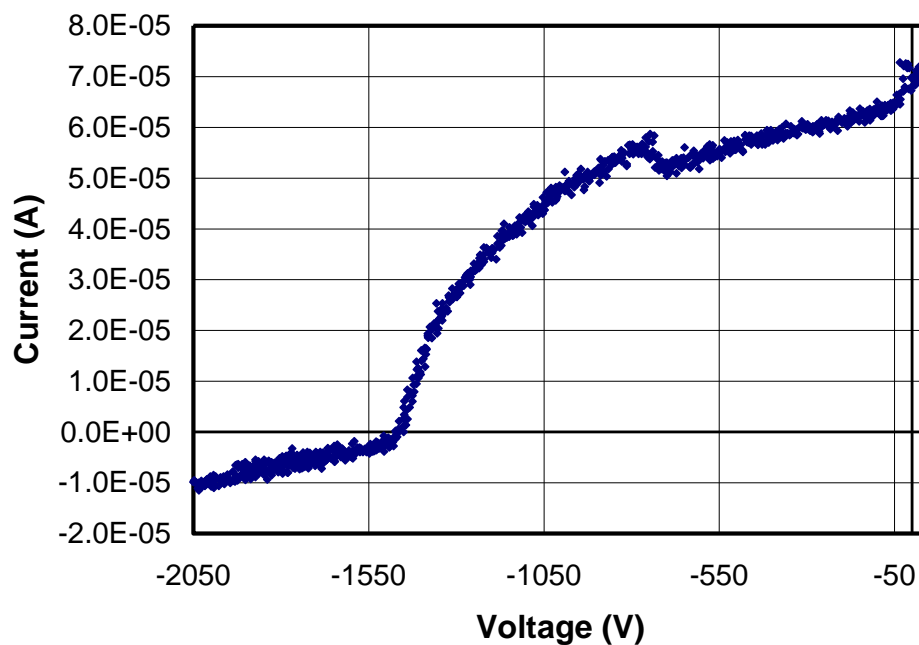


Fig. 107: Single probe I-V curve obtained with disk 2 (farthest from the cathode grid wire) of double probe d2 inserted into Probe Location 1, as shown in Fig. 46. The trace is obtained at a position  $r = 8$  cm with a cathode radius of 4.7cm. The discharge characteristics for this case are  $V_s = -5.04$ kV,  $I_s = 11.52$ mA and  $P = 1.02$  mA kV<sup>-3/2</sup>.

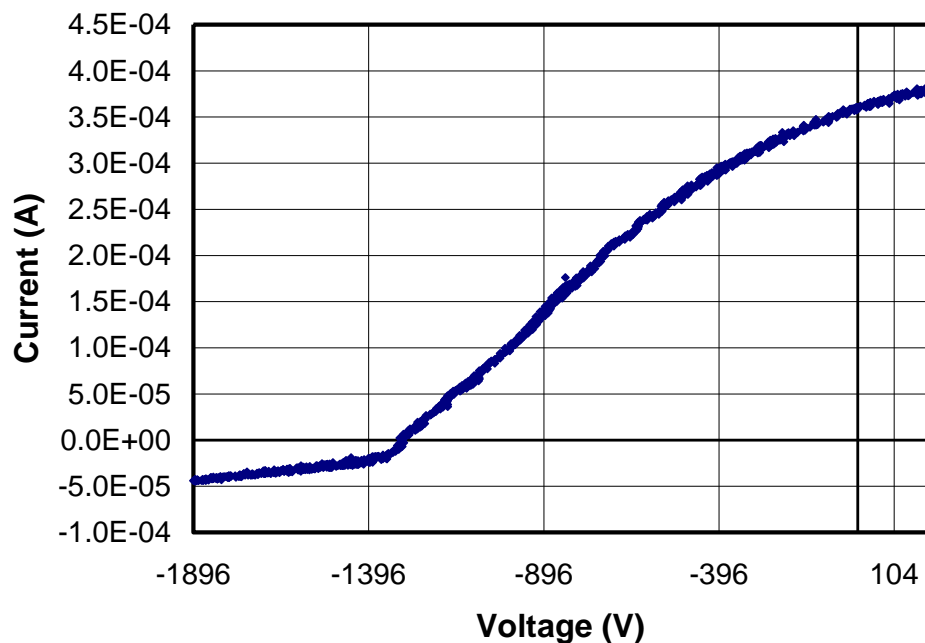


Fig. 108: Single probe I-V curve obtained with disk 1 (nearest the cathode grid wire) of double probe d2 inserted into Probe Location 1, as shown in Fig. 46. The trace is obtained at a position  $r = 8$  cm with a cathode radius of 4.7cm. The discharge characteristics for this case are  $V_s = -5.05$ kV,  $I_s = 28.91$ mA and  $P = 2.55$  mA kV<sup>-3/2</sup>.

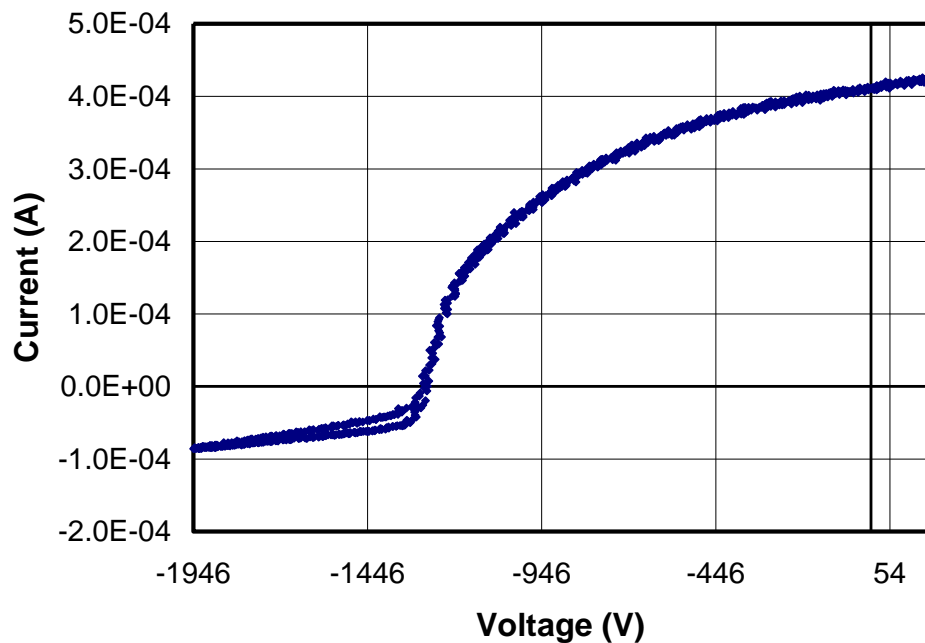


Fig. 109: Single probe I-V curve obtained with disk 2 (farthest from the cathode grid wire) of double probe d2 inserted into Probe Location 1, as shown in Fig. 46. The trace is obtained at a position  $r = 8$  cm with a cathode radius of 4.7cm. The discharge characteristics for this case are  $V_s = -5.04$ kV,  $I_s = 28.33$ mA and  $P = 2.5$  mA kV<sup>-3/2</sup>.

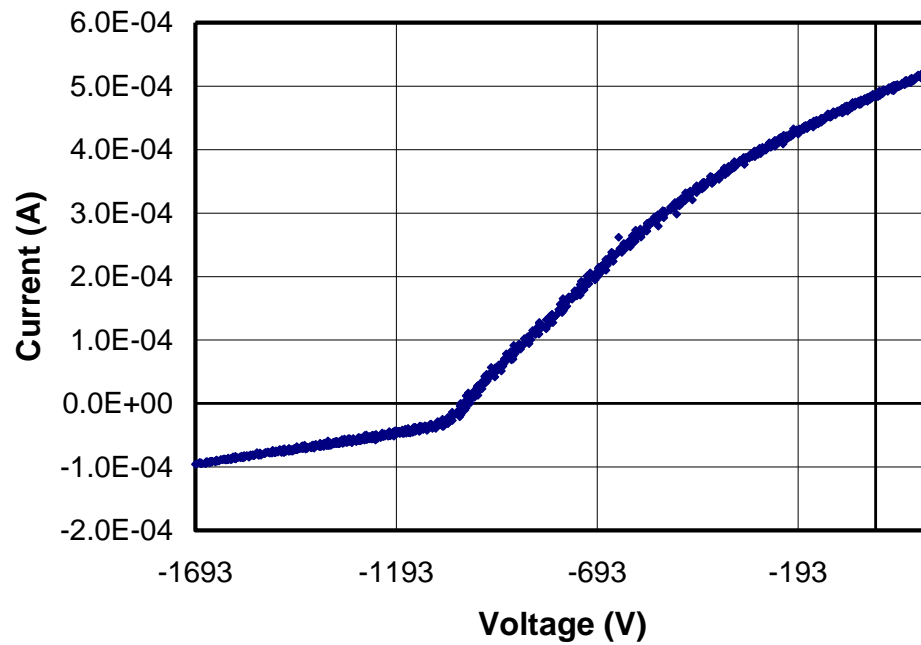


Fig. 110: Single probe I-V curve obtained with disk 1 (nearest the cathode grid wire) of double probe d2 inserted into Probe Location 1, as shown in Fig. 46. The trace is obtained at a position  $r = 8$  cm with a cathode radius of 4.7cm. The discharge characteristics for this case are  $V_s = -4.67$ kV,  $I_s = 39.97$ mA and  $P = 3.96$  mA kV<sup>-3/2</sup>.

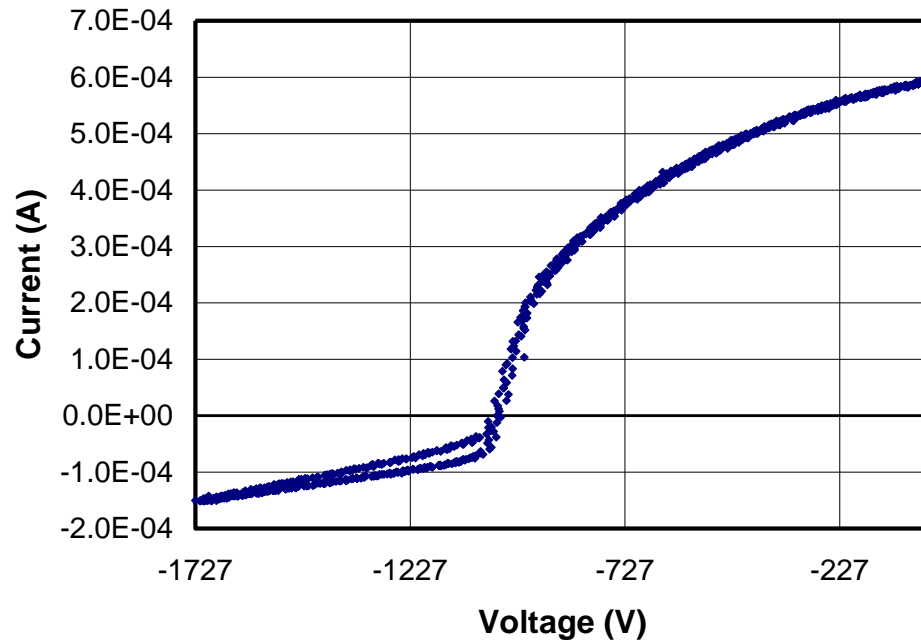


Fig. 111: Single probe I-V curve obtained with disk 2 (farthest from the cathode grid wire) of double probe d2 inserted into Probe Location 1, as shown in Fig. 46. The trace is obtained at a position  $r = 8$  cm with a cathode radius of 4.7cm. The discharge characteristics for this case are  $V_s = -4.7$ kV,  $I_s = 39.97$ mA and  $P = 3.93$  mA kV<sup>-3/2</sup>.

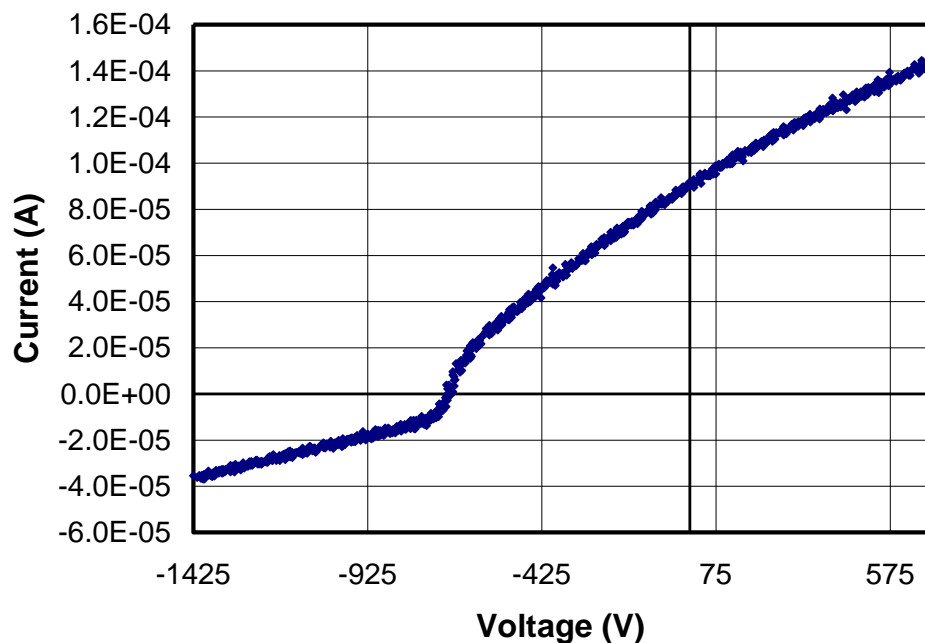


Fig. 112: Single probe I-V curve obtained with disk 1 (nearest the cathode grid wire) of double probe d2 inserted into Probe Location 1, as shown in Fig. 46. The trace is obtained at a position  $r = 8$  cm with a cathode radius of 4.7cm. The discharge characteristics for this case are  $V_s = -3.89$ kV,  $I_s = 39.97$ mA and  $P = 5.21$  mA kV<sup>-3/2</sup>.

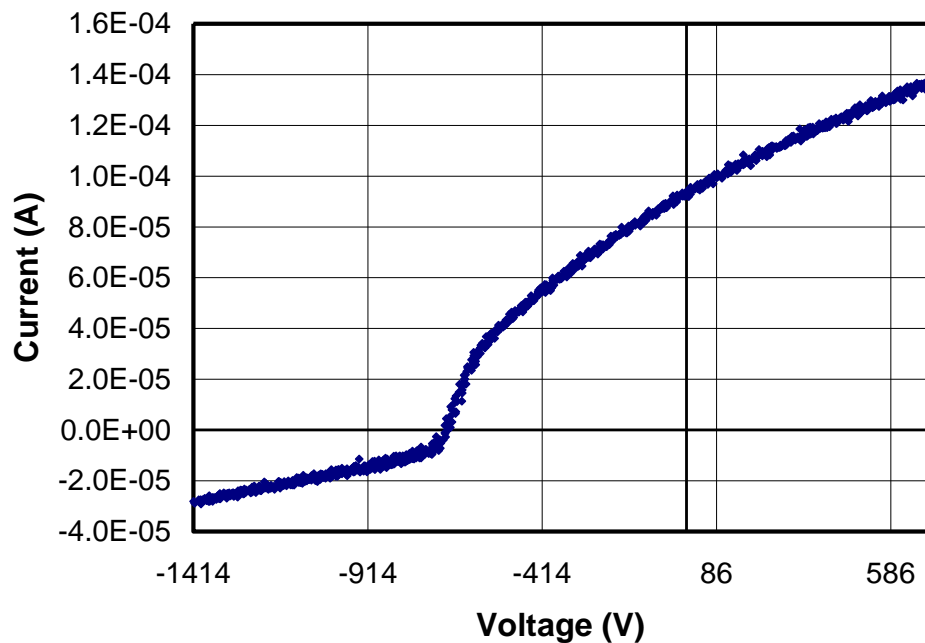


Fig. 113: Single probe I-V curve obtained with disk 2 (farthest from the cathode grid wire) of double probe d2 inserted into Probe Location 1, as shown in Fig. 46. The trace is obtained at a position  $r = 8$  cm with a cathode radius of 4.7cm. The discharge characteristics for this case are  $V_s = -3.89$ kV,  $I_s = 39.97$ mA and  $P = 5.2$  mA kV<sup>-3/2</sup>.

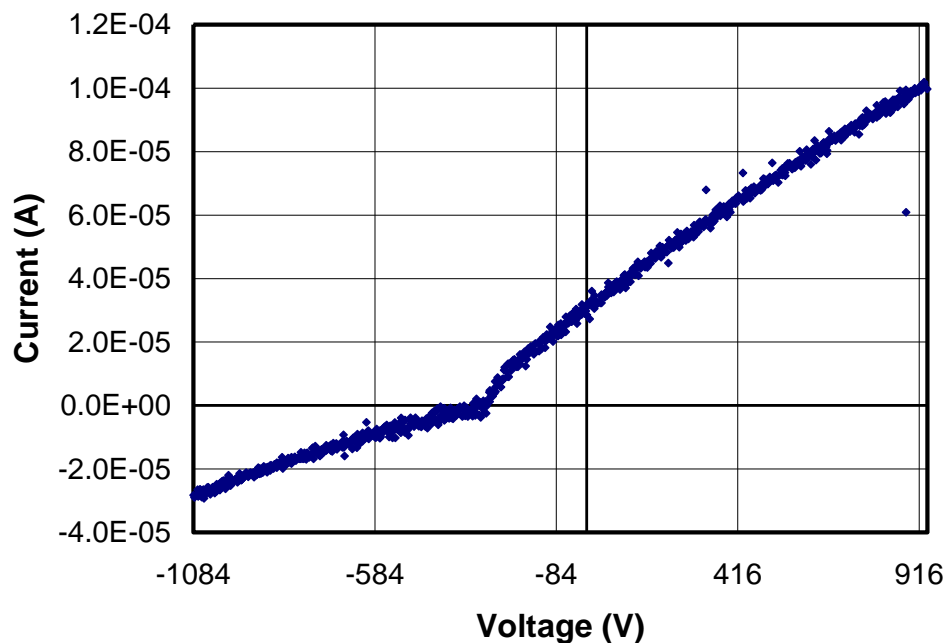


Fig. 114: Single probe I-V curve obtained with disk 1 (nearest the cathode grid wire) of double probe d2 inserted into Probe Location 1, as shown in Fig. 46. The trace is obtained at a position  $r = 8$  cm with a cathode radius of 4.7cm. The discharge characteristics for this case are  $V_s = -2.53$ kV,  $I_s = 39.97$ mA and  $P = 9.96$  mA kV<sup>-3/2</sup>.

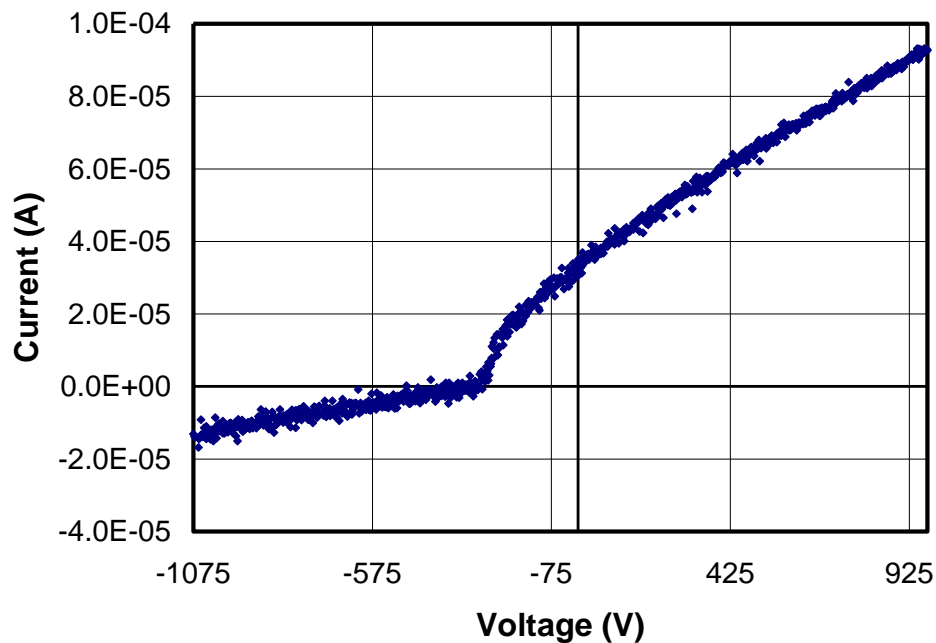


Fig. 115: Single probe I-V curve obtained with disk 2 (farthest from the cathode grid wire) of double probe d2 inserted into Probe Location 1, as shown in Fig. 46. The trace is obtained at a position  $r = 8$  cm with a cathode radius of 4.7cm. The discharge characteristics for this case are  $V_s = -2.55$ kV,  $I_s = 39.97$ mA and  $P = 9.84$  mA kV<sup>-3/2</sup>.

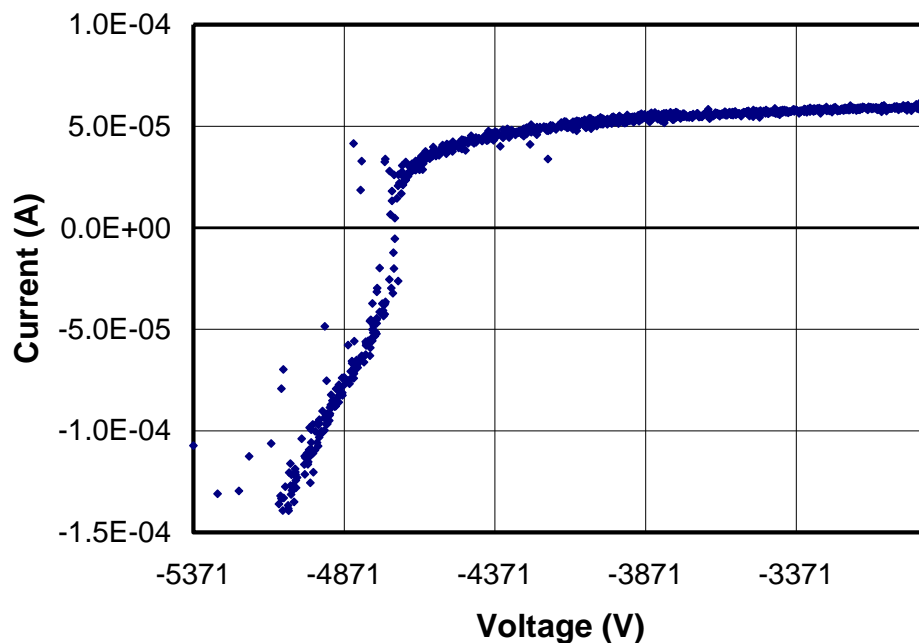


Fig. 116: Single probe I-V characteristic obtained with disk 1 (nearest to cathode grid wire) of probe d2 at Probe Location 1 as indicated in Fig. 46. This curve is obtained at a radial position of  $r = 0$  cm from the center of the device. Discharge charge conditions are  $V_s = -5.04$  kV,  $I_s = 10.5$  mA and  $P = 0.93$  mA kV<sup>-3/2</sup>. The cathode grid radius is  $R_g = 4.7$  cm.

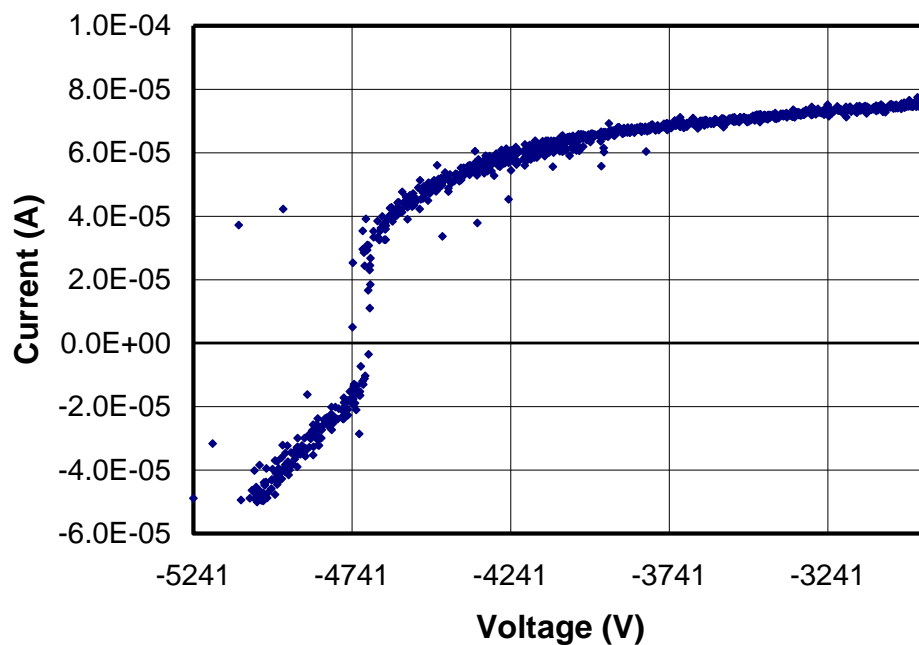


Fig. 117: Single probe I-V characteristic obtained with disk 2 (farthest from the cathode grid wire) of probe d2 at Probe Location 1 as indicated in Fig. 46. This curve is obtained at a radial position of  $r = 0$  cm from the center of the device. Discharge charge conditions are  $V_s = -5.04$  kV,  $I_s = 11.52$  mA and  $P = 1.02$  mA kV<sup>-3/2</sup>. The cathode grid radius is  $R_g = 4.7$  cm.

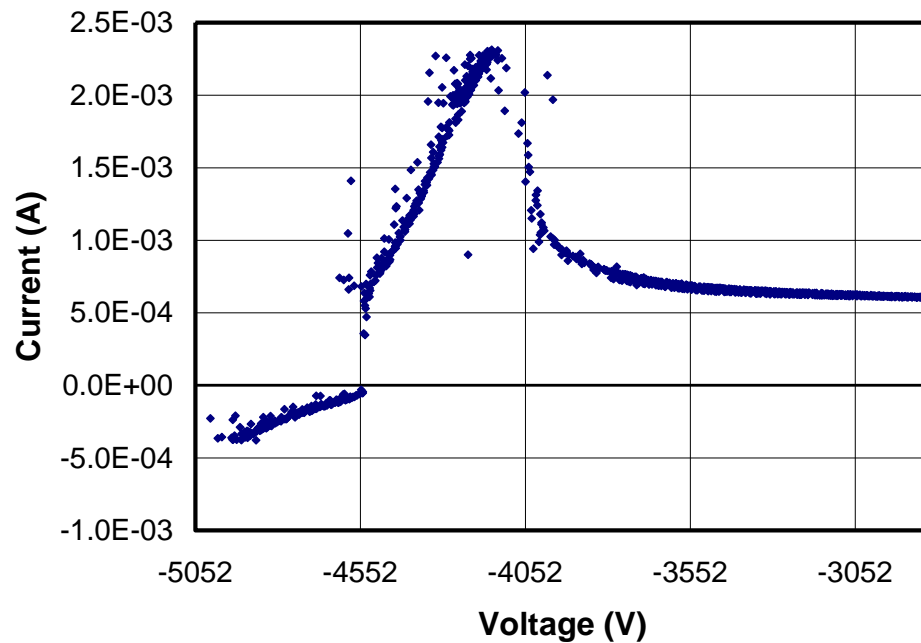


Fig. 118: Single probe I-V characteristic obtained with disk 1 (nearest to cathode grid wire) of probe d2 at Probe Location 1 as indicated in Fig. 46. This curve is obtained at a radial position of  $r = 0.8$  cm from the center of the device. Discharge charge conditions are  $V_s = -5.04$  kV,  $I_s = 10.5$  mA and  $P = 0.93$  mA kV<sup>-3/2</sup>. The cathode grid radius is  $R_g = 4.7$  cm.

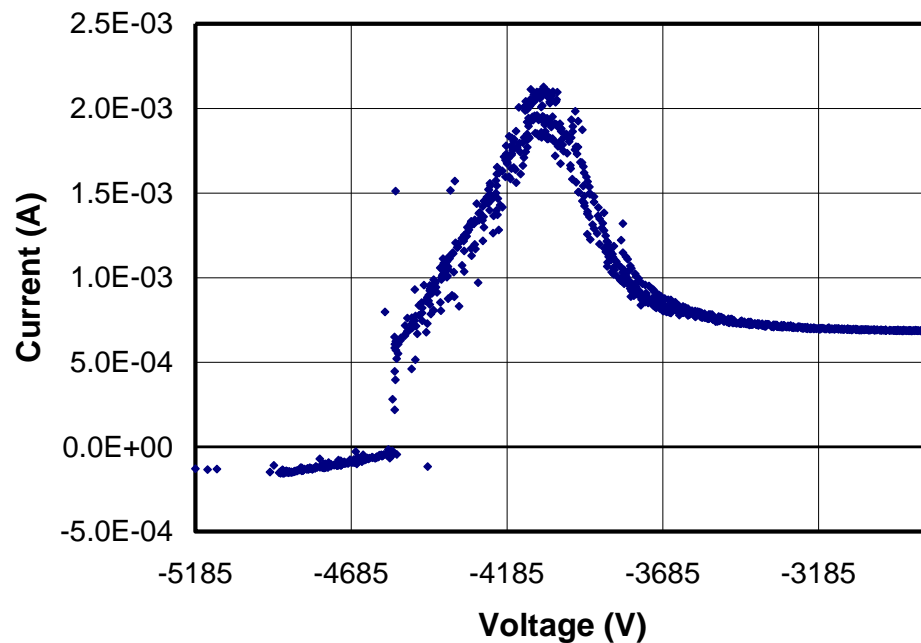


Fig. 119: Single probe I-V characteristic obtained with disk 2 (farthest from the cathode grid wire) of probe d2 at Probe Location 1 as indicated in Fig. 46. This curve is obtained at a radial position of  $r = 0.7$  cm from the center of the device. Discharge charge conditions are  $V_s = -5.04$  kV,  $I_s = 11.52$  mA and  $P = 1.02$  mA kV<sup>-3/2</sup>. The cathode grid radius is  $R_g = 4.7$  cm.

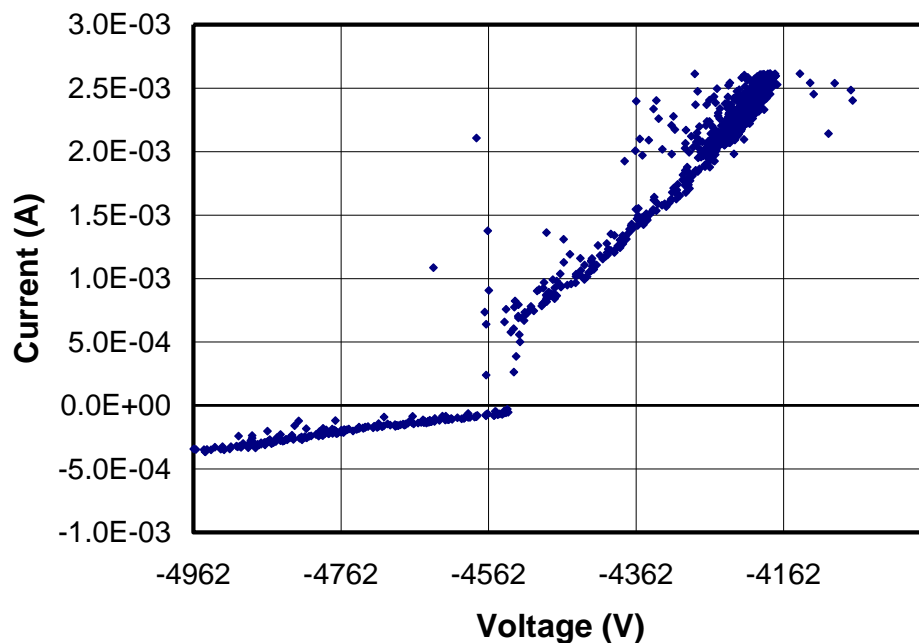


Fig. 120: Single probe I-V characteristic obtained with disk 1 (nearest to cathode grid wire) of probe d2 at Probe Location 1 as indicated in Fig. 46. This curve is obtained at a radial position of  $r = 1.0$  cm from the center of the device. Discharge charge conditions are  $V_s = -5.04$  kV,  $I_s = 10.5$  mA and  $P = 0.93$  mA kV<sup>-3/2</sup>. The cathode grid radius is  $R_g = 4.7$  cm.

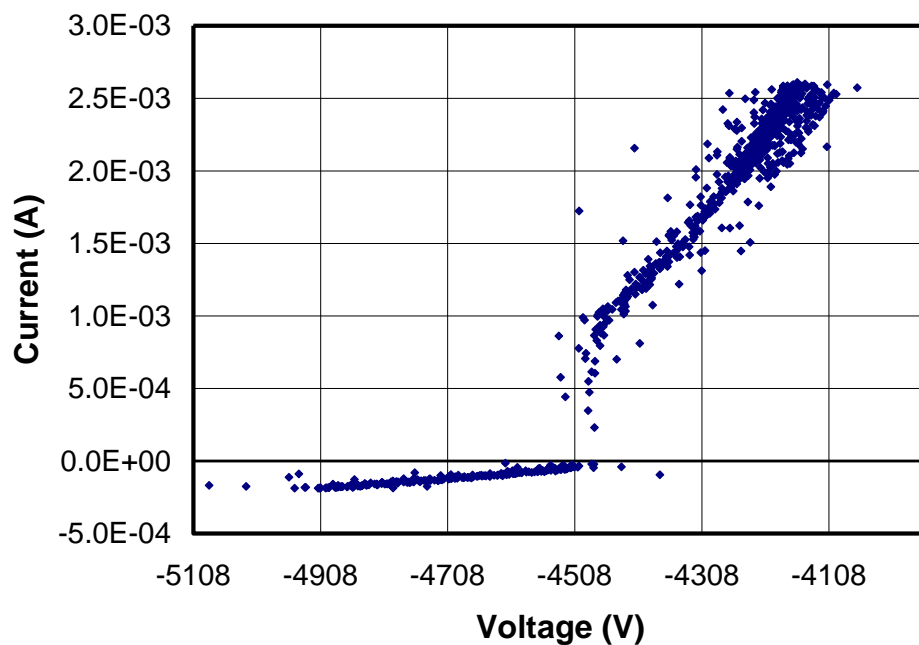


Fig. 121: Single probe I-V characteristic obtained with disk 2 (farthest from the cathode grid wire) of probe d2 at Probe Location 1 as indicated in Fig. 46. This curve is obtained at a radial position of  $r = 1.0$  cm from the center of the device. Discharge charge conditions are  $V_s = -5.04$  kV,  $I_s = 11.52$  mA and  $P = 1.02$  mA kV<sup>-3/2</sup>. The cathode grid radius is  $R_g = 4.7$  cm.

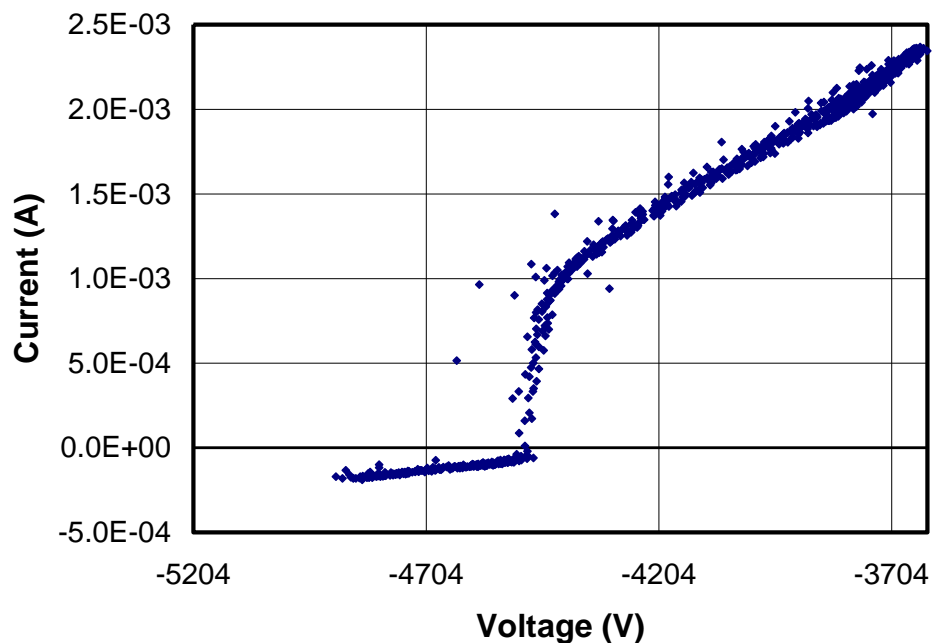


Fig. 122: Single probe I-V characteristic obtained with disk 1 (nearest to cathode grid wire) of probe d2 at Probe Location 1 as indicated in Fig. 46. This curve is obtained at a radial position of  $r = 2.0$  cm from the center of the device. Discharge charge conditions are  $V_s = -5.04$  kV,  $I_s = 10.5$  mA and  $P = 0.93$  mA  $\text{kV}^{-3/2}$ . The cathode grid radius is  $R_g = 4.7$  cm.

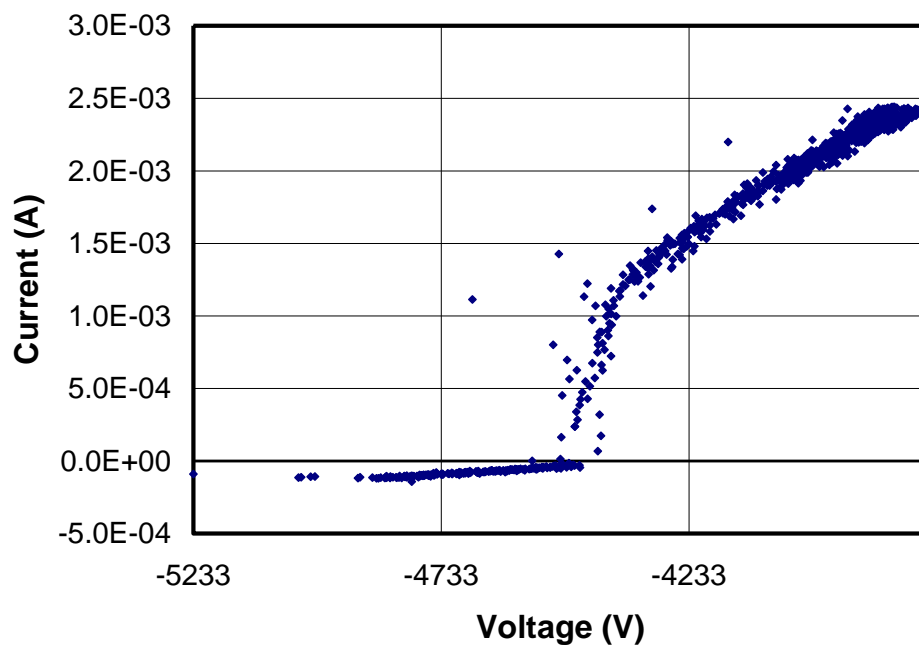


Fig. 123: Single probe I-V characteristic obtained with disk 2 (farthest from the cathode grid) of probe d2 at Probe Location 1 as indicated in Fig. 46. This curve is obtained at a radial position of  $r = 2.0$  cm from the center of the device. Discharge charge conditions are  $V_s = -5.04$  kV,  $I_s = 11.52$  mA and  $P = 1.02$  mA  $\text{kV}^{-3/2}$ . The cathode grid radius is  $R_g = 4.7$  cm.

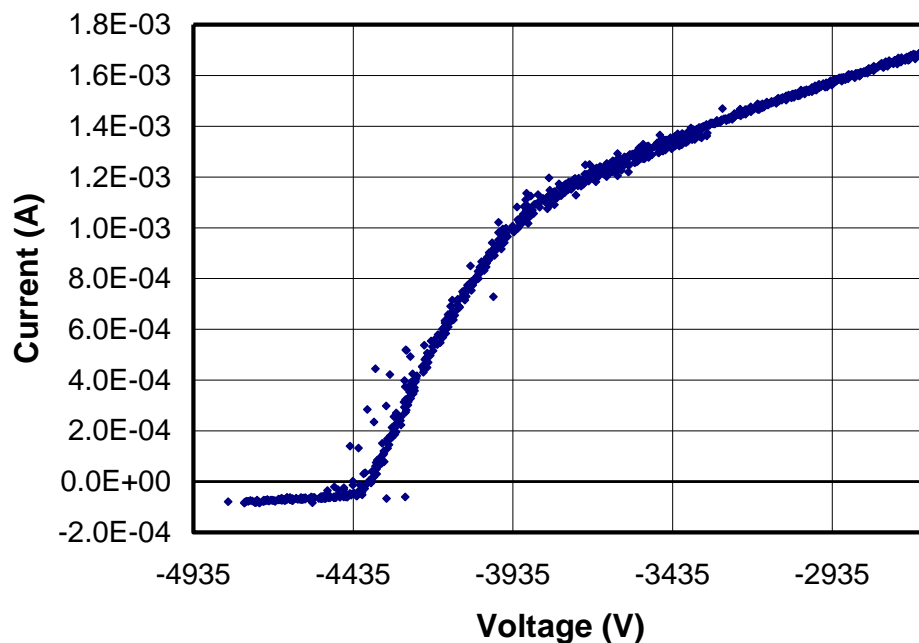


Fig. 124: Single probe I-V characteristic obtained with disk 1 (nearest to cathode grid wire) of probe d2 at Probe Location 1 as indicated in Fig. 46. This curve is obtained at a radial position of  $r = 3.0$  cm from the center of the device. Discharge charge conditions are  $V_s = -5.04$  kV,  $I_s = 10.5$  mA and  $P = 0.93$  mA kV<sup>-3/2</sup>. The cathode grid radius is  $R_g = 4.7$  cm.

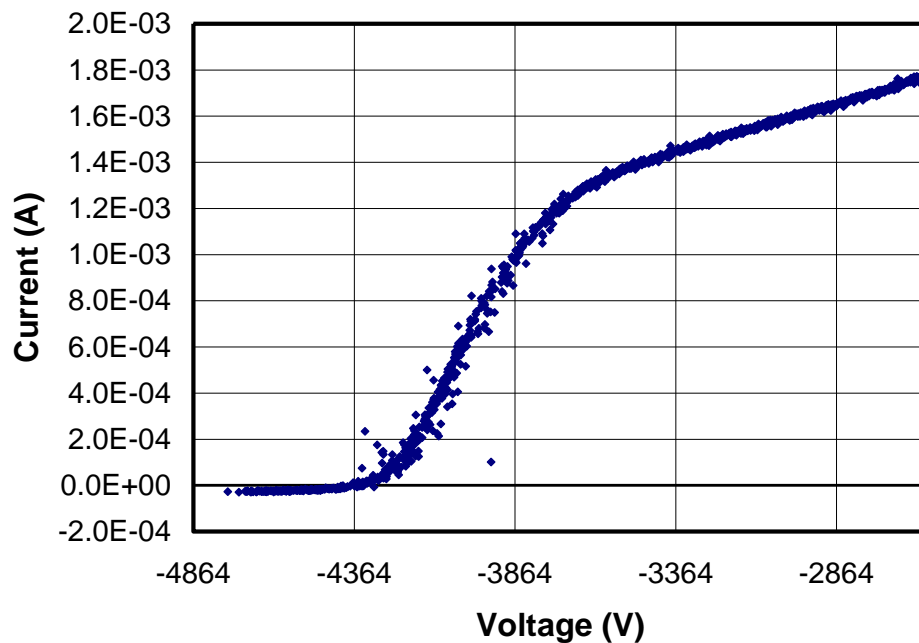


Fig. 125: Single probe I-V characteristic obtained with disk 2 (farthest from the cathode grid wire) of probe d2 at Probe Location 1 as indicated in Fig. 46. This curve is obtained at a radial position of  $r = 3.0$  cm from the center of the device. Discharge charge conditions are  $V_s = -5.04$  kV,  $I_s = 11.52$  mA and  $P = 1.02$  mA kV<sup>-3/2</sup>. The cathode grid radius is  $R_g = 4.7$  cm.

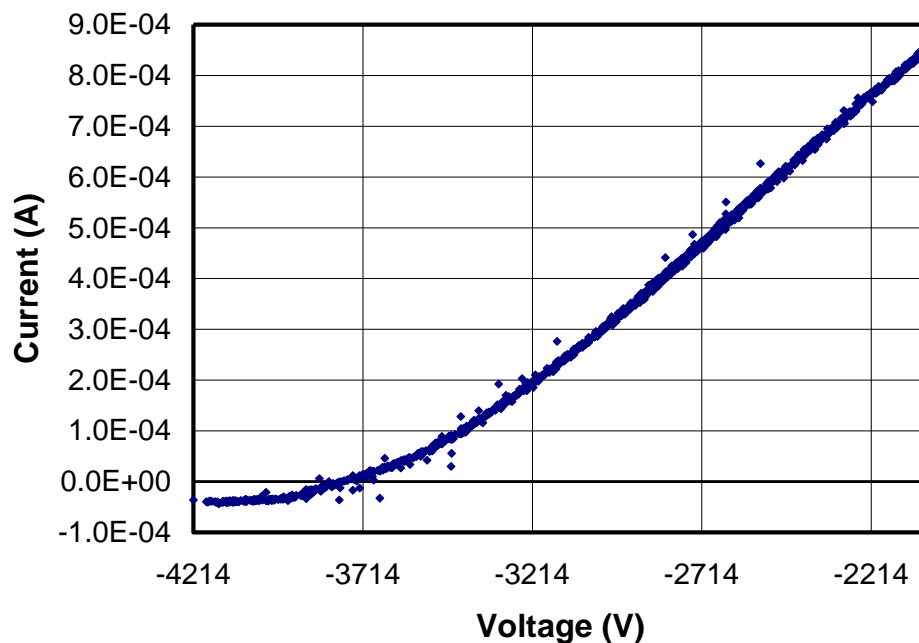


Fig. 126: Single probe I-V characteristic obtained with disk 1 (nearest to cathode grid wire) of probe d2 at Probe Location 1 as indicated in Fig. 46. This curve is obtained at a radial position of  $r = 4.0$  cm from the center of the device. Discharge charge conditions are  $V_s = -5.04$  kV,  $I_s = 10.5$  mA and  $P = 0.93$  mA kV<sup>-3/2</sup>. The cathode grid radius is  $R_g = 4.7$  cm.

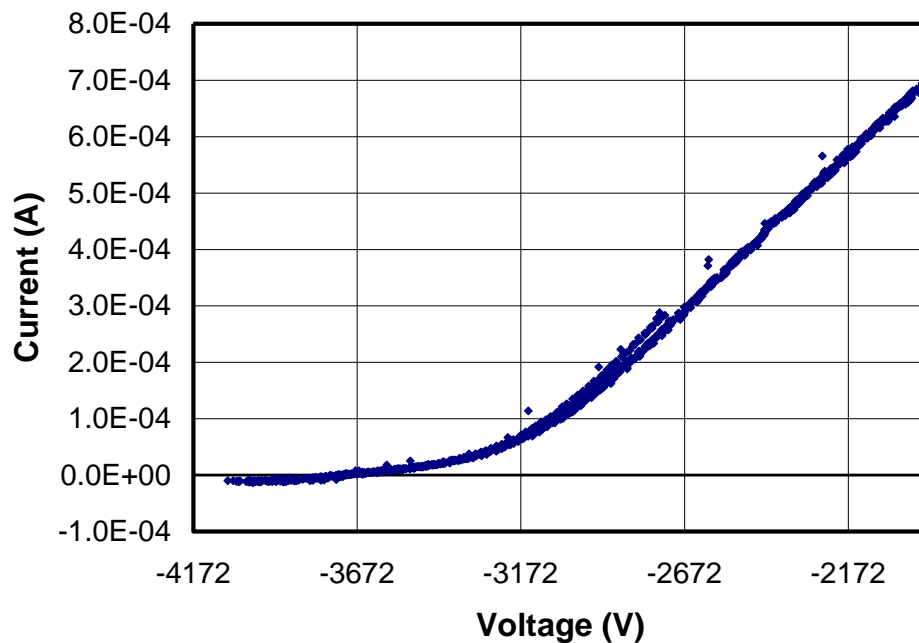


Fig. 127: Single probe I-V characteristic obtained with disk 2 (farthest from the cathode grid wire) of probe d2 at Probe Location 1 as indicated in Fig. 46. This curve is obtained at a radial position of  $r = 4.0$  cm from the center of the device. Discharge charge conditions are  $V_s = -5.04$  kV,  $I_s = 11.52$  mA and  $P = 1.02$  mA kV<sup>-3/2</sup>. The cathode grid radius is  $R_g = 4.7$  cm.

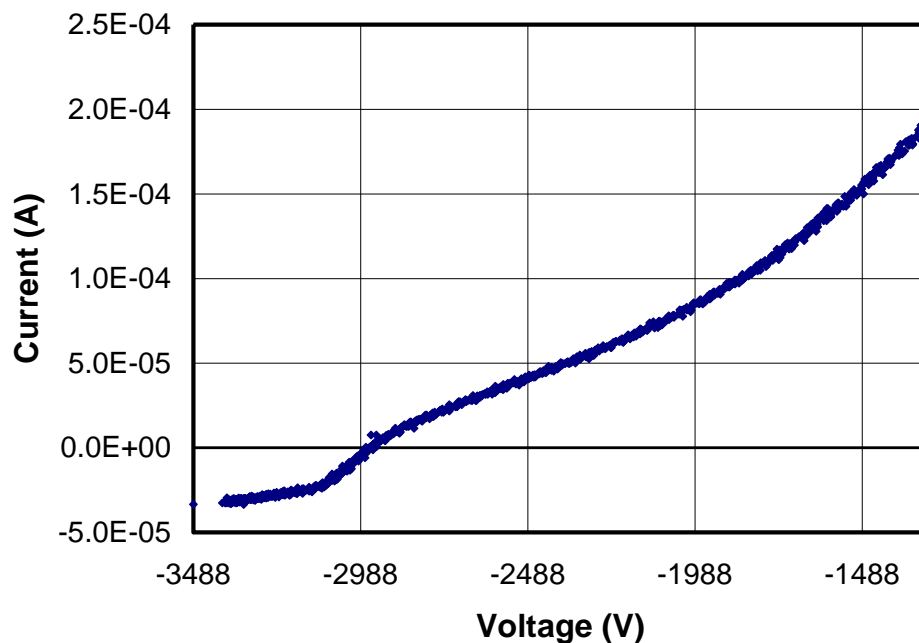


Fig. 128: Single probe I-V characteristic obtained with disk 1 (nearest to cathode grid wire) of probe d2 at Probe Location 1 as indicated in Fig. 46. This curve is obtained at a radial position of  $r = 5.0$  cm from the center of the device. Discharge charge conditions are  $V_s = -5.04$  kV,  $I_s = 10.5$  mA and  $P = 0.93$  mA kV<sup>-3/2</sup>. The cathode grid radius is  $R_g = 4.7$  cm.

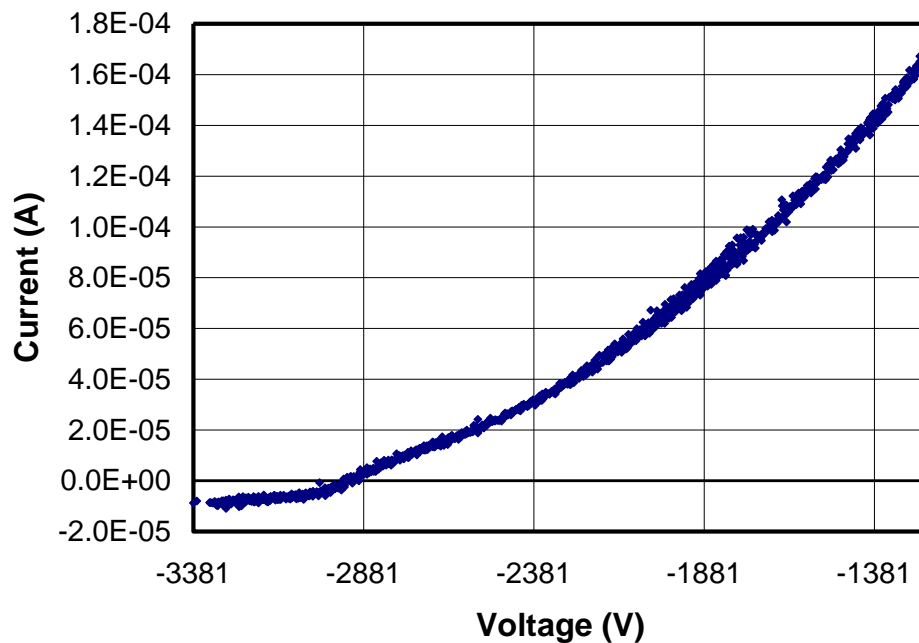


Fig. 129: Single probe I-V characteristic obtained with disk 2 (farthest from the cathode grid wire) of probe d2 at Probe Location 1 as indicated in Fig. 46. This curve is obtained at a radial position of  $r = 5.0$  cm from the center of the device. Discharge charge conditions are  $V_s = -5.04$  kV,  $I_s = 11.52$  mA and  $P = 1.02$  mA kV<sup>-3/2</sup>. The cathode grid radius is  $R_g = 4.7$  cm.

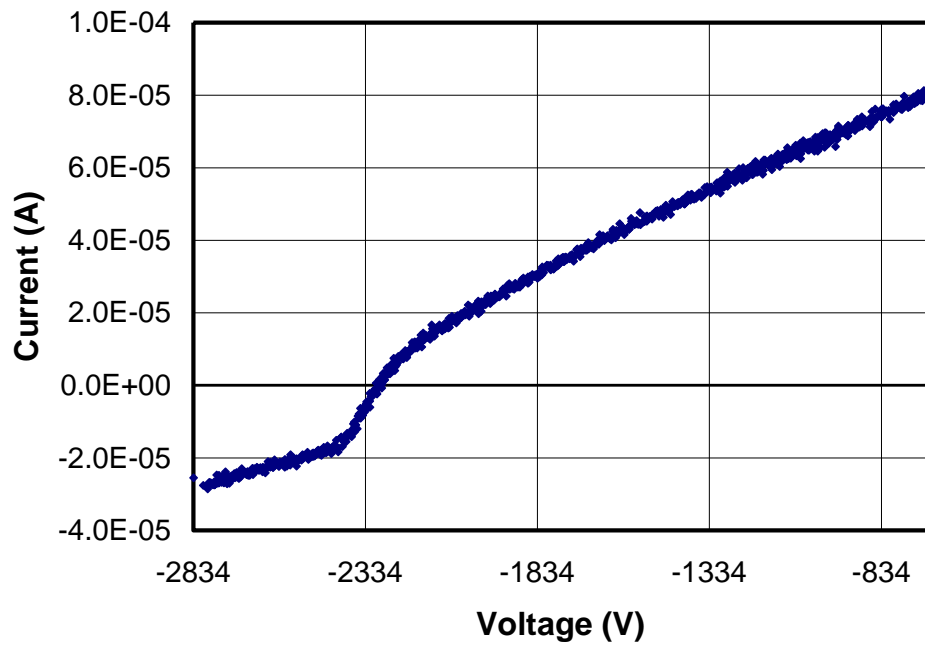


Fig. 130: Single probe I-V characteristic obtained with disk 1 (nearest to cathode grid wire) of probe d2 at Probe Location 1 as indicated in Fig. 46. This curve is obtained at a radial position of  $r = 6.0$  cm from the center of the device. Discharge charge conditions are  $V_s = -5.04$  kV,  $I_s = 10.5$  mA and  $P = 0.93$  mA kV<sup>-3/2</sup>. The cathode grid radius is  $R_g = 4.7$  cm.

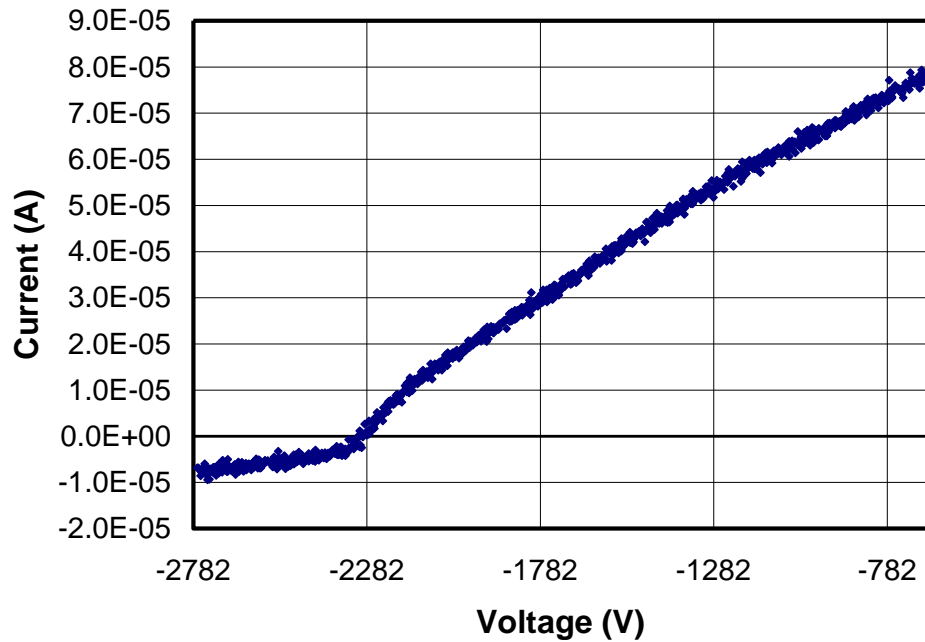


Fig. 131: Single probe I-V characteristic obtained with disk 2 (farthest from the cathode grid wire) of probe d2 at Probe Location 1 as indicated in Fig. 46. This curve is obtained at a radial position of  $r = 6.0$  cm from the center of the device. Discharge charge conditions are  $V_s = -5.04$  kV,  $I_s = 11.52$  mA and  $P = 1.02$  mA kV<sup>-3/2</sup>. The cathode grid radius is  $R_g = 4.7$  cm.

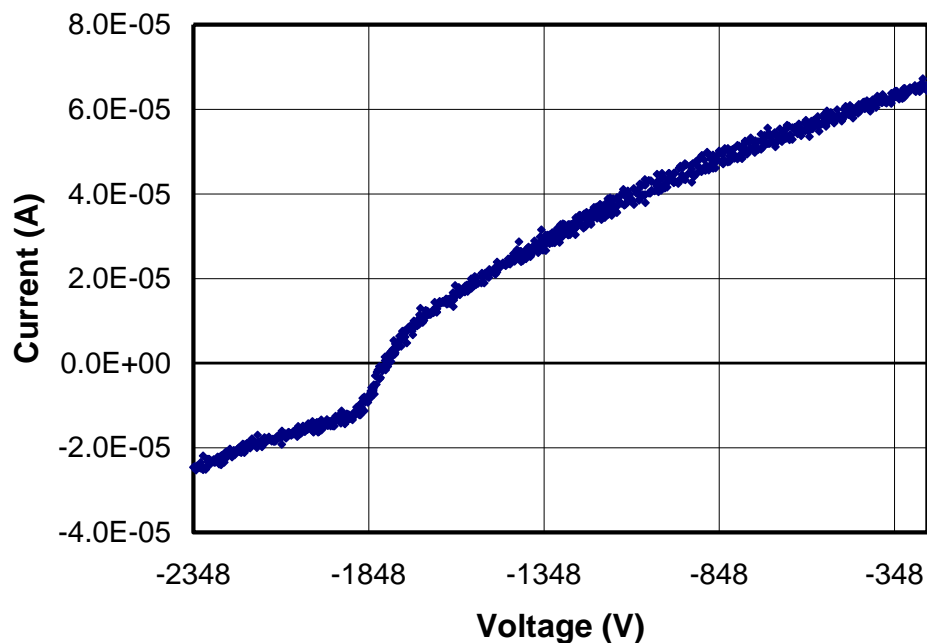


Fig. 132: Single probe I-V characteristic obtained with disk 1 (nearest to cathode grid wire) of probe d2 at Probe Location 1 as indicated in Fig. 46. This curve is obtained at a radial position of  $r = 7.0$  cm from the center of the device. Discharge charge conditions are  $V_s = -5.04$  kV,  $I_s = 10.5$  mA and  $P = 0.93$  mA kV<sup>-3/2</sup>. The cathode grid radius is  $R_g = 4.7$  cm.

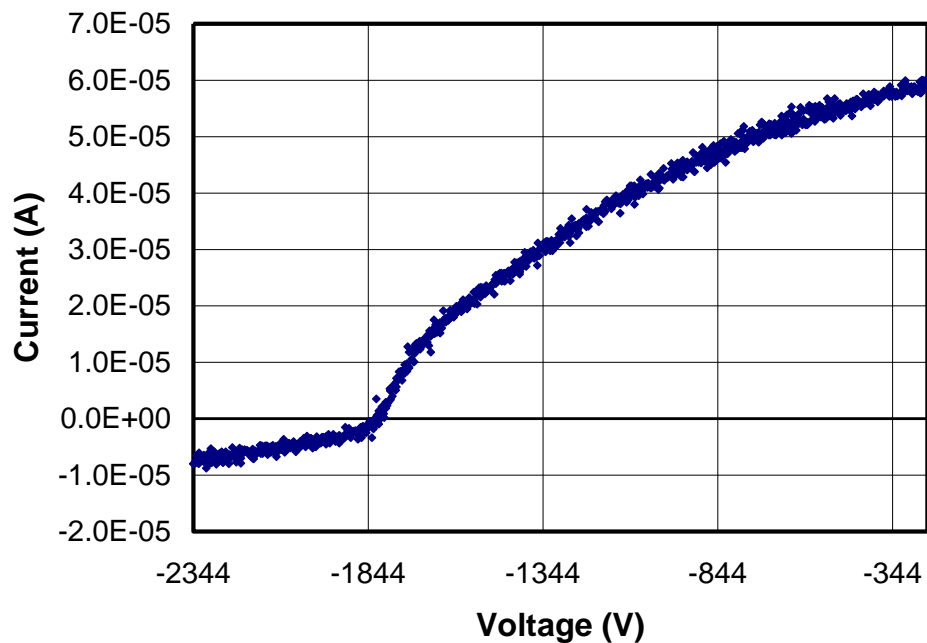


Fig. 133: Single probe I-V characteristic obtained with disk 2 (farthest from the grid wire) of probe d2 at Probe Location 1 as indicated in Fig. 46. This curve is obtained at a radial position of  $r = 7.0$  cm from the center of the device. Discharge charge conditions are  $V_s = -5.04$  kV,  $I_s = 11.52$  mA and  $P = 1.02$  mA kV<sup>-3/2</sup>. The cathode grid radius is  $R_g = 4.7$  cm.

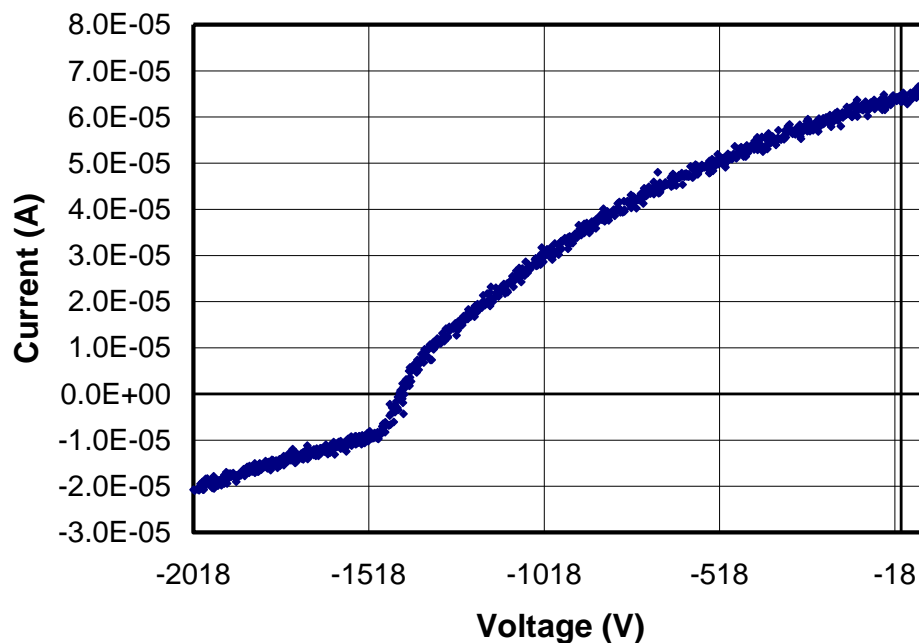


Fig. 134: Single probe I-V characteristic obtained with disk 1 (nearest to cathode grid wire) of probe d2 at Probe Location 1 as indicated in Fig. 46. This curve is obtained at a radial position of  $r = 8.0$  cm from the center of the device. Discharge charge conditions are  $V_s = -5.04$  kV,  $I_s = 10.5$  mA and  $P = 0.93$  mA kV<sup>-3/2</sup>. The cathode grid radius is  $R_g = 4.7$  cm.

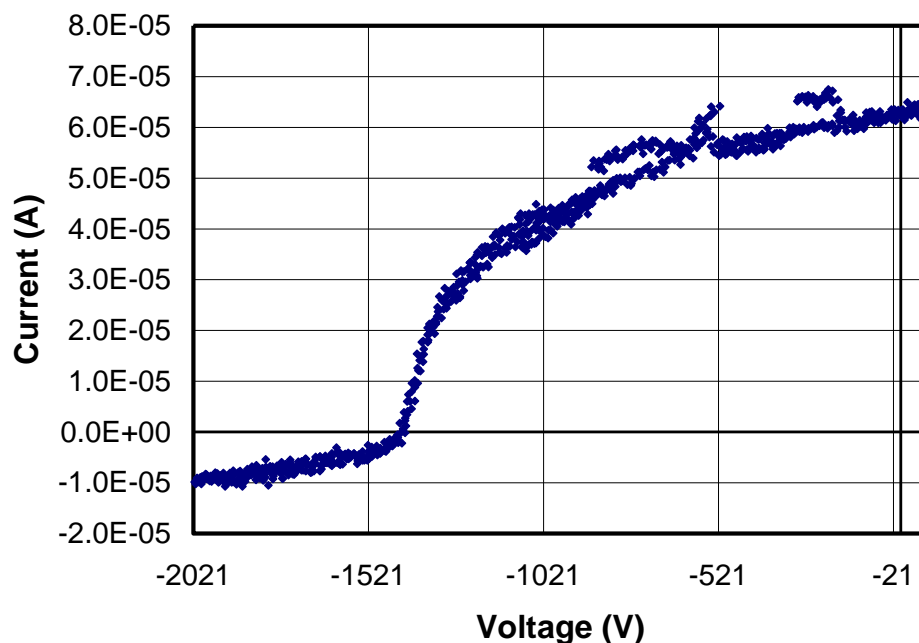


Fig. 135: Single probe I-V characteristic obtained with disk 2 (farthest from the cathode grid wire) of probe d2 at Probe Location 1 as indicated in Fig. 46. This curve is obtained at a radial position of  $r = 8.0$  cm from the center of the device. Discharge charge conditions are  $V_s = -5.04$  kV,  $I_s = 11.52$  mA and  $P = 1.02$  mA kV<sup>-3/2</sup>. The cathode grid radius is  $R_g = 4.7$  cm.

Table VIII: Legend for electron density,  $n_e$ , and electron temperature,  $T_e$ , measurements obtained from single probe investigations.

#		$V_s$ (kV)	$I_s$ (mA)	$P$ (mA kV $^{-3f^2}$ )	Mode	Disk
1	●	-5.03	3.58	0.32	Star Mode	2
2	■	-5.03	4.19	0.37	Star Mode	1
3	▲	-5.04	10.50	0.93	Star Mode	1
4	▼	-5.04	11.52	1.02	Star Mode	2
5	◆	-4.70	39.97	3.93	Star Mode	2
6	■	-4.67	39.97	3.96	Star Mode	1
7	●	-3.98	39.97	5.20	Jet Mode	2
8	♣	-3.08	39.97	7.41	Jet Mode	1
9	♠	-2.53	39.97	9.96	Jet Mode	1

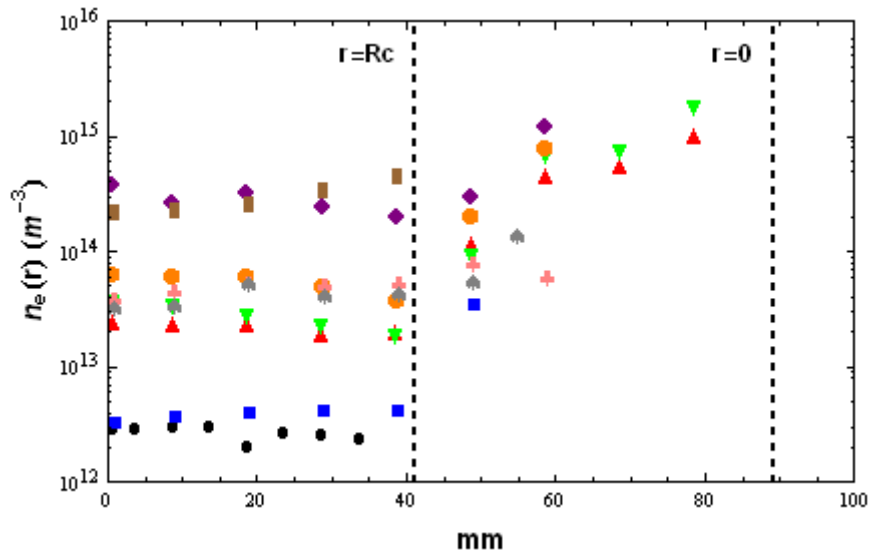


Fig. 136: Portions of electron density profiles,  $n_e(r)$ , for several discharge conditions listed in Table VIII.

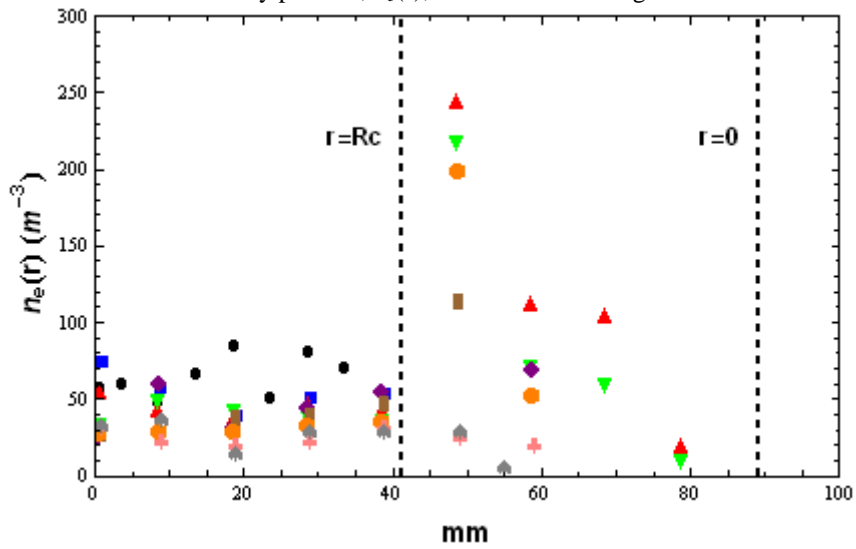


Fig. 137: Portions of electron temperature profiles,  $T_e(r)$ , for several discharge conditions listed in Table VIII.

Table IX: Legend for probe shadowing data collected with double probe d1 inserted into Probe Location 1 as indicated in Fig. 46.

#		$V_s$ (kV)	$I_s$ (mA)	$P$ (mA kV <sup>-3/2</sup> )	Mode
1	■	-5.04	1.51	0.13	Star Mode
2	●	-5.06	5.22	0.46	Star Mode
3	▲	-5.06	5.42	0.48	Star Mode
4	▼	-5.09	9.92	0.87	Star Mode
5	◆	-5.10	11.65	1.01	Star Mode
6	♣	-5.12	14.76	1.28	Star Mode
7	♠	-5.12	17.35	1.49	Star Mode
8	★	-5.17	23.93	2.03	Star Mode
9	□	-5.21	31.17	2.62	Star Mode
10	○	-5.21	31.96	2.69	Star Mode
11	△	-5.08	34.62	3.02	Star Mode
12	▽	-4.85	37.92	3.54	Star Mode
13	◇	-4.72	39.19	3.82	Star Mode

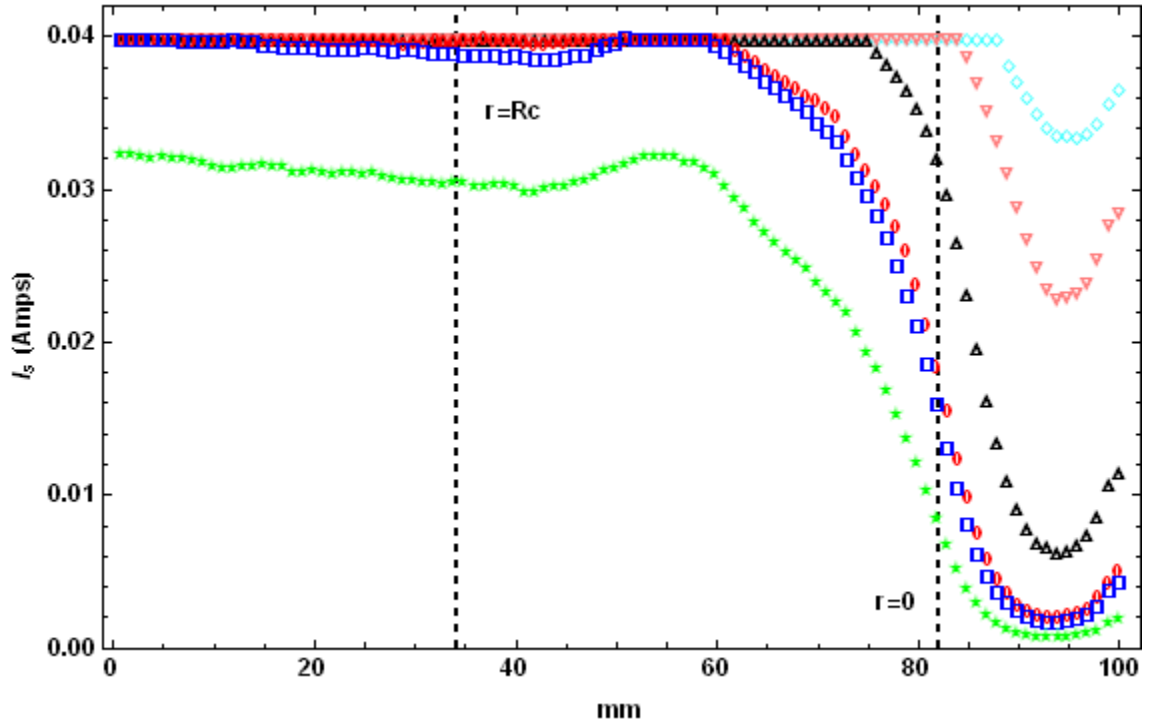


Fig. 138: Measurements of the power supply current,  $I_s$ , are plotted as a function of radius to indicate the shadowing effect of a probe as it is inserted into the center of a GD IXL SIEC device. These plots are for cases  $P = 2.03, 2.62, 2.69, 3.02, 3.54,$  and  $3.82 \text{ mA kV}^{-3/2}$ . The legend for this plot is provided in Table IX.

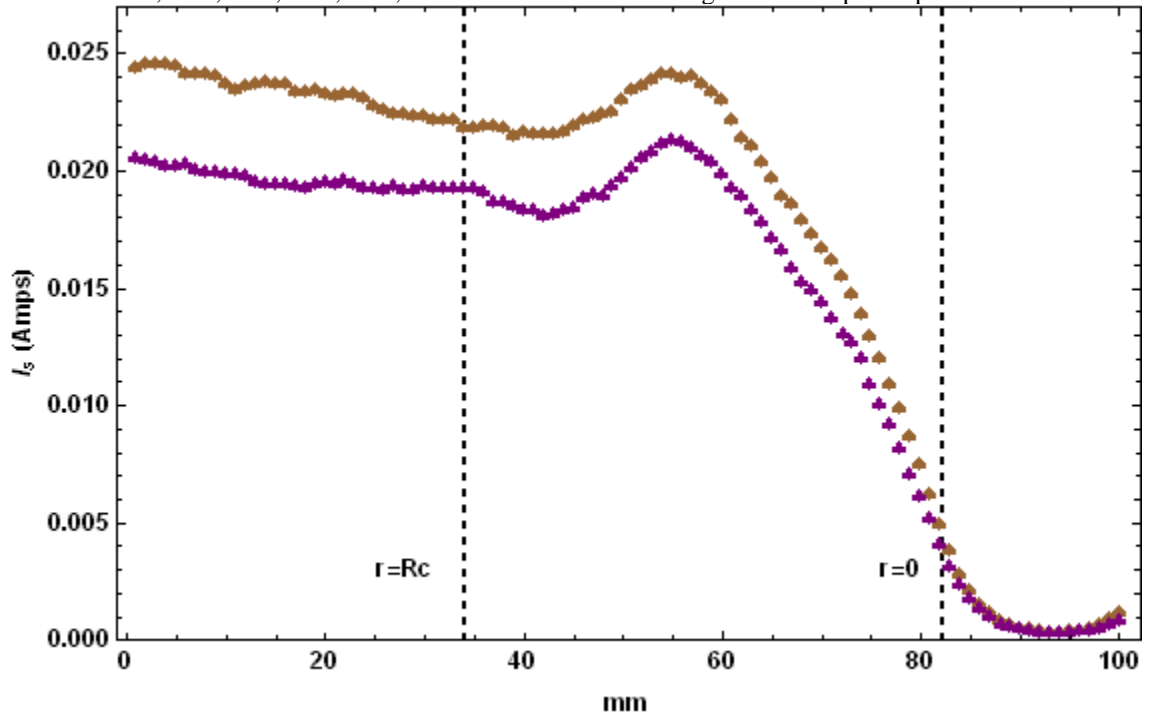


Fig. 139: Measurements of the power supply current,  $I_s$ , are plotted as a function of radius to indicate the shadowing effect of a probe as it is inserted into the center of a GD IXL SIEC device. These plots are for cases  $P = 1.28$  and  $1.49 \text{ mA kV}^{-3/2}$ . The legend for this plot is provided in Table IX.

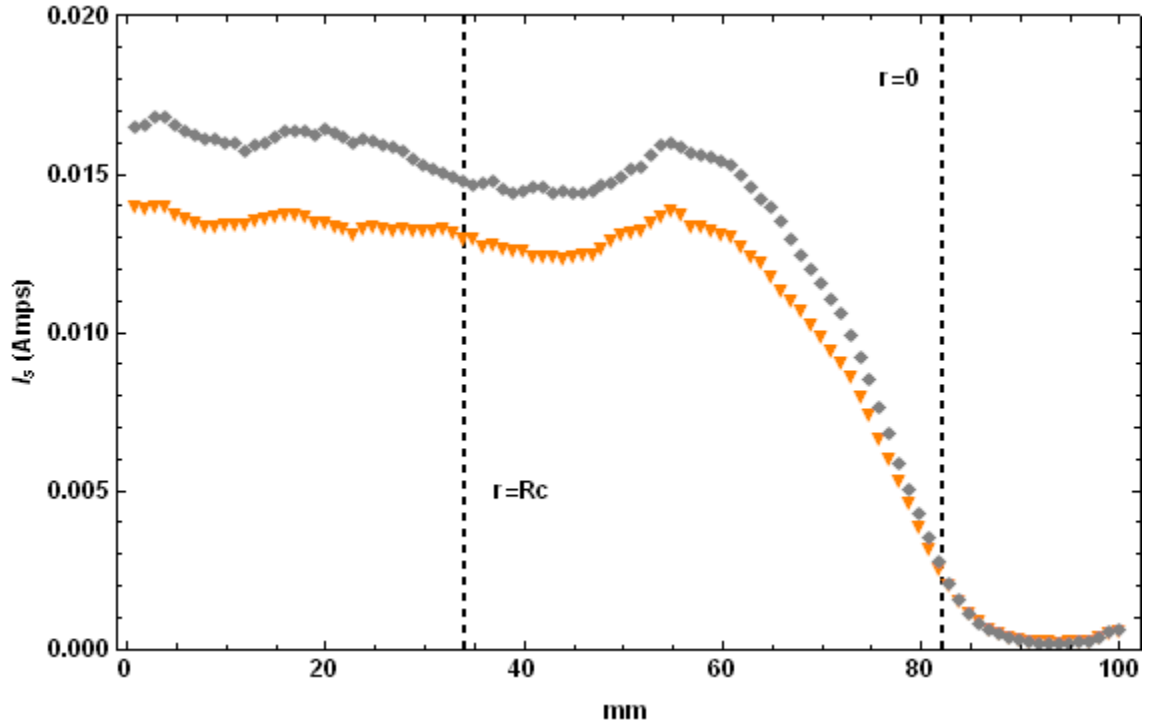


Fig. 140: Measurements of the power supply current,  $I_s$ , are plotted as a function of radius to indicate the shadowing effect of a probe as it is inserted into the center of a GD IXL SIEC device. These plots are for cases  $P = 0.87$  and  $1.01 \text{ mA kV}^{-3/2}$ . The legend for this plot is provided in Table IX.

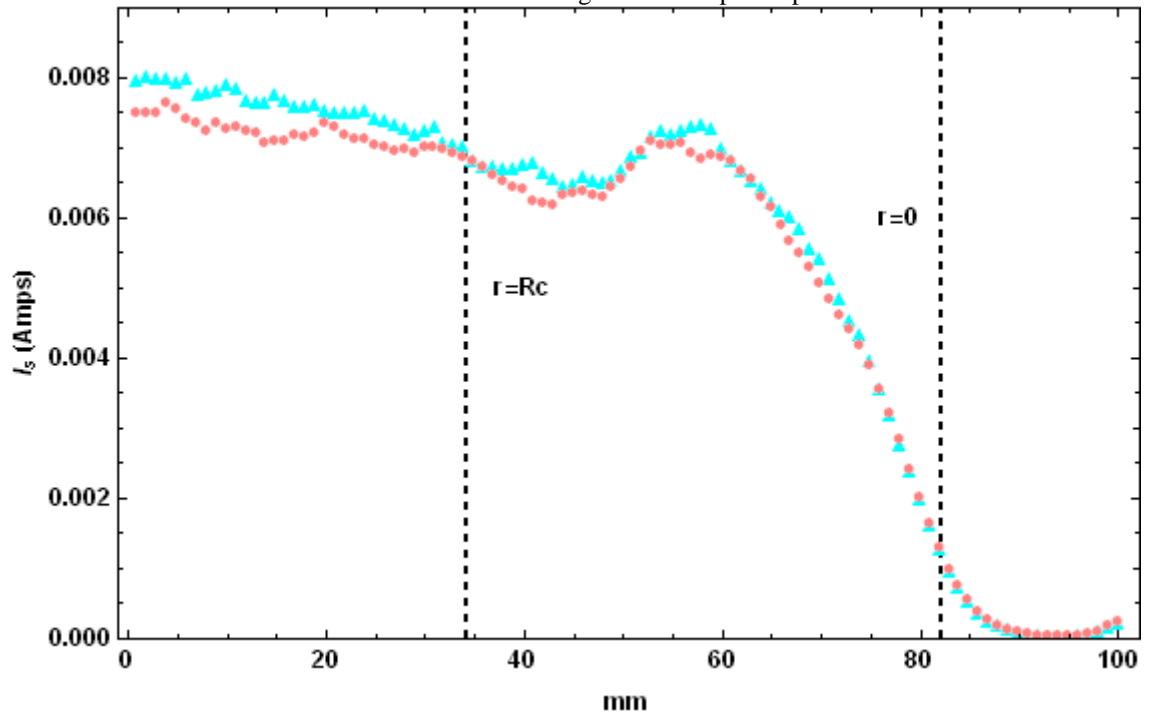


Fig. 141: Measurements of the power supply current,  $I_s$ , are plotted as a function of radius to indicate the shadowing effect of a probe as it is inserted into the center of a GD IXL SIEC device. These plots are for cases  $P = 0.46$  and  $0.48 \text{ mA kV}^{-3/2}$ . The legend for this plot is provided in Table IX.

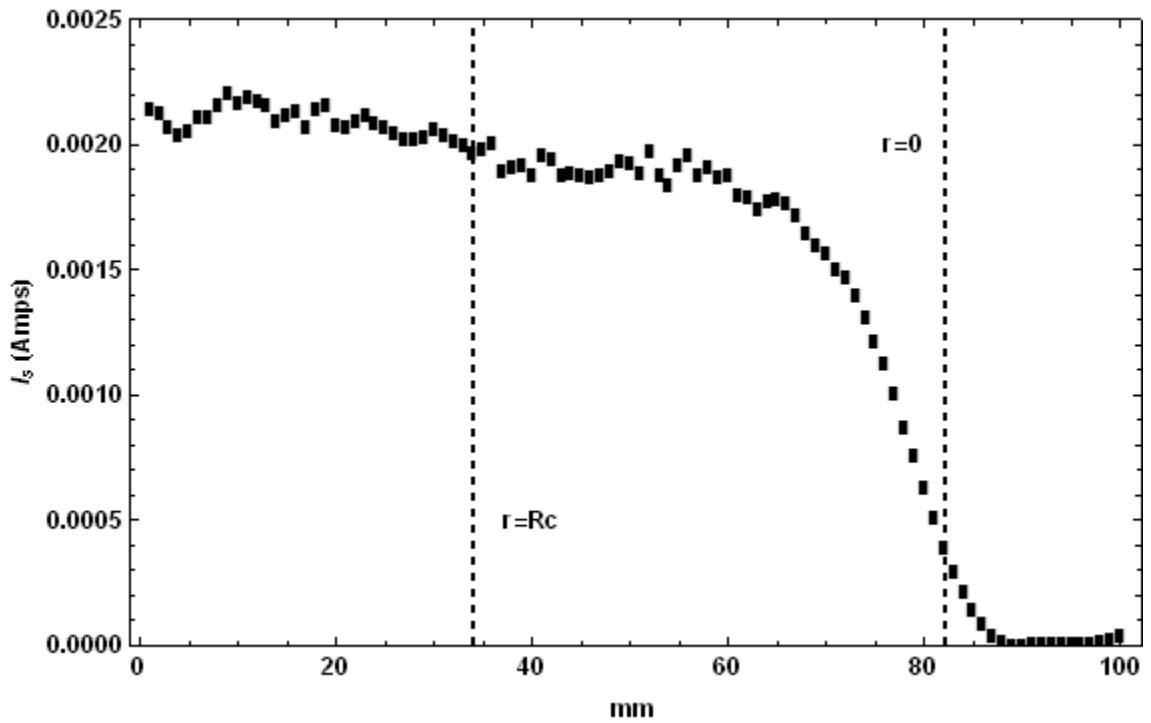


Fig. 142: Measurements of the power supply current,  $I_s$ , are plotted as a function of radius to indicate the shadowing effect of a probe as it is inserted into the center of a GD IXL SIEC device. This plot is for the case  $P = 0.13 \text{ mA kV}^{-3/2}$ . The legend for this plot is provided in Table IX.

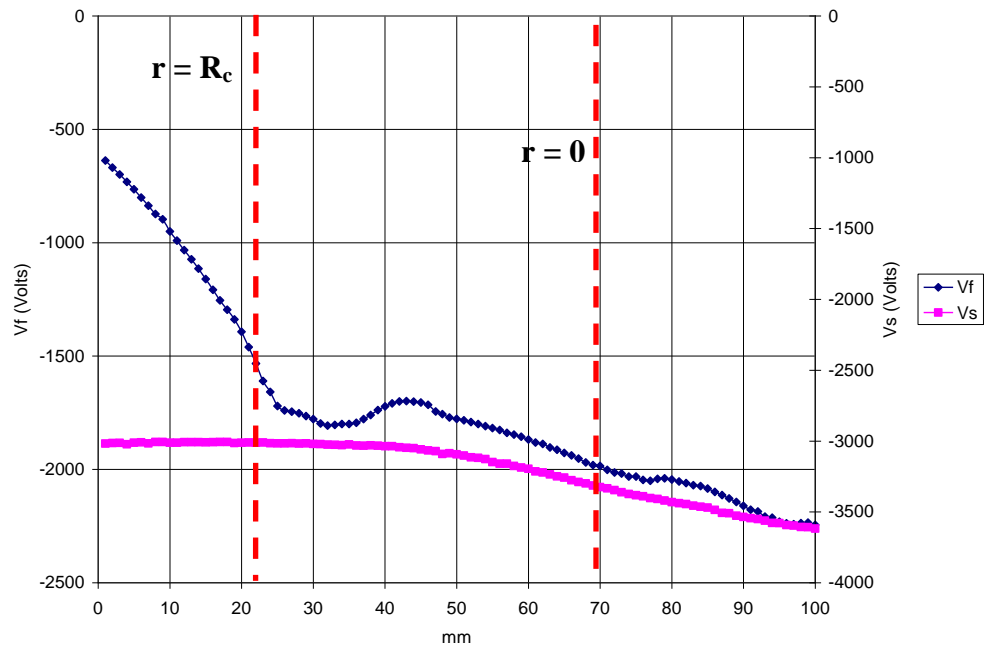


Fig. 143: Radial floating potential profile,  $V_f(r)$ , for a supply voltage of  $V_s = -3.2 \text{ kV}$ , a supply current of  $I_s = 39.92 \text{ mA}$ , and  $P = 6.97 \text{ mA kV}^{-3/2}$ . These measurements are obtained with single probe s2 inserted into Probe Location 2.

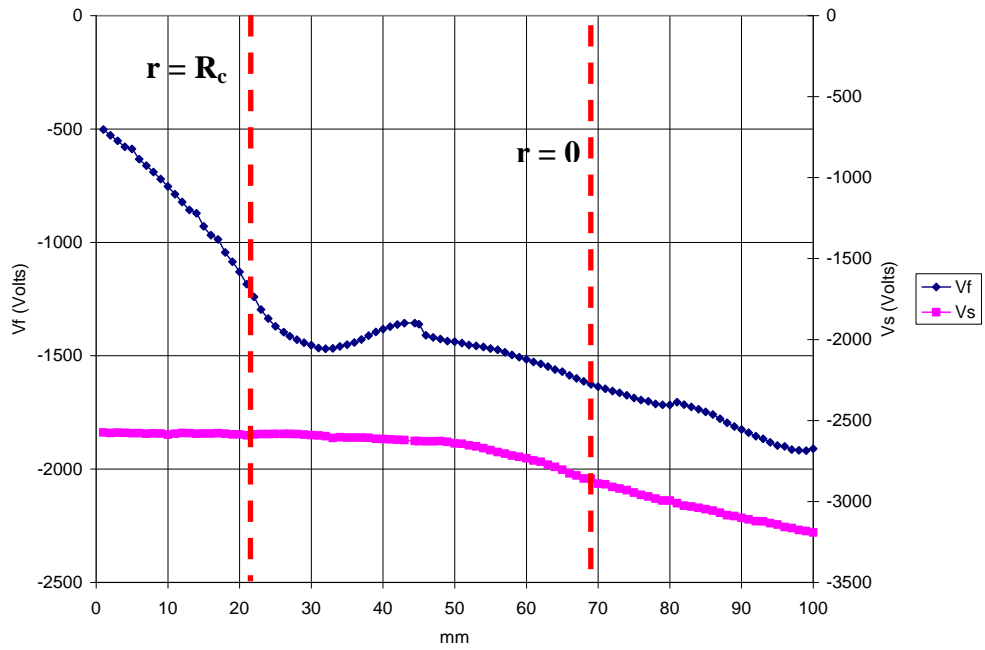


Fig. 144: Radial floating potential profile,  $Vf(r)$ , for a supply voltage of  $V_s = -2.76$  kV, a supply current of  $I_s = 39.92$  mA, and  $P = 8.69$  mA  $kV^{-3/2}$ . These measurements are obtained with single probe s2 inserted into Probe Location 2.

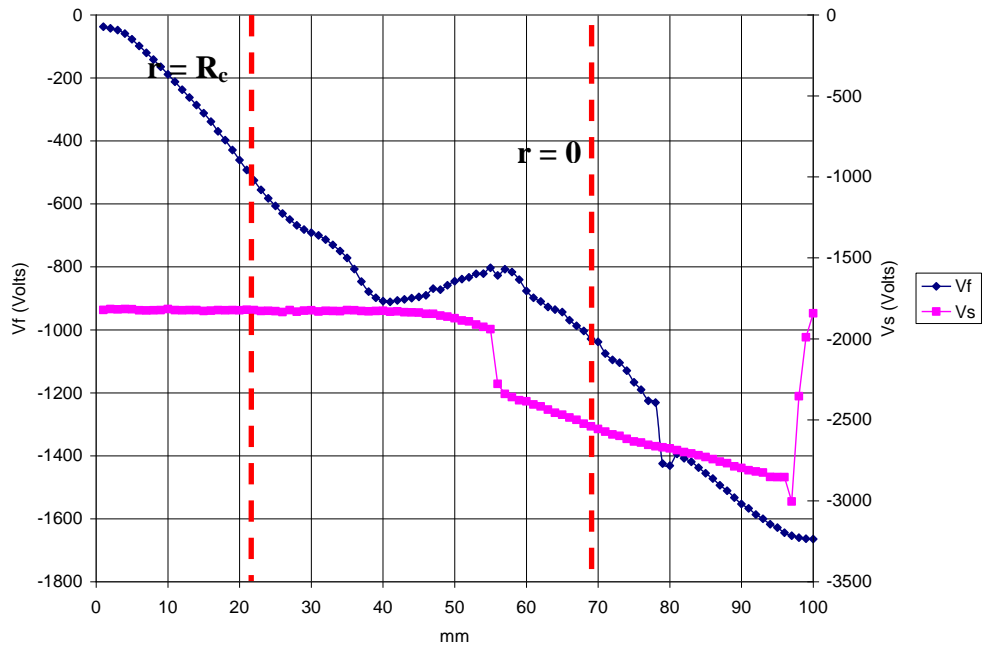


Fig. 145: Radial floating potential profile,  $Vf(r)$ , for a supply voltage of  $V_s = -2.17$  kV, a supply current of  $I_s = 39.93$  mA, and  $P = 12.45$  mA  $kV^{-3/2}$ . These measurements are obtained with single probe s2 inserted into Probe Location 2.

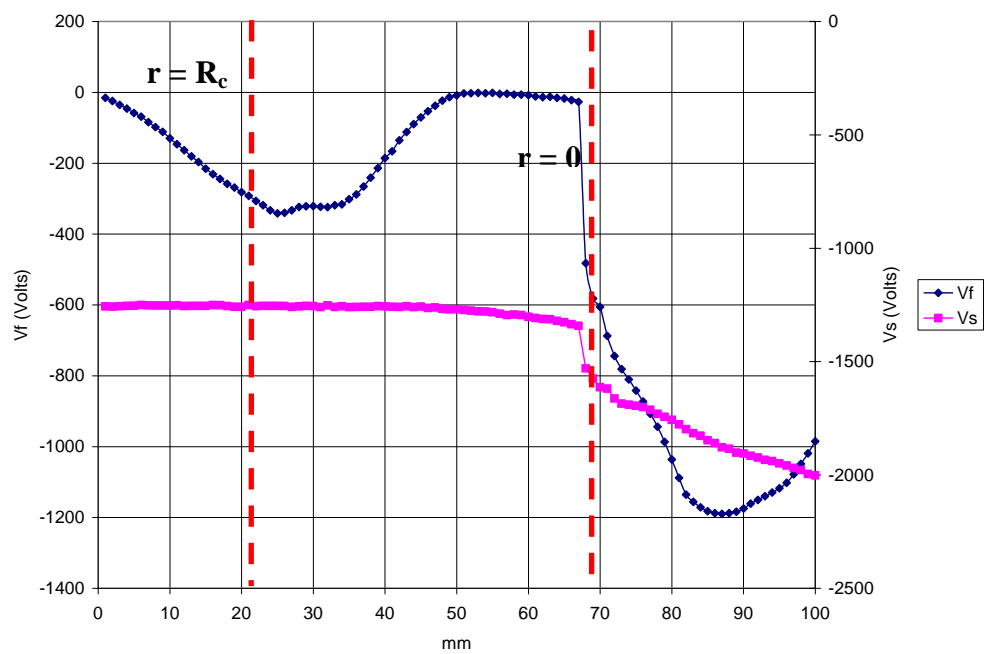


Fig. 146: Radial floating potential profile,  $V_f(r)$ , for a supply voltage of  $V_s = -1.45$  kV, a supply current of  $I_s = 39.92$  mA, and  $P = 22.93$  mA kV<sup>-3/2</sup>. These measurements are obtained with single probe s2 inserted into Probe Location 2.

## VI. Discussions

Several assumptions are made in the analysis of the probe characteristics. The most tenuous assumptions being that a) the plasma is quasi-neutral ( $n_i \approx n_e$ ), that b)  $kT_i \ll kT_e$ , and that c) the electron distribution can be described as a single Maxwellian population. We can not determine  $kT_i$ , but assumption b) is especially weak at the very center of the device where ions are converging from all directions resulting in an ion distribution with a very large  $kT_i$ . Single probe measurements provide some way to evaluate assumptions (a and (c.

### A. *Quasi-neutrality in Micro-Channels*

When assumptions a), b), and c) are met, a collecting probe will float at a potential negative with respect to the plasma potential by an amount,

$$e(V_f - V_b) = -\frac{kT_e}{2} \text{Log}\left(\frac{m_i}{2.3m_e}\right). \quad (28)$$

Plasma and floating potential measurements obtained from the individual collectors of double probe d2, in Probe Location 1, are provided in Fig. 147 through Fig. 150. These figures show that  $V_\infty \gg V_f$  with the exception of Fig. 147, which represents the profiles for  $P = 0.37 \text{ mA kV}^{-3/2}$ . In this case, it is apparent that the ion flux,  $\Gamma_0$ , is greater than the electron flux,  $\Gamma_1$ , to the collector as the collector approaches the cathode grid, causing the probe to float positively with respect to the plasma. Inside of the cathode grid, the difference  $V_\infty - V_f$  is noticeably larger than in the inter-electrode space.

Double probe measurements of the plasma density, as shown in Fig. 100 through Fig. 102, are averaged over values within the inter-electrode space for the various

discharge conditions. The same thing is done with electron density measurements obtained with the single probe in Fig. 136, and with single probe measurements of the electron density from Probe Location 2. These results are together in Fig. 151. These results show that at lower values of  $P$  ( $\sim < 1 \text{ mA kV}^{-3/2}$ ), single probe measurements of  $n_e$  are approximately an order of magnitude less than estimates from the double probe. As  $P$  is increased, the difference remains approximately at a factor of 2-3 until  $P \sim 4 \text{ mA kV}^{-3/2}$ . The results indicate that the ion micro-channels of “Star Mode” satisfy the quasi-neutrality condition near  $P = 4 \text{ mA kV}^{-3/2}$ .

### ***B. Heterogeneous Structure***

The ion micro-channels are found to satisfy the quasi-neutrality condition over a relatively narrow range of discharge conditions. Within the cathode, where ionization processes are most intense, the quasi-neutrality condition is satisfied over a very wide range of discharge conditions as shown with Fig. 152 and Fig. 153. Finally, data collected from Probe Location 2, in Fig. 151, shows that  $n_e$  is significantly less in the inter-electrode space when micro-channeling is absent. Together with the curves in Fig. 103 through Fig. 105, we conclude that ion flow is highly dominant in regions where micro-channeling is absent. We can also see that “Jet Mode” discharge conditions result in an inter-electrode flow region that is still very heterogeneous despite its visual appearance.

### ***C. “Star-Mode” to “Jet-Mode” Transition***

“Star-Mode” transitions to “Jet-Mode” as the device pressure is increased and thus, the perveance,  $P$ , is increased. This is indicated in the curves of Fig. 151. We see

that particle densities increase with increasing  $P$  for low values of  $P$ . At some point, the curve peaks and decreases sharply. Continuing to higher values of  $P$ , the curves take a linear shape with a slight negative slope. The peaks in the curves occur near  $4 \text{ mA kV}^{-3/2}$ , which is the same value plasma neutrality is observed. The regions around these peaks indicate where the discharge transitions from “Star Mode” to “Jet Mode”. In “Jet Mode” the densities decrease slowly with increasing  $P$  in a micro-channel region.

#### ***D. Electron Populations***

In Chapter I Section C, it is noted that three populations of electrons are identifiable in the negative glow region of a discharge. Double probe sweeps indicate the presence of primary electrons after passing through the cathode grid. A typical sequence of traces is shown in Fig. 154 through Fig. 161. This distinct feature in these curves can be attributed to secondary emission from the collecting probe due to the bombardment by high energy electrons.<sup>80</sup> These probe sweeps are taken as the probe has mostly passed to the inside of the grid wires, so it does not appear that the cathode grid could be the origin of these electrons. Also, the feature appears at 55mm along the start of the probe’s injection, or 34mm from the center of the device. We can see from plots of the floating potential in Fig. 96 and Fig. 97 that the distinct feature in the curve appears just at the point where significant radial electric fields occur. From Fig. 154 through Fig. 161, we conclude that both the energy of the electrons and their energy spread is increasing as the probe continues to move out from the center. This population of electrons consists of low temperature electrons born inside the cathode by ionization that are “sucked-out” by the electric field as they drift out from the center of the device. This population should be fairly mono-energetic if the intra-cathode potential is flat.

### ***E. Ion Flow Characterization***

Most of the “Star Mode” density profiles in Fig. 100 through Fig. 102 are severely influenced by shadowing effects. Therefore, ion density profile characteristics have only been computed for three cases which appear to be least influenced by shadowing. The core radius ( $CR$ ) and  $HWHM$  for three of the discharge conditions represented in Fig. 100 through Fig. 102 are provided in Table X. The results show a dramatic change between  $2.97 \text{ mA kV}^{-3/2}$  and  $3.42 \text{ mA kV}^{-3/2}$  as the  $HWHM$  decreases from  $0.41$  ( $1.94 \text{ cm}$ ) to  $0.27$  ( $1.25 \text{ cm}$ ). However, this could be due to shadowing effects. Another dramatic difference is indicated in  $CF$  measurements for  $4.22 \text{ mA kV}^{-3/2}$  versus the other two cases. Overall, these results indicate decreasing angular energy spread of injected particles with increasing values of  $P$  above  $2.97 \text{ mA kV}^{-3/2}$ , as shown in Table X. The values for angular energy spread in the table are obtained from a comparison of the data with Fig. 17 and Fig. 18. Orbital modeling predicts the opposite trend as space charge spreading is more important at high  $P$ . However, in glow discharge devices, the inner-cathode region is neutralized. In addition, we see that the micro-channels become more neutral with increasing  $P$  up to  $P \sim 4 \text{ mA kV}^{-3/2}$ .

The “hump” observed in the Monte Carlo simulations of ion shadowing by our double Langmuir probe, shown in Fig. 73 through Fig. 78, is also observed experimentally, as depicted in Fig. 138 through Fig. 142. It is encouraging that the simulations have reproduced the “hump” and that it occurs in the same location. However, the Monte Carlo simulations deviate significantly for most of the profile. In addition, this deviation between the Monte Carlo results and experiment is worse for the smaller core sizes. This is probably due to a modeling error. In the present model, ion

trajectories are chosen randomly, but their initial positions are not. Essentially, the ions originate from a fixed discrete grid structure. It is the sparseness of this grid that causes much of the deviation observed. The modeling program needs to be updated to randomly select the initial ion positions, and perhaps increase the number of ion walks. Despite this, data in Fig. 162 through Fig. 164 indicate that CR is increasing, in particular from  $R_g/R_c \sim 10$  at  $P = 0.87 \text{ mA kV}^{-3/2}$  to  $R_g/R_c \sim 6$  at  $P = 3.02 \text{ mA kV}^{-3/2}$ .

#### ***F. Virtual Electrodes***

Floating potential measurements within the “Jet Mode” regime generally indicate a more complex potential profile, as shown in Fig. 143 through Fig. 146. Some evidence suggests the evolution of virtual electrodes as one transition out of “Star-Mode” into a higher pressure regime.<sup>70,71</sup> However, the profiles in Fig. 143 through Fig. 146 are not of the true plasma potential, and are therefore not conclusive evidence of virtual electrode formation.

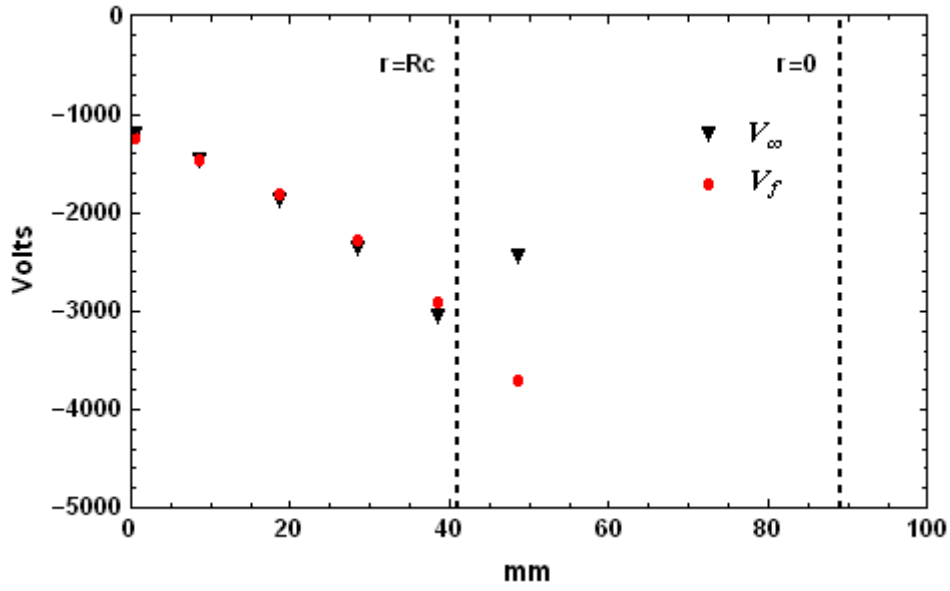


Fig. 147: Plasma potential,  $V_\infty$ , and floating potential,  $V_f$ , profiles for the discharge conditions  $I_s = 4.19$  mA,  $V_s = -5.03$  kV, and  $P = 0.37$  mA kV<sup>-3/2</sup> from Table VIII.

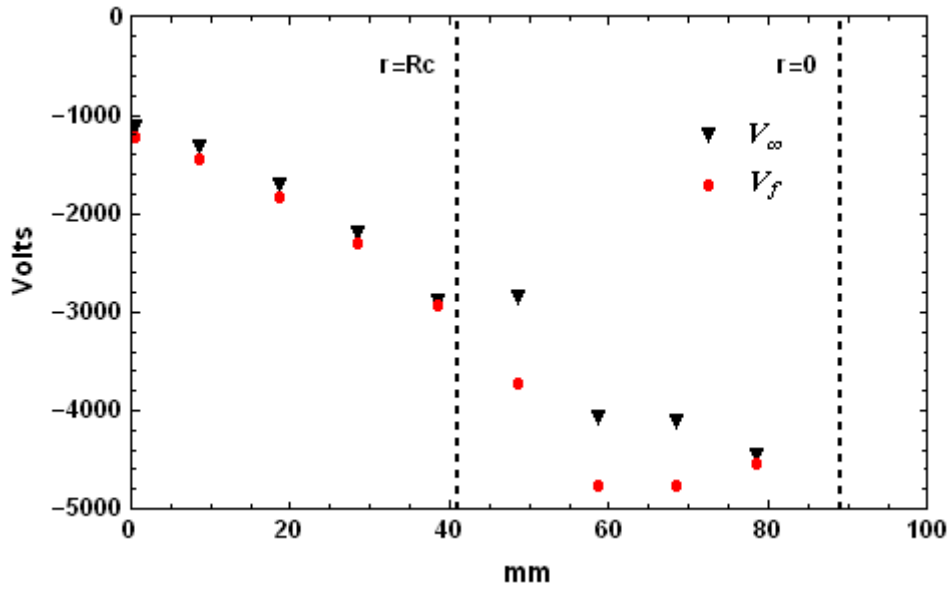


Fig. 148: Plasma potential,  $V_\infty$ , and floating potential,  $V_f$ , profiles for the discharge conditions  $I_s = 11.52$  mA,  $V_s = -5.04$  kV, and  $P = 1.02$  mA kV<sup>-3/2</sup> from Table VIII.

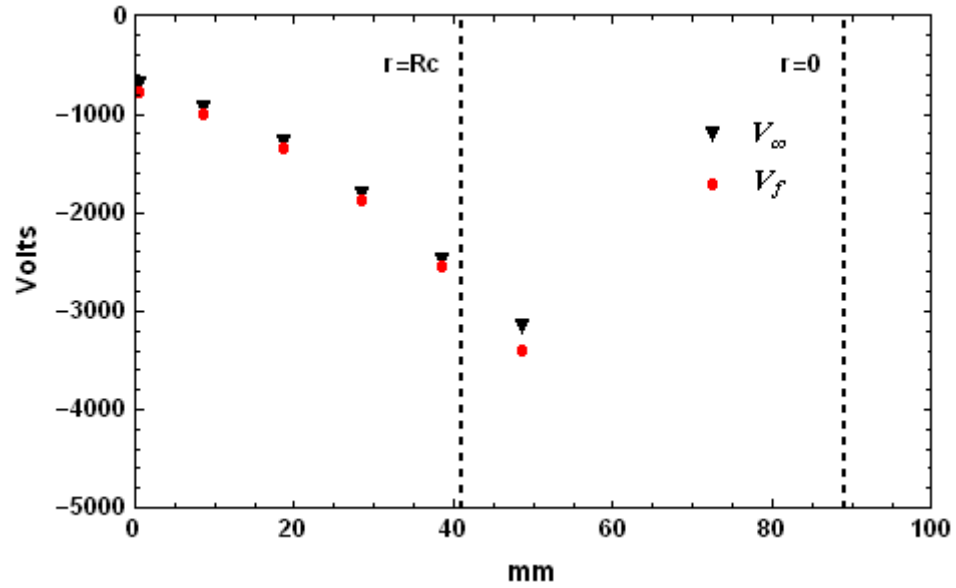


Fig. 149: Plasma potential,  $V_\infty$ , and floating potential,  $V_f$ , profiles for the discharge conditions  $I_s = 39.97$  mA,  $V_s = -4.67$  kV, and  $P = 3.96$  mA kV<sup>-3/2</sup> from Table VIII.

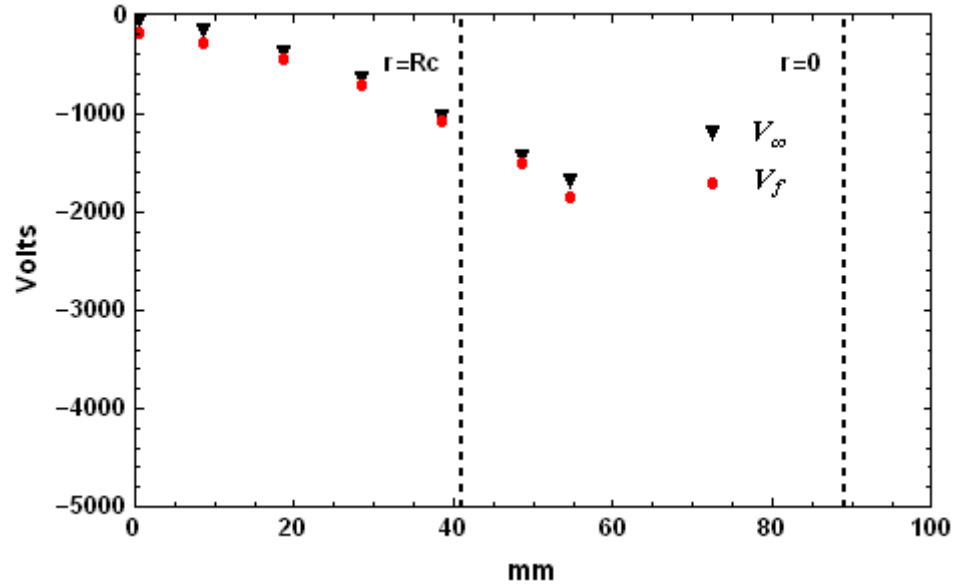


Fig. 150: Plasma potential,  $V_\infty$ , and floating potential,  $V_f$ , profiles for the discharge conditions  $I_s = 39.97$  mA,  $V_s = -2.53$  kV, and  $P = 9.96$  mA kV<sup>-3/2</sup> from Table VIII.

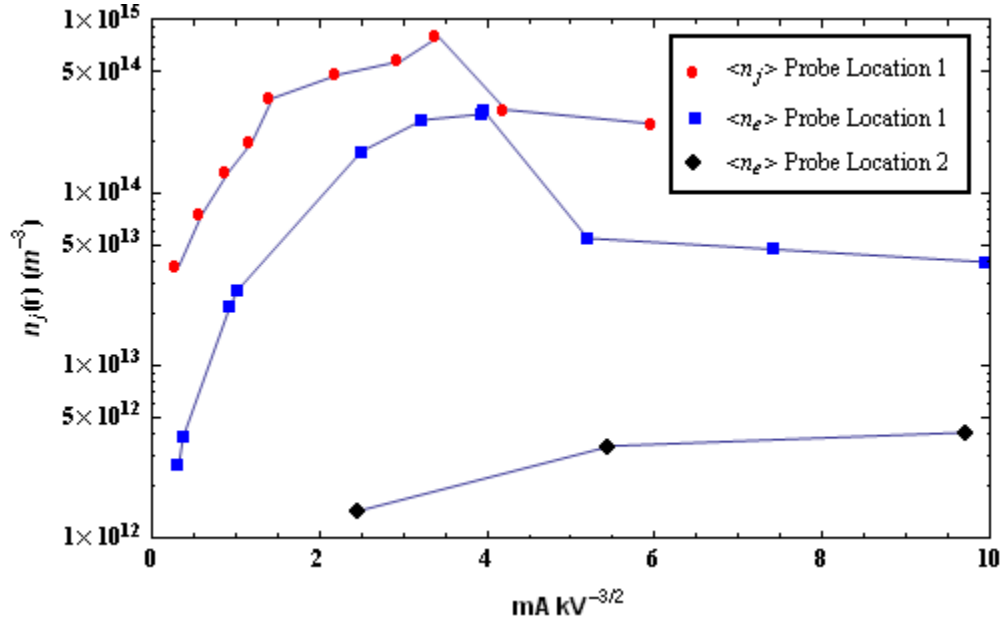


Fig. 151: Electron density measurements averaged over the inter-electrode space,  $\langle n_e \rangle$ , and plasma or ion density measurements over the inter-electrode space,  $\langle n_j \rangle$ , for a number of discharge conditions. In this case,  $\langle n_j \rangle$  is obtained from double probe, d2, and the conditions in Table VII, and  $\langle n_e \rangle$  are obtained from single probe sweeps for conditions in Table VIII.

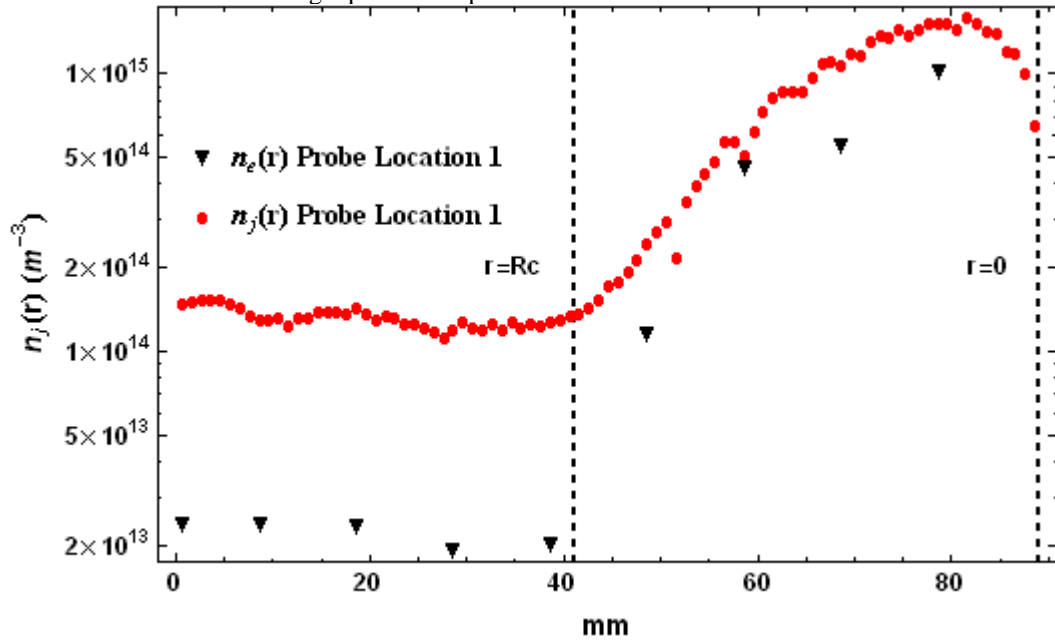


Fig. 152: Radial electron density profile,  $n_e(r)$ , obtained with single probe sweeps for the discharge conditions  $I_s = 10.50$  mA,  $V_s = -5.04$  kV, and  $P = 0.93$  mA  $kV^{-3/2}$  from Table VIII. Radial plasma, or ion density profile,  $n_j(r)$ , obtained with double probe, d2, for the discharge conditions  $I_s = 10.06$  mA,  $V_s = -4.97$  kV, and  $P = 0.91$  mA  $kV^{-3/2}$  from Table VII.

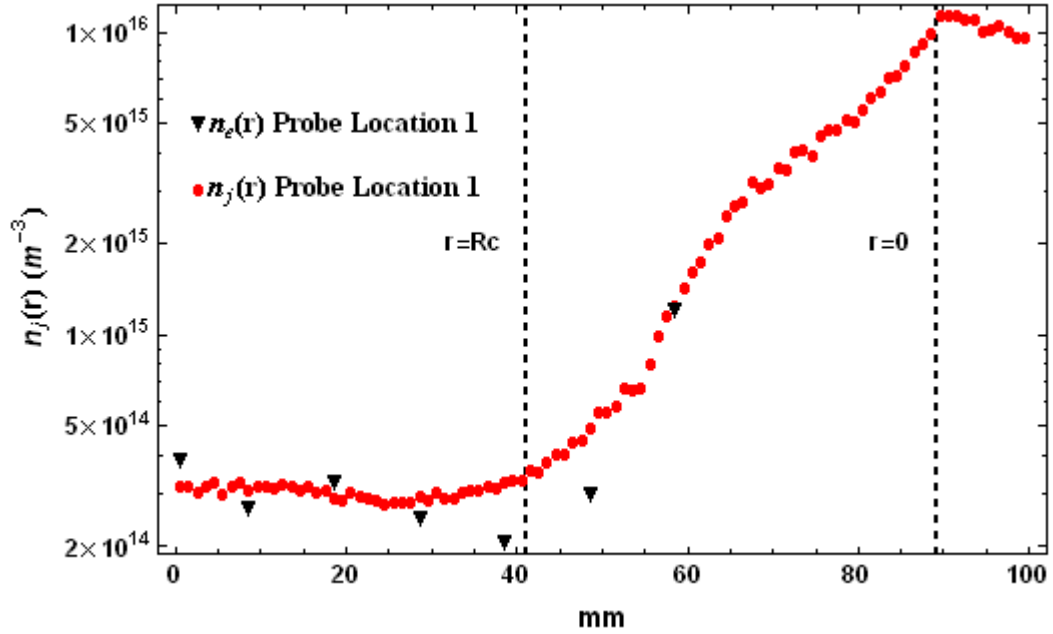


Fig. 153: Radial electron density profile,  $n_e(r)$ , obtained with single probe sweeps for the discharge conditions  $I_s = 39.97$  mA,  $V_s = -4.70$  kV, and  $P = 3.93$  mA  $\text{kV}^{-3/2}$  from Table VIII. Radial plasma, or ion density profile,  $n_i(r)$ , obtained with double probe, d2, for the discharge conditions  $I_s = 38.73$  mA,  $V_s = -4.38$  kV, and  $P = 4.22$  mA  $\text{kV}^{-3/2}$  from Table VII.

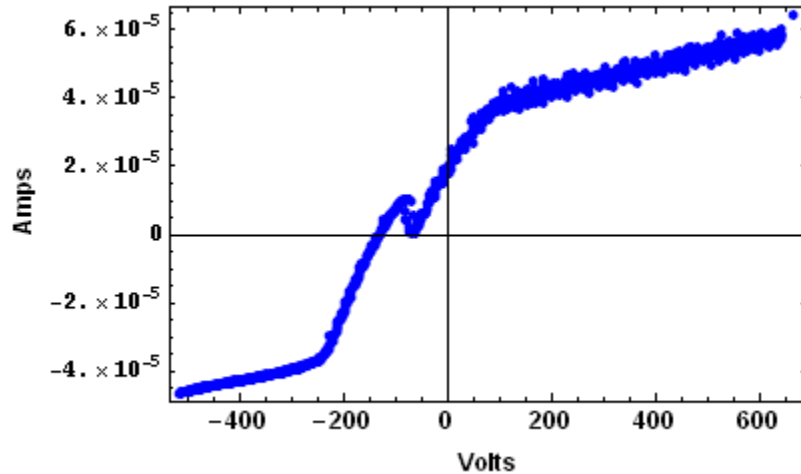


Fig. 154: I-V characteristic obtained with double probe, d2, for the discharge conditions  $I_s = 38.73$  mA,  $V_s = -4.38$  kV, and  $P = 4.22$  mA  $\text{kV}^{-3/2}$  from Table VII at a location of 55 mm along the probes path, and where the grid is located at 42 mm and the device center is at 89 mm for reference.

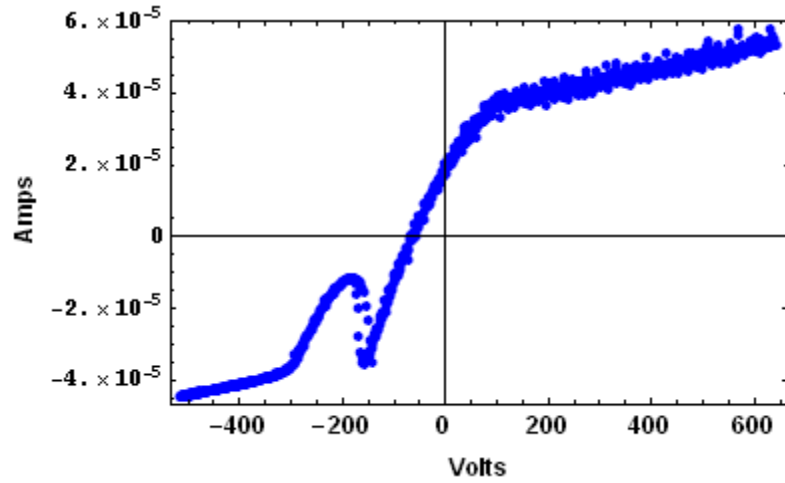


Fig. 155: I-V characteristic obtained with double probe, d2, for the discharge conditions  $I_s = 38.73$  mA,  $V_s = -4.38$  kV, and  $P = 4.22$  mA kV<sup>-3/2</sup> from Table VII at a location of 54 mm along the probes path, and where the grid is located at 42 mm and the device center is at 89 mm for reference.

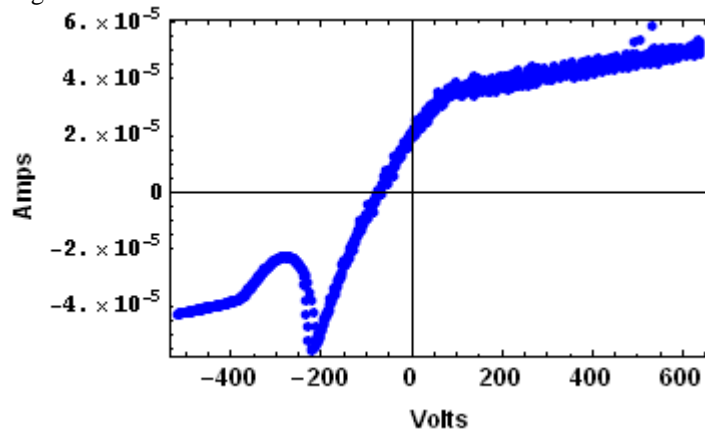


Fig. 156: I-V characteristic obtained with double probe, d2, for the discharge conditions  $I_s = 38.73$  mA,  $V_s = -4.38$  kV, and  $P = 4.22$  mA kV<sup>-3/2</sup> from Table VII at a location of 53 mm along the probes path, and where the grid is located at 42 mm and the device center is at 89 mm for reference.

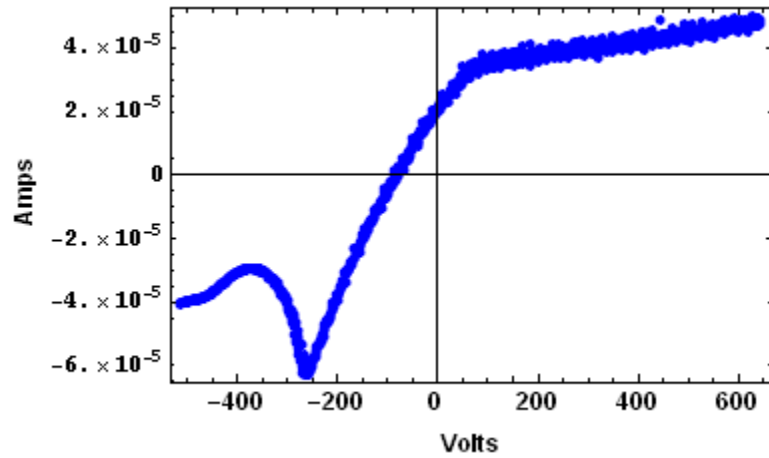


Fig. 157: I-V characteristic obtained with double probe, d2, for the discharge conditions  $I_s = 38.73$  mA,  $V_s = -4.38$  kV, and  $P = 4.22$  mA  $\text{kV}^{-3/2}$  from Table VII at a location of 52 mm along the probes path, and where the grid is located at 42 mm and the device center is at 89 mm for reference.

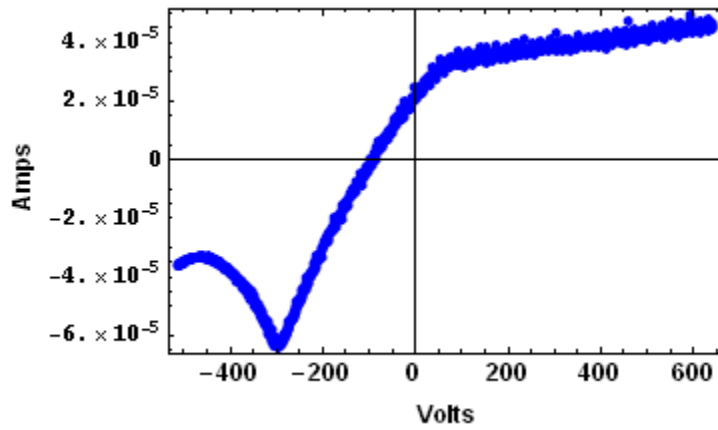


Fig. 158: I-V characteristic obtained with double probe, d2, for the discharge conditions  $I_s = 38.73$  mA,  $V_s = -4.38$  kV, and  $P = 4.22$  mA  $\text{kV}^{-3/2}$  from Table VII at a location of 51 mm along the probes path, and where the grid is located at 42 mm and the device center is at 89 mm for reference.

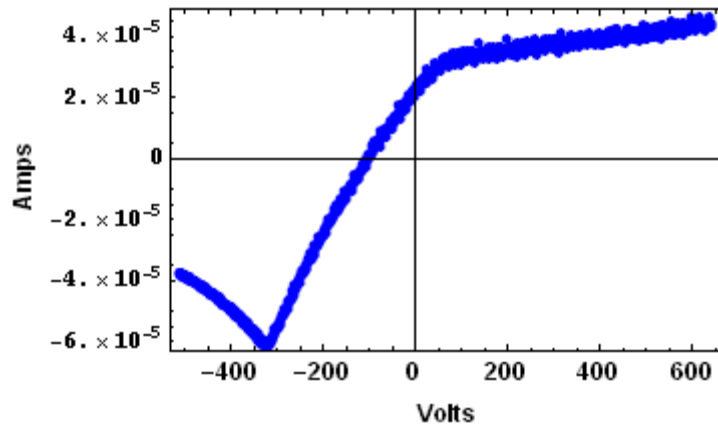


Fig. 159: I-V characteristic obtained with double probe, d2, for the discharge conditions  $I_s = 38.73$  mA,  $V_s = -4.38$  kV, and  $P = 4.22$  mA kV<sup>-3/2</sup> from Table VII at a location of 50 mm along the probes path, and where the grid is located at 42 mm and the device center is at 89 mm for reference.

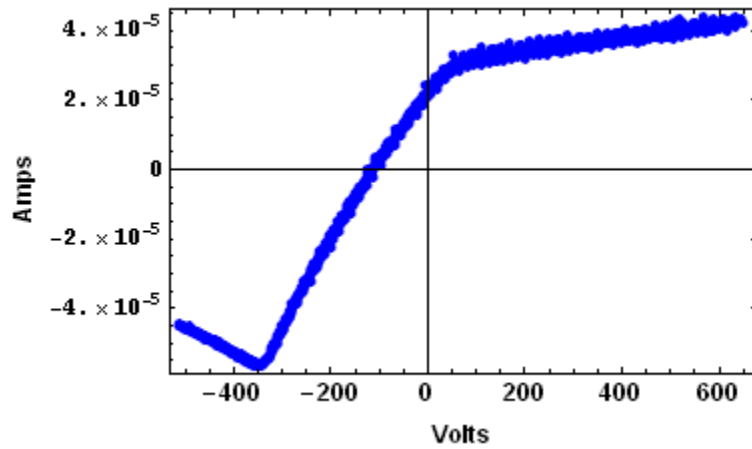


Fig. 160: I-V characteristic obtained with double probe, d2, for the discharge conditions  $I_s = 38.73$  mA,  $V_s = -4.38$  kV, and  $P = 4.22$  mA kV<sup>-3/2</sup> from Table VII at a location of 49 mm along the probes path, and where the grid is located at 42 mm and the device center is at 89 mm for reference.

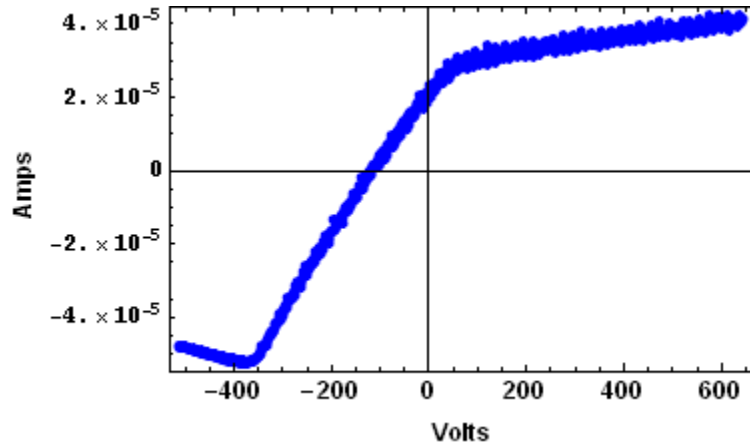


Fig. 161: I-V characteristic obtained with double probe, d2, for the discharge conditions  $I_s = 38.73$  mA,  $V_s = -4.38$  kV, and  $P = 4.22$  mA kV<sup>-3/2</sup> from Table VII at a location of 48 mm along the probes path, and where the grid is located at 42 mm and the device center is at 89 mm for reference.

Table X: Ion density profile characteristics for three of the discharge conditions represented in Fig. 100 through Fig. 102.

$kV$	$mA$	$\frac{mA}{kV^{3/2}}$	$Mode$	$n_0(0) m^{-3}$	$CF$	$HWHM$	$\sigma_{i\phi}$
-4.98	33.07	2.97	Star	$6.45 \cdot 10^{15}$	10.7	0.41	$\sim 0.15$
-4.83	36.37	3.42	Star	$1.16 \cdot 10^{16}$	15.0	0.27	$\sim 0.05-0.10$
-4.38	38.73	4.22	Jet	$9.09 \cdot 10^{15}$	27.3	0.24	$\sim 0.05$

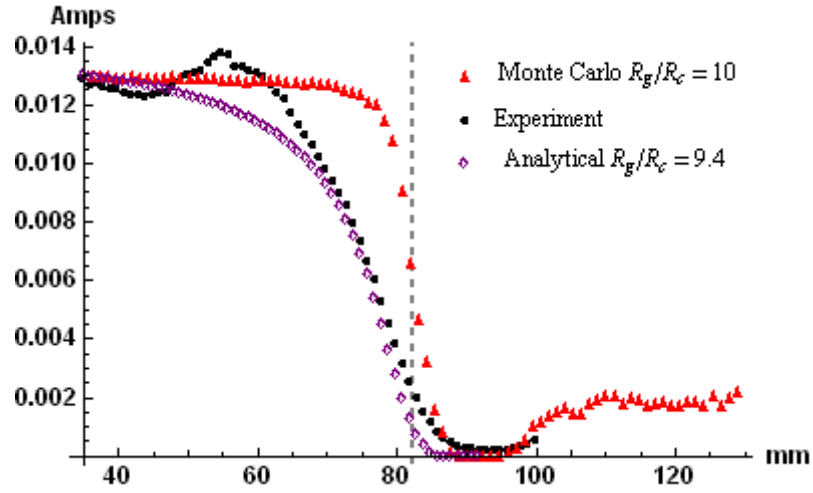


Fig. 162: Supply current,  $I_s$ , as a function of probe position for discharge conditions  $I_s = 9.92$  mA,  $V_s = -5.09$  kV, and  $P = 0.87$  mA kV<sup>-3/2</sup>. Experimental data is compared with theoretical results obtained with the analytical expression in Eq. (27) with  $R_g/R_c = 9.4$  and from Monte Carlo simulations with  $R_g/R_c = 10$ .

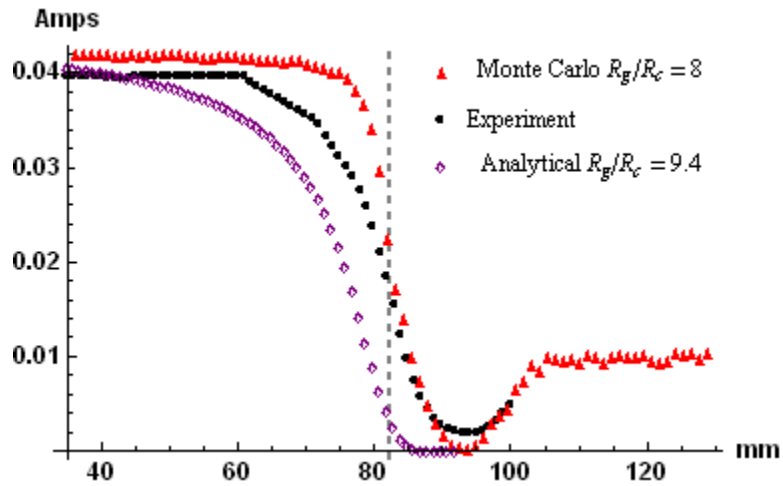


Fig. 163: Supply current,  $I_s$ , as a function of probe position for discharge conditions  $I_s = 31.96$  mA,  $V_s = -5.21$  kV, and  $P = 2.69$  mA kV<sup>-3/2</sup>. Experimental data is compared with theoretical results obtained with the analytical expression in Eq. (27) with  $R_g/R_c = 9.4$  and from Monte Carlo simulations with  $R_g/R_c = 8$ .

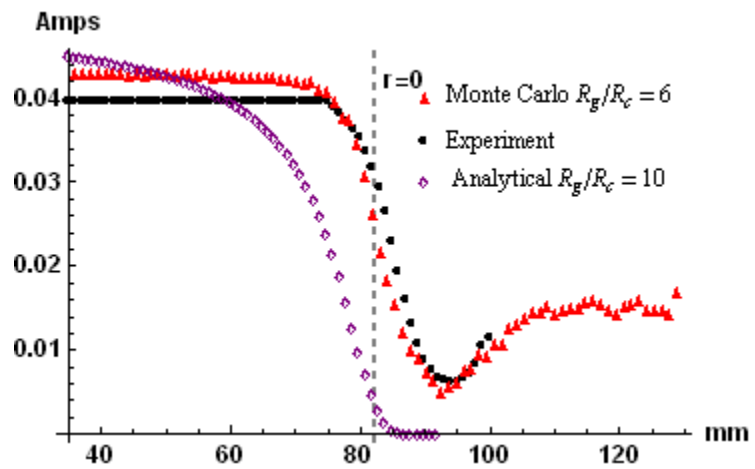


Fig. 164: Supply current,  $I_s$ , as a function of probe position for discharge conditions  $I_s = 34.62$  mA,  $V_s = -5.08$  kV, and  $P = 3.02$  mA kV<sup>-3/2</sup>. Experimental data is compared with theoretical results obtained with the analytical expression in Eq. (27) with  $R_g/R_c = 9.4$  and from Monte Carlo simulations with  $R_g/R_c = 6$ .

## VII. Conclusions, Contributions, Future Work

This dissertation has the following objectives: 1) to map out theoretical double potential well regimes employing the 1-D orbital model, 2) to experimentally verify the micro-channeling phenomena, 3) to characterize glow discharge modes of operation by experimental investigation, 4) to characterize ion flow in glow discharge devices. In addition to mapping out theoretical double potential well regimes, we have managed to map several other observables with respect to control variables such as core electron and ion densities ( $n_I(0)$  and  $n_O(0)$ ), minimum inter-cathode potential ( $Y_{min}$ ), the core potential ( $Y_{core}$ ), and double well width ( $width$ ), and provide these results in Appendix A.

### A. Conclusions and Contributions

#### 1. Theoretical Mapping of Observables

Results of the 1-D orbital modeling indicate that for uni-polar devices, splitting of the injected particle density profile,  $n_O(r)$ , due to space charge repulsion, places a lower limit on the minimum achievable angular energy spread of the particles. This splitting is seen to occur when the  $FWD$  is approximately 70-80%. Practically, this implies that space charge effects should have contributed significantly to core radius ( $CR$ ) scaling with pressure observed by Thorson as  $FWD$  measurements greater than 70% were observed. The bi-polar 1-D orbital modeling results show that an optimal ratio of electrons to ions exists for double potential well formation. In addition, the double well depth ( $DWD$ ) is relatively insensitive to the angular energy spread of the injected

particles. In fact, small spreads in angular energy of the injected particles should be avoided.

## **2. Verification of Ion Micro-Channeling, Characterization of Glow Discharge Modes**

We have obtained experimental verification of micro-channeling as the luminous spokes of “Star Mode” contain an increased number of electrons and ions compared to regions absent of micro-channels. The neutrality of the micro-channels has been evaluated and it is seen that ion flow in micro-channels is dominant at low values of perveance,  $P$ . As  $P$ , and hence, the pressure are increased, the micro-channels become more neutral until strict neutrality is achieved near  $P \sim 4 \text{ mA kV}^{-3/2}$ .

A conceptual picture of the heterogeneous structure of “Star-Mode” is formed. The region within the cathode is largely neutral over a large range of discharge conditions, while the micro-channels are weakly non-neutral. Typically, it is estimated that the ion density is greater than the electron density by a factor of 2~3 in the micro-channels. At low values of  $P$ , the ion density is nearly an order of magnitude greater than the electron density. In regions where micro-channeling is absent, non-neutrality is more severe as the floating potential is positive with respect to the plasma potential. Although we do not have an estimate of ion densities in these regions, it is probably 1-2 orders of magnitude greater than the electron density. The electron densities within the micro-channels are  $10^{13} - 10^{14} \text{ m}^{-3}$  while electron densities in micro-channel absent regions are  $10^{12} \text{ m}^{-3}$ . Finally, Fig. 151 reveals that the transition from “Star Mode” to “Jet Mode” occurs near  $P \sim 4 \text{ mA kV}^{-3/2}$ . The structure remains largely heterogeneous in “Jet Mode” as well, despite the more uniform appearance.

### 3. Ion Flow Characterization

Limited observations of the core radius ( $CR$  or  $R_c$ ) scaling with  $P$  are provided in the previous chapter. The results in Table X are obtained directly from radial density profiles in Fig. 100 through Fig. 102. However, shadowing effects could contribute to the larger values of  $HWHM$  and  $CF$  calculated for  $P = 2.97 \text{ mA kV}^{-3/2}$  and  $3.42 \text{ mA kV}^{-3/2}$  cases.

Measurements of the supply current,  $I_s$ , vs. probe position,  $l$ , are obtained, and compared to modeling efforts which determine the fraction of ions blocked as a function of  $l$ . Monte Carlo modeling is able to reproduce the “hump” observed experimentally in Fig. 138 through Fig. 142. Otherwise, a significant difference exists between the Monte Carlo profile and the experimentally obtained curves. This inhibits the possibility of obtaining solid conclusions regarding ion core size. The Monte Carlo code is currently being upgraded. If new results match the experimentally obtained curves, then more definitive statements about the core size should be possible.

### 4. Contributions

This dissertation makes the following theoretical contributions:

- Find that double potential wells may flourish despite space charge spreading
- Find that electrons play a crucial role in double well formation
- Identified the condition for core splitting –  $FWD \sim 0.7-0.8$
- Provide the most extensive double potential well search with respect to control variables
- Provide extensive maps for other observables

This dissertation makes the following experimental contributions:

- First experimental measurement of complete radial plasma density profile
- Identified experimental technique to sample tangential electrical field component
- Identified experimental technique to evaluate ion flow focus via shadowing phenomena
- Direct experimental verification of “Star Mode” micro-channeling phenomena
- Characterize the neutrality of “Star Mode” micro-channels; most non-neutral, except near  $P = 4 \text{ mA kV}^{-3/2}$  for our case
- Direct experimental verification and characterization of heterogeneous nature of “Star Mode” plasma;
- Find that micro-channeling persists within “Jet Mode”
- Experimental determination of “Star-Mode” to “Jet Mode” transition threshold
- Discovery of a beam component of the electron population due to the electric field

### ***B. Narrow Suggestions***

Means to improve these experiments and to supplement the results of this dissertation will now be discussed. Separation between the two planar disks of the double probe is significant ( $\sim 9 \text{ mm}$ ). This could be reduced to shrink the double probe and minimize shadowing effects.

Single probe data within the grid is sparse due to the large amount of current collected by the probe. The single probe was observed to collect nearly %10 of the supply current when positioned inside of the cathode grid. The disturbance to the plasma in this case is obvious. An oscillation of the supply current was observed on the power supply ammeter at the same frequency as the probe sweep. The diameter of the single probe collector should be reduced at least by a factor of two (from 1/8" to 1/16"). An alternative is to construct a single probe with a cylindrical or spherical collector.

Extensive plasma potential measurements would be useful in verifying that the plasma and floating potential profiles have similar shapes. Also, floating potential profiles indicate the formation of a virtual electrode in "Jet Mode". Plasma potential measurements could help determine if they are genuine. To do this, it is suggested to use an emissive probe, because the infrastructure for probe measurements is already in place. In addition, the author has already constructed the circuitry necessary for the measurements.

An energy analyzer could be built and used with the current probe infrastructure. In this case, a saddle point reflector could be employed to avoid the usage of wire mesh. The energy analyzer would allow more accurate measurements of ion parameters in non-neutral regions of the device.

Pressure indications are noticeably absent in the presentation of experimental results. The pressure gauges mentioned in Chapter III do not accurately provide measurements in pressure ranges of greatest interest, 1-50 mTorr. The gauges could not be calibrated with each other, because there was insufficient overlap in their detection

ranges. While the pressure readings are within the expected range, they are not always consistent. The vacuum monitoring system should be improved.

Finally, an attempt should be made to effectively shield the target from RF emissions. This would allow a reduction in circuit shielding and significantly reduce the leakage capacitance of the probe sweeping circuit. Doing so would allow a faster sweep rate, and would be a time saver.

### *C. Broader Suggestions*

In glow discharge devices, beam-background reactions dominate. The fusion output of such of a device can be increased by limiting losses to the cathode and cathode feedthrough and/or by increasing the ionization fraction while maintaining the background density. Otherwise, favorable neutron scaling can be obtained with a complex well structure. Due to short mean free paths, “Jet Mode” has not been identified as a desirable operational mode, although some evidence suggests interesting potential well formations. It could be that an unfortunate set of circumstances prevent the formation of double potential wells in “Star Mode”, however, a dedicated exploration of virtual electrodes within “Jet Mode” is likely to provide further understanding of the phenomena, and perhaps provide clues to how a complex well structure can be sustained in a more favorable discharge mode. Perhaps double potential wells can be induced at “Star Mode” like pressure and voltages with some trickery of the cathode grid. The cathode grid could be designed such that incoming ions are deliberately defocused. In addition, the cathode grid could be heated so that it emits electrons, with the expectation that some of the electrons will migrate to the intra-cathode region. Electrons could also

be delivered to the intra-cathode space by physically inserting a filament inside of the cathode.

A more advanced reactor would require the mounting of ion and electron guns onto a spherical shell. The electrons could be trapped via magnetic fields similar to the Polywell™ concept, but the ion beams would be deliberately defocused. Further theoretical study may be warranted before pursuing elaborate experiments. It was noted earlier that the electrons will be energetically coupled. This raises some questions about double well formation in practice, because the 1D orbital modeling suggests fairly tight constraints exist on the electron temperature.

## BIBLIOGRAPY

1. P. T. Farnsworth, "Electric Discharge Device for Producing Interactions Between Nuclei," U.S. Patent #3,258,402, June 1966.
2. P. T. Farnsworth, "Method and Apparatus for Producing Nuclear Fusion Reactions," U.S. Patent # 3,386,883, June 1968.
3. O. A. Lavrent'ev, "Investigation of an electromagnetic trap," AEC-tr-7002, (1970).
4. O. A. Lavrent'ev, "Electrostatic and Electromagnetic High-Temperature Plasma Traps," *Annals N.Y. Acad. Sci.*, vol. 251, pp. 152, 1975.
5. N.A. Krall, "The Polywell™: A Spherically Convergent Ion Focus Concept," *Fus. Tech.*, vol. 22, pp. 42-49, Aug. 1992.
6. W. M. Nevins, "Can inertial electrostatic confinement work beyond the ion-ion collisional time scale?," *Phys. Plasmas*, vol. 2, no. 10, pp. 3804, Oct. 1995.
7. T. H. Rider, "A general critique of inertial-electrostatic confinement fusion systems," *Phys. Plasmas*, vol. 2, no. 6, pp. 1853, June 1995.
8. G. H. Miley, H. Momota, "A collimator-converter system for IEC propulsion," *Space Technology and Applications International Forum-STAIIF 2002*, 2002, pp. 768-779.
9. G. H. Miley, R. Burton, H. Momota, N. Richardson, M. Coventry, Y. Shaban, "High performance manned interplanetary space vehicle using D-<sup>3</sup>He inertial electrostatic fusion", *Space Technology and Applications International Forum-STAIIF 2002*, 2002, pp. 819-827.
10. R. W. Bussard, "An advanced fusion energy system for outer-planet space propulsion", *Space Technology and Applications International Forum-STAIIF 2002*, 2002, pp. 768-779.
11. T.J McGuire and R.J. Sedwick, "Improved Confinement in Inertial Electrostatic Confinement for Fusion Space Power Reactors", *J. of Propulsion and Power*, vol. 21, no. 4, pg 697-705, July-Aug. 2005.
12. T.J. McGuire, "Improved Lifetimes and Synchronization Behavior in Multi-grid Inertial Electrostatic Confinement Fusion Devices", Ph.D. Dissertation, Massachusetts Institute of Technology, Feb. 2007.

13. C.C. Dietrich, "Improved Particle Confinement in Inertial Electrostatic Fusion for Spacecraft Power and Propulsion", Ph.D. Dissertation, Massachusetts Institute of Technology, Feb. 2007.
14. L. Chacon and G.H. Miley, "IEC Breeder For D-<sup>3</sup>He Satellite Systems," *Fusion Technology*, vol. 30, pp. 1320-1325, Dec. 1996.
15. L. Chacon and G.H. Miley, "Inertial Electrostatic Confinement <sup>3</sup>He Breeder For D-<sup>3</sup>He Satellite Systems," *Fusion Technology*, vol. 33, pp. 182-209, March 1998.
16. J.H. Nadler, "Space-Charge Dynamics and Neutron Generation in an Inertial-Electrostatic Confinement Device", Ph.D. Dissertation, University of Illinois-Urbana-Champaign, 1992.
17. B. Jurczyk, "Theory and development of a sealed Deuterium-Tritium Inertial Electrostatic Confinement Neutron Generator," M.S. Thesis, University of Illinois Urbana-Champaign, 1997.
18. J. B. Javedani, Y. B. Gu, M. J. Williams, J. Hartwell, R. L. Anderl, G. H. Miley, J. H. Nadler, J. L. Jones, R. A. Nebel, and D. C. Barnes, "Studies of the IEC Accelerator-Plasma Target Fusion Neutron Source for activation analysis," *Bulletin of the American Physical Society*, vol. 39, no. 7, pp. 1768, 1994.
19. R.F. Radel, R.P. Ashley, and G.L. Kulcinski., "Detection of Highly Enriched Uranium Using a Pulsed IEC Fusion Device," US-Japan Workshop on Small Plasma and Accelerator Neutron Sources, Argonne National Laboratory (ANL), Argonne, Ill., May 22-24, 2007.
20. K. Yoshikawa, K. Masuda, T. Takamatsu, S. Shiroya, T. Misawa, Y. Takahashi, E. Hotta, K. Yamauchi, M. Ohnishi, and H. Osawa, "Anti-Personnel Landmine Detection by Use of an IEC Neutron Source", US-Japan Workshop on Small Plasma and Accelerator Neutron Sources, Argonne National Laboratory (ANL), Argonne, Ill., May 22-24, 2007.
21. D. Donovan, "Detection of Nitrogen Based Explosives using the UW IEC Device," US-Japan Workshop on Small Plasma and Accelerator Neutron Sources, Argonne National Laboratory (ANL), Argonne, Ill., May 22-24, 2007.
22. J. W. Weidner, "The Production of <sup>13</sup>N from Inertial Electrostatic Confinement Fusion", M.S. Thesis, University of Wisconsin-Madison, 2003.
23. J. W. Weidner, G. L. Kulcinski, J. F. Santarius, R. P. Ashley, G. Piefer, B. Cipiti, R. Radel, S. Krupakar Murali, "Production of <sup>13</sup>N via inertial electrostatic confinement fusion", *Fusion Science and Technology*, vol. 44, pp. 539, 2003.

24. S.J. Zenobia, G.L. Kulcinski, T. Knowles, R.F. Radel, D.R. Boris, C. Seyfert, D. Donovan, A. Creuziger, J. Nacker, "Steady State Implantation of He<sup>+</sup> and D<sup>+</sup> in Carbon-Carbon Velvet," US-Japan Workshop on Small Plasma and Accelerator Neutron Sources, Argonne National Laboratory (ANL), Argonne, Ill., May 22-24, 2007.
25. R.W. Bussard, "Method and Apparatus for Controlling Charged Particles," U.S. Patent #4,826,646, May 1989.
26. R.W. Bussard, "Some Physics Considerations of Magnetic Inertial-Electrostatic Confinement: A New Concept For Spherical Converging-Flow Fusion", *Fusion Technology*, vol. 19, pg. 273-293, March 1991.
27. D.C. Barnes, R.A. Nebel, and L. Turner, "Production and Application of Dense Penning Trap Plasmas," *Phys. Of Fluids B*, vol. 5, no. 10, pp. 3651-3660, Oct. 1993.
28. D.C. Barnes, T.B. Mitchell, and M.M. Schauer, "Beyond the Brillouin limit with the Penning Fusion Experiment," *Phys. Of Plasmas*, vol. 4, no. 5, pp. 1745-1751, May 1997.
29. R.A. Nebel, and D.C. Barnes, "The Periodically Oscillating Plasma Sphere," *Fus. Tech.*, vol. 34, pg. 28-45, Aug. 1998.
30. Alexander Klein, private communications.
31. Y. Gu, M. Williams, R. Stubbers, and G. Miley, "Pulsed Operation of Spherical Inertial-Electrostatic Confinement Device," *Fusion Technology*, vol. 30, pp. 1342-1346, Dec. 1996.
32. I.V. Tzonev, "Effect of Large Ion Angular Momentum Spread and High Current on Inertial Electrostatic Confinement Potential Structures," M.S. Thesis, University of Illinois-Urbana-Champaign, 1996.
33. W.C. Elmore, J.L. Tuck, and K.M. Watson, "On the Inertial-Electrostatic Confinement of a Plasma", *Phys. of Fluids*, vol. 2, no. 3, pp. 239-246, 1959.
34. R.L. Hirsch, "Inertial-Electrostatic Confinement of Ionized Fusion Gases", *J. of Applied Physics*, vol. 38, no. 11, pp. 4522, Oct. 1967.
35. T.J. Dolan, J.T. Verdeyen, D.J. Meeker, and B.E. Cherrington, "Electrostatic-Inertial Plasma Confinement", *J. Appl. Phys.*, vol. 43, no. 4, April 1972.
36. T. J. Dolan, "Electrostatic-Inertial Plasma Confinement," Ph. D. Dissertation, University of Illinois-Urbana-Champaign, 1975.

37. B.E. Cherrington, J.T. Verdeyan, and D.A. Swanson, "Recent Developments in Electrostatic Confinement-Theoretical", *Annals of N.Y. Acad. of Sci.*, vol. 251, pp. 139, 1975.
38. D. A. Swanson, "Theoretical Study of a Spherical Inertial Electrostatic Plasma Confinement Device," Ph. D. Dissertation, University of Illinois-Urbana-Champaign, 1975.
39. K.M Hu and Klevans, "On the theory of electrostatic confinement of plasmas with ion injection," *The Physics of Fluids*, vol. 17, no. 1, January 1974.
40. W.M. Black and E.H. Klevans, "Theory of potential-well formation in an electrostatic confinement device," *J. of App. Phys.*, vol. 45, no. 6, pp. 2502, June 1974.
41. G.R. Imel, "A Theoretical Model of a Spherical Electrostatic Confinement Device", M.S. Thesis, Pennsylvania State University, 1973.
42. E.H. Klevans, "Theoretical Models of Electrostatic Confinement Experiments," *Annals N.Y. Acad. Sci.*, vol. 251, pp. 190, 1975.
43. I. Langmuir and K. E. Blodgett "Currents limited by space charge between concentric spheres," *Phys. Rev.*, vol. 24, pp. 49, 1924.
44. R. W. Hockney, "Formation and stability of virtual electrodes in a cylinder," *J. Appl. Phys.*, vol. 39, no. 9, pp. 4166, Aug. 1968.
45. C. W. Barnes, "Computer Simulation of Electrostatic Confinement of Plasmas," *Annals New York Academy of Sciences*, vol. 251, pp. 370, 1975.
46. R.L. Hirsch, "Experimental Studies of a Deep, Negative, Electrostatic Potential Well in Spherical Geometry", *Phys. of Fluids*, vol. 11, no. 11, Nov. 1968.
47. D.A. Swanson, B.E. Cherrington, and J.T. Verdeyen, "Potential well structure in an inertial electrostatic plasma confinement device," *Phys. of Fluids*, vol. 16, no. 11, pp. 1939, Nov. 1973.
48. W.M. Black and J.W. Robinson, "Measuring rotationally symmetric potential profiles with an electron-beam probe", *J. of Appl. Physics*, vol. 45, no. 6, pp. 2479, June 1974.
49. W.M. Black, "Potential Well Formation in an Electrostatic Confinement Device", PhD Dissertation, Pennsylvania State University, 1971.

50. D.J. Meeker, J.T. Verdeyen, and B.E. Cherrington, "Measurement of electron density in a cylindrical inertial electrostatic plasma confinement device," *J. Appl. Phys.*, vol. 44, no. 12, Dec. 1973.
51. W.H. Grush, "Electrical Density Measurement of an Electrostatically-Confined, Spherically Symmetric, Helium Plasma Using A Microwave Cavity Resonance Shift Technique," M.S. Thesis, Pennsylvania State University, 1973.
52. A.L. Gardner, D.M. Hatch, A.I.Y. Chan, and R.P. Evans, "Measurement of a Spherical Electrostatic Confinement System Employing Six Ion Guns," *Annals N.Y. Acad. Sci.*, vol. 251, pp. 179, 1975.
53. G.H. Miley, Y. Gu, J.M. Demora, R.A. Stubbers, T.A. Hochberg, J.H. Nadler, and R.A. Anderl, "Discharge Characteristics of the Spherical Inertial Electrostatic Confinement (IEC) Device," *IEEE Transactions on Plasma Science*, vol. 25, no. 4, pp. 733-739, Aug. 1997.
54. Y. Gu and G.H. Miley, "Experimental Study of Potential Structure in a Spherical IEC Fusion Device," *IEEE Trans. on Plasma Sci.*, vol. 28, no. 1, pp. 331, Feb. 2000.
55. T.A. Hochberg, "Characterization and Modelling of the Gas Discharge in a SFID Neutron Generator," M.S. Thesis, University of Illinois-Urbana-Champaign, 1992.
56. B.P. Bromley, "Approximate Modeling of the Inertial Electrostatic Confinement Cylindrical Device," M.S. Thesis, University of Illinois-Urbana-Champaign, 1998.
57. J.M. Demora, "Cathode Grid Optimization Studies for the Spherical Inertial Electrostatic Confinement Device," M.S. Thesis, University of Illinois-Urbana-Champaign, 1999.
58. G.H. Miley, J. DeMora, R.A. Anderl, J.H. Nadler, and R. Nebel, "Optimization of IEC Grid Design For Maximum Neutron Production," *Fusion Technology*, vol. 30, pp. 1315-1319, Dec. 1996.
59. B.E. Jurczyk, "Research on Edge Ionization and Star Mode Discharge Physics in Inertial Electrostatic Confinement Neutron/Proton Sources", Ph.D. Dissertation, University of Illinois-Urbana-Champaign, 2001.
60. R.A. Stubbers, "Two Dimensional Modeling of a Radially-Convergent Cylindrical Inertial Electrostatic Confinement (IEC) Fusion Device," Ph.D. Dissertation, University of Illinois-Urbana-Champaign, 2002.

61. H. Momota and G.H. Miley, "Virtual Cathode in a Stationary Spherical Inertial Electrostatic Confinement," *Fusion Science and Technology*, vol. 40, pp. 56, July 2001.
62. H. Matsuura, T. Takaki, Y. Nakao, and K. Kudo, "Radial profile of neutron production rate in spherical inertial electrostatic confinement plasmas," *Fusion Technology*, vol. 39, pp. 1167, May 2001.
63. C.C. Dobson and I. Hrbub, "Electron density and two-channel neutron emission measurements in steady-state spherical inertial-electrostatically confined plasmas, with review of the one-dimensional kinetic model", *J. Appl. Phys.*, vol. 96, no. 1, pg. 94-107, July 1, 2004.
64. R. M. Meyer, S. K. Loyalka, and M. A. Prelas, "Potential Well Structures in Spherical Inertial Electrostatic Confinement Devices," *IEEE Trans. on Plasma Science*, vol. 33, no. 4, pp. 1377-1394, Aug. 2005.
65. R. M. Meyer, S. K. Loyalka, and M. A. Prelas, "Double Potential Well Regimes in Collisionless Spherical Discharges," *IEEE Trans. on Plasma Science*, vol. 35, no. 2, pp. 354-360, April 2007.
66. T.A. Thorson, R.D. Durst, R.J. Fonck, and L.P. Wainwright "Convergence, electrostatic potential, and density measurements in a spherically convergent ion focus", *Physics of Plasmas*, vol. 4, no. 1, pp. 4-15, Jan. 1997.
67. T.A. Thorson, "Ion Flow and Fusion Reactivity Characterization of a Spherically Convergent Ion Focus", Ph.D. Dissertation, University of Wisconsin-Madison, 1996.
68. J. Kachan, "Spatial distribution of ion energies in an inertial electrostatic confinement device," vol. 10, no. 3, pp. 596, March 2003.
69. A.J. Satsangi, "Light Intensity Measurements of an Inertial Electrostatic Confinement Fusion Plasma," M.S. Thesis, University of Illinois-Urbana-Champaign, 1996.
70. K. Yoshikawa, K. Takiyama, T. Koyama, K. Taruya, K. Masuda, Y. Yamamoto T. Toku, T. Kii, H. Hashimoto, N. Inoue, M. Ohnishi, and H. Horiike., "Measurement of Strongly Localized Potential Well Profiles in an Inertial-Electrostatic Fusion Neutron Source", *Nuc. Fus.*, vol. 41, no. 6, pg. 717-720, 2001.

71. K. Yoshikawa, K. Masuda, H. Toku, A. Nagafuchi, T. Mizutani, H. Hashimoto, K. Nagasaki, Y. Yamamoto, K. Takiyama, M. Ohnishi, H. Matsuura, K. Funakoshi, Y. Nakao, "Potential Profiles in the Central Core of the Cathode in the Star Mode Operation in an Inertial-Electrostatic Fusion Neutron Source," 19<sup>th</sup> IAEA Fusion Energy Conference, Oct. 14-19 2002, Lyon, France.
72. G.L. Kulcinski, E.C. Alderson, R.P. Ashley, D.R. Boris, L. Campbell, D.C. Donovan, B.J. Egle, G. A. Emmert, G.R. Piefer, R.F. Radel, P. Rusch, J.H. Sorebo, J.F. Santarius, S.J. Zenobia, "Overview of the University of Wisconsin-Madison IEC Program," US-Japan Workshop on Small Plasma and Accelerator Neutron Sources, Argonne National Laboratory (ANL), Argonne, Ill., May 22-24, 2007.
73. G.L. Kulcinski, E.C. Alderson, R.P. Ashley, D.R. Boris, L. Campbell, D.C. Donovan, B.J. Egle, G. A. Emmert, G.R. Piefer, R.F. Radel, P. Rusch, J.H. Sorebo, J.F. Santarius, S.J. Zenobia, "Overview of the University of Wisconsin-Madison IEC Program," US-Japan Workshop on Small Plasma and Accelerator Neutron Sources, Argonne National Laboratory (ANL), Argonne, Ill., May 22-24, 2007.
74. G. R. Piefer, J. F. Santarius, R. P. Ashley, G. L. Kulcinski, "Measurement of  $3\text{He}(3\text{He},2p)4\text{He}$  Reactions in an IEC Device," US-Japan Workshop on Small Plasma and Accelerator Neutron Sources, Argonne National Laboratory (ANL), Argonne, Ill., May 22-24, 2007.
75. K. Yamauchi, K. Nozaki, M. Watanabe, A. Okino and E. Hotta, "Low Pressure IECF Operation Using Differentially-Pumped Ion Sources", US-Japan Workshop on Small Plasma and Accelerator Neutron Sources, Argonne National Laboratory (ANL), Argonne, Ill., May 22-24, 2007.
76. R.J. Sedwick, T.J. McGuire, C.C. Dietrich, N.Z. Warner, and D.A. Zayas, "Multi-Grid IEC Fusion for Space Power and Propulsion," ???
77. M.A. Lieberman and A.J. Lichtenberg, "Principles of Plasma Discharges and Materials Processing," Wiley-Interscience, New York, pp. 451, 1994.
78. B. Chapman, "Glow Discharge Processes: Sputtering and Plasma Etching," Wiley-Interscience, New York, pp. 79, 1980.
79. A. von Engel, "Ionized Gases," AIP Press, New York, pp. 218, 1965.
80. N. Hershkowitz, in "Plasma Diagnostics", O. Auciello and D.L. Flamm, eds., Academic Press, New York, 1989.
81. J.F. Santarius, private communications.

## APPENDIX A: Bi-polar 1-D Orbital Results

Several observables are mapped in the control variable spaces with the 1D orbital model of a bi-polar discharge, from Chapter II. In Chapter II, several double well depth (*DWD*) calculations are presented. Here, we present the results for the rest of the observables, namely: core electron and ion densities ( $n_i(0)$  and  $n_o(0)$ ), minimum inter-cathode potential ( $Y_{min}$ ), core potential ( $Y_{core}$ ), and the width of the double potential wells as defined in Chapter I. The results are dispersed among Fig. 165 through Fig. 229 as follows:

Table XI: Maps of observables in control variable space are given in Fig. 165 through Fig. 229 as indicated.

<i>Observable</i>	<i>Control Variables</i>	<i>Figure</i>
width	$P_0 - \beta$	Fig. 165 - Fig. 166
width	$\sigma_{i\phi} - \sigma_{e\phi}$	Fig. 167 - Fig. 174
$Y_{min}$	$P_0 - \beta$	Fig. 175 - Fig. 176
$Y_{min}$	$\sigma_{i\phi} - \sigma_{e\phi}$	Fig. 177 - Fig. 184
$Y_{core}$	$P_0 - \beta$	Fig. 185 - Fig. 187
$Y_{core}$	$\sigma_{i\phi} - \sigma_{e\phi}$	Fig. 188 - Fig. 199
$n_e(0)$	$P_0 - \beta$	Fig. 200 - Fig. 202
$n_e(0)$	$\sigma_{i\phi} - \sigma_{e\phi}$	Fig. 203 - Fig. 214
$n_i(0)$	$P_0 - \beta$	Fig. 215 - Fig. 217
$n_i(0)$	$\sigma_{i\phi} - \sigma_{e\phi}$	Fig. 218 - Fig. 229

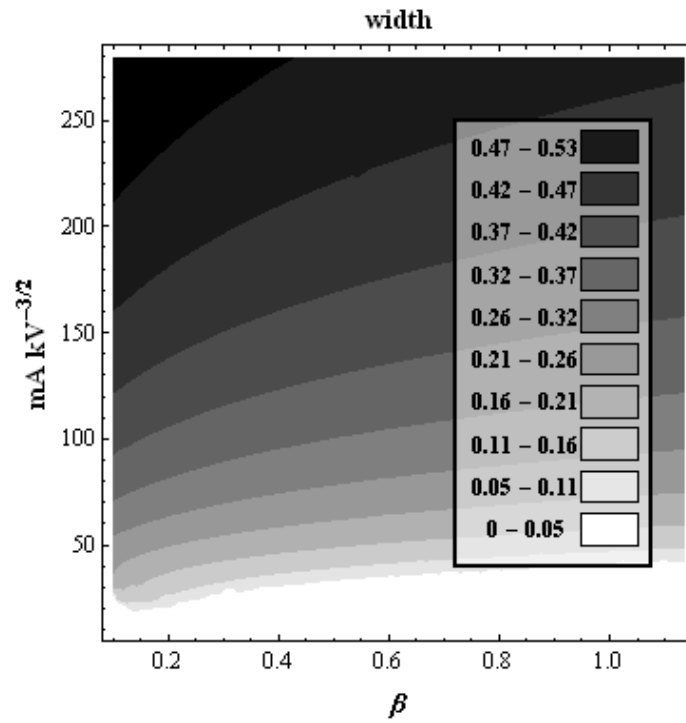


Fig. 165: "Width" with respect to  $P_i$  and  $\beta$ . This plot is computed with  $\sigma_{e\phi} = 0.005$  and  $\sigma_{i\phi} = 0.05$ .

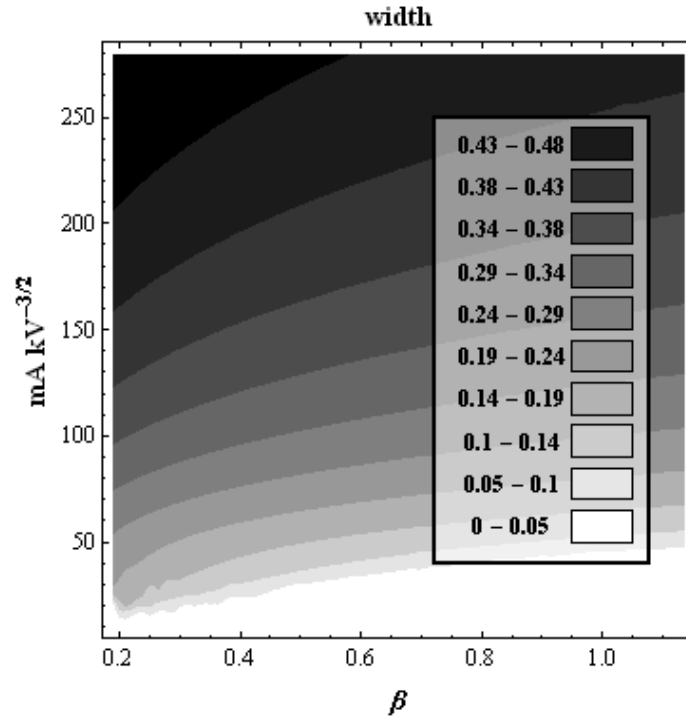


Fig. 166: "Width" with respect to  $P_i$  and  $\beta$ . This plot is computed with  $\sigma_{e\phi} = 0.005$  and  $\sigma_{i\phi} = 0.10$ .

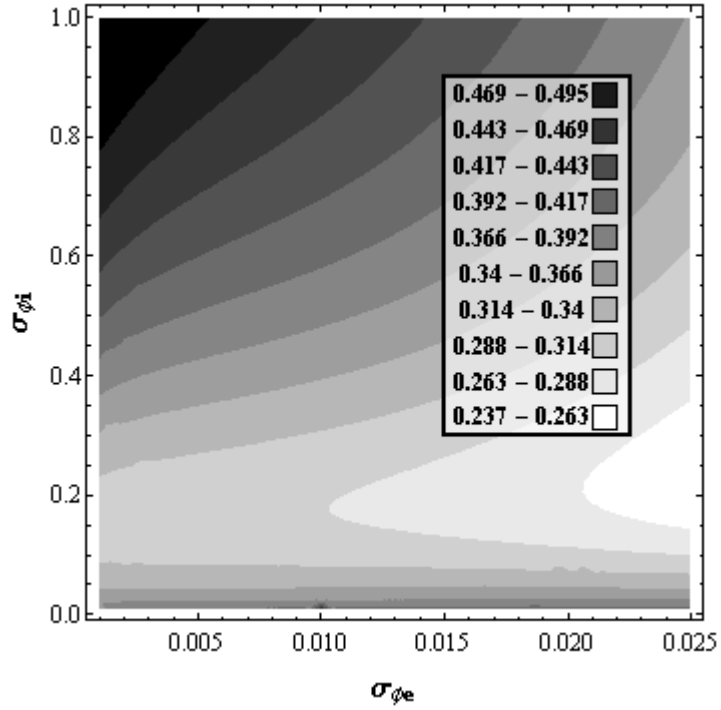


Fig. 167: “Width” with respect to  $\sigma_{e\phi}$  and  $\sigma_{i\phi}$ . This plot is computed with  $P_i = 100 \text{ mA kV}^{-3/2}$  and  $\beta = 0.25$ .

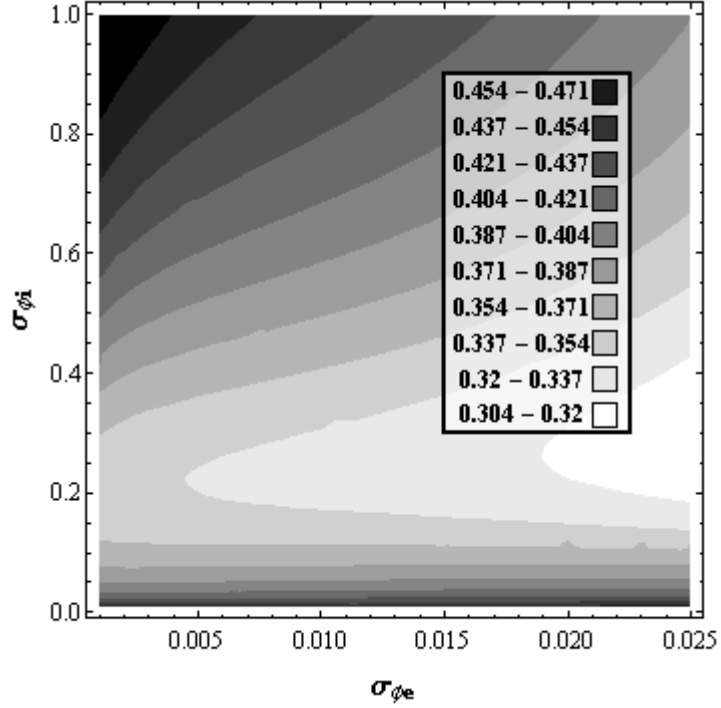


Fig. 168: “Width” with respect to  $\sigma_{e\phi}$  and  $\sigma_{i\phi}$ . This plot is computed with  $P_i = 138 \text{ mA kV}^{-3/2}$  and  $\beta = 0.25$ .

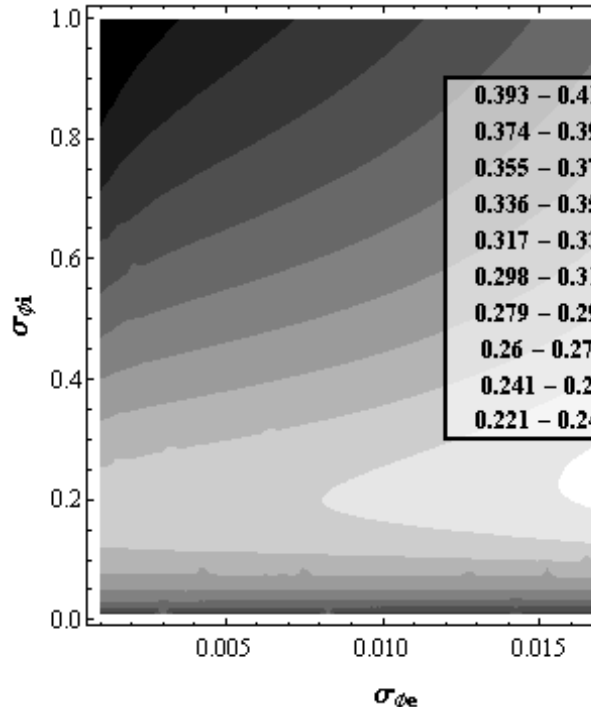


Fig. 169: “Width” with respect to  $\sigma_{e\phi}$  and  $\sigma_{i\phi}$ . This plot is computed with  $P_i = 100 \text{ mA kV}^{-3/2}$  and  $\beta = 0.33$ .

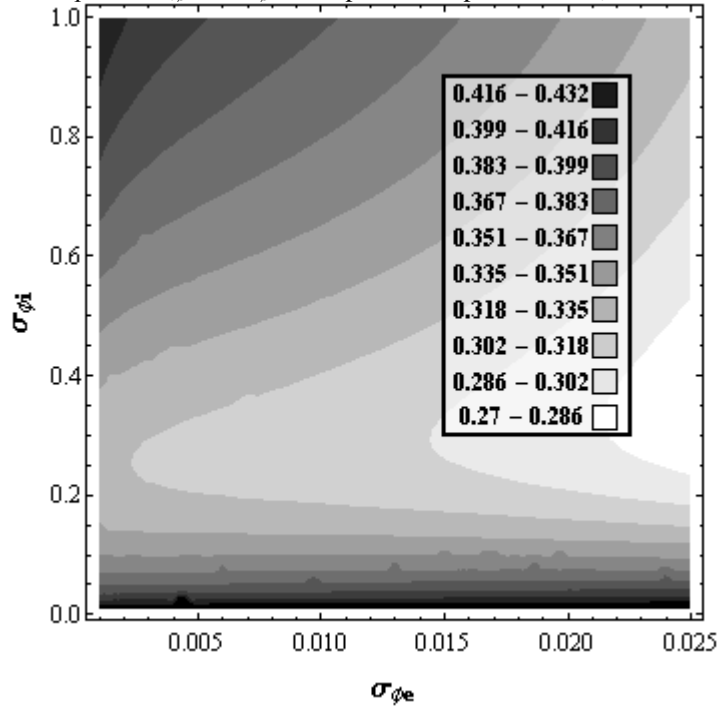


Fig. 170: “Width” with respect to  $\sigma_{e\phi}$  and  $\sigma_{i\phi}$ . This plot is computed with  $P_i = 138 \text{ mA kV}^{-3/2}$  and  $\beta = 0.33$ .

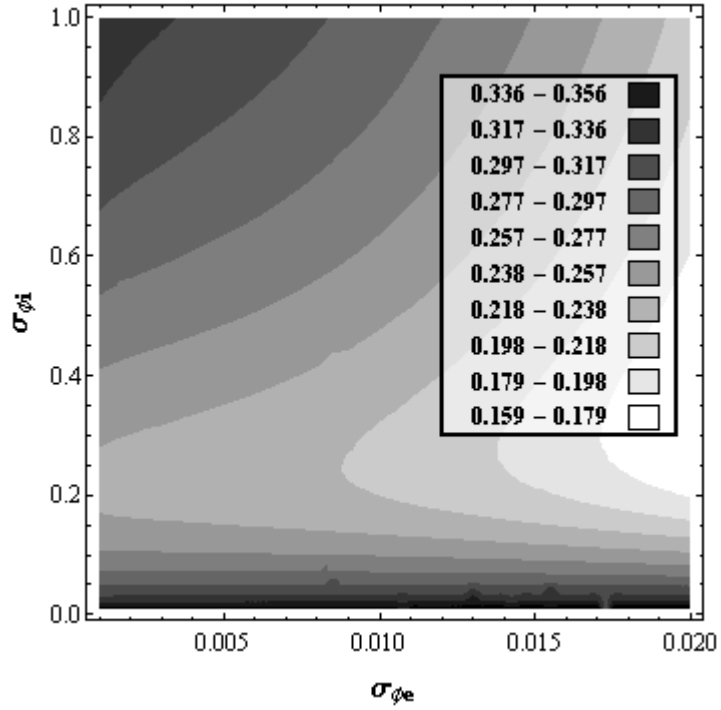


Fig. 171: “Width” with respect to  $\sigma_{e\phi}$  and  $\sigma_{i\phi}$ . This plot is computed with  $P_i = 100 \text{ mA kV}^{-3/2}$  and  $\beta = 0.50$ .

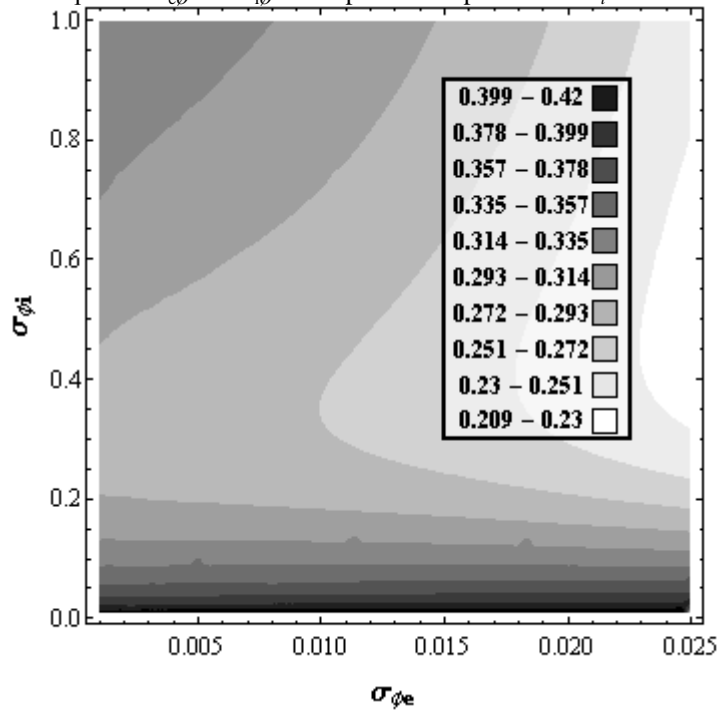


Fig. 172: “Width” with respect to  $\sigma_{e\phi}$  and  $\sigma_{i\phi}$ . This plot is computed with  $P_i = 138 \text{ mA kV}^{-3/2}$  and  $\beta = 0.50$ .

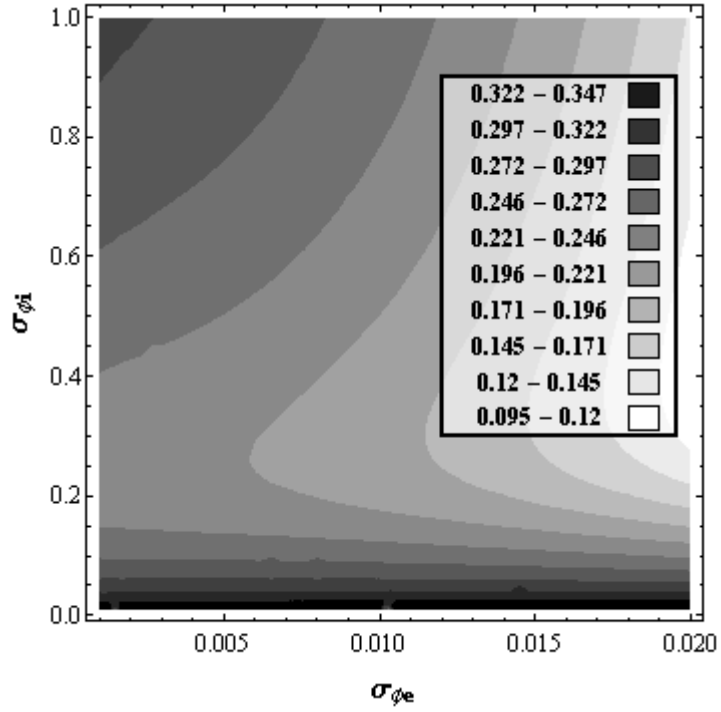


Fig. 173: “Width” with respect to  $\sigma_{e\phi}$  and  $\sigma_{i\phi}$ . This plot is computed with  $P_i = 100 \text{ mA kV}^{-3/2}$  and  $\beta = 0.67$ .

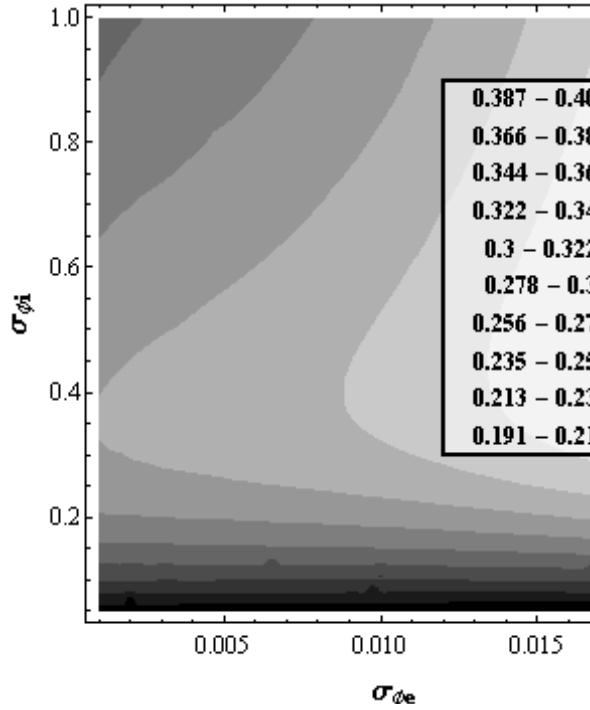


Fig. 174: “Width” with respect to  $\sigma_{e\phi}$  and  $\sigma_{i\phi}$ . This plot is computed with  $P_i = 138 \text{ mA kV}^{-3/2}$  and  $\beta = 0.67$ .

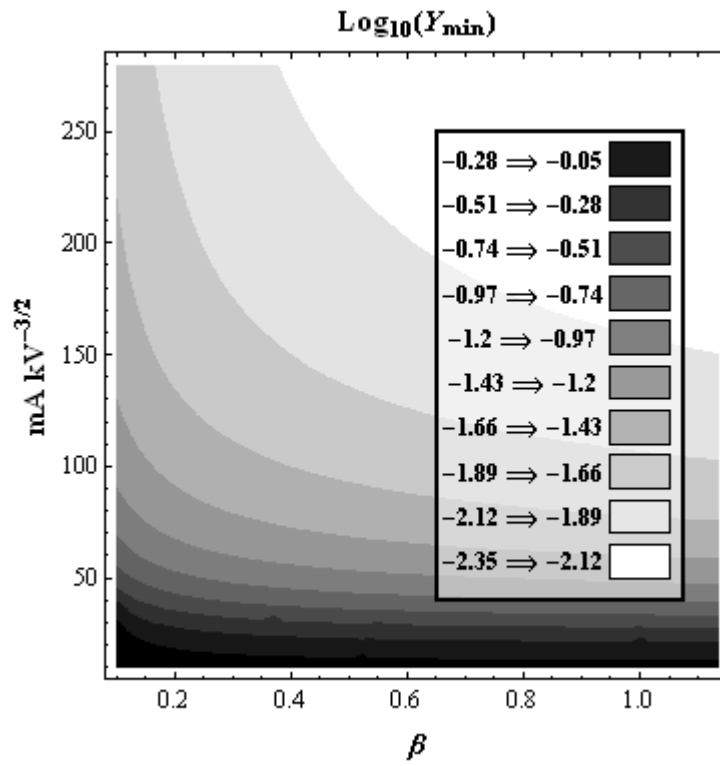


Fig. 175:  $\text{Log}_{10}(Y_{\min})$  with respect to  $P_i$  and  $\beta$ . This plot is computed with  $\sigma_{e\theta} = 0.005$  and  $\sigma_{i\theta} = 0.05$ .

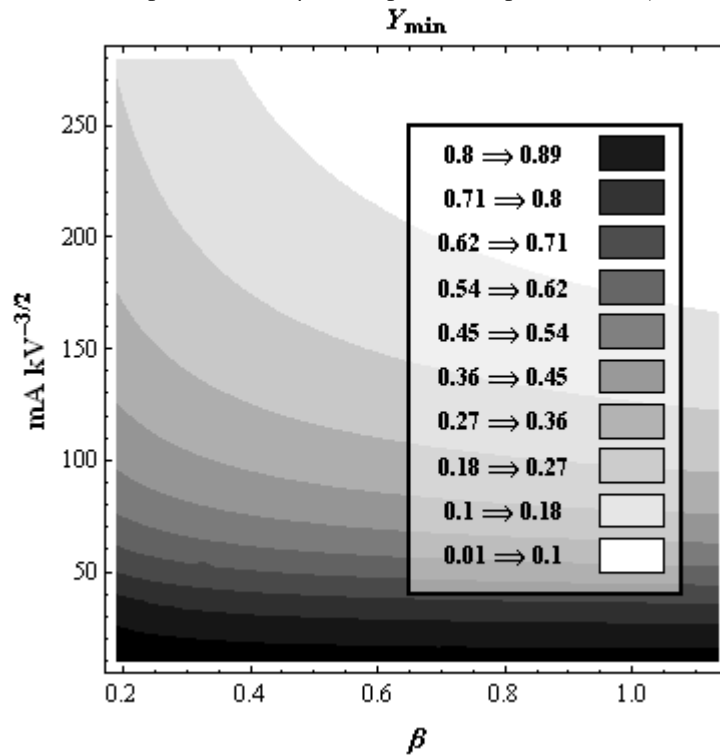


Fig. 176:  $Y_{\min}$  with respect to  $P_i$  and  $\beta$ . This plot is computed with  $\sigma_{e\theta} = 0.005$  and  $\sigma_{i\theta} = 0.10$ .

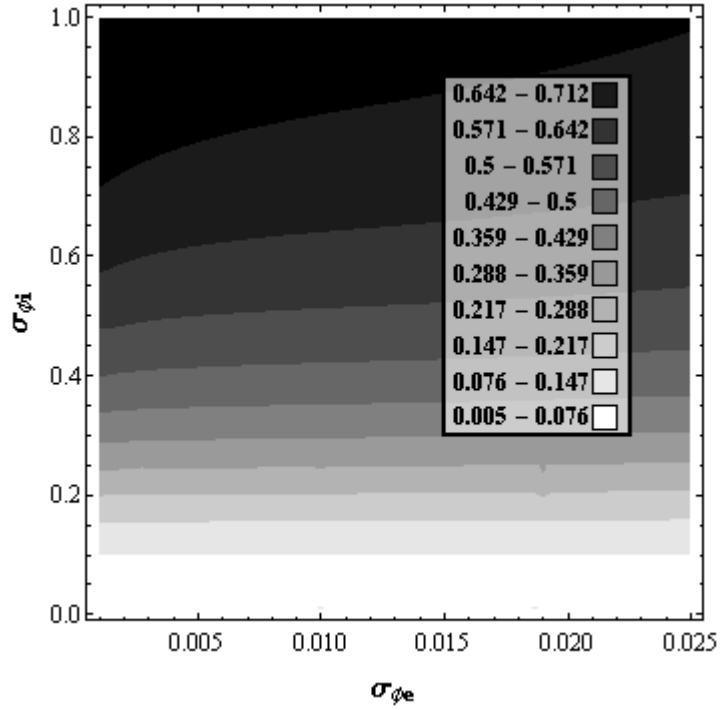


Fig. 177:  $Y_{\min}$  with respect to  $\sigma_{e\theta}$  and  $\sigma_{i\theta}$ . This plot is computed with  $P_i = 100 \text{ mA kV}^{-3/2}$  and  $\beta = 0.25$ .

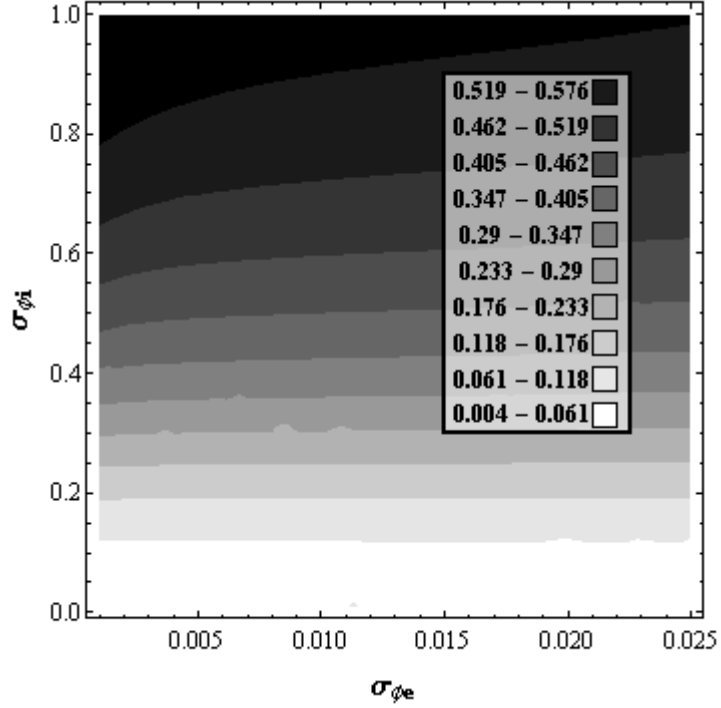


Fig. 178:  $Y_{\min}$  with respect to  $\sigma_{e\theta}$  and  $\sigma_{i\theta}$ . This plot is computed with  $P_i = 138 \text{ mA kV}^{-3/2}$  and  $\beta = 0.25$ .

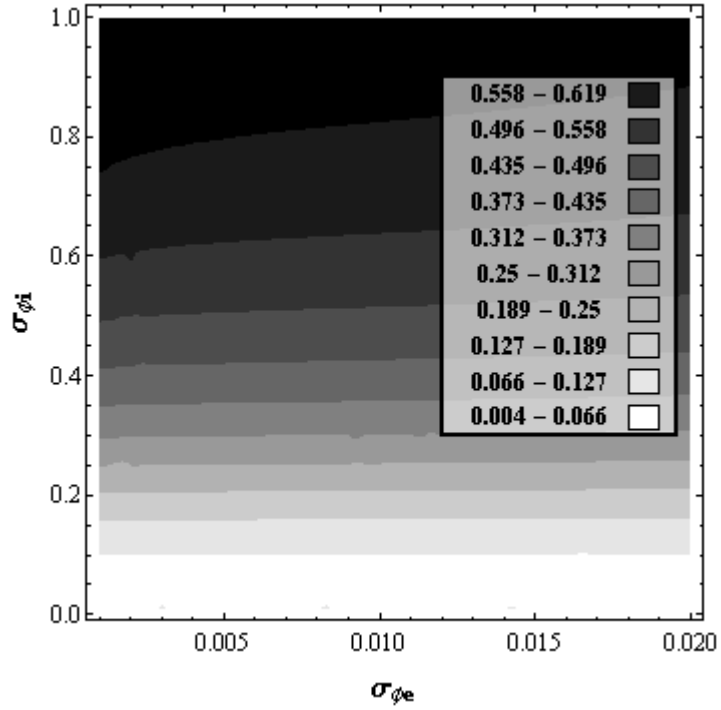


Fig. 179:  $Y_{\min}$  with respect to  $\sigma_{e\phi}$  and  $\sigma_{i\phi}$ . This plot is computed with  $P_i = 100 \text{ mA kV}^{-3/2}$  and  $\beta = 0.33$ .

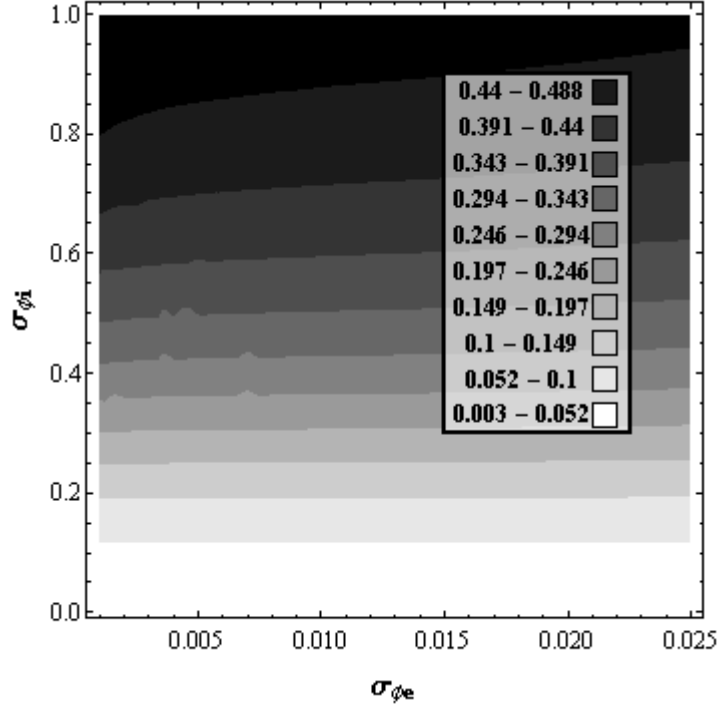


Fig. 180:  $Y_{\min}$  with respect to  $\sigma_{e\phi}$  and  $\sigma_{i\phi}$ . This plot is computed with  $P_i = 138 \text{ mA kV}^{-3/2}$  and  $\beta = 0.33$ .

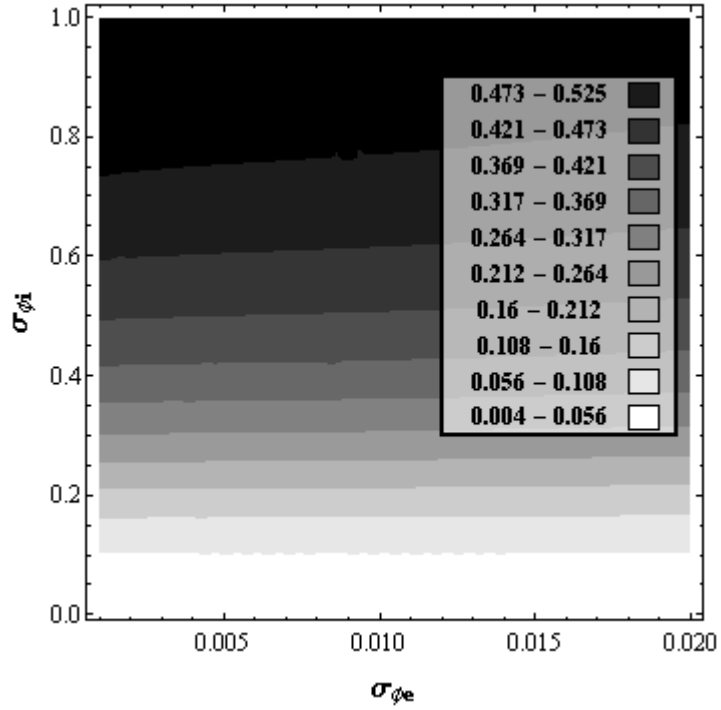


Fig. 181:  $Y_{\min}$  with respect to  $\sigma_{e\theta}$  and  $\sigma_{i\theta}$ . This plot is computed with  $P_i = 100 \text{ mA kV}^{-3/2}$  and  $\beta = 0.50$ .

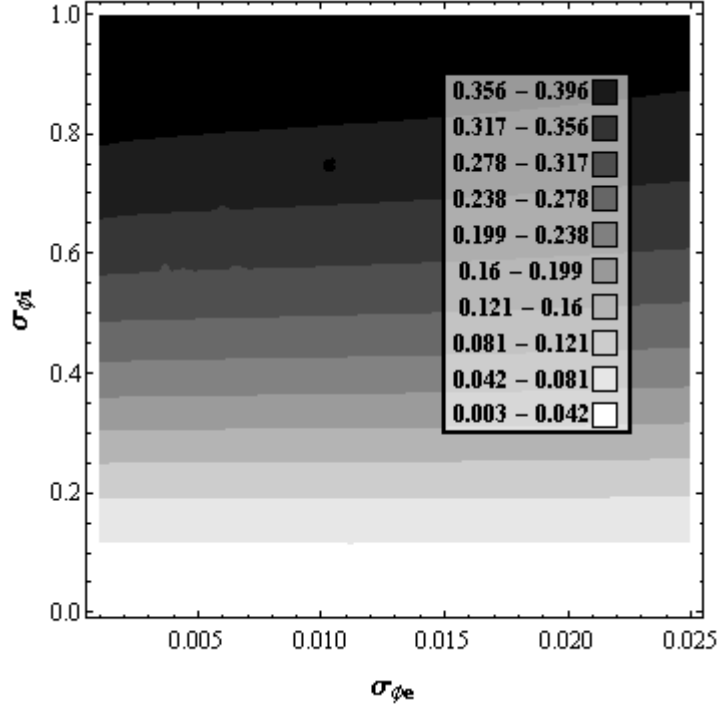


Fig. 182:  $Y_{\min}$  with respect to  $\sigma_{e\theta}$  and  $\sigma_{i\theta}$ . This plot is computed with  $P_i = 138 \text{ mA kV}^{-3/2}$  and  $\beta = 0.50$ .

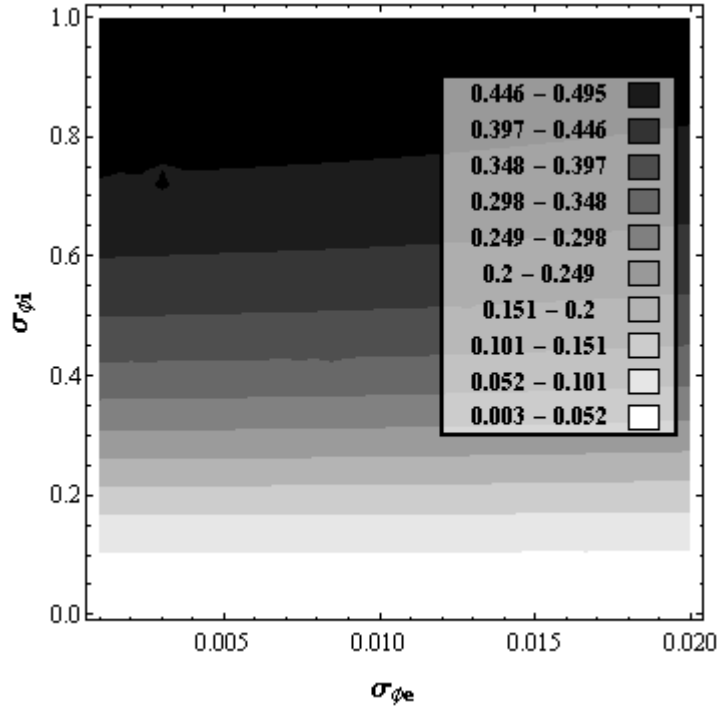


Fig. 183:  $Y_{\min}$  with respect to  $\sigma_{e\theta}$  and  $\sigma_{i\theta}$ . This plot is computed with  $P_i = 100 \text{ mA kV}^{-3/2}$  and  $\beta = 0.67$ .

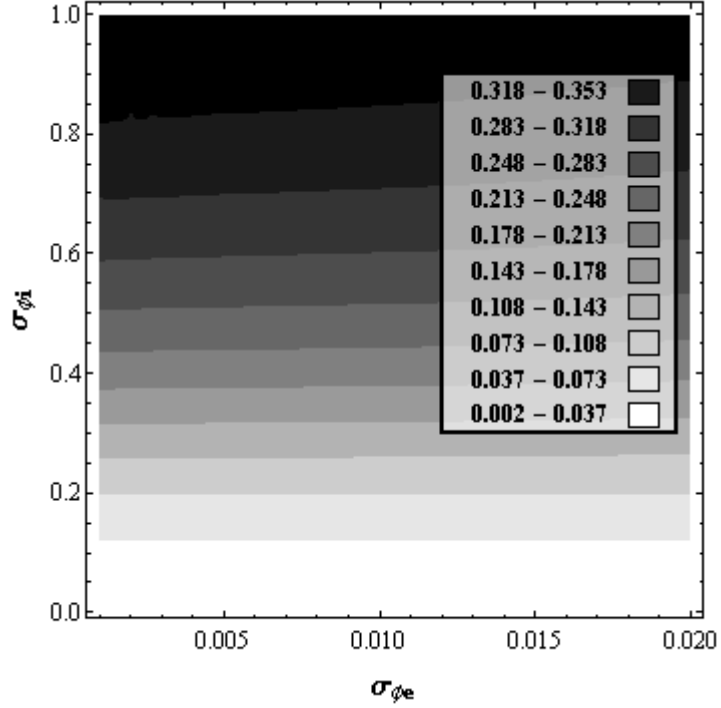


Fig. 184:  $Y_{\min}$  with respect to  $\sigma_{e\theta}$  and  $\sigma_{i\theta}$ . This plot is computed with  $P_i = 138 \text{ mA kV}^{-3/2}$  and  $\beta = 0.67$ .

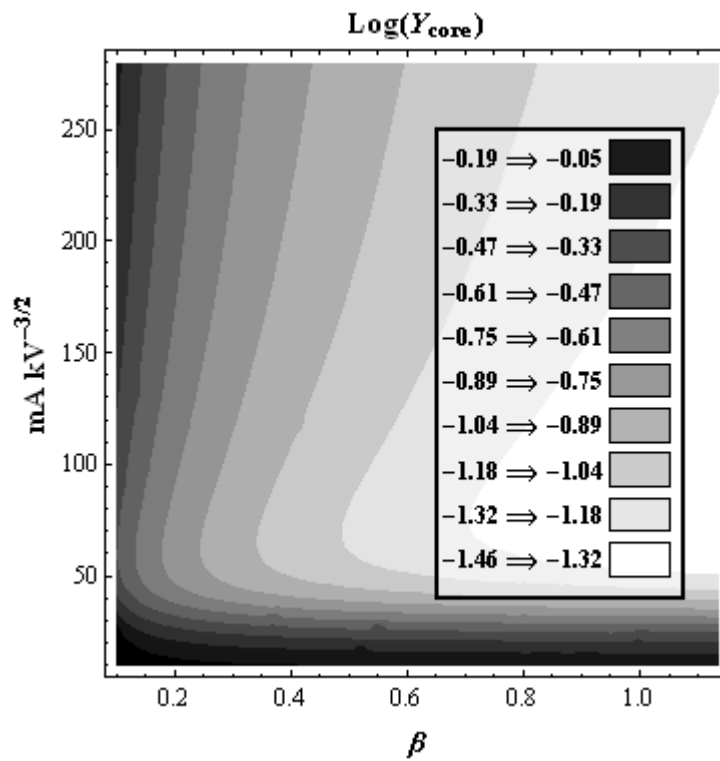


Fig. 185:  $\text{Log}_{10}(Y_{\text{core}})$  with respect to  $P_i$  and  $\beta$ . This plot is computed with  $\sigma_{e0} = 0.005$  and  $\sigma_{i0} = 0.05$ .

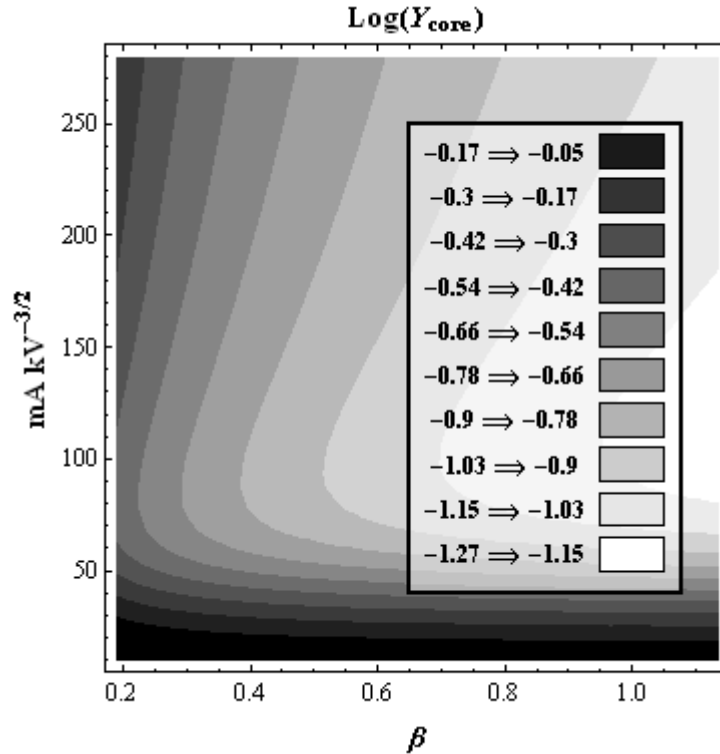


Fig. 186:  $\text{Log}_{10}(Y_{\text{core}})$  with respect to  $P_i$  and  $\beta$ . This plot is computed with  $\sigma_{e0} = 0.005$  and  $\sigma_{i0} = 0.10$ .

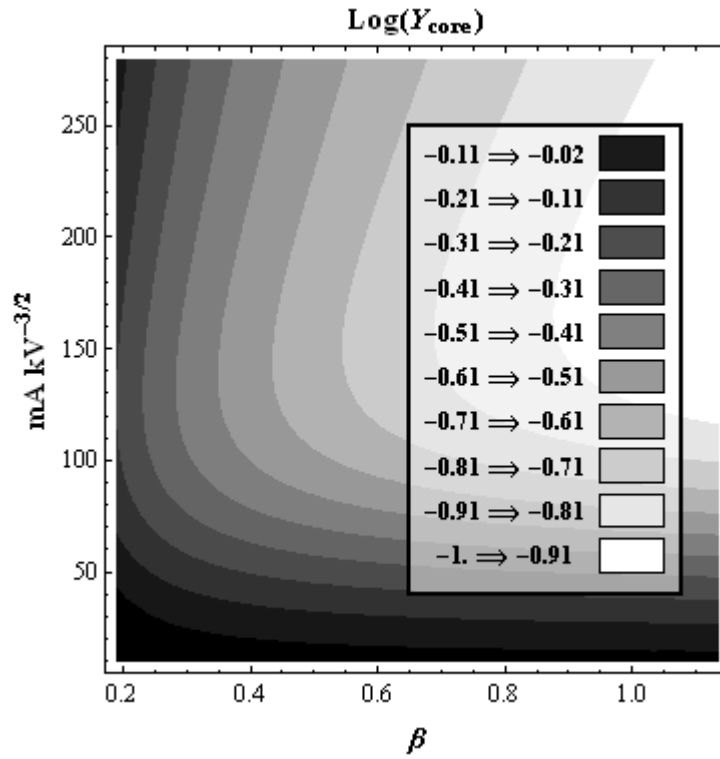


Fig. 187:  $\text{Log}_{10}(Y_{\text{core}})$  with respect to  $P_i$  and  $\beta$ . This plot is computed with  $\sigma_{e\phi} = 0.005$  and  $\sigma_{i\phi} = 0.25$ .

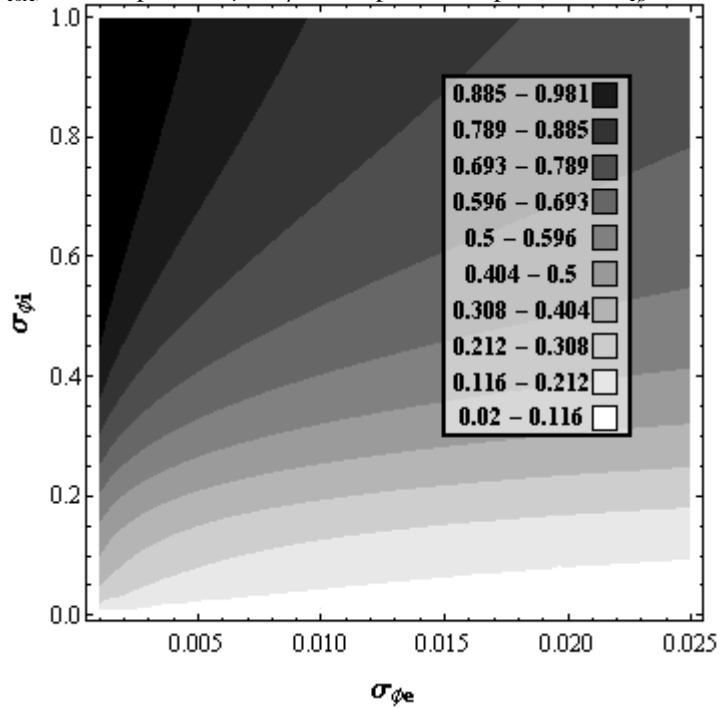


Fig. 188:  $Y_{\text{core}}$  with respect to  $\sigma_{e\phi}$  and  $\sigma_{i\phi}$ . This plot is computed with  $P_i = 100 \text{ mA kV}^{-3/2}$  and  $\beta = 0.25$ .

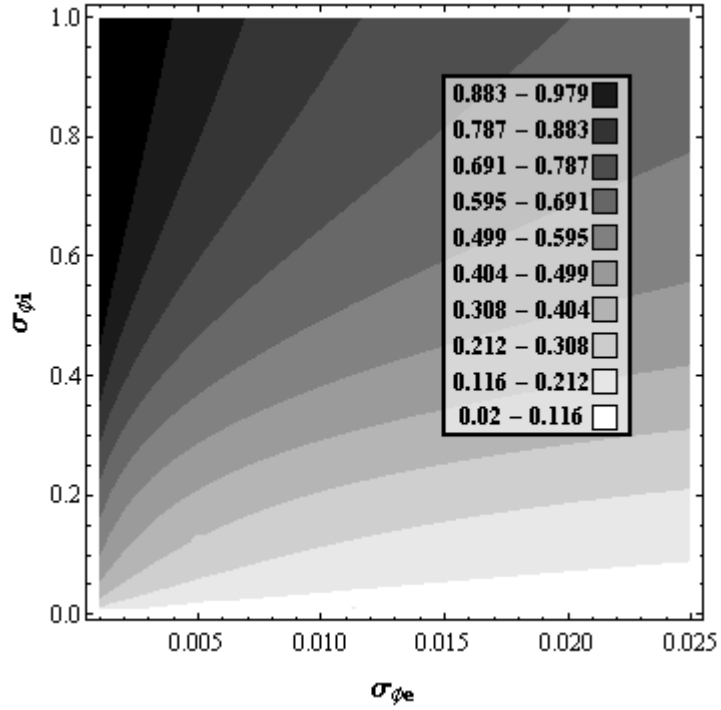


Fig. 189:  $Y_{\text{core}}$  with respect to  $\sigma_{e\theta}$  and  $\sigma_{i\theta}$ . This plot is computed with  $P_i = 138 \text{ mA kV}^{-3/2}$  and  $\beta = 0.25$ .

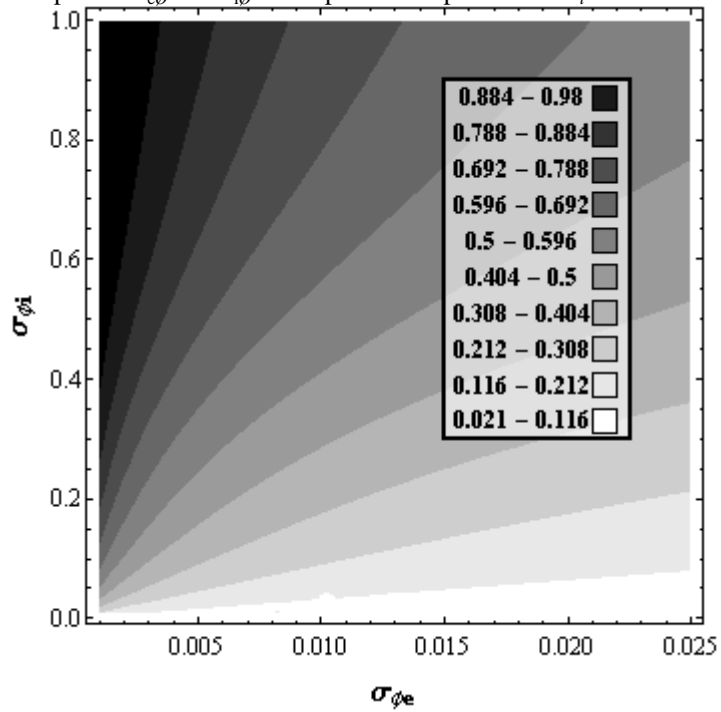


Fig. 190:  $Y_{\text{core}}$  with respect to  $\sigma_{e\theta}$  and  $\sigma_{i\theta}$ . This plot is computed with  $P_i = 200 \text{ mA kV}^{-3/2}$  and  $\beta = 0.25$ .

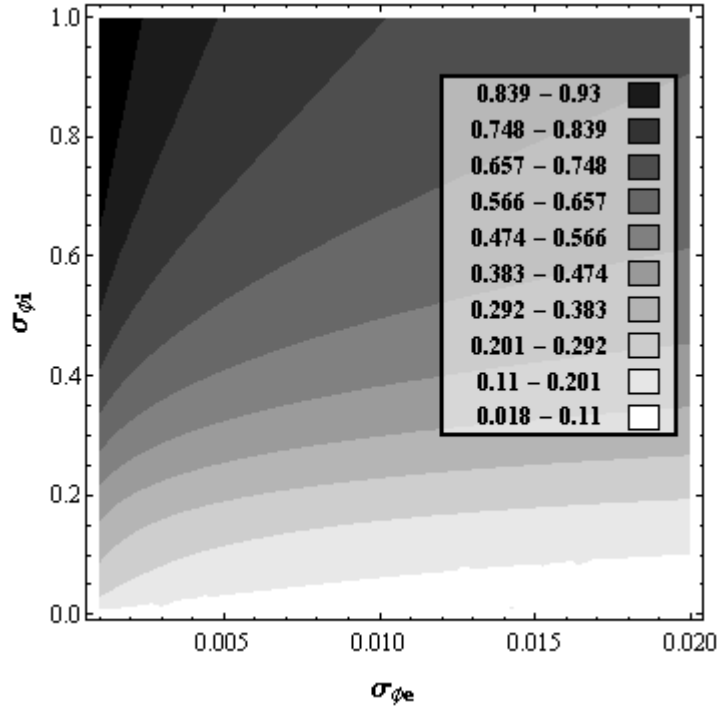


Fig. 191:  $Y_{\text{core}}$  with respect to  $\sigma_{e\theta}$  and  $\sigma_{i\theta}$ . This plot is computed with  $P_i = 100 \text{ mA kV}^{-3/2}$  and  $\beta = 0.33$ .

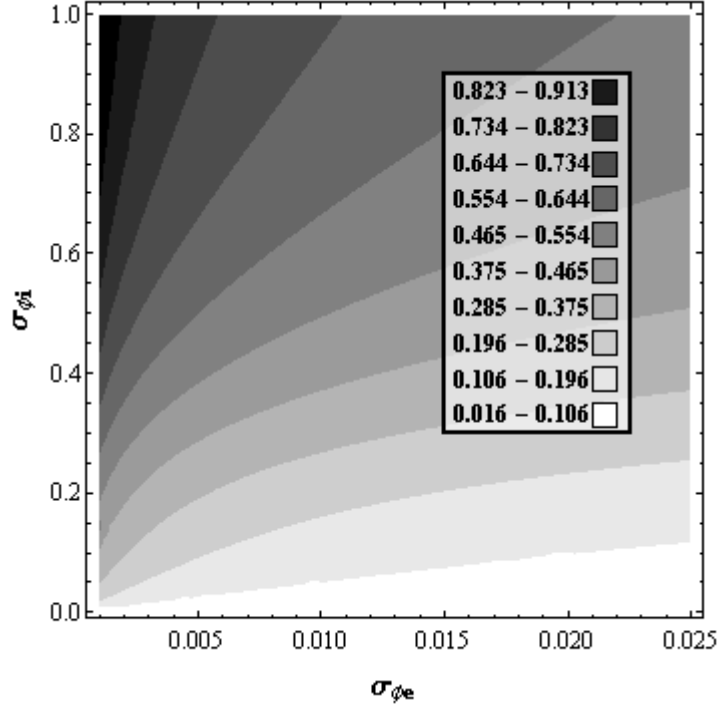


Fig. 192:  $Y_{\text{core}}$  with respect to  $\sigma_{e\theta}$  and  $\sigma_{i\theta}$ . This plot is computed with  $P_i = 138 \text{ mA kV}^{-3/2}$  and  $\beta = 0.33$ .

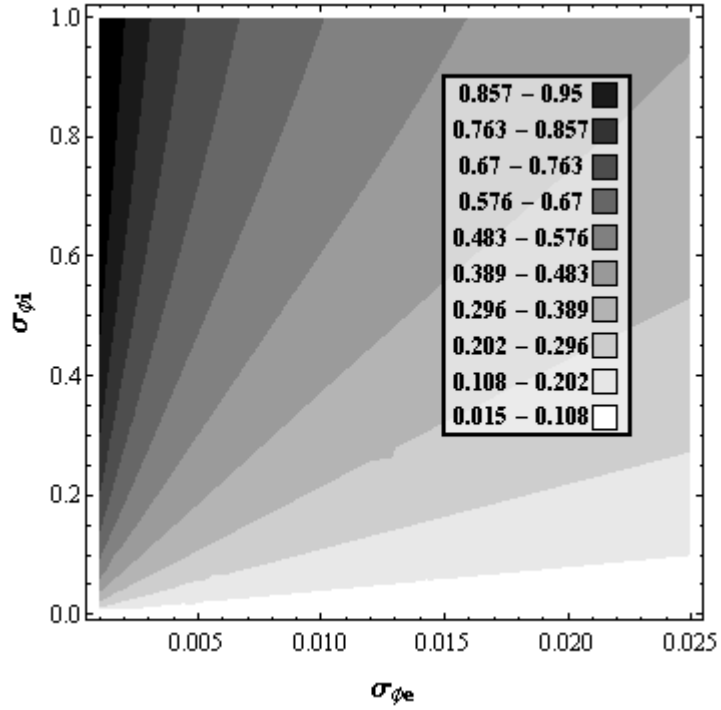


Fig. 193:  $Y_{\text{core}}$  with respect to  $\sigma_{e\theta}$  and  $\sigma_{i\theta}$ . This plot is computed with  $P_i = 276 \text{ mA kV}^{-3/2}$  and  $\beta = 0.33$ .

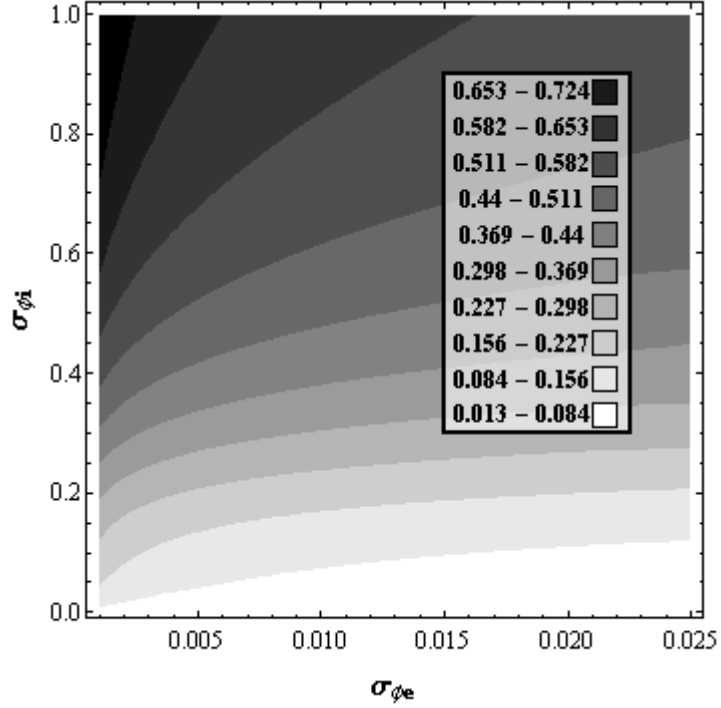


Fig. 194:  $Y_{\text{core}}$  with respect to  $\sigma_{e\theta}$  and  $\sigma_{i\theta}$ . This plot is computed with  $P_i = 100 \text{ mA kV}^{-3/2}$  and  $\beta = 0.50$ .

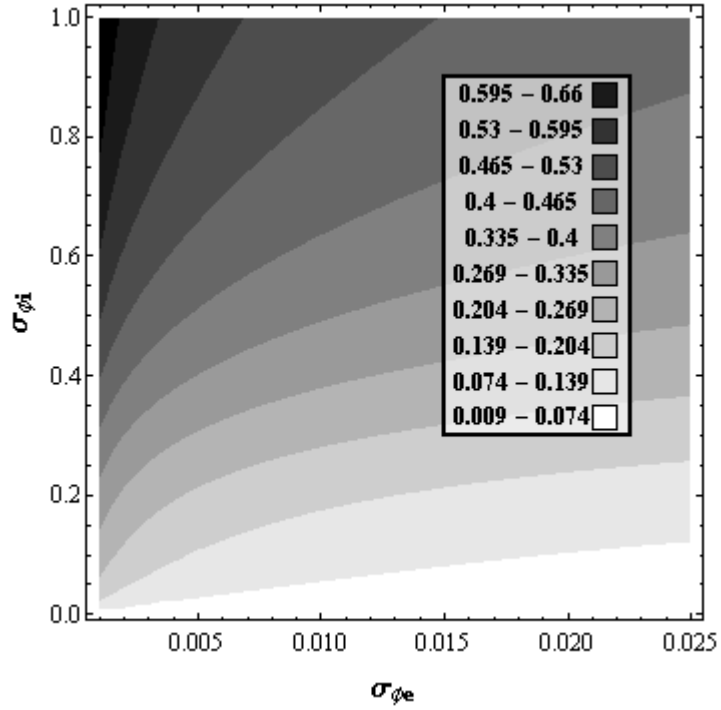


Fig. 195:  $Y_{\text{core}}$  with respect to  $\sigma_{e\theta}$  and  $\sigma_{i\theta}$ . This plot is computed with  $P_i = 138 \text{ mA kV}^{-3/2}$  and  $\beta = 0.50$ .

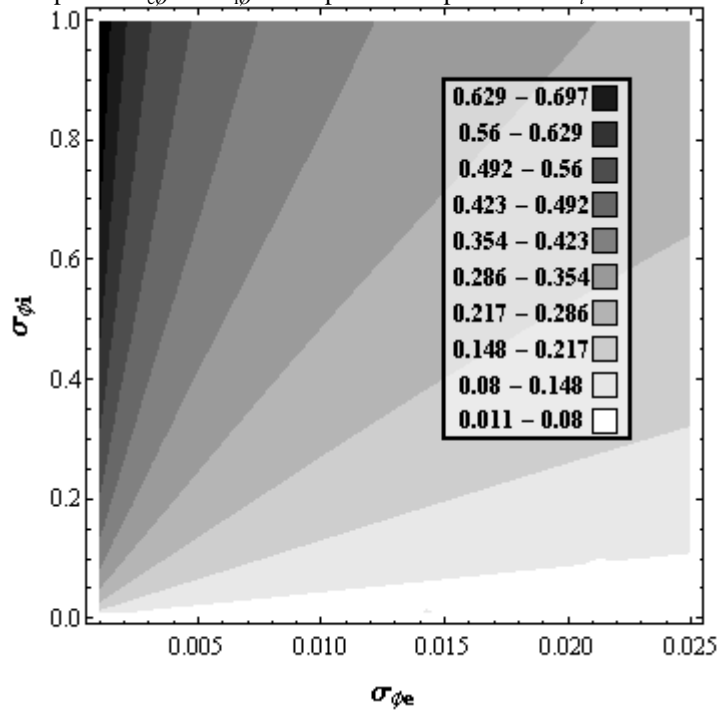


Fig. 196:  $Y_{\text{core}}$  with respect to  $\sigma_{e\theta}$  and  $\sigma_{i\theta}$ . This plot is computed with  $P_i = 276 \text{ mA kV}^{-3/2}$  and  $\beta = 0.50$ .

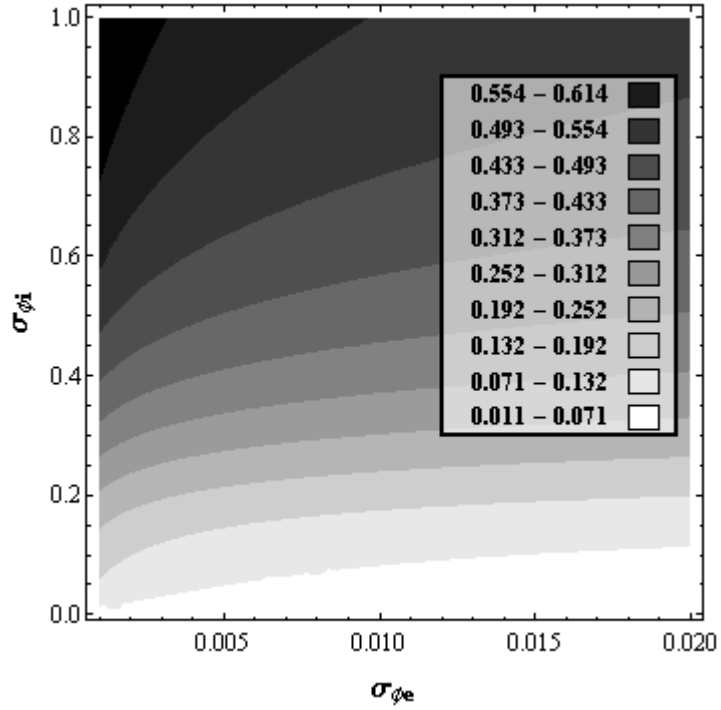


Fig. 197:  $Y_{\text{core}}$  with respect to  $\sigma_{e\theta}$  and  $\sigma_{i\theta}$ . This plot is computed with  $P_i = 100 \text{ mA kV}^{-3/2}$  and  $\beta = 0.67$ .

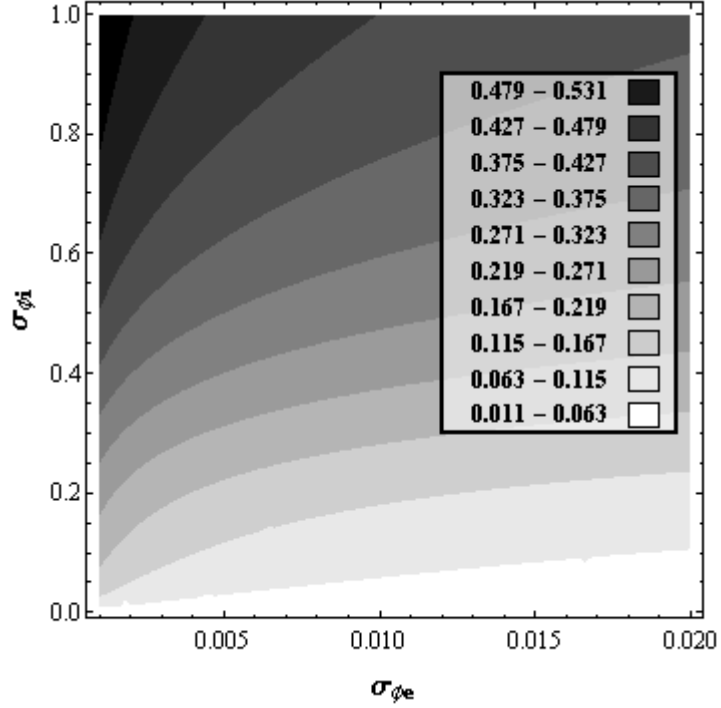


Fig. 198:  $Y_{\text{core}}$  with respect to  $\sigma_{e\theta}$  and  $\sigma_{i\theta}$ . This plot is computed with  $P_i = 138 \text{ mA kV}^{-3/2}$  and  $\beta = 0.67$ .

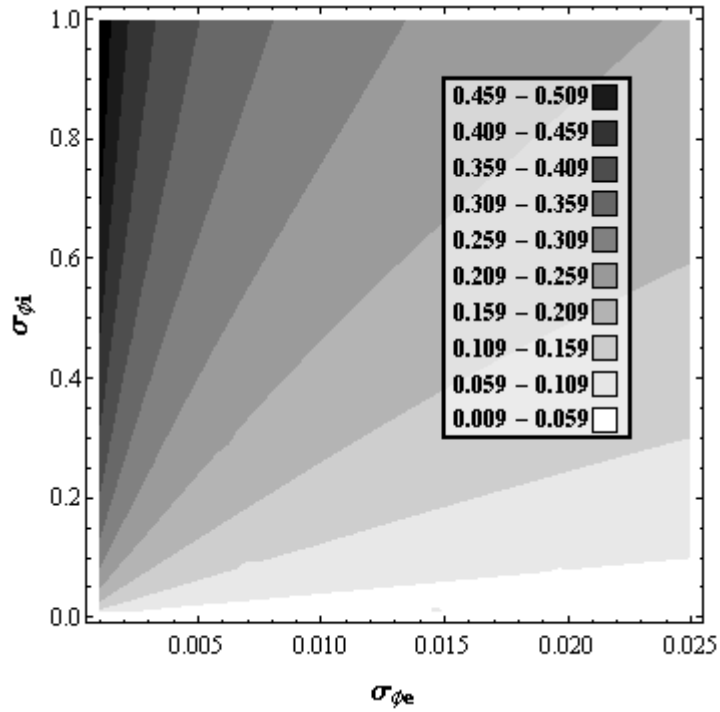


Fig. 199:  $Y_{\text{core}}$  with respect to  $\sigma_{e\phi}$  and  $\sigma_{i\phi}$ . This plot is computed with  $P_i = 276 \text{ mA kV}^{-3/2}$  and  $\beta = 0.67$ .

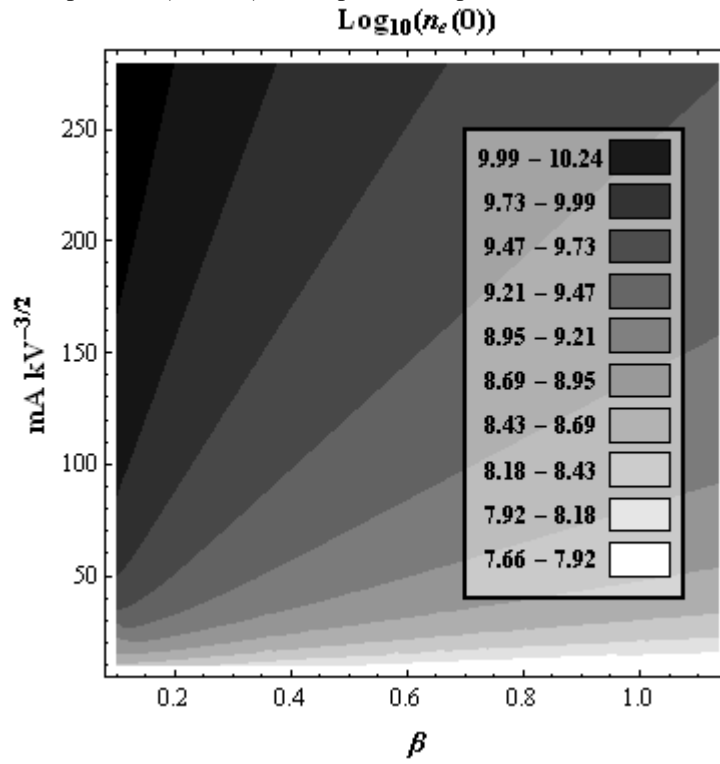


Fig. 200:  $\text{Log}_{10}(n_e(0))$  with respect to  $P_i$  and  $\beta$ . This plot is computed with  $\sigma_{e\phi} = 0.005$  and  $\sigma_{i\phi} = 0.05$ . The units are  $V^{-1} \text{ cm}^{-1}$  as density scales with  $|V_g|/R_g^2$  where  $V_g$  is the grid potential and  $R_g$  is the grid radius.

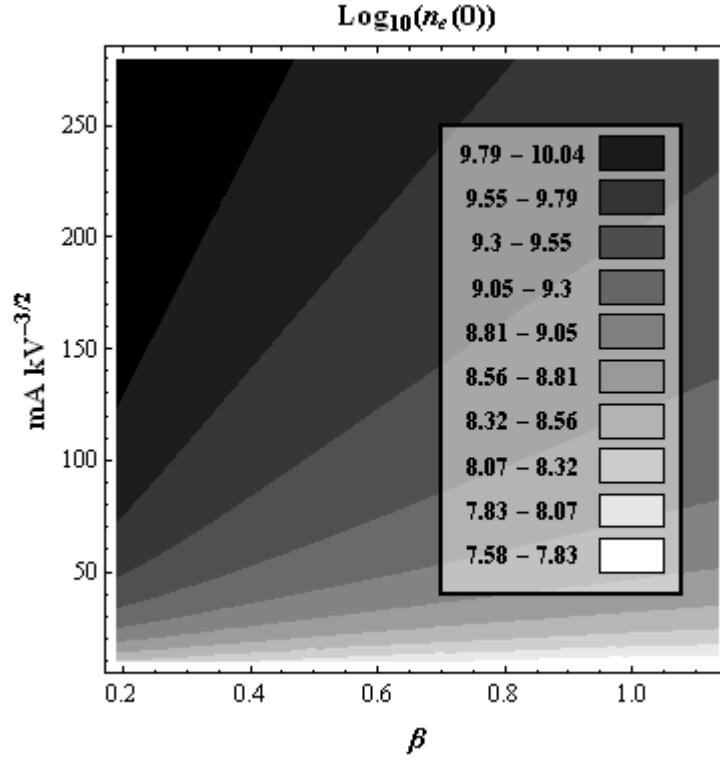


Fig. 201:  $\text{Log}_{10}(n_e(0))$  with respect to  $P_i$  and  $\beta$ . This plot is computed with  $\sigma_{e\phi} = 0.005$  and  $\sigma_{i\phi} = 0.10$ . The units are  $V^{-1} \text{cm}^{-1}$  as density scales with  $|V_g|/R_g^2$  where  $V_g$  is the grid potential and  $R_g$  is the grid radius.

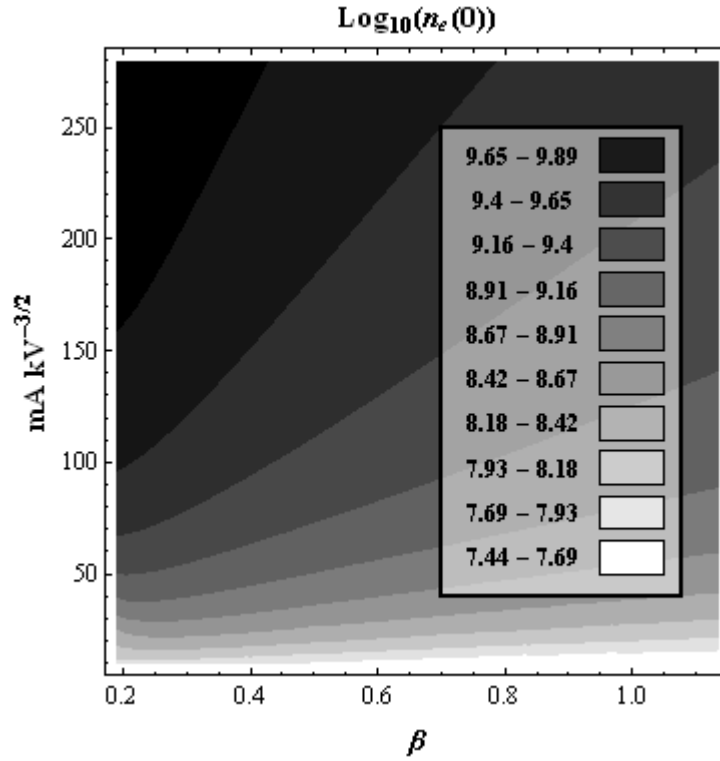


Fig. 202:  $\text{Log}_{10}(n_e(0))$  with respect to  $P_i$  and  $\beta$ . This plot is computed with  $\sigma_{e\phi} = 0.005$  and  $\sigma_{i\phi} = 0.10$ . The units are  $V^{-1} \text{cm}^{-1}$  as density scales with  $|V_g|/R_g^2$  where  $V_g$  is the grid potential and  $R_g$  is the grid radius.

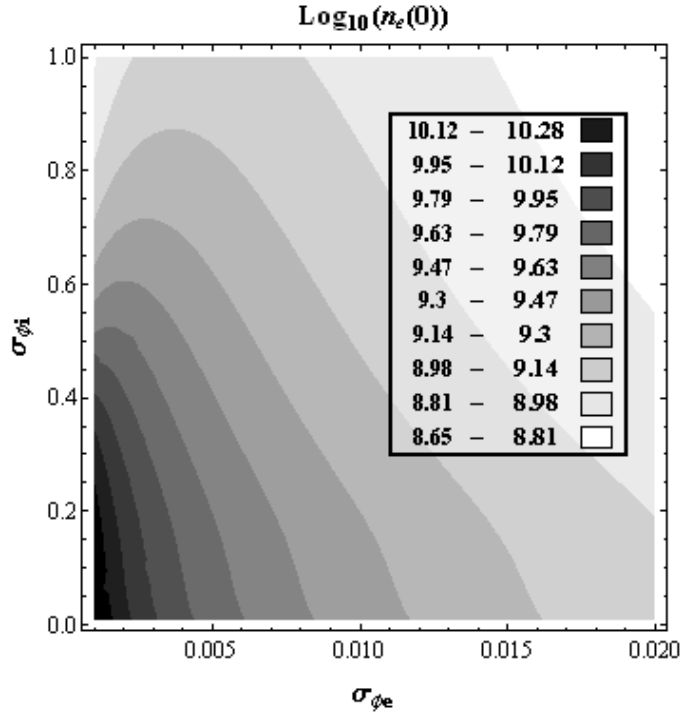


Fig. 203:  $\text{Log}_{10}(n_e(0))$  with respect to  $\sigma_{e\phi}$  and  $\sigma_{i\phi}$ . This plot is computed with  $P_i = 100 \text{ mA kV}^{-3/2}$  and  $\beta = 0.25$ . The units are  $V^{-1} \text{ cm}^{-1}$  as density scales with  $|V_g|/R_g^2$  where  $V_g$  is the grid potential and  $R_g$  is the grid radius.

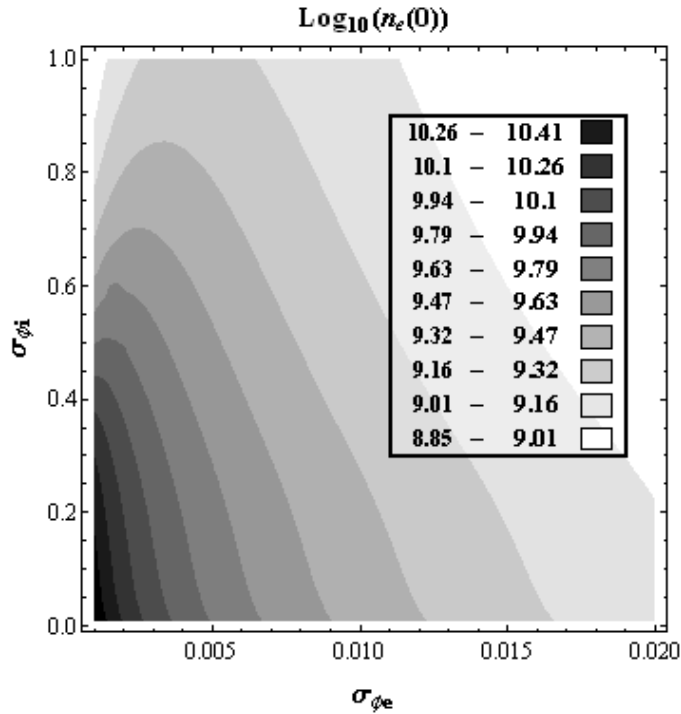


Fig. 204:  $\text{Log}_{10}(n_e(0))$  with respect to  $\sigma_{e\phi}$  and  $\sigma_{i\phi}$ . This plot is computed with  $P_i = 138 \text{ mA kV}^{-3/2}$  and  $\beta = 0.25$ . The units are  $V^{-1} \text{ cm}^{-1}$  as density scales with  $|V_g|/R_g^2$  where  $V_g$  is the grid potential and  $R_g$  is the grid radius.

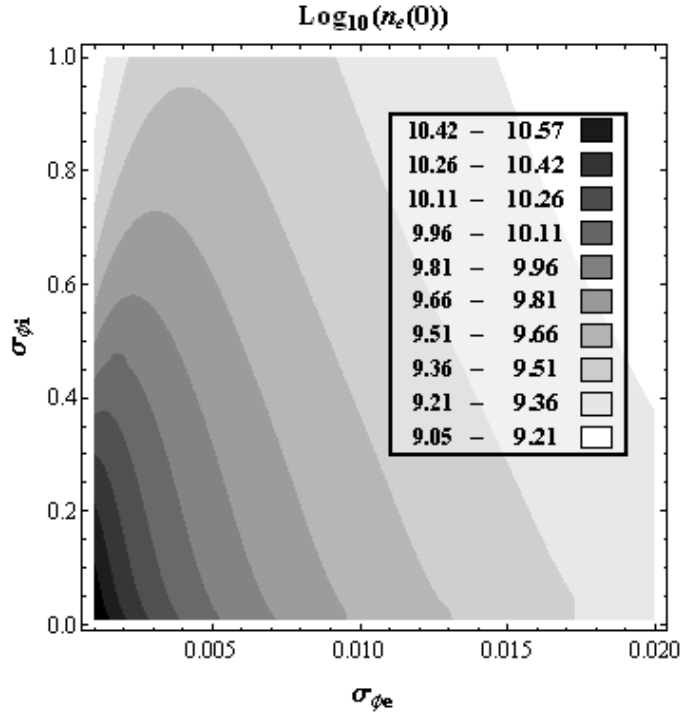


Fig. 205:  $\text{Log}_{10}(n_c(0))$  with respect to  $\sigma_{e\phi}$  and  $\sigma_{i\phi}$ . This plot is computed with  $P_i = 200 \text{ mA kV}^{-3/2}$  and  $\beta = 0.25$ . The units are  $V^{-1} \text{ cm}^{-1}$  as density scales with  $|V_g|/R_g^2$  where  $V_g$  is the grid potential and  $R_g$  is the grid radius.

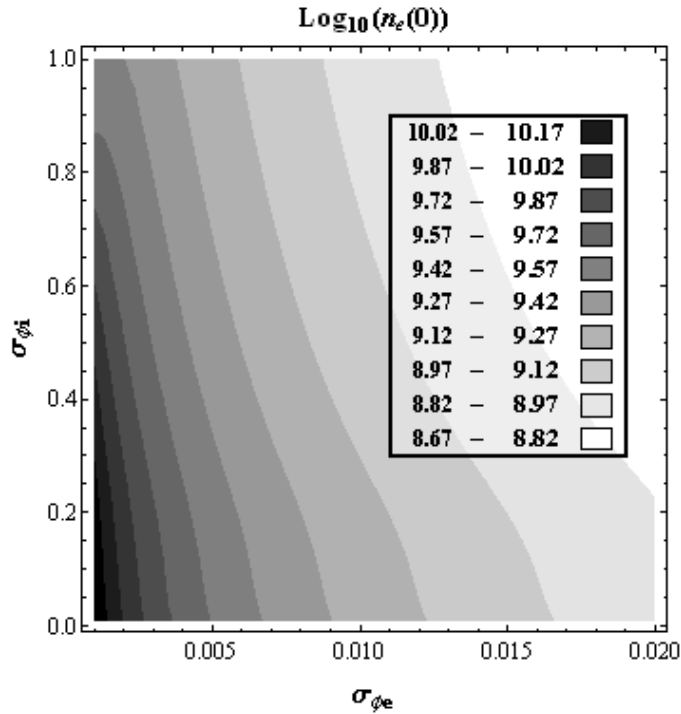


Fig. 206:  $\text{Log}_{10}(n_c(0))$  with respect to  $\sigma_{e\phi}$  and  $\sigma_{i\phi}$ . This plot is computed with  $P_i = 100 \text{ mA kV}^{-3/2}$  and  $\beta = 0.33$ . The units are  $V^{-1} \text{ cm}^{-1}$  as density scales with  $|V_g|/R_g^2$  where  $V_g$  is the grid potential and  $R_g$  is the grid radius.

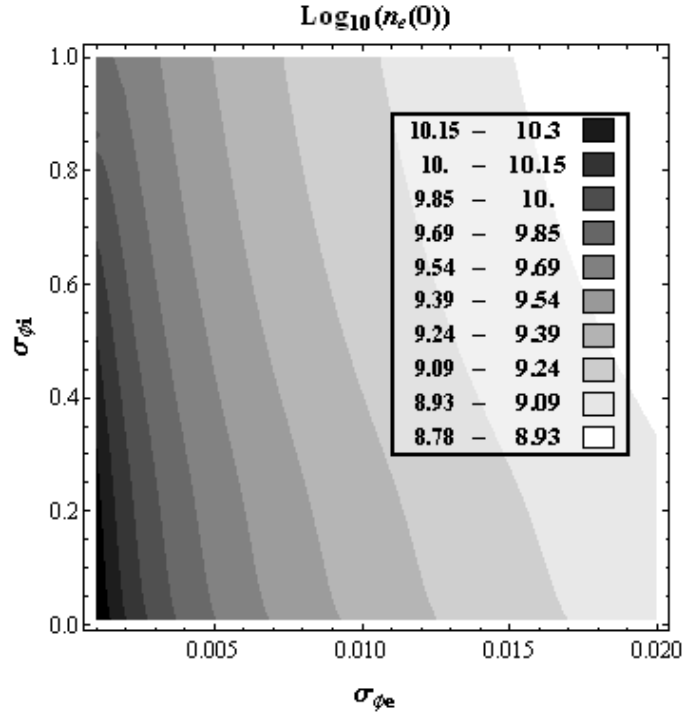


Fig. 207:  $\text{Log}_{10}(n_e(0))$  with respect to  $\sigma_{e\phi}$  and  $\sigma_{i\phi}$ . This plot is computed with  $P_i = 138 \text{ mA kV}^{-3/2}$  and  $\beta = 0.33$ . The units are  $V^{-1} \text{ cm}^{-1}$  as density scales with  $|V_g|/R_g^2$  where  $V_g$  is the grid potential and  $R_g$  is the grid radius.

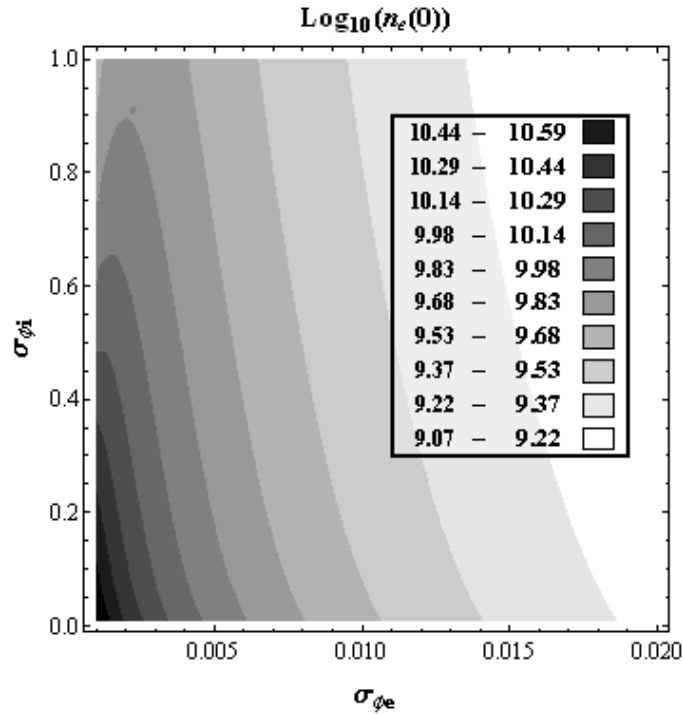


Fig. 208:  $\text{Log}_{10}(n_e(0))$  with respect to  $\sigma_{e\phi}$  and  $\sigma_{i\phi}$ . This plot is computed with  $P_i = 276 \text{ mA kV}^{-3/2}$  and  $\beta = 0.33$ . The units are  $V^{-1} \text{ cm}^{-1}$  as density scales with  $|V_g|/R_g^2$  where  $V_g$  is the grid potential and  $R_g$  is the grid radius.

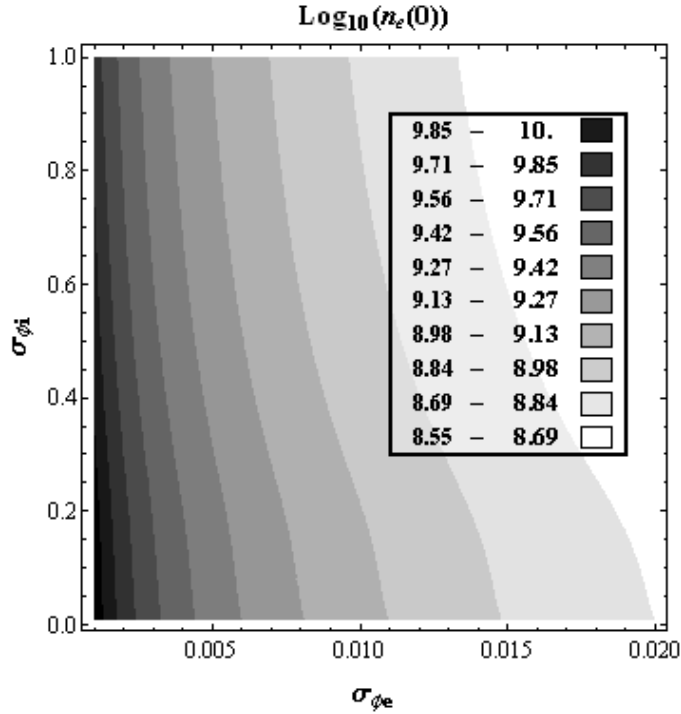


Fig. 209:  $\text{Log}_{10}(n_e(0))$  with respect to  $\sigma_{e\phi}$  and  $\sigma_{i\phi}$ . This plot is computed with  $P_i = 100 \text{ mA kV}^{-3/2}$  and  $\beta = 0.50$ . The units are  $V^{-1} \text{ cm}^{-1}$  as density scales with  $|V_g|/R_g^2$  where  $V_g$  is the grid potential and  $R_g$  is the grid radius.

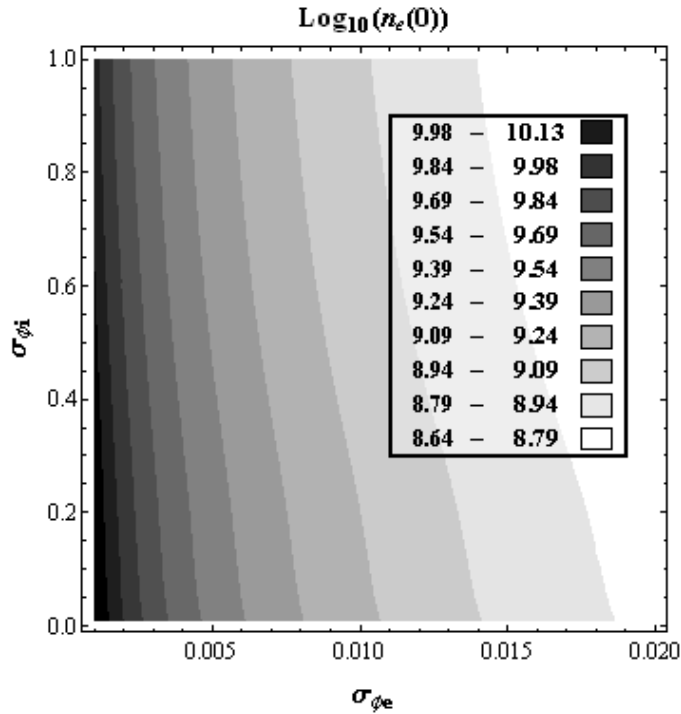


Fig. 210:  $\text{Log}_{10}(n_e(0))$  with respect to  $\sigma_{e\phi}$  and  $\sigma_{i\phi}$ . This plot is computed with  $P_i = 138 \text{ mA kV}^{-3/2}$  and  $\beta = 0.50$ . The units are  $V^{-1} \text{ cm}^{-1}$  as density scales with  $|V_g|/R_g^2$  where  $V_g$  is the grid potential and  $R_g$  is the grid radius.

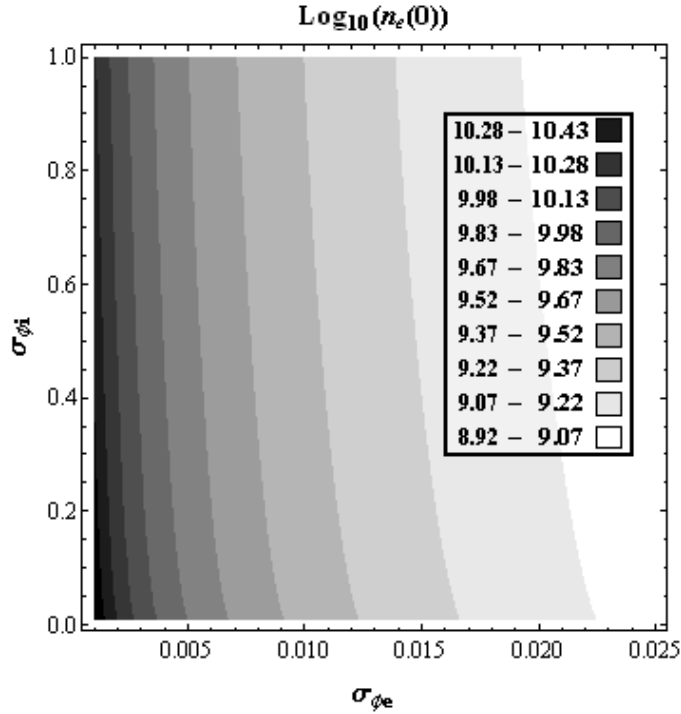


Fig. 211:  $\text{Log}_{10}(n_e(0))$  with respect to  $\sigma_{e\phi}$  and  $\sigma_{i\phi}$ . This plot is computed with  $P_i = 276 \text{ mA kV}^{-3/2}$  and  $\beta = 0.50$ . The units are  $V^{-1} \text{ cm}^{-1}$  as density scales with  $|V_g|/R_g^2$  where  $V_g$  is the grid potential and  $R_g$  is the grid radius.

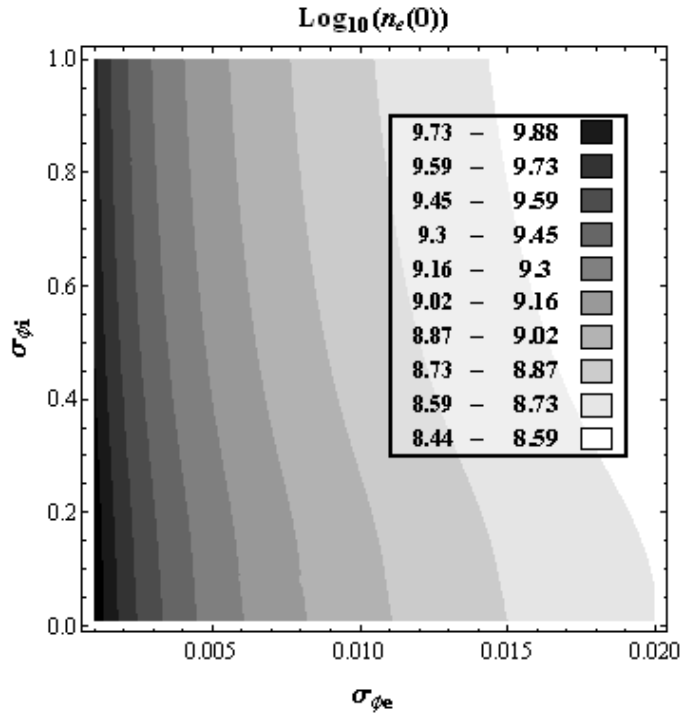


Fig. 212:  $\text{Log}_{10}(n_e(0))$  with respect to  $\sigma_{e\phi}$  and  $\sigma_{i\phi}$ . This plot is computed with  $P_i = 100 \text{ mA kV}^{-3/2}$  and  $\beta = 0.67$ . The units are  $V^{-1} \text{ cm}^{-1}$  as density scales with  $|V_g|/R_g^2$  where  $V_g$  is the grid potential and  $R_g$  is the grid radius.

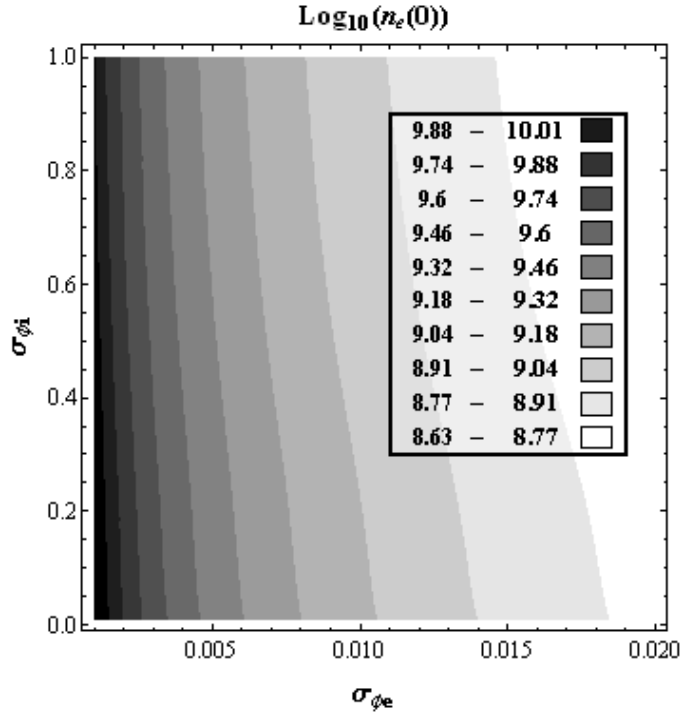


Fig. 213:  $\text{Log}_{10}(n_c(0))$  with respect to  $\sigma_{e\phi}$  and  $\sigma_{i\phi}$ . This plot is computed with  $P_i = 138 \text{ mA kV}^{-3/2}$  and  $\beta = 0.67$ . The units are  $V^{-1} \text{ cm}^{-1}$  as density scales with  $|V_g|/R_g^2$  where  $V_g$  is the grid potential and  $R_g$  is the grid radius.

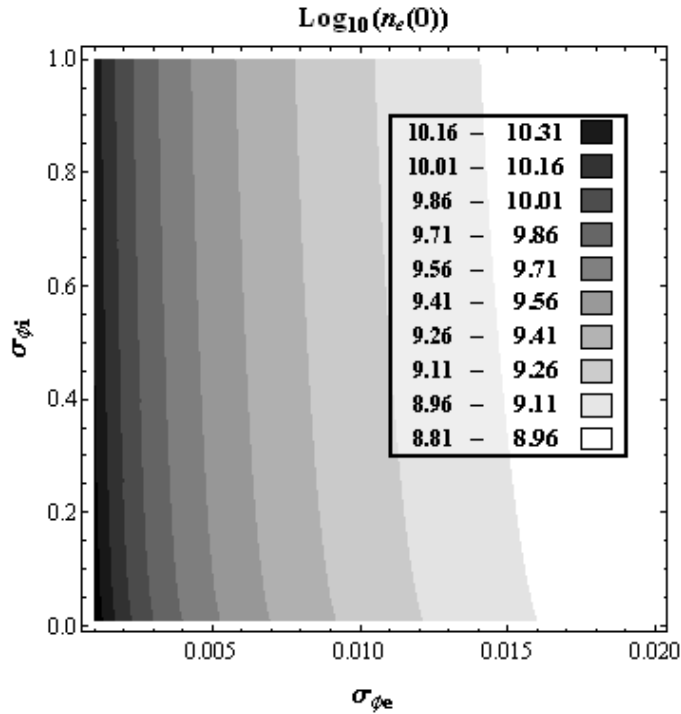


Fig. 214:  $\text{Log}_{10}(n_c(0))$  with respect to  $\sigma_{e\phi}$  and  $\sigma_{i\phi}$ . This plot is computed with  $P_i = 276 \text{ mA kV}^{-3/2}$  and  $\beta = 0.67$ . The units are  $V^{-1} \text{ cm}^{-1}$  as density scales with  $|V_g|/R_g^2$  where  $V_g$  is the grid potential and  $R_g$  is the grid radius.

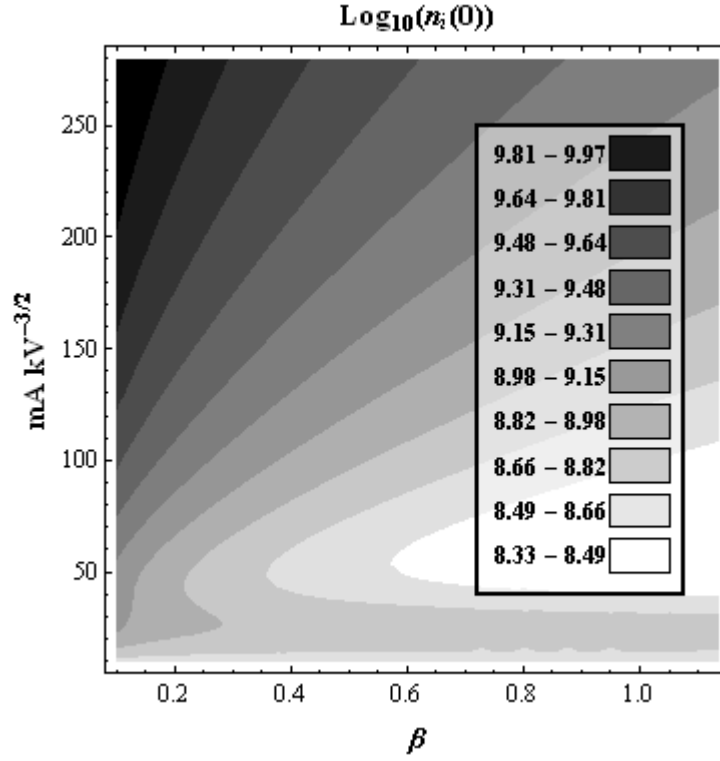


Fig. 215:  $\text{Log}_{10}(n_i(0))$  with respect to  $P_i$  and  $\beta$ . This plot is computed with  $\sigma_{e\phi} = 0.005$  and  $\sigma_{i\phi} = 0.05$ . The units are  $V^{-1} \text{cm}^{-1}$  as density scales with  $|V_g|/R_g^2$  where  $V_g$  is the grid potential and  $R_g$  is the grid radius.

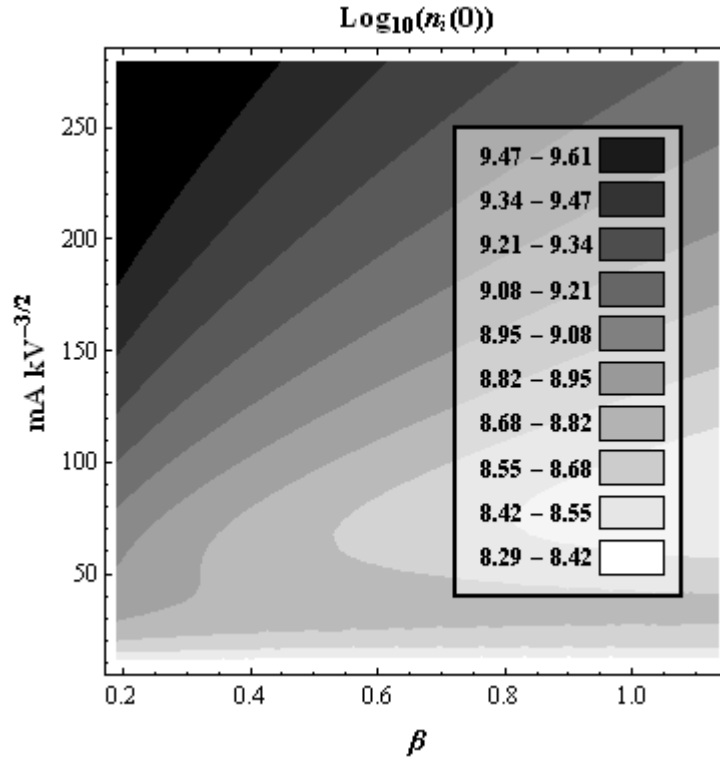


Fig. 216:  $\text{Log}_{10}(n_i(0))$  with respect to  $P_i$  and  $\beta$ . This plot is computed with  $\sigma_{e\phi} = 0.005$  and  $\sigma_{i\phi} = 0.10$ . The units are  $V^{-1} \text{cm}^{-1}$  as density scales with  $|V_g|/R_g^2$  where  $V_g$  is the grid potential and  $R_g$  is the grid radius.

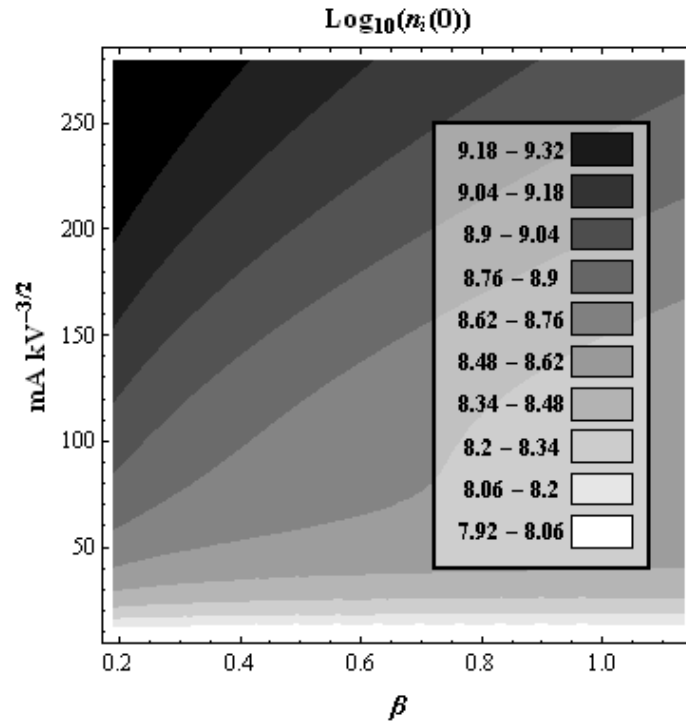


Fig. 217:  $\text{Log}_{10}(n_i(0))$  with respect to  $P_i$  and  $\beta$ . This plot is computed with  $\sigma_{e\phi} = 0.005$  and  $\sigma_{i\phi} = 0.25$ . The units are  $V^{-1} \text{cm}^{-1}$  as density scales with  $|V_g|/R_g^2$  where  $V_g$  is the grid potential and  $R_g$  is the grid radius.

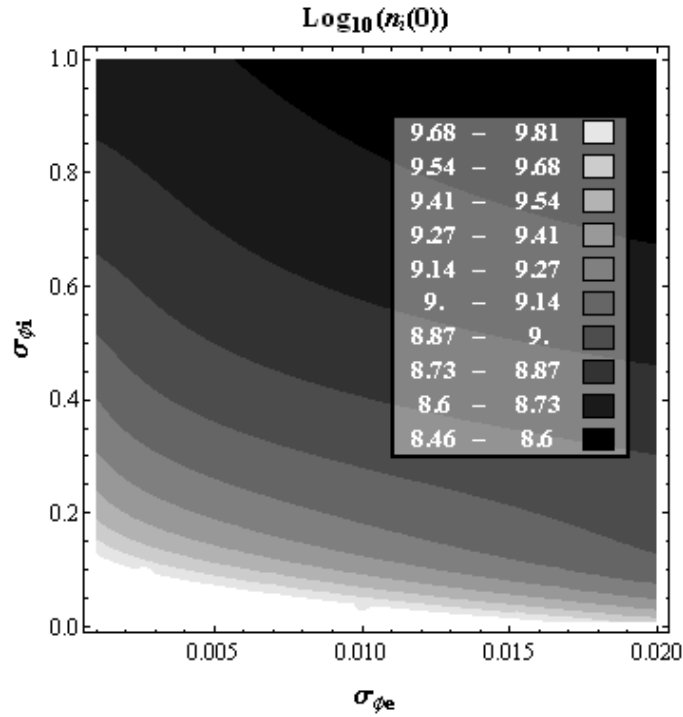


Fig. 218:  $\text{Log}_{10}(n_i(0))$  with respect to  $\sigma_{e\phi}$  and  $\sigma_{i\phi}$ . This plot is computed with  $P_i = 100 \text{ mA kV}^{-3/2}$  and  $\beta = 0.25$ . The units are  $V^{-1} \text{cm}^{-1}$  as density scales with  $|V_g|/R_g^2$  where  $V_g$  is the grid potential and  $R_g$  is the grid radius.

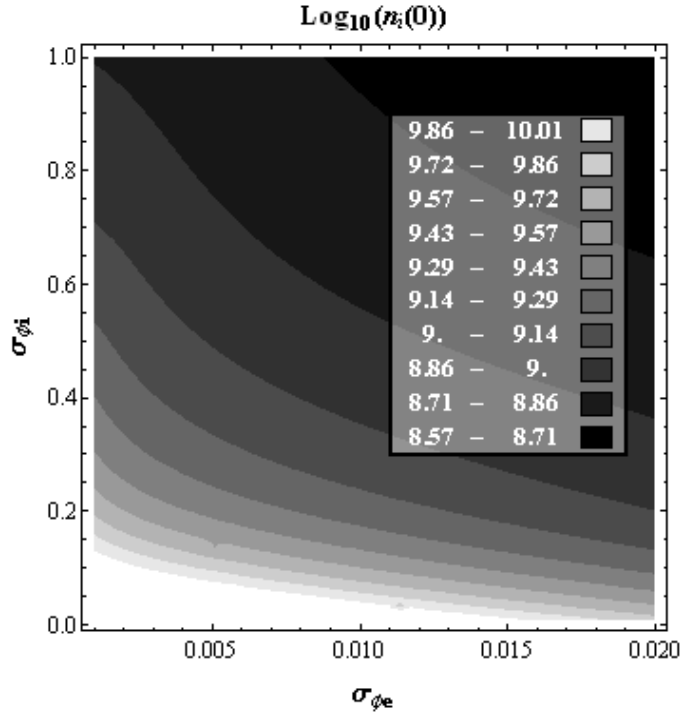


Fig. 219:  $\text{Log}_{10}(n_i(0))$  with respect to  $\sigma_{e\phi}$  and  $\sigma_{i\phi}$ . This plot is computed with  $P_i = 138 \text{ mA kV}^{-3/2}$  and  $\beta = 0.25$ . The units are  $V^{-1} \text{ cm}^{-1}$  as density scales with  $|V_g|/R_g^2$  where  $V_g$  is the grid potential and  $R_g$  is the grid radius.

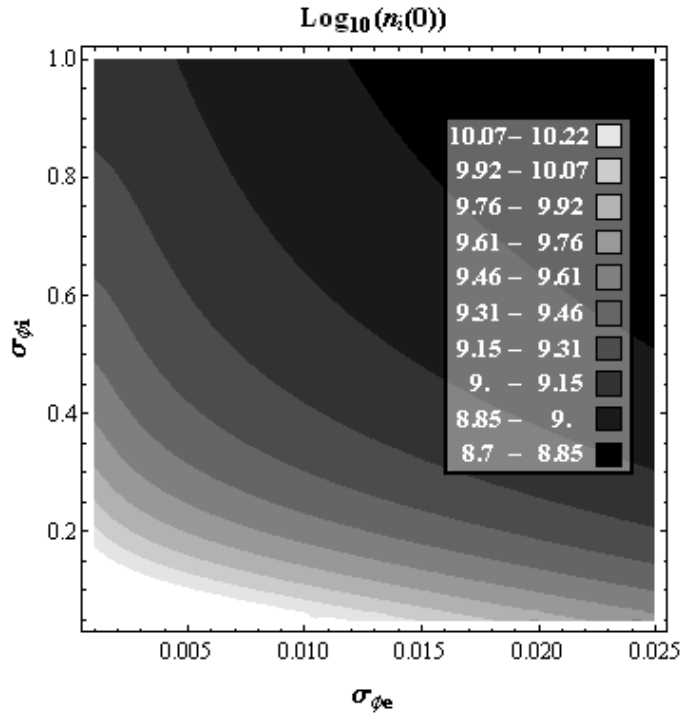


Fig. 220:  $\text{Log}_{10}(n_i(0))$  with respect to  $\sigma_{e\phi}$  and  $\sigma_{i\phi}$ . This plot is computed with  $P_i = 200 \text{ mA kV}^{-3/2}$  and  $\beta = 0.25$ . The units are  $V^{-1} \text{ cm}^{-1}$  as density scales with  $|V_g|/R_g^2$  where  $V_g$  is the grid potential and  $R_g$  is the grid radius.

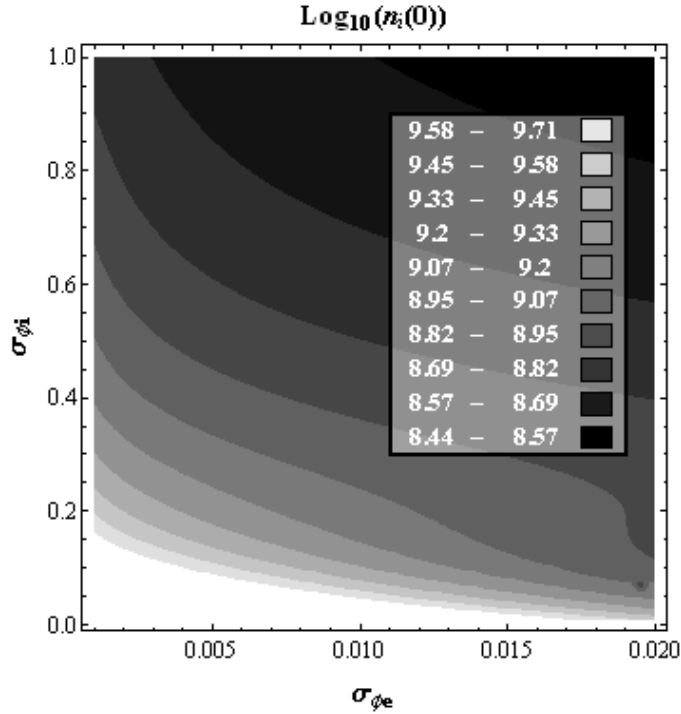


Fig. 221:  $\text{Log}_{10}(n_i(0))$  with respect to  $\sigma_{e\phi}$  and  $\sigma_{i\phi}$ . This plot is computed with  $P_i = 100 \text{ mA kV}^{-3/2}$  and  $\beta = 0.33$ . The units are  $V^{-1} \text{ cm}^{-1}$  as density scales with  $|V_g|/R_g^2$  where  $V_g$  is the grid potential and  $R_g$  is the grid radius.

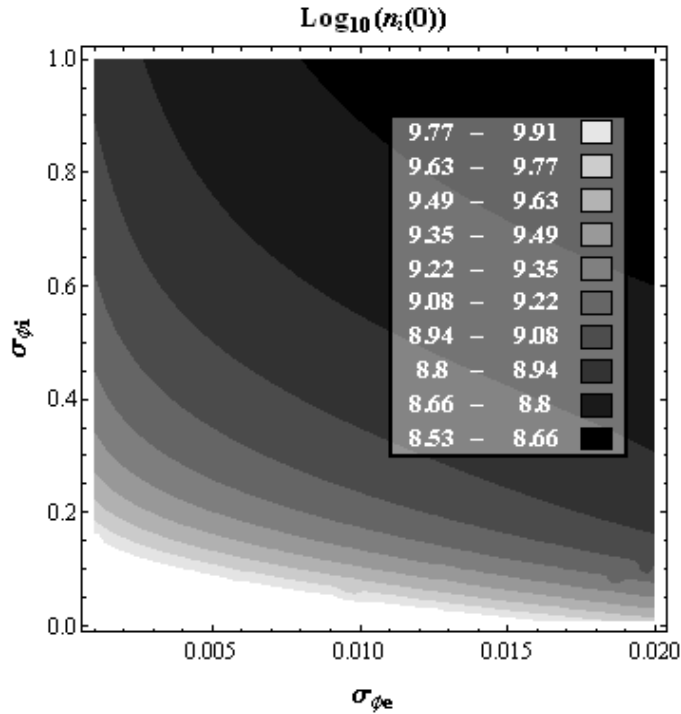


Fig. 222:  $\text{Log}_{10}(n_i(0))$  with respect to  $\sigma_{e\phi}$  and  $\sigma_{i\phi}$ . This plot is computed with  $P_i = 138 \text{ mA kV}^{-3/2}$  and  $\beta = 0.33$ . The units are  $V^{-1} \text{ cm}^{-1}$  as density scales with  $|V_g|/R_g^2$  where  $V_g$  is the grid potential and  $R_g$  is the grid radius.

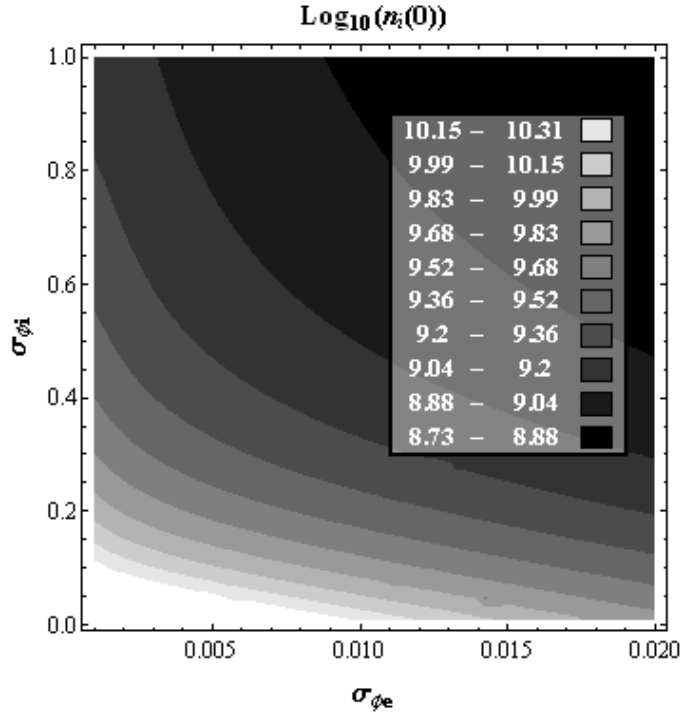


Fig. 223:  $\text{Log}_{10}(n_i(0))$  with respect to  $\sigma_{e\phi}$  and  $\sigma_{i\phi}$ . This plot is computed with  $P_i = 276 \text{ mA kV}^{-3/2}$  and  $\beta = 0.33$ . The units are  $V^{-1} \text{ cm}^{-1}$  as density scales with  $|V_g|/R_g^2$  where  $V_g$  is the grid potential and  $R_g$  is the grid radius.

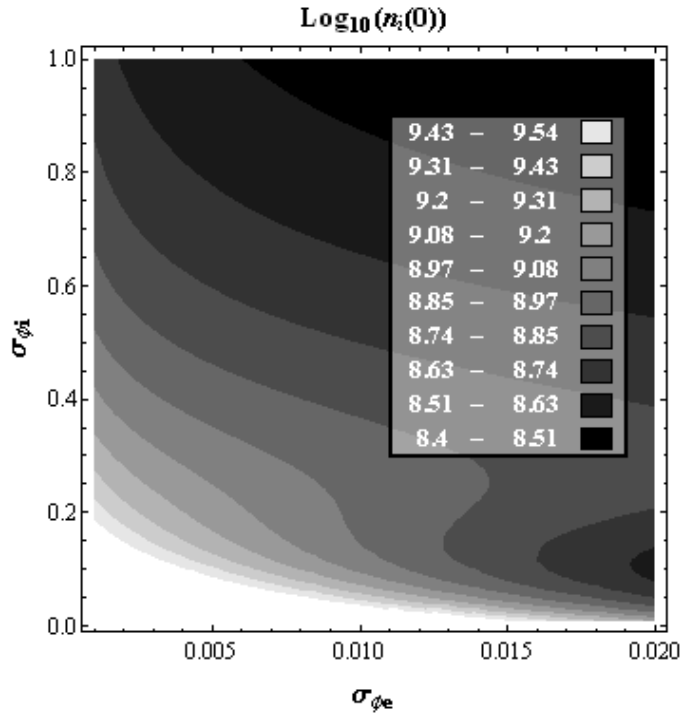


Fig. 224:  $\text{Log}_{10}(n_i(0))$  with respect to  $\sigma_{e\phi}$  and  $\sigma_{i\phi}$ . This plot is computed with  $P_i = 100 \text{ mA kV}^{-3/2}$  and  $\beta = 0.50$ . The units are  $V^{-1} \text{ cm}^{-1}$  as density scales with  $|V_g|/R_g^2$  where  $V_g$  is the grid potential and  $R_g$  is the grid radius.

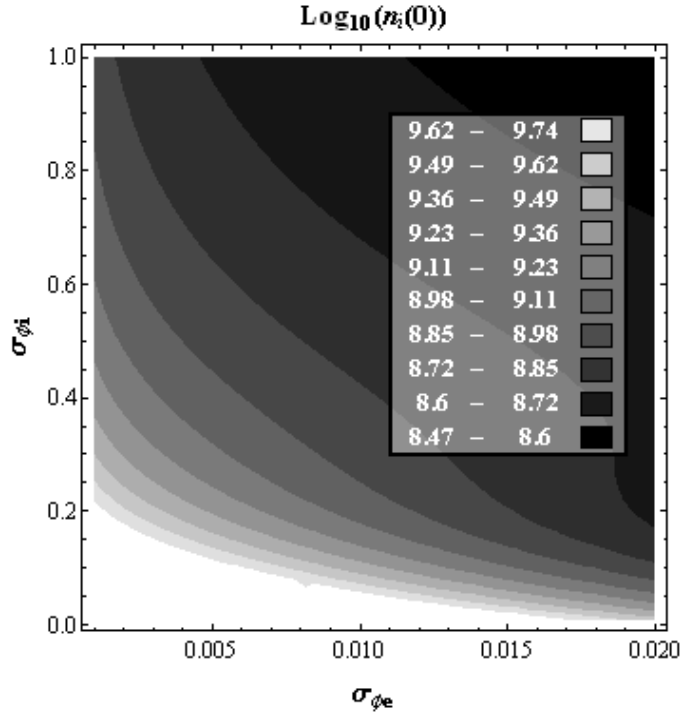


Fig. 225:  $\text{Log}_{10}(n_i(0))$  with respect to  $\sigma_{e\phi}$  and  $\sigma_{i\phi}$ . This plot is computed with  $P_i = 138 \text{ mA kV}^{-3/2}$  and  $\beta = 0.50$ . The units are  $V^{-1} \text{ cm}^{-1}$  as density scales with  $|V_g|/R_g^2$  where  $V_g$  is the grid potential and  $R_g$  is the grid radius.

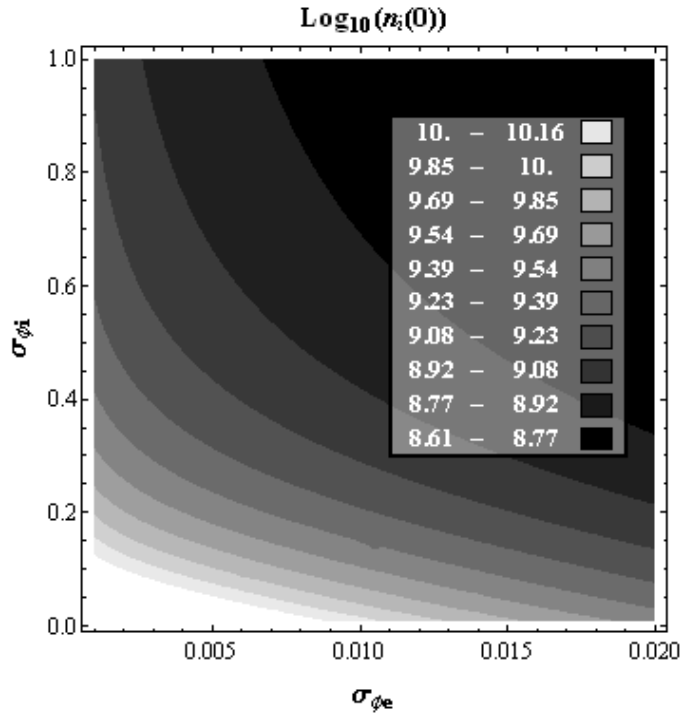


Fig. 226:  $\text{Log}_{10}(n_i(0))$  with respect to  $\sigma_{e\phi}$  and  $\sigma_{i\phi}$ . This plot is computed with  $P_i = 276 \text{ mA kV}^{-3/2}$  and  $\beta = 0.50$ . The units are  $V^{-1} \text{ cm}^{-1}$  as density scales with  $|V_g|/R_g^2$  where  $V_g$  is the grid potential and  $R_g$  is the grid radius.

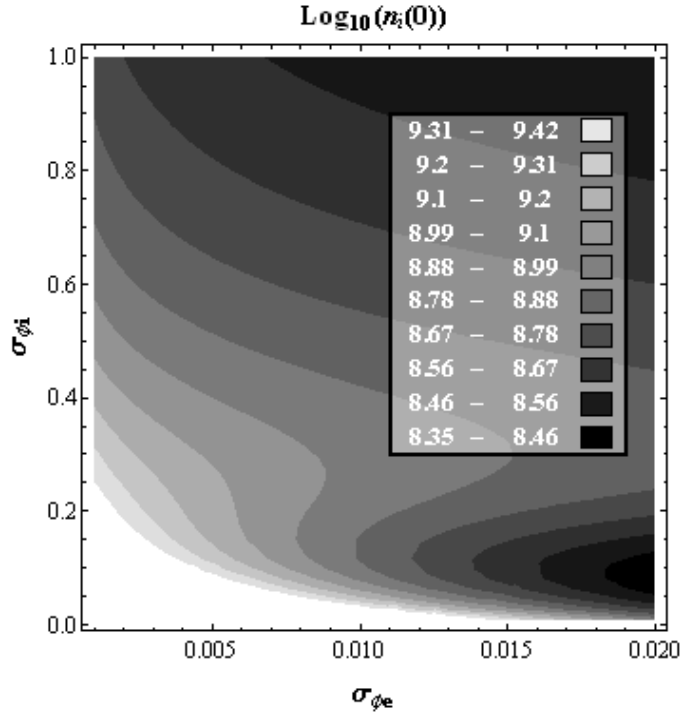


Fig. 227:  $\text{Log}_{10}(n_i(0))$  with respect to  $\sigma_{e\phi}$  and  $\sigma_{i\phi}$ . This plot is computed with  $P_i = 100 \text{ mA kV}^{-3/2}$  and  $\beta = 0.67$ . The units are  $V^{-1} \text{ cm}^{-1}$  as density scales with  $|V_g|/R_g^2$  where  $V_g$  is the grid potential and  $R_g$  is the grid radius.

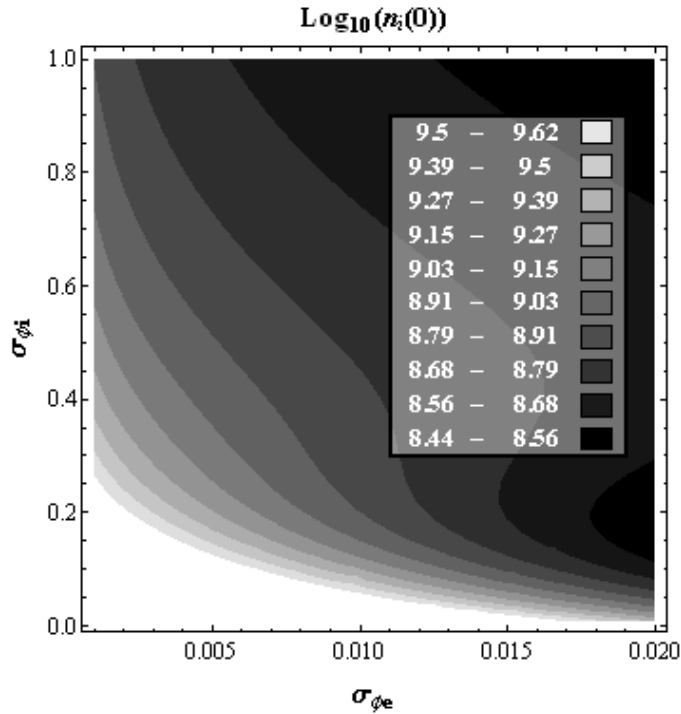


Fig. 228:  $\text{Log}_{10}(n_i(0))$  with respect to  $\sigma_{e\phi}$  and  $\sigma_{i\phi}$ . This plot is computed with  $P_i = 138 \text{ mA kV}^{-3/2}$  and  $\beta = 0.67$ . The units are  $V^{-1} \text{ cm}^{-1}$  as density scales with  $|V_g|/R_g^2$  where  $V_g$  is the grid potential and  $R_g$  is the grid radius.

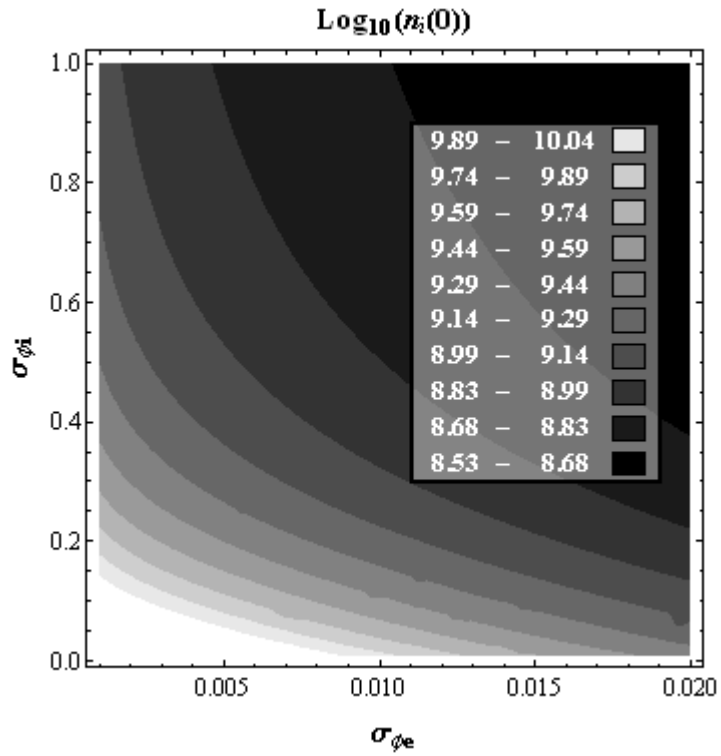


Fig. 229:  $\text{Log}_{10}(n_i(0))$  with respect to  $\sigma_{e\phi}$  and  $\sigma_{i\phi}$ . This plot is computed with  $P_i = 276 \text{ mA kV}^{-3/2}$  and  $\beta = 0.67$ . The units are  $V^{-1} \text{ cm}^{-1}$  as density scales with  $|V_g|/R_g^2$  where  $V_g$  is the grid potential and  $R_g$  is the grid radius.

## APPENDIX B: Langmuir Probe Analysis

The methods employed for analyzing the I-V curves from the double and single probes are discussed here. Planar disk collectors are used in the experiments, and the method of analysis is based on a thin, collision-less sheath assumption, such that  $x_s \ll \lambda$  and  $x_s \ll a$ , where  $\lambda$  represents the mean free path of ions or electrons,  $x_s$  is the sheath thickness, and  $a$  is the diameter of the planar collecting disk. In this case, the collected current is assumed to be equal to the amount of current which flows through the sheath boundary adjacent to the planar probe surface.

### A. *Sheath Structure*

In quasi-neutral plasma where the electrons and ions have equal energies, the electron flux normal to an adjacent surface will be much greater than the ion flux because of the much greater electron mobility. Thus, if this surface is absorbing, it will quickly collect an excess of negative charge, pulling the potential of the surface negative with respect to the rest of the plasma. The potential of the surface will continue to decrease until enough electrons become repelled by the negative field, that the surface collects equal numbers of electrons and positive ions. The negative potential of the surface also accelerates a number of ions so that in the immediate proximity of the surface, a region of high ion density and negligible electron density forms. This region of high ion density, over which most of the potential drop occurs is commonly referred to as the sheath, and is depicted in Fig. 230. It has further been shown that for situations in which  $kT_i \ll kT_e$ , ions are accelerated by the weak electric field in the pre-sheath region so that they arrive at the sheath edge,  $x_s$ , with a velocity given by Eq. (29). The sheath-presheath boundary

$$v_b = \sqrt{\frac{kT_e}{m_i}} \quad (29)$$

is defined such that quasi-neutrality is satisfied up to this boundary, ( $n_i \sim n_e$ ). As a result, the ion density can be inferred from the electron density in this region. Considering that the voltage drop from the bulk plasma to the sheath-presheath boundary,  $x_s$ , is  $V_\infty - V_s$ , then, by conservation of energy, we have Eq. (30), where  $V_\infty$  bulk plasma potential, and  $V_s$  is the potential at  $x_s$ . From Boltzmann's relation, we can thus see that the ion density at  $x_s$  is  $\sim 0.61 n_\infty$ , where  $n_\infty$  is the bulk plasma density.

$$e(V_\infty - V_s) = \frac{kT_e}{2} \quad (30)$$

### **B. Current Collected by a Negatively Biased Probe**

The current of ions ( $j = 0$ ) or electrons ( $j = 1$ ) flowing to a collecting surface can be represented by Eq. (31), where  $I_j$  is the total current due to species  $j$ ,  $n_j$  is the number density of species  $j$ ,  $v_j$  is the velocity of species  $j$ ,  $e$  is the magnitude of electronic charge,  $V_b$  is the bias potential applied to the collector, and  $A$  is the collecting area. First, we can consider the ion flow to a negatively biased collector. In this case,  $n_0 \sim 0.61 n_\infty$ , and  $v_0$  is as given in Eq. (29). The result is that the ion current can be represented by Eq. (32), while the electron current is given in Eq. (33).

$$I_j = (-1)^j e n_j v_j A \quad (31)$$

$$I_0 = 0.61 e n_\infty \left( \frac{kT_e}{m_i} \right)^{1/2} A \quad (32)$$

$$I_1 = -\frac{1}{4} e n_\infty \left( \frac{8kT_e}{\pi m_e} \right)^{1/2} e^{-e(V_\infty - V_b)/kT_e} A \quad (33)$$

### C. *Single Langmuir Probe Analysis*

The electron temperature can be determined from the electron current by taking the natural logarithm of the expression for electron current in Eq. (33), resulting in Eq. (34). This expression can be differentiated with respect to the probe bias,  $V_b$  to determine the electron temperature  $kT_e$ , with Eq. (35).

$$\text{Log}(I_1) = \text{const.} - \frac{e(V_\infty - V_b)}{kT_e} \quad (34)$$

$$\frac{\partial \text{Log}(I_i)}{\partial V_b} = \frac{e}{kT_e} \quad (35)$$

This represents the ideal case, however, when no ion current is present. When the probe collects an appreciable ion current, one measures the total current  $I = I_1 + I_0$ . In this case, the ion current,  $I_0$ , must be subtracted off before plotting the logarithm of the current. Equations (34) and (35) are modified in Eqs. (36) and (37).

$$\text{Log}(I - I_0) = \text{const.} - \frac{e(V_\infty - V_b)}{kT_e} \quad (36)$$

$$\frac{\partial \text{Log}(I - I_0)}{\partial V_b} = \frac{e}{kT_e} \quad (37)$$

The plot of Eq. (37) reveals a kink in the curve at the plasma potential, beyond which electrons experience an accelerating force instead of a repelling force. Straight lines can be fit to portions of the curve on either side of the kink, as illustrated in Fig. 231. The slope of line a-a' determines the electron temperature per Eq. (37). The intersection of lines a-a' and b-b' yield the plasma potential,  $V_\infty$  and electron saturation current  $I_{es}$ . An expression for  $I_{es}$  is found by setting  $V_b = V_\infty$  in Eq. (33). The electron density can be calculated once  $I_{es}$  is known, as shown,

$$n_e = \frac{4I_{es}}{e \left( \frac{8kT_e}{\pi m_e} \right)^{1/2} A}. \quad (38)$$

#### D. Double Probe Analysis

The double probe usually consists of two disks of nearly equal area. Both disks float with respect to the plasma and no net current is drained from the plasma as a result. If we consider the ratio of electron currents flowing to disk a and disk b, then by Eq. (33), we have,

$$\frac{I_{1a}}{I_{1b}} = \frac{A_1}{A_2} e^{(V_{ba}-V_{bb})/kT_e}. \quad (39)$$

From Kirchoff's current law,

$$I = I_{0a} + I_{1a} = -(I_{0b} + I_{1b}), \quad (40)$$

where  $I$  is the total current flowing through the probe. Equation (40) can be solved for  $I_{1a}$  and  $I_{1b}$  and inserted into Eq. (39), to get the following,

$$\frac{I_0 - I}{I_0 + I} = e^{(V_{ba}-V_{bb})/kT_e}, \quad (41)$$

assuming that  $A_1 = A_2$ , then  $I_0 = I_{0a} = I_{0b}$ . In this case, Eq. (41) can be written in the form,

$$I = I_0 \operatorname{Tan} \left( \frac{e(V_{ba} - V_{bb})}{2kT_e} \right). \quad (42)$$

The procedure for calculating  $kT_e$  is further simplified as it is known that the slope of the curve at the origin provides this information,

$$\left. \frac{dI}{d(V_{ba} - V_{bb})} \right|_{V_{ba}=V_{bb}} = \frac{eI_0}{kT_e}. \quad (43)$$

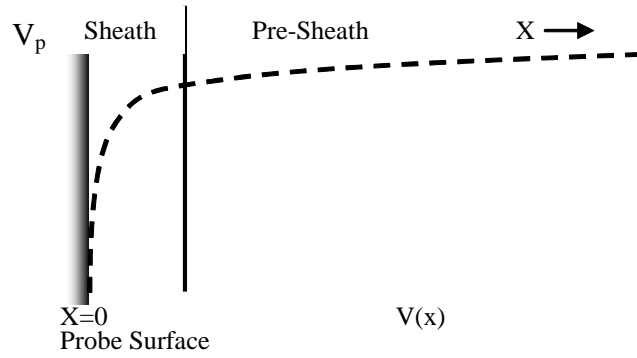


Fig. 230: Depiction of sheath and pre-sheath regions adjacent to a planar probe surface.

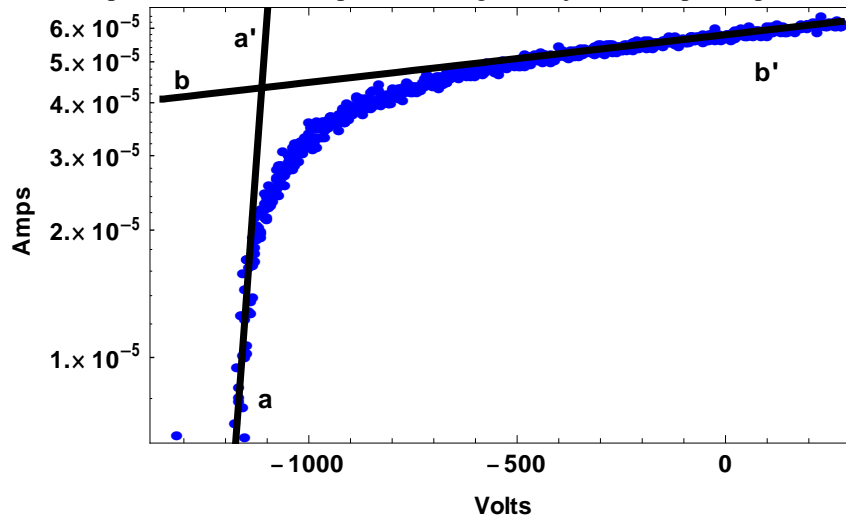


Fig. 231: Straight lines a-a' and b-b' are fit to portions of the curve on either side of the kink that occurs near the plasma potential. The slope of line a-a' determines  $kT_e$  while the intersection of lines a-a' and b-b' can determine the plasma potential,  $V_\infty$  and electron saturation current,  $I_{es}$ .

## APPENDIX C: List of Materials and Components

Table XII: List of materials and components for double and single Langmuir probe measurements

<i>Description</i>	<i>Manufacturer</i>	<i>Supplier</i>	<i>Part #</i>	<i>Website</i>
Linear Manipulator		KJ Lesker	KZLDS27504S	www.lesker.com
		Huntington	L-2151-4-A	www.huntvac.com
Stepper Motor		Lin Engineering	5718X-18DE-01	www.linengineering.com
		Olympus Controls	5718X-18DE-XX	www.olympus-controls.com
Stepper Motor Drivers		Ebay		
Optical Encoders		US Digital	E2-1000-250-IT	www.usdigital.com
Nipples and Tees		MDC Vacuum		www.mdcvacuum.com
		Duniway Stockroom		www.duniway.com
Alumina tubing for probe shaft		Vesuvius McDanel	AXS-750-b-30	www.techceramics.com
Alumina silicate		McMasterCarr	8479K92	www.mcmaster.com
Shaft collars		McMasterCarr	61005K41	www.mcmaster.com
Alumina adhesive		Aremco	Ceramabond 569	www.aremco.com
HV coaxial feedthroughs		Ceramtec	18001-01-CF	www.ceramtec.com
HV coaxial plugs	Kings Electronics	Allied Electronics	1709-1	www.alliedelec.com
Micro-coaxial cable		MDC Vacuum	680502	www.mdcvacuum.com
0.127mm Molybdenum foil		Alfa Aesar	41764	www.alfa.com
Isolation Transformers	Hammond	Allied Electronics	836-2075	www.alliedelec.com
Bi-polar Operational Amplifiers (BOPs)	Kepeco	Kandel Electronics		www.kandelelectronics.com
Isolation Amplifier IC	Analog Devices	Digikey	AD210AN-ND	www.digikey.com
Isolation Amplifier Socket	Analog Devices	Digikey	AC1059-ND	www.digikey.com
USB-6251 M Series DAQ	National Instruments	National Instruments	779627-01	www.ni.com
LabView	National Instruments	National Instruments	776670-09	www.ni.com

## VITA

Ryan Michael Meyer was born on August 25, 1980, and raised in Conception Junction, Missouri by his parents, Gerald and Rose Ann Meyer. He has obtained the following degrees in engineering from the University of Missouri in Columbia, Missouri: B.S. in Electrical Engineering (2002), M.S. in Nuclear Engineering (2004), Ph.D. in Nuclear Engineering (2007).

Ryan will begin work as a professor of Electrical Engineering at Prince of Songkhla University in Hat Yai, Thailand. There, he will join his fiancé, Pimphan (Aye) Kiatsimkul as an engineering faculty member.